Bioinspired oxidation reactions involving mono- and poly-nuclear transition metal complexes: hydrogen atom abstraction and group transfer reactions

Dissertation

zur Erlangung des akademischen Grades

doctor rerum naturalium

(Dr. rer. nat.)

im Fach Chemie

eingereicht an der

Mathematisch-Naturwissenschaftlichen Fakultät
der Humboldt-Universität zu Berlin

von

M. Sc. Inés Monte Pérez

Präsidentin der Humboldt-Universität zu Berlin
Prof. Dr.-Ing. Dr. Sabine Kunst

Dekan der Mathematisch-Naturwissenschaftlichen Fakultät
Prof. Dr. Elmar Kulke

Gutachter/innen:

1. Prof. Dr. Kallol Ray

2. Prof. Dr. Christian Limberg

Tag der mündlichen Prüfung:21.03.2017

Abstract

High-valent metal-oxo, -peroxo and -nitrene cores of late transition metals have been proposed as reactive intermediates in transformations, like the activation of C−H bonds in hydrocarbons and the reduction of dioxygen, that are both technologically attractive and fundamental for the functioning of biological systems. The isolation and characterization of such intermediates, despite being challenging, can provide valuable information about the mechanisms of the reactions performed and can help in the design of improved catalysts. In this Thesis, we have worked with three different kinds of intermediates, namely iron-oxo, cobalt-peroxo and copper-nitrenes, with the aim of examining the effect that small changes in the ligand system, the participating metal centers or the nitrene sources, have on the behavior of a given reactive system.

In our work with non-haem oxoiron(IV) complexes we found that, by placing the iron center in a weaker ligand-field environment - via the insertion of oxygen donors in the ligand system - the reactivity of the high-valent intermediate can be increased. Such increase in reactivity was assigned to a combination of factors such as the greater accessibility of the S = 2 state and the reduction of the steric hindrance around the iron-oxo core. An effect of the asymmetry of the ligand on the reactivity was also detected.

In our work with a hexanuclear cobalt complex, we could assign both nucleophilic and electrophilic character to a cobalt-peroxo intermediate formed in solution from the reaction of the hexanuclear cobalt complex with dioxygen. Interestingly, we found that the hexanuclear complex can also catalytically reduce dioxygen, in the presence of electron and proton sources, to H_2O_2 or H_2O depending on the temperature. This behavior proved to be in sharp contrast with the reaction performed by a hexanuclear iron complex supported by the same ligand that performs O−O bond formation, thus showing the enormous effect that the metal center has on the reactivity of a system.

Finally, we found that the nitrene source has an enormous impact on the stability and reactivity of terminal copper-nitrenes; *via* nitrene-source design we could -for the first time- isolate two terminal copper-nitrenes both as free species and as their Lewis acid-adducts. We also determined that the reactivity and the electronic structure of the copper-nitrene adducts are independent of the Lewis acid employed to stabilize them.

Taken together, we show in this work that the reactivity patterns of the high-valent reactive intermediates here studied depend greatly on subtle changes in the ligand system, the metal center and the oxidant employed.

Zusammenfassung

Hochvalente Metall-oxo-, -peroxo- und -nitrenzentren später Übergangsmetalle werden als reaktive Intermediate vieler technologisch interessanter und biologischer Transformationsreaktionen wie die Oxidation von Kohlenwasserstoffen, Hydroxylierung, Aminierung, Aziridierung und Sauerstoffreduktion angenommen. Die Isolierung und Charakterisierung solcher Intermediate, wenngleich sie sich schwierig gestaltet, kann wichtige Informationen zum Mechanismus solcher Reaktionen liefern und kann somit zu einer gezielten Optimierung und Herstellung von verbesserten Katalysatoren genutzt werden. In dieser Arbeit wurden drei unterschiedliche Intermediate – Eisenoxo-, Kobaltperoxo- und Kupfernitrenkomplexe – näher untersucht, mit dem Ziel den Einfluss des Ligandsystems bzw. des Zentralmetalls oder der Nitrenquelle auf das Reaktionsverhalten der Systeme zu ergründen.

Im Falle der nicht-Häm Eisen(IV)oxokomplexe konnte gezeigt werden, dass der Austausch eines Stickstoffdonors des Liganden durch einen Sauerstoffdonor zu einer erhöhten Reaktivität des Intermediates führt. Die erhöhte Reaktivität wurde durch eine Kombination mehrerer Faktoren begründet: Zum einen besteht ein erleichterter Zugang des S = 2 Zustands, zum anderen findet eine Reduktion der sterischen Abschirmung des Eisenoxo-Kerns statt. Zudem konnte gezeigt werden, dass die Asymmetrie des Liganden eine Erhöhung der Reaktivität zur Folge hat.

Bei der Umsetzung eines hexanuklearen Kobaltsystems mit molekularem Sauerstoff konnte ein Kobaltperoxointermediat in Lösung detektiert werden, welches sowohl nukleophilen als auch elektrophilen Charakter aufweist. Ebenso konnte gezeigt werden, dass der hexanukleare Komplex in der Lage ist Disauerstoff abhängig von der Temperatur und in Anwesenheit einer Elektronen- und Protonenquelle katalytisch entweder zu H_2O_2 oder H_2O zu reduzieren. Dies steht im starken Kontrast zu der Reaktivät, die für den entsprechenden hexanuklearen Eisenkomplex berichtet wurde. Dieser ist in der Lage an O–O-Bindungsknüpfungsreaktionen teilzunehmen, was den großen Effekt des Zentralmetalls auf die Reaktivität demonstriert.

Abschließend konnte durch die Untersuchung der Kupfernitrene gezeigt werden, dass die eingesetzte Nitrenquelle einen großen Effekt auf Stabilität und Reaktivität der gebildeten terminalen Kupfernitrenverbindung hat. Erstmalig gelang es, durch ein gezieltes Design der Nitrenquelle zwei terminale Kupfernitrene, sowohl als freie Spezies als auch als das Lewis-Säure-Addukt, zu isolieren. Es konnte ebenfalls gezeigt werden, dass die Reaktivität und die elektronische Struktur der Kupfernitrenkerne unabhängig von der zur Stabilisierung eingesetzten Lewis-Säure sind.

Es konnte somit in dieser Arbeit gezeigt werden, dass die Reaktivität der hier untersuchten hoch-valenten reaktiven Intermediate maßgeblich abhängig vom Ligandsystem, dem Zentralmetall und dem verwendeten Oxidanten sind.

This work was developed under the supervision of Prof. Dr. Kallol Ray from October 2012 to September 2016 at the Institut für Chemie of the Mathematisch-Naturwissenschaftliche Fakultät I at the Humboldt-Universität zu Berlin.

Acknowledgments

Firstly, I would like to express my sincere gratitude to Prof. Dr. Kallol Ray for the continuous support of my PhD studies, for his motivation and immense knowledge. He provided an enthusiastic guidance throughout the past four years that, though hard sometimes, allowed me to grow both professionally and personally.

I am indebted to Prof. Dr. Christian Limberg for the valuable suggestions and discussions during the group seminars and for being the second reviewer of my Thesis. I'm also thankful to him for allowing me to participate in the activities of his group and for giving me access to the instruments and equipment much necessary for the development of my work.

I would like to thank the members of the Ray group that accompanied me throughout the demanding process of learning to do independent research. My special thanks go to Xenia Engelmann, who has helped me the most during the last years with insightful discussions, amusing coffee-breaks and providing always a solidary and friendly hand; I am also thankful to her for the studies on oxoiron complexes that I present in this Thesis and that we developed together. Thanks to the former members of the group: Dr. Subrata Kundu, Dr. Florian Pfaff and Dr. Florian Heims, from whom I learned a lot and to whom I will always be grateful. I am particularly grateful to Dr. Subrata Kundu, whose research served as a starting point for most of the work that I present in this Thesis, to Dr. Florian Pfaff for the rRaman and Möβbauer measurements, to Vikoria Steck for the initial work on copper-nitrenes with substituted nitrene sources and to Sarah-Luise Abram for the starting studies on the copper-mesityl azide system. Thank you also to the current group members: Katrin Warm, Anirban Chandra and Jennifer Deutscher, for the nice atmosphere in the laboratory and for their comradeship.

I am thankful to the members of the groups of Prof. Dr. Christian Limberg and Dr. Matthias Schwalbe for providing a nice working atmosphere. Especially, I am grateful to Dr. Fabian Schax for the XRD measurement, to Dr. Iweta Pryjomska-Ray for the support and advice from the beginning of my time here and for her help with ESI-MS and GC-MS measurements and to Dr. Corinna Matlachowski, Siu Ting-Li and Marie-Louise Wind for the fruitful discussions and their continuous help. I am especially thankful to Malu for reading and correcting this Thesis.

I am grateful to the scientific, technical and administrative staff of the Institut für Chemie of the Humboldt Universiät zu Berlin, particularly, to Mrs.Ursula Kätel for the elemental analysis and to the NMR department for measuring my samples.

I would like to acknowledge the contributions of the following groups and individuals to the development of this Thesis. They kindly provided their facilities and expertise in different techniques that allowed us to make interesting chemistry.

- I am thankful to Dr. Eckhard Bill at the Max-Plank-Institut für Chemische Energiekonversion (Germany) for his support with EPR and Magnetic Möβbauer measurements.

- Thanks to Erik Farquhar at the Brookhaven National Laboratory (USA) for the X-Ray absorption studies.

- I am grateful to Prof. Dr. Marcel Swart from the Universitat de Girona (Spain), who performed DFT calculations on our systems.

- I am also thankful to Prof. Nicolai Lehnert and Casey van Stappen from the University of Michigan (USA) for their work on the challenging characterization of the hexanuclear cobalt complex.

- I am grateful also to Prof. Jason England from the Nanyang Technological University (Singapore) for the NMR measurements.

- I would like to thank also Dr. Alexander Schnegg from the Helmholtz Zentrum Berlin (Germany) for the access to the EPR under their supervision.

- I am also grateful to Prof. Dr. Peter Hildebrandt and Dr. Uwe Kuhlmann in the Technische-Universität Berlin (Germany) for the access to the rRaman.

My most sincere thanks go to the BIG-NSE and UniCat for the economic and academic support, and for providing an open and inclusive learning atmosphere. Especially, I want to thank Dr. Lonjaret (JP) for his kindness and support throughout this process.

Finally, I want to thank my family and friends for their never-ending love and support. Thank you to my parents and my brother for always being there for me, no matter how far away we are. Thank you to Andrés, my husband, for standing with me in the good and the bad times and for being the best life companion one could ever have.

Contents

Chapter 1:
General Introduction

The activation of small molecules such as N_2, O_2, H_2, CO_2 or CH_4 has been in the spotlight of chemical research and technology development for some decades; the interest in activating such molecules stems from the context of the current environmental crisis and the demand for cleaner chemical processes and energy sources.[1] Some small molecules, like H_2 and O_2, have the potential to be used as clean energy alternatives to fossil fuels in devices such as fuel cells. The activation of other molecules, like N_2 and O_2, would allow the fixation of their elements in atom-efficient ways and may lead to the generation of value-added chemicals like ammonia and oxidized hydrocarbons, some of which are essential for sustaining life on our planet. The activation of a third group of molecules that includes CO_2 and NO_x, which act as pollutants and greenhouse gases, would facilitate their removal from the atmosphere, thus significantly improving environmental conditions.

Finally, the activation of CH_4 is also of particular relevance in the context of efficient natural energy resource use. Methane is the main component in natural gas, but is also one of the most prevalent greenhouse gases, with a comparative impact on climate change 25 times greater than CO_2 over a 100-year period. Its characteristics give methane two contrasting facets: on the one hand, with the depletion of oil reserves, methane has the potential to become the most important hydrocarbon feedstock for the generation of chemicals;[2] on the other hand, given its environmental impact, a large amount of methane released in crude oil extraction is being flared because of the lack of technology to properly transport the gas to marketplaces.[3,4] The activation of methane, for example by oxidation to methanol, would prevent the need to flare it by making it easier to transport as a liquid, and would provide a starting point for the generation of value-added chemicals, thus promoting the exploitation of methane resources in a cleaner and more efficient way.[5] The activation of methane is, however, not an easy process and is still not employed to its full potential in the chemical industry. This is because methane is highly stable, since it has four strong and localized C−H bonds with high bond-dissociation energies (104 kcal mol^{-1}) and lacks any low-energy empty orbitals or high-energy filled molecular orbitals.[2] The activation of the C−H bonds of methane and other alkanes into useful functional groups has therefore become an active and expanding field of research that could revolutionize the chemical industry and greatly impact the environment.[2,6]

Transition metals play an important role in the activation of small molecules by providing low-barrier reaction pathways for their transformations. A number of examples of synthetic C−H bond activation reactions promoted by transition metal centers have been reported in the past decades.[7,8] So far, the most efficient known catalyst for methane activation is the platinum-based Periana catalyst; however, its potential industrial applications are limited by the cost of platinum – a

non-abundant metal – as well as by the extreme reaction conditions required.[9] Nature, on the other hand, uses cheap non-toxic transition metals (like Fe, Cu and Mn) at the active sites of metalloenzymes, for the oxidation and selective functionalization of strong C−H bonds in atom-economical transformations under mild pressure and temperature conditions.[10] Interestingly, in natural systems the controlled oxidation of organic substrates is coupled with the activation of yet another small molecule: dioxygen. Thus, in a great variety of metalloenzymes, the activation of oxygen – the cheapest and most naturally abundant oxidant – precedes the activation of strong C−H bonds (including those of methane) and their conversion to their oxidized counterparts.

1.1 O_2 activation

The use of molecular oxygen as a terminal oxidant, as employed in biological systems, is desirable because O_2 is both naturally abundant and inexpensive. Nonetheless, it is not straightforward to use, as evidenced by the fact that oxygen coexists with a number of combustibles under ambient conditions without oxidizing them. From a thermodynamic point of view, dioxygen is potentially reactive; however, the direct oxidation of organic molecules with O_2 is kinetically prevented. The reason for this lies in the electronic configuration of the molecules involved. Oxygen has a triplet ground state (S = 1) (Figure 1.1) unlike the organic compounds that have diamagnetic (S = 0) ground state configurations. The addition of O_2 to organic compounds is spin-forbidden, since the starting compounds have a total spin S = 1 whereas the oxidation products are diamagnetic with S = 0. In order to overcome this prohibition, O_2 can react with species that contain

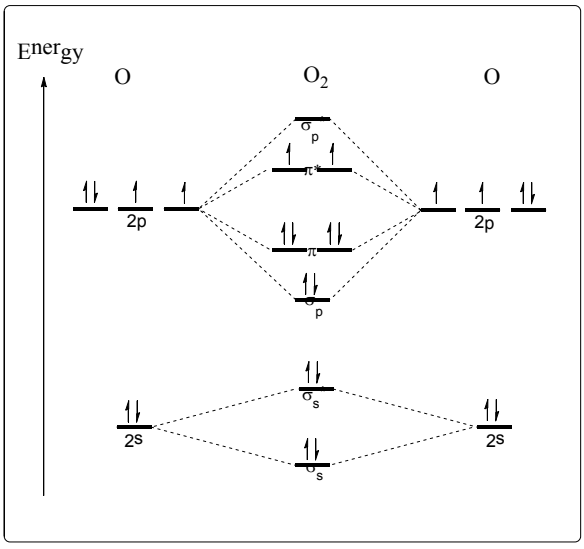

Figure 1.1: Molecular orbitals of the O_2 molecule.

unpaired electrons or are able to undergo single-electron transfer reactions, such as free radicals (as in combustion), photochemical-induced excited triplet states or transition metals. Nature's preferred strategy is the use of transition metals.[1]

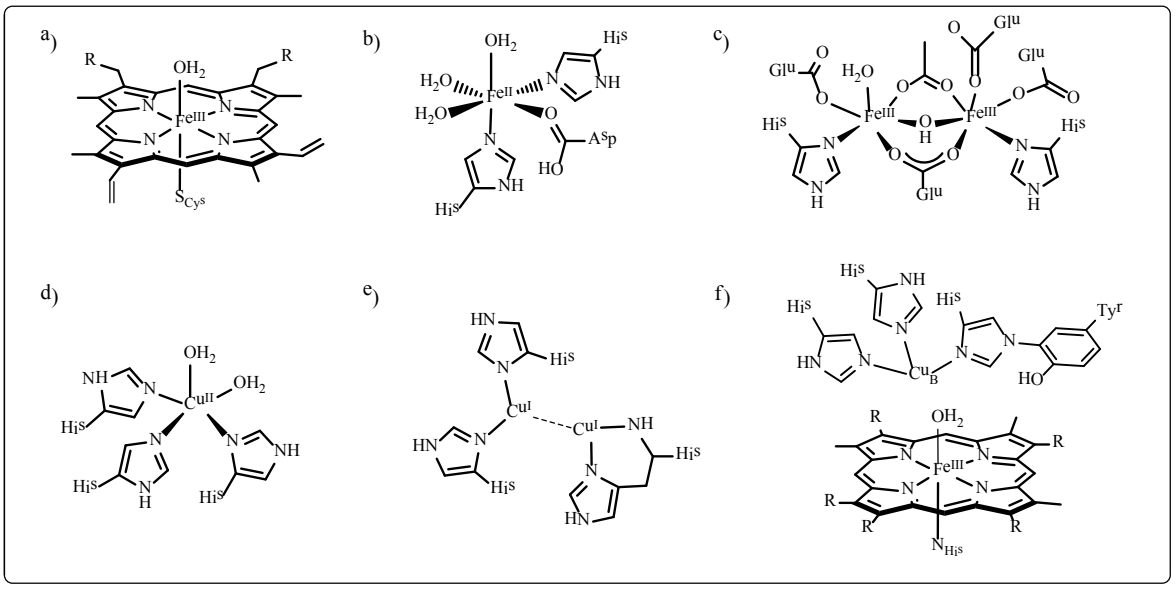

Figure 1.2: Structures of representative active sites employed in biology for oxygen activation. a) Mononuclear haem iron unit in Cytochrome P450; b) mononuclear non-haem iron core in Taurine dioxygenase; c) dinuclear non-haem site in soluble Methane monooxygenase; d) mononuclear copper site in Copper amine oxidase; e) dinuclear copper site in particulate Methane monooxygenase and f) heterodinuclear Cu/Fe center in Cytochrome *c* oxidase.

Metalloenzymes employ a wide variety of metallic sites to activate O_2, such as mononuclear haem and non-haem iron units, mononuclear copper centers, homodinuclear iron and copper centers, as well as heterodinuclear iron/copper centers (Figure 1.2).[11,12] In these active sites, O_2 is activated in a controlled manner to generate a variety of reactive intermediates that lead to the selective oxidation of suitable substrates by avoiding any over-oxidation of products as well as the dangerous oxidation of the protein subunit surrounding the active metal site. A common mechanism for the activation of O_2 in metalloenzymes has been proposed (Scheme 1.1).[13] In this mechanism, the oxygen first binds to the metal center to generate a metal-superoxo species, converting the kinetically inert triplet ground state of O_2 to a more reactive doublet state in $O_2^{\bullet-}$. The metal-superoxo intermediate can further gain an electron to generate a metal-peroxo species and subsequently a proton to generate a metal-hydroperoxo core or directly abstract a hydrogen atom to form the metal-hydroperoxo intermediate. Finally, this species can undergo either O−O bond homo- or heterolysis to generate a highly reactive metal-oxo intermediate (Scheme 1.1 a). In dinuclear

systems, the unified mechanism is similar but the intermediates formed are the superoxo-, peroxo- and the high-valent metal-oxo species shown in Scheme 1.1 b. Although Scheme 1.1 presents a general unified method for the biological activation of dioxygen, the catalytic cycle of each enzyme is unique and dependent on its own function and structure.

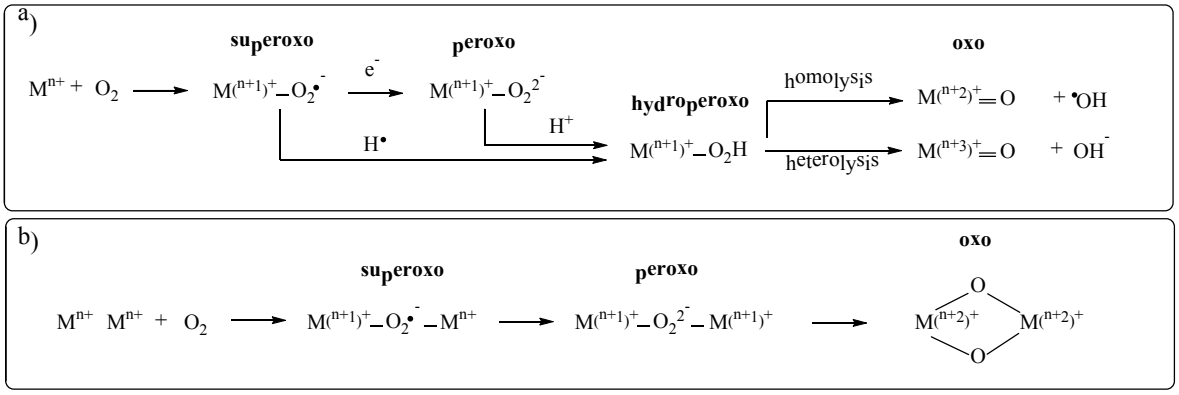

Scheme 1.1: Proposed unified mechanisms for the activation of O_2 at a) mononuclear and b) dinuclear enzymatic active sites.

1.2. Relevant enzymatic mechanisms and their intermediates

Enzymes are the perfect catalysts. They are able to perform reactions – that are otherwise too energy-demanding – in mild conditions *via* the generation and reaction of the above-mentioned reactive intermediates. Metalloenzymes provide access to these species in a controlled fashion, thus regulating the reaction's mechanism and selectivity. In the following sections, detailed descriptions of the catalytic cycles of four relevant metalloenzymes are provided, with special emphasis on the nature of their key reactive intermediates.

1.2.1 Cytochrome P450 monooxygenases

Cytochrome P450s (P450s) are a family of haem-containing enzymes ubiquitous to most biochemical systems. They play a vital role in the synthesis of biomolecules and the metabolism of exogenous substances like drugs and toxicants by catalyzing reactions such as aliphatic C−H bond hydroxylation, olefin epoxidation and the oxidation of aromatic compounds and aldehydes.[14] The most common P450s are monooxygenases, as they activate O_2 and incorporate one oxygen atom into a substrate while the other oxygen atom is reduced to water.

The accepted catalytic cycle of P450 monooxygenases is presented in Scheme 1.2.[1,14,15] The active site of this family of enzymes contains an iron-protoporphyrin IX complex, where the

iron is coordinated to the sulfur atom from a cysteine residue in one of the axial positions (Figure 1.2 a); in the resting state, the sixth coordination site of the Fe(III) is occupied by a molecule of water. When the organic substrate binds within the active site, the water molecule is displaced and a penta-coordinated Fe(III) complex is formed, which makes the iron center susceptible to reduction to a high-spin Fe(II) compound. In this reduced state, the iron center is able to bind O_2, generating a low-spin Fe(III)-superoxo complex. This species is subsequently reduced and protonated to generate an Fe(II)-hydroperoxo intermediate, known as Compound 0 (Cpd-0). The protonation of Cpd-0 results in heterolytic O−O bond cleavage, the liberation of water, and the generation of a high-valent oxoiron(IV) haem cation radical species known as Compound I[16] (Cpd-I, Scheme 1.2 center). Cpd-I is believed to be the most reactive intermediate of the cycle and able to abstract a hydrogen atom from the substrate to generate an Fe(IV)-hydroxo complex (Compound II) and a carbon-centered radical.[17] Following the "rebound" mechanism,[18-20] the substrate radical is hydroxylated, and a molecule of water replaces the hydroxylated product bound to the iron center, thereby regenerating the complex in its resting state.

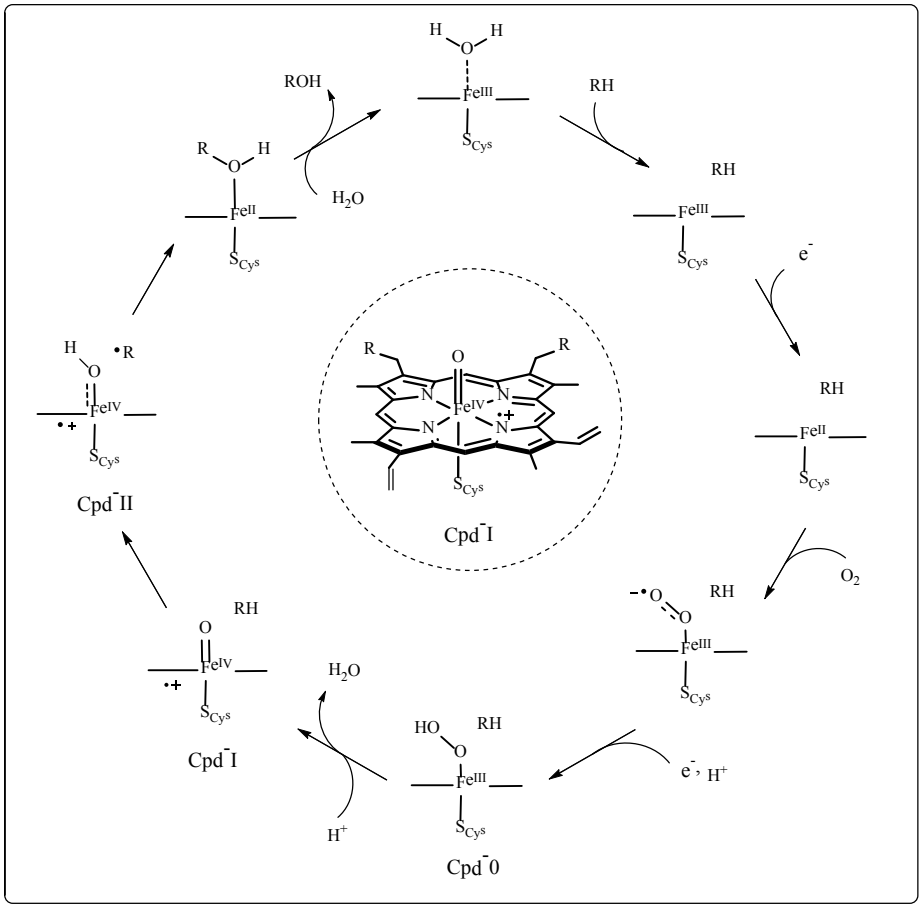

Scheme 1.2: Catalytic cycle of P450 enzymes and structure of Compound I (Cpd-I).

1.2.2 Taurine dioxygenase

Taurine Dioxygenase (TauD) is a member of the large and diverse family of the α-ketoglutarate (α-KG)-dependent dioxygenases. Notably, dioxygenases – in contrast to monooxygenases – catalyze the oxidation of a substrate without reducing one of the oxygen atoms from O_2 into a water molecule; instead, both oxygen atoms are incorporated into a substrate or a co-substrate.[21] The α-KG-dependent dioxygenases often employ in their active sites a monomeric non-haem Fe(II) center, facially coordinated by the array of two histidines and one aspartate or glutamate (Figure 1.2 b). The iron center activates O_2 to effectuate the decarboxylation of the α-KG, acting as a co-substrate, and the two-electron oxidation of the substrate, which is typically a hydroxylation but can also be a desaturation or a cyclization reaction. The biological functions of this family of enzymes include the degradation of xenobiotics and the biosynthesis of connective tissue, antibiotics and secondary metabolites, as well as the reparation of methylated DNA and RNA and the control of oxygen and iron homeostasis.[22] TauD, in particular, plays a fundamental role in the metabolism of cysteine, an important amino acid that is toxic in high concentrations, by regulating its concentration in the body.[21] TauD's catalytic cycle is commonly regarded as representative of those of the α-KG dependent dioxygenases since the first reactive intermediate trapped in this family of enzymes was the intermediate-J from the TauD enzyme.[23]

The accepted catalytic mechanism of TauD is shown in Scheme 1.3.[21,22,24] In the resting state the Fe(II) center is coordinated to the 2-His/1-Carboxylate ligand motif that links the iron center to the enzyme, and the three remaining coordination sites are occupied by water molecules. Upon coordination of the co-substrate, α-KG, two water molecules are released. The third water molecule is liberated after the substrate, taurine, docks in the active site, leaving the Fe(II) center penta-coordinated. The O_2 molecule then binds to the iron center, generating an Fe(III)-superoxo intermediate, which presumably attacks the α-keto position of the α–KG, forming a structure whose subsequent decarboxylation leads to the formation of a high-valent $S = 2$ oxoiron(IV) species known as Intermediate-J[23,24] (Scheme 1.3 center). Intermediate-J is believed to be responsible for hydrogen atom abstraction from the substrate, followed by O-rebound to yield the hydroxylated product. Further departure of the succinate, together with the coordination of water molecules, returns the iron center to the resting state.

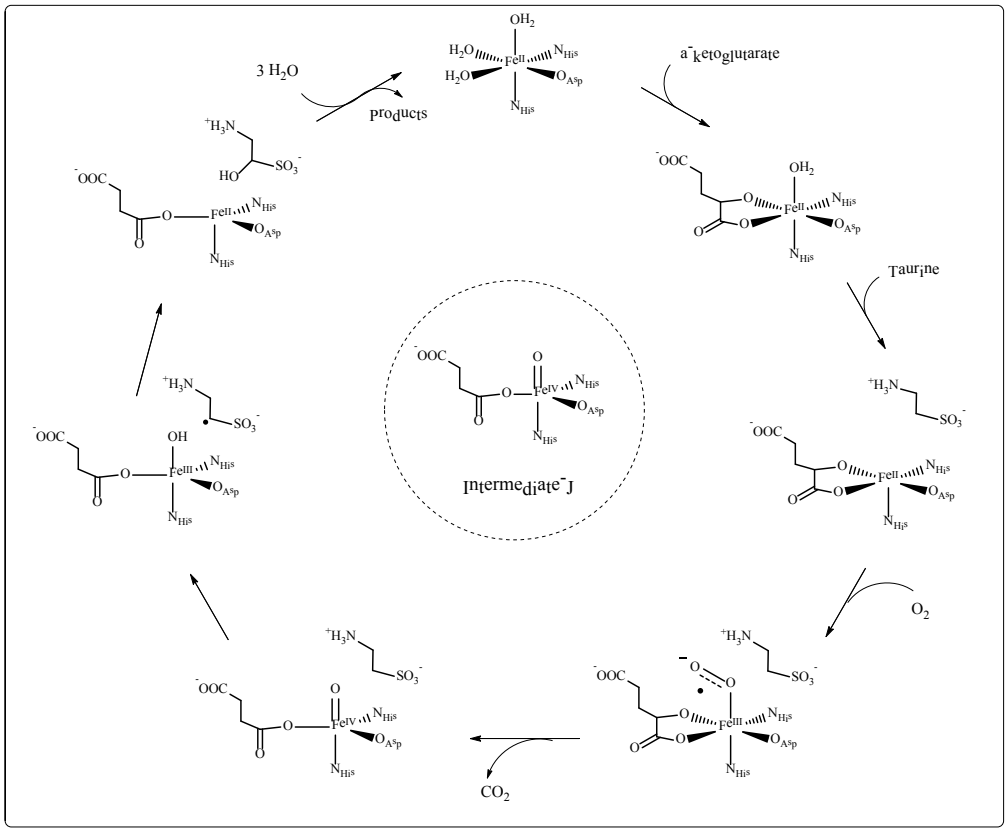

Scheme 1.3: Catalytic cycle of Taurine Dioxygenase (TauD) and structure of the Intermediate-J.

1.2.3. Soluble methane monooxygenase

Enzymes capable of transforming methane into methanol are of particular interest since, as discussed before, this reaction is one of the most promising catalytic processes for the development of cleaner energies and efficient use of carbon sources.[5] Two metalloenzymes are known that perform this reaction, namely, the membrane-bound particulate methane monooxygenase (pMMO),[25] and the soluble methane monooxygenase (sMMO).[26] Methane monooxygenases (MMOs) are present in all methanotrophs as the main enzymes of their metabolic pathways. The most common of all MMOs are pMMOs, which have a dinuclear copper core in their active sites (Figure 1.2 e),[25] whereas sMMOs are formed under copper-limited conditions and rely on a carboxylate-bridged dinuclear iron center (Figure 1.2 c) to perform the selective hydroxylation of methane to methanol.

In the last few decades, sMMOs have been intensively investigated given their ease of isolation, in comparison to pMMOs, which are found embedded in membranes; the catalytic cycle of sMMOs is therefore better understood and is shown in Scheme 1.4.[26-29] The resting state of the

enzyme is the oxidized di-iron(III) cluster that is further reduced by two electrons to yield the reduced di-iron(II) species; this reactive species binds O_2 to generate a peroxo-di-iron(III) intermediate. The further cleavage of the O−O bond yields the reactive species MMO-Q (Scheme 1.4 center) that contains a high-valent bis(μ-oxo)diiron(IV) core. The MMO-Q intermediate is recognized as the key oxidizing species of the sMMO catalytic cycle. Spectroscopic studies suggest that it possesses a unique $[Fe^{IV}_2(\mu\text{-}O)_2]^{4+}$ diamond core where the iron centers are in a high-spin configuration (S = 2) and strongly exchange-coupled.[28] The formulation of the exact structure of the MMO-Q intermediate is still debated;[26,29] however, the schematic structure presented in Scheme 1.4 is the most widely accepted, where a high-valent oxodiron(IV) diamond core can be observed.

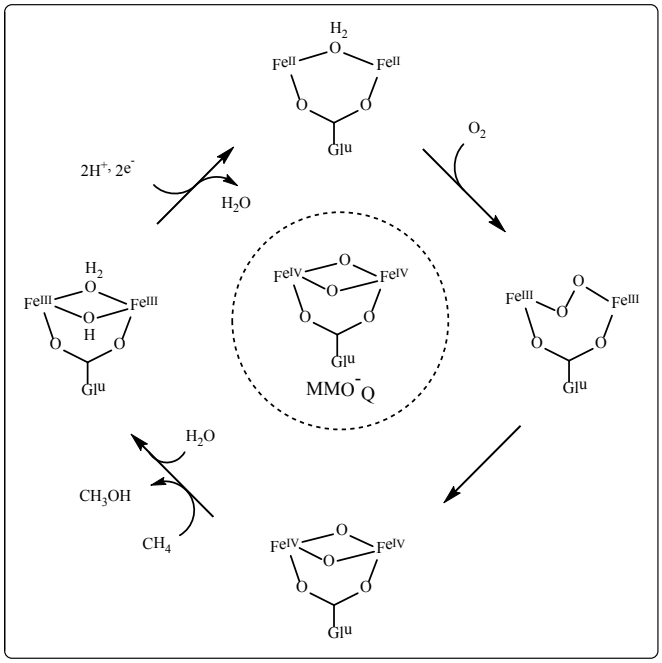

Scheme 1.4: Overview of the catalytic cycle of the soluble methane monooxygenase (sMMO).

1.2.4 Cytochrome *c* oxidase

Besides the controlled activation of C−H bonds, metalloenzymes perform other vital processes that involve the activation of O_2, like the four-electron reduction of dioxygen to water. Redox reactions such as this one are performed by enzymes known as oxidases. Cytochrome *c* oxidase[30] (CcO) is a vital enzyme in the respiratory pathway of aerobic organisms. It is capable of reducing dioxygen as a part of the cellular process to generate energy in the form of ATP molecules. The protein CcO contains two iron-porphyrin units (haem *a* and haem a_3) and two mononuclear copper sites (Cu_A and Cu_B). The haem *a* and Cu_A cores act as electron transfer sites,

while the haem a_3 and Cu_B form a dinuclear active site that activates dioxygen (Figure 1.2 f).[12,31] The roles of the different amino acid residues and metals of the active site of CcO are still under discussion[32-34] However, based on the intermediates that have been spectroscopically detected, the catalytic cycle shown in Scheme 1.5 has been proposed.[35] Even when the active site is bimetallic, the reduction of O_2 involves intermediates that are very similar to those observed in monometallic enzymes, including the iron-superoxo and the oxoiron(IV) species.

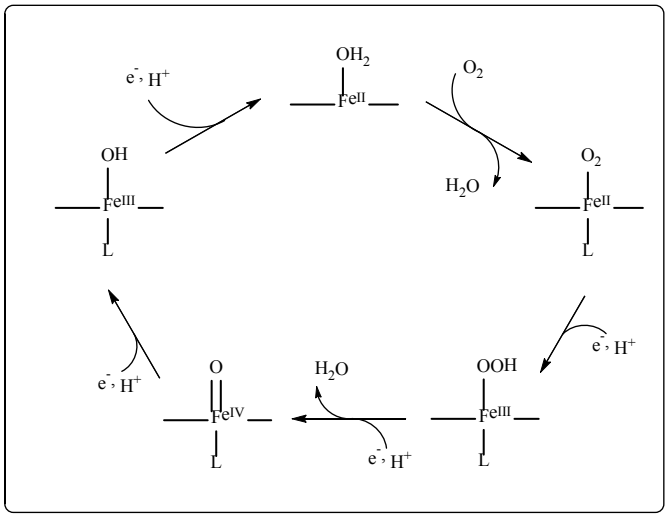

Scheme 1.5: Overview of the catalytic O_2 reduction performed in the active site of the Cytochrome *c* oxidase.

1.3. Synthetic model systems

The previously described enzymes are all distinct and perform unique and specific reactions; nevertheless they all proceed *via* the same classes of intermediates. A full comprehension of these reactive species -including their generation, structure and reactivity- is necessary to achieve a better understanding of the catalytic enzymatic mechanisms and for the further design of synthetic catalysts capable of performing similar processes. The study of these reactive species in the active sites of metalloenzymes presents multiple challenges related to their location within a complex protein environment, in addition to the difficulty of altering them directly – for example, through variation of their ligand system or metallic cores. The reduced size of synthetic biomimetic models, on the other hand, enables them to be easily isolated and spectroscopically studied. Furthermore, the ligand environments of the models can be modified both sterically and electronically to get more insights into the catalytic mechanisms and structural proprieties of biological systems.[27,36] Models can provide information on unclear enzymatic mechanisms or boost our understanding of known biological intermediates, but they can also deviate from the biological structural resemblance and be employed for the development of better catalysts with potential applications.[36,37]

Based on the enzymatic catalytic cycles presented above, it is clear that metal-oxo species play a fundamental role in nature. Given their relevance, vast studies on synthetic metal-oxo complexes have been carried out.[10,35,38-41] Of special interest for this work are mononuclear non-haem oxoiron(IV) complexes. Over 60 synthetic non-haem oxoiron(IV) complexes have been reported in the last 15 years,[10-35,42–54] most of which have been fully characterized, and their reactivities in oxidation reactions have been intensively tested.[10] The most important non-haem oxoiron(IV) models are discussed in detail in Chapter 2. It is important to state that until very recently all the reported non-haem oxoiron(IV) complexes failed to mimic the actual spin state of the enzymatic active sites (S = 2) and were also not successful in activating C−H bonds at the same rates as the natural reactive intermediates. However, in 2015, Que Jr. and coworkers stabilized an oxoiron(IV) complex in a high-spin configuration that activates C−H bonds at rates comparable with those of the Intermediate-J of TauD, which represented a major breakthrough in the field.[47]

Despite the clear scientific interest in synthesizing complexes that closely mimic the active species of biological systems, an attractive feature of the bioinspired modeling is that the chemistry can be taken one step further and new systems can be built beyond the scope of the typical biological choices. Gas phase studies,[55,56] together with theoretical calculations[57] on methane activation processes mediated by different metal-oxo systems, have suggested that metal-oxo cores with metals beyond iron, such as nickel and cobalt, are more reactive towards hydrocarbon functionalization than their oxoiron counterparts due to the weaker metal-oxo bonds in their naked $[MO]^{n+}$ cores. The search for high-valent metal-oxo cores with later transition metals such as cobalt and nickel has engendered a new working field that includes the search for terminal copper(III)-oxo cores, a structure that has also been proposed as a plausible intermediate in natural and artificial systems, but which has yet to be isolated.[13] The challenges posed by this emerging field are related to the anticipated strong repulsion between the electron-rich oxo ligand and the late transition metal, and the bonding considerations that will be discussed later in this Chapter.

Another attractive field in synthetic bioinorganic chemistry deals with multi-nuclear complexes. Many enzymes choose polynuclear sites to perform important oxidative transformations. Some use dinuclear active sites, like sMMO and CcO, as has already been discussed. Others occupy active centers with higher nuclearity, like nitrogenase, which employs a Fe_7MoS_9C cofactor to reduce nitrogen to ammonia, or photosystem II, where water oxidation takes place in a Mn_4CaO_5 cluster. Synthetic polynuclear complexes can reveal information on the importance of cooperativity for the reactivity of these enzymes and their intermediates. This topic

will be further addressed in Chapter 3, which will deal with the activation of O_2 with a hexanuclear cobalt system.

Finally, the chemistry of the metal-oxo complexes can also be extended to include the isoelectronic metal-nitrene cores (where nitrenes are NR^{2-}). Notably, metal-nitrene species are relevant in synthetic processes as they have been proposed as the active intermediates in C−H bond functionalization for the generation of valuable C−N bonds.[39,58] Furthermore, metal-nitrene species are often more stable than the corresponding metal-oxo species, owing to the additional steric protection provided by the substituent of the $–NR^{2-}$ used. Correspondingly, metal-nitrene units can in some cases provide information about the properties of elusive metal-oxo cores. Of particular importance for this work are the copper-nitrene systems, and the advancements in this field of research are discussed in Chapter 4.

1.4 Bonding of metal-oxo and metal-nitrene complexes

The relevance of the metal-oxo cores as key oxidizing species in a variety of enzymatic catalytic cycles has been evidenced. The importance of this species is, however, not limited to nature; academic and industrial laboratories also rely on metal-mediated oxidative transformations, many of which also proceed through metal-oxo complexes.[59-61] The related terminal metal-nitrene cores have also been proposed as the key reactive intermediates in a number of transition metal-mediated synthetic conversions of C−H to C−N bonds.[39,58] The analysis of the qualitative *d* orbital splitting patterns of the terminal metal-oxo and metal-nitrene cores facilitates the understanding of the stability and reactivity of these species. Figure 1.3 presents the qualitative splitting patterns that would be expected for metal-oxo and metal-nitrene cores as derived from ligand field theory for different geometries around the metal center.[39]

The ligand field splitting of the *d* orbitals of metal-oxo complexes in an octahedral geometry (C_{4v} symmetry) is a result of the tetragonal compression associated with the strong M=O bond. The compression along the z-axis, where the oxo ligand is situated, produces a lifting of the degeneracies of the *d* orbitals, which leads to the energy ordering shown in Figure 1.3. The orbitals d_{z^2} and $d_{x^2-y^2}$, which point to the axes where the ligands are situated, form strong σ* antibonding combinations with the σ orbitals of the ligands. The orbitals d_{xz} and d_{yz}, on the other hand, are of π* antibonding character as a result of their interaction with the p_x and p_y orbitals of the oxo ligand. Finally, the orbital d_{xy} is of a non-bonding nature. As a result of this orbital splitting, in C_{4v} symmetry, a metal-oxo double bond is only possible for metals with four or fewer *d* electrons since

further occupation of the π* orbitals would result in a loss of the metal-oxo π bonding and the resulting metal-oxo species would be highly unstable.

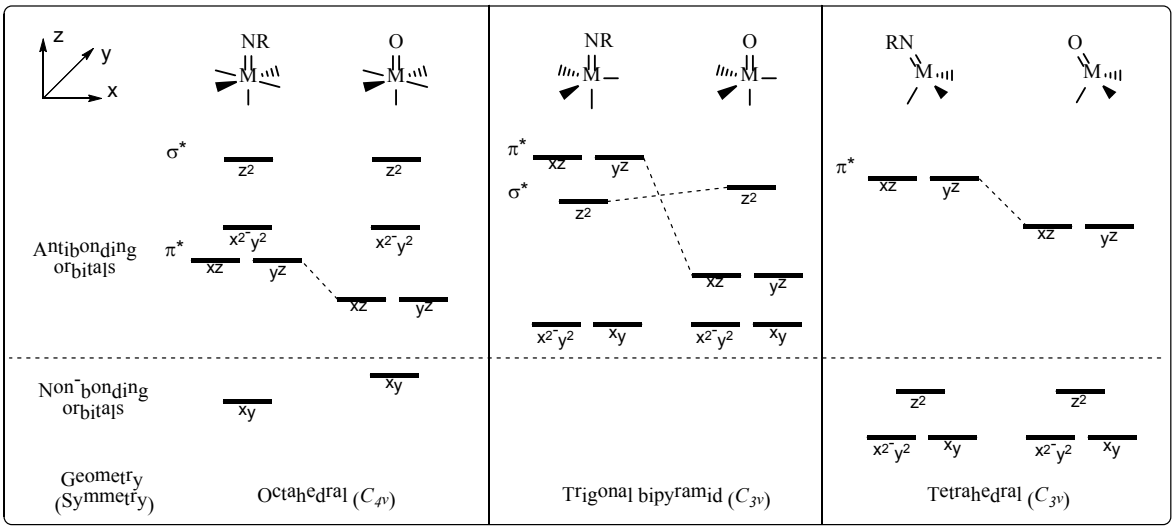

Figure 1.3: Qualitative ligand field splitting of the *d* orbitals for metal-oxo and metal-nitrene complexes in C_{3v} and C_{4v} symmetry.

In the tetragonal bipyramid geometry (TBP), with C_{3v} symmetry, the metal-oxo complexes exhibit a different ligand field *d* orbital splitting. The d_{z^2} orbital is of σ* antibonding nature and is at a significantly higher energy level than the other orbitals. The orbitals d_{xz} and d_{yz} form a degenerate set of π* antibonding orbitals, while the d_{xy} and $d_{x^2-y^2}$ orbitals form a degenerate set of a σ* antibonding nature. The relative energy order between these two sets of degenerate orbitals depends on the strength of the equatorial ligand field. Given that in a TBP environment the set of σ* degenerate orbitals can accommodate four electrons and the π* degenerate set two electrons without decreasing the metal-oxo bond order, the M=O species should be accessible for metals with a *d* electron count of six or fewer. Notably, d^6 configurations would lead to the destabilizing orbital filling where the d_{xy} and $d_{x^2-y^2}$ orbitals are completely full; however, penta-coordinated M=O species with a d^6 electron count have been reported.[62,63]

Finally, the ligand field splitting for the metal *d* orbitals of a metal-oxo complex in a pseudo-tetrahedral geometry, also with C_{3v} geometry, shows a very different orbital energetic order. Contrary to what was observed for TBP and octahedral geometries, the d_{z^2} orbital is much lower in energy and has a non-bonding nature instead of a σ* antibonding character; this can be explained by the fact that the d_{z^2} orbital is not engaged in the metal-oxo bonding. It has also been postulated that

the possibility of the d_{z^2} orbital getting hybridized by mixing with the 4*s* and $4p_z$ orbitals of the metal, a phenomenon allowed in non-centrosymmetric geometries, lowers its energy and mitigates its antibonding character.[64] Higher *d*-electron counts of up to eight electrons in low-spin configuration could stabilize metal-oxo complexes in tetrahedral geometry.

The orbital splitting patterns discussed for the metal-oxo systems also apply for the metal-nitrene cores, with small variations. The oxo (O^{2-}) and nitrene (NR^{2-}) ligands are isoelectronic; however, they differ in their nuclear effective charge (Z*). The nitrene ligand has a smaller Z* than the oxo since it possesses the same number of electrons but fewer protons. The filled *p* orbitals of the nitrene are therefore higher in energy than those in the oxo, which makes them better energetically matched with the *d* orbitals of the metal and results in the observed character of the nitrene ligand being a better π donor than the oxo ligand. The better π donor character of the nitrene ligand results in a stronger destabilization of the π* d_{xz} and d_{yz} orbitals of the metal relative to those of the metal-oxo complexes (see Figure 1.3), which alters the qualitative ligand field splitting in the C_{4v} symmetry, giving rise to a 1+3+1 splitting pattern.

The ligand field *d* orbital splitting patterns can be useful to rationalize the occurrence of transition metals M=X systems (X= O^{2-} or NR^{2-}), especially the metal-oxo ones, which are more common and well-studied.[59] In an octahedral geometry, up to two electrons can fill the non-bonding orbital d_{xy} for the complexes to maintain a bond order of three and be stable; hence, oxo-complexes of early transition metals with low electron counts ($d \leq 2$) are ubiquitous and unreactive. With every electron added to the system, the bond order is reduced by 0.5, the metal-oxo bond is activated and the resulting species are more reactive. The M=O bond remains a double bond up to a *d* electron count of four. However, with $d > 4$ electrons, the metal-oxo bond is weakened and the stabilization of such species is harder. Hence, as we move right in the periodic table, M=X cores become rarer and more strongly oxidizing. Nature typically selects oxoiron(IV) complexes for oxidizing substrates with strong C−H bonds. Since the Fe(IV) centers have four *d*-electrons, they form metal-oxo complexes that are right at the balance point between stability and reactivity: they can be generated but they are highly reactive. Indeed, at this balance point between stability and reactivity lies the biggest challenge in the study of reactive intermediates.

1.5. Stabilizing late transition metal-oxo and metal-nitrene complexes

The stabilization of first-row high-valent late transition metal-oxo or -nitrene cores presents difficulties due to the repulsive interactions between the electron-rich terminal oxo or nitrene ligands and the electrons of the metal center, which are related to the above-discussed bonding

considerations. Accordingly, given that d^4 metals can preserve the double bond character of the M=O core, over 50 synthetic oxoiron(IV) complexes have been stabilized; however, metal-oxo cores with later metals such as cobalt have only been trapped in a couple of cases, and only in the form of Lewis acid adducts.[65,66] The strategy of utilizing external redox-innocent Lewis acids, such as Sc(III) and similar cations, for stabilizing the short-lived intermediates has been employed in the successful trapping of a low-spin (S = 1/2)[65] and an intermediate-spin (S = 3/2)[66] cobalt(IV)-oxo intermediates in the form of [Co^{IV}-O-Sc^{3+}] cores, as well as for the trapping of a Lewis acid adduct of a cationic copper-tosylnitrene species in the form of a [Cu^{II}-(NTs$^{\bullet}$)-Sc] core.[67] These three species are shown in Figure 1.4. It is believed that the effect of the external electron withdrawing group in these systems is related to its interaction with the M=X core, that lowers the electronic repulsion between the metal and the ligand.[68]

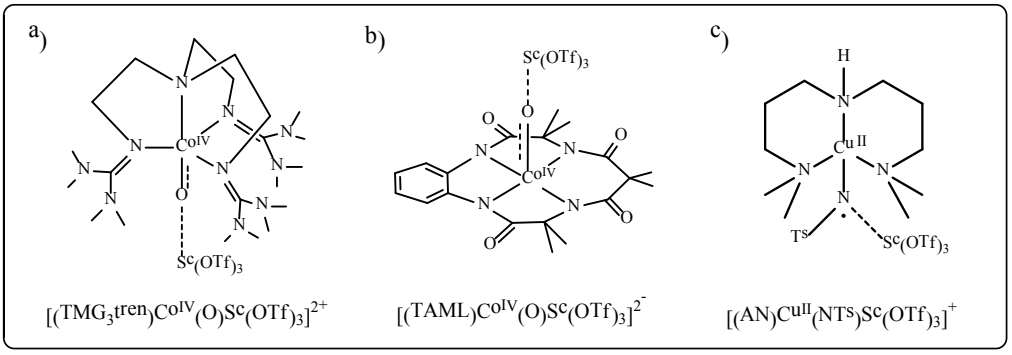

Figure 1.4: Non-covalent interactions with external Lewis acids for the stabilization of the otherwise elusive Co^{IV}-oxo and terminal Cu-nitrene species in the complexes a) $[(TMG_3tren)Co^{IV}(O)\text{-}Sc(OTf)_3]^{2+}$, b)$[(TAML)Co^{IV}(O)\text{-}Sc(OTf)_3]^{2-}$ and c) $[(AN)Cu^{II}(NTs^{\bullet})\text{-}Sc(OTf)_3]^{+}$ where Ts= tosyl group.

Other important factor that must be considered for the trapping of high-valent reactive intermediates is the design of the ligand that anchors the metal center. The ligands can be chosen to enforce a certain geometry around the metal center; this strategy has been employed by several groups to stabilize high-spin oxoiron(IV) complexes by using bulky tripodal ligands that enforce a trigonal-bipyramidal geometry around the iron center.[49,54,69] The structure and nature of the donor atoms of the ligand can also be chosen to provide a suitable ligand field environment to favor certain electronic configuration on the metal center; for example Que Jr. and coworkers reported the stabilization of the most reactive synthetic high-spin non-haem oxoiron(IV) complex by employing a tripodal ligand with weaker field donors.[47] Additionally, ligands with sites capable of providing non-covalent interactions with the terminal oxo or nitrene ligands have been also designed; the most notorious example is the ligand H_3Buea, employed by Borovik and coworkers, which is able to

mimic the secondary interactions of the enzyme by hydrogen-bond stabilization of an Fe(III)−hydroxo complex.[54]

A purposeful ligand design is, hence, necessary for the stabilization of highly reactive M=X cores. For systems dealing with late transition metals with high *d* electron counts, the introduction of electron withdrawing groups that can alter the electronic distribution of the metal-oxo or metal-nitrene cores must also be considered. Other aspects, like the solvent and temperature used for the generation and testing of the M=X species, are also important in achieving the proper balance between stability and reactivity of these species. All of these factors will be considered and discussed in this work, which deals with the generation, trapping and reactivity testing of reactive intermediates.

1.6. The aim of this work

The importance of, and interest in, the isolation and characterization of reactive intermediates such as metal-oxo and metal-nitrene cores with late transition metals has been widely discussed. During my doctoral research, I worked with a series of reactive intermediates with terminal oxo and nitrene ligands. My work is divided into three different projects, according to the metal center and the kind of ligand employed in each case. The aim of these projects was to examine the effect that small changes in the ligand system, the participating metal centers or the nitrene sources, have on the behavior of a given reactive system.

In the first project (Chapter 2), a new oxoiron(IV) complex, namely $[(TMCO)Fe^{IV}(O)]^{2+}$, was synthesized. The ligand **TMCO** is analogous to the existing **TMC** ligand but instead of having four nitrogen donors, it has three nitrogen donors and an oxygen donor, which places the iron center in a weaker field environment. The effect that this change has on the stability, electronic structure and reactivity of this set of oxoiron(IV) complexes was thoroughly investigated.

In the second project (Chapter 3), the reactivity of a hexanuclear cobalt system $[(L_6)Co_6^{II}]$ was studied. It has been reported that $[(L_6)Co_6^{II}]$ reacts with O_2 to generate a peroxo and subsequently an oxo intermediate.[70] The nucleophilic and electrophilic reactivity of the detected intermediates was evaluated. The ability of $[(L_6)Co_6^{II}]$ to catalytically reduce O_2 was also studied, and proved to contrast with the previously reported analogous iron compound $[(L_6)Fe_6^{II}]$ that performed the O−O bond formation reaction.[71]

Finally, in the third project (Chapter 4), a complete series of terminal copper-nitrenes was studied. The effect that the Lewis acids (**M**) have on the generation and reactivity of the Lewis-acid

copper-nitrene adducts [(AN)Cu(NTs)(M)] was evaluated. Different nitrene sources were also employed to test the role that the nitrene plays in the stabilization of terminal copper-nitrenes. For the first time, it was possible to isolate two terminal copper nitrenes without a bound Lewis acid together with their related Lewis acid adducts and characterize them.

The performed studies were supported by spectroscopic characterizations including isotope-labeling experiments. Density functional theory (DFT) studies were also included to provide deeper insights in the analysis of the experimental data. In order to complete the studies of the three different systems, a significant number of collaborations took place both within our working group and with external collaborators; all of them receive proper recognition for their work in the acknowledgment section of this Thesis.

1.7. References

[1] W. B. Tolman, Ed., *Activation of Small Molecules*, Wiley-VCH Verlag GmbH & Co. KGaA, Weinheim, Germany, **2006**.

[2] P. Tang, Q. Zhu, Z. Wu, D. Ma, *Energy Environ. Sci.* **2014**, *7*, 2580.

[3] Editorial, *Nature* **2013**, *495*, 281.

[4] J. Tollefson, *Nat. News* **2016**.

[5] G. A. Olah, A. Goeppert, G. K. S. Prakash, *Beyond Oil Gas Methanol Econ,*.2nd Ed. **2009**.

[6] R. G. Bergman, *Nature* **2007**, *446*, 391–393.

[7] A. E. Shilov, G. B. Shulpin, *Chem. Rev.* **1997**, *97*, 2879–2932.

[8] J. A. Labinger, J. E. Bercaw, *Nature* **2002**, *417*, 507–514.

[9] R. A. Periana, D. J. Taube, S. Gamble, H. Taube, T. Satoh, H. Fujii, *Science* **1998**, *280*, 560–564.

[10] X. Engelmann, I. Monte-Pérez, K. Ray, *Angew. Chem. Int. Ed.* **2016**, *55*, 7632–7649.

[11] R. H. Holm, P. Kennepohl, E. I. Solomon, E. I. Solomon, *Chem. Rev.* **1996**, *96*, 2239–2314.

[12] C. R. Hess, R. W. D. Welford, J. P. Klinman, *Wiley Encycl. Chem. Biol.* **2008**, *DOI:10.1002/9780470048672.wecb431*.

[13] K. Ray, F. Felix, B. Wang, W. Nam, *J. Am. Chem. Soc.* **2014**, *136*, 13942–13958.

[14] M. Swart, M. Costas, Eds., *Spin States in Biochemistry and Inorganic Chemistry*, Wiley, Singapore, **2016**.

[15] A. B. McQuarters, M. W. Wolf, A. P. Hunt, N. Lehnert, *Angew. Chem. Int. Ed.* **2014**, *53*, 4750–4752.

[16] J. Rittle, M. T. Green, *Science* **2010**, *330*, 933–938.

[17] M. J. Cryle, J. J. De Voss, *Angew. Chem. Int. Ed.* **2006**, *45*, 8221–8223.

[18] J. T. Groves, G. A. McClusky, *J. Am. Chem. Soc.* **1976**, *98*, 859–861.

[19] F. Ogliaro, N. Harris, S. Cohen, M. Filatov, S. P. de Visser, S. Shaik, *J. Am. Chem. Soc.* **2000**, *122*, 8977–8989.

[20] S. Shaik, S. Cohen, S. P. de Visser, P. K. Sharma, D. Kumar, S. Kozuch, F. Ogliaro, D. Danovich, *Eur. J. Inorg. Chem.* **2004**, 207–226.

[21] S. P. de Visser, *Coord. Chem. Rev.* **2009**, *253*, 754–768.

[22] J. M. Bollinger, J. C. Price, L. M. Hoffart, E. W. Barr, C. Krebs, *Eur. J. Inorg. Chem.* **2005**, 4245–4254.

[23] J. C. Price, E. W. Barr, B. Tirupati, J. M. Bollinger, C. Krebs, *Biochemistry* **2003**, *42*, 7497–7508.

[24] S. P. de Visser, J. U. Rohde, Y. M. Lee, J. Cho, W. Nam, *Coord. Chem. Rev.* **2013**, *257*, 381–393.

[25] R. L. Lieberman, A. C. Rosenzweig, *Nature* **2005**, *434*, 177–182.

[26] M. Merkx, D. A. Kopp, M. H. Sazinsky, J. L. Blazyk, J. Müller, S. J. Lippard, *Angew. Chem. Int. Ed.* **2001**, *40*, 2782–2807.

[27] I. Siewert, C. Limberg, *Chem. - A Eur. J.* **2009**, *15*, 10316–10328.

[28] T. C. Brunhold, *Proc. Natl. Acad. Sci. U. S. A.* **2007**, *104*, 20641–20642.

[29] C. E. Tinberg, S. J. Lippard, *Acc. Chem. Res.* **2011**, *44*, 280–288.

[30] S. Ferguson-Miller, G. T. Babcock, *Chem. Rev.* **1996**, *96*, 2889–2907.

[31] S. Yoshikawa, A. Shimada, *Chem. Rev.* **2015**, *115*, 1936–1989.

[32] A. A. Konstantinov, *FEBS Lett.* **2012**, *586*, 630–639.

[33] M. R. A. Blomberg, *Biochemistry* **2016**, *55*, 489–500.

[34] M. Wikström, *Biochim. Biophys. Acta - Bioenerg.* **2012**, *1817*, 468–475.

[35] K. Ray, F. Heims, M. Schwalbe, W. Nam, *Curr. Opin. Chem. Biol.* **2015**, *25*, 159–171.

[36] E. Bouwman, J. Reedijk, *Coord. Chem. Rev.* **2005**, *249*, 1555–1581.

[37] D. J. Xiao, E. D. Bloch, J. a Mason, W. L. Queen, M. R. Hudson, N. Planas, J. Borycz, A. L. Dzubak, P. Verma, K. Lee, F. Bonino, V. Crocella, J. Yano, S. Bordiga, D. G. Truhlar, L. Gagliardi, C. M. Brown, J. R. Long, *Nat. Chem.* **2014**, *6*, 590–595.

[38] S. Kundu, M. Schwalbe, K. Ray, *Bioinorg. React. Mec.* **2012**, *8*, 41–57.

[39] K. Ray, F. Heims, F. F. Pfaff, *Eur. J. Inorg. Chem.* **2013**, 3784–3807.

[40] A. S. Borovik, *Chem. Soc. Rev.* **2011**, *40*, 1870–1874.

[41] K. Gunay, A.; Theopold, *Chem. Rev.* **2010**, 1060–1081.

[42] J. Cho, R. Sarangi, W. Nam, *Acc. Chem. Res.* **2012**, *45*, 1321–1330.

[43] C. Krebs, D. G. Fujimori, C. T. Walsh, J. M. Bollinger, *Acc. Chem. Res.* **2007**, *40*, 484–492.

[44] L. Que Jr., *Acc. Chem. Res.* **2007**, *40*, 493–500.

[45] D. Wang, K. Ray, M. J. Collins, E. R. Farquhar, J. R. Frisch, L. Gomez, T. A. Jackson, M. Kerscher, A. Waleska, P. Comba, M. Costas, L. Que Jr., *Chem. Sci.* **2013**, *4*, 282–291.

[46] S. Fukuzumi, Y. Morimoto, H. Kotani, P. Naumov, Y.-M. Lee, W. Nam, *Nat. Chem.* **2010**, *2*, 756–759.

[47] A. N. Biswas, M. Puri, K. K. Meier, W. N. Oloo, G. T. Rohde, E. L. Bominaar, E. Münck, L. Que Jr., *J. Am. Chem. Soc.* **2015**, *137*, 2428–2431.

[48] S. T. Kleespies, W. N. Oloo, A. Mukherjee, L. Que Jr., *Inorg. Chem.* **2015**, *54*, 5053–5064.

[49] J. England, M. Martinho, E. R. Farquhar, J. R. Frisch, E. L. Bominaar, E. Münck, L. Que Jr., *Angew. Chem. Int. Ed.* **2009**, *48*, 3622–3626.

[50] J. Hohenberger, K. Ray, K. Meyer, *Nat. Commun.* **2012**, *3*, 720.

[51] C. V. Sastri, M. J. Park, T. Ohta, T. A. Jackson, A. Stubna, M. S. Seo, J. Lee, J. Kim, T. Kitagawa, E. Münck, L. Que Jr., W. Nam, *J. Am. Chem. Soc.* **2005**, *127*, 12494–12495.

[52] J. Kaizer, E. J. Klinker, N. Y. Oh, J. Rohde, W. J. Song, A. Stubna, J. Kim, E. Munck, W. Nam, L. Que Jr., *J. Am Chem. Soc.* **2004**, *126*, 472–473.

[53] S. T. Kleespies, W. N. Oloo, A. Mukherjee, L. Que Jr., *Inorg. Chem.* **2015**, *54*, 5053–5064.

[54] D. C. Lacy, R. Gupta, K. L. Stone, J. Greaves, J. W. Ziller, M. P. Hendrich, A. S. Borovik, *J. Am. Chem. Soc.* **2010**, *132*, 12188–12190.

[55] D. Schroder, H. Schwarz, *Angew. Chem. Int. Ed.* **1995**, *34*, 1973–1995.

[56] M. Schlangen, H. Schwarz, *Chem. Commun.* **2010**, *46*, 1878–80.

[57] Y. Shiota, K. Yoshizawa, *J. Am. Chem. Soc.* **2000**, *122*, 12317–12326.

[58] R. T. Gephart, T. H. Warren, *Organometallics* **2012**, *31*, 7728–7752.

[59] C. Limberg, *Angew. Chem. Int. Ed.* **2009**, *48*, 2270–2273.

[60] J. A. Labinger, *Nature* **2016**, *536*, 280–281.

[61] B. E. R. Snyder, P. Vanelderen, M. L. Bols, S. D. Hallaert, L. H. Böttger, L. Ungur, K. Pierloot, R. A. Schoonheydt, B. F. Sels, E. I. Solomon, *Nature* **2016**, *536*, 317–321.

[62] I. Efremenko, E. Poverenov, J. M. L. Martin, D. Milstein, *J. Am. Chem. Soc.* **2010**, *132*, 14886–14900.

[63] E. Poverenov, I. Efremenko, A. I. Frenkel, Y. Ben-David, L. J. W. Shimon, G. Leitus, L.

Konstantinovski, J. M. L. Martin, D. Milstein, *Nature* **2008**, *455*, 1093–1096.

[64] J. J. Scepaniak, M. D. Fulton, R. P. Bontchev, E. N. Duesler, M. L. Kirk, Je. M. Smith, *J. Am. Chem. Soc.* **2008**, *130*, 10515–10517.

[65] S. Hong, F. F. Pfaff, E. Kwon, Y. Wang, M. S. Seo, E. Bill, K. Ray, W. Nam, *Angew. Chem. Int. Ed.* **2014**, *53*, 10403–10407.

[66] F. F. Pfaff, S. Kundu, M. Risch, S. Pandian, F. Heims, I. Pryjomska-Ray, P. Haack, R. Metzinger, E. Bill, H. Dau, P. Comba, K. Ray, *Angew. Chem. Int. Ed.* **2011**, *50*, 1711–5.

[67] S. Kundu, E. Miceli, E. Farquhar, F. F. Pfaff, U. Kuhlmann, P. Hildebrandt, B. Braun, C. Greco, K. Ray, *J. Am. Chem. Soc.* **2012**, *134*, 14710–14713.

[68] I. Monte-Pérez, S. Kundu, K. Ray, *Zeitschrift für Anorg. und Allg. Chemie* **2015**, *641*, 78-82.

[69] J. P. Bigi, W. H. Harman, B. Lassalle-Kaiser, D. M. Robles, T. A. Stich, J. Yano, R. D. Britt, C. J. Chang, *J. Am. Chem. Soc.* **2012**, *134*, 1536–1542.

[70] S. Kundu, *PhD Thesis: Synthesis, Spectroscopic Characterization and Reactivity of the High-Valent Metal-Oxo/Imido Cores of the Late Transition Metals*, Humboldt-Universität zu Berlin, Berlin, **2013**.

[71] S. Kundu, E. Matito, S. Walleck, F. F. Pfaff, F. Heims, B. Rábay, J. M. Luis, A. Company, B. Braun, T. Glaser, K. Ray, *Chem.- Eur. J.* **2012**, *18*, 2787–91.

Chapter 2:
Trapping and Characterization of a New Fe^{IV}=O Intermediate with Enhanced Reactivity due to Innovative Ligand Design

Compounds discussed in Chapter 2

Ligand	Fe(II) complex	Oxoiron(IV) intermediate
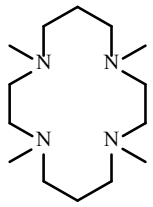	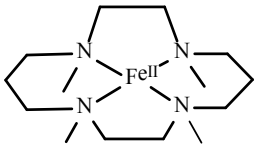	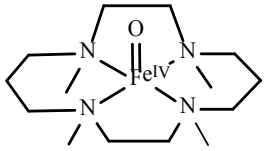
TMC		**Fe-TMC**
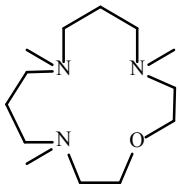	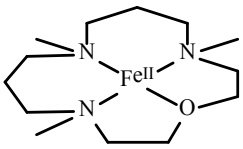	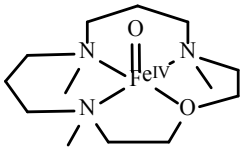
TMCO	**Fe-1**	**Fe-2**
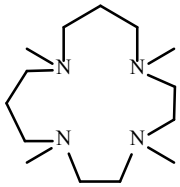	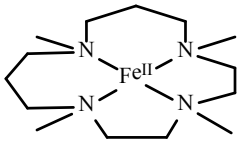	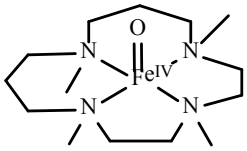
TMCN	**Fe-3**	**Fe-4**
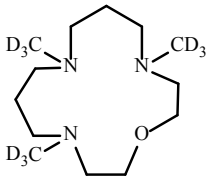	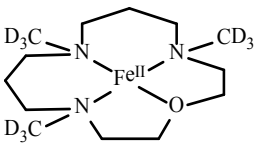	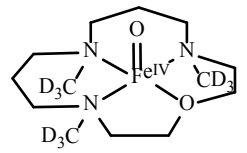
TMCO-d	**Fe-1d**	**Fe-2d**
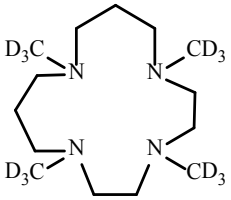	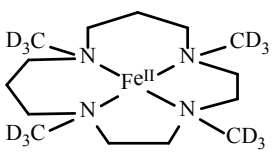	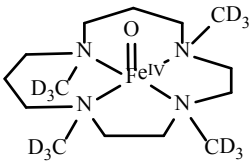
TMCN-d	**Fe-3d**	**Fe-4d**

2.1. Introduction

High-valent oxoiron species have been proposed, and in many cases identified, as key reactive intermediates in the catalytic cycles of iron enzymes responsible for processes that couple the activation of dioxygen with the oxidation of substrates. The reactions catalyzed by these species are as diverse as hydroxylation, halogenation, cyclization, epoxidation and desaturation, many of which are vital for processes like respiration, catabolism and angiogenesis.[1] Oxoiron species have been trapped in enzymes with haem and non-haem active sites, the latter ones involving both mono-metallic as well as di-metallic active sites.

The first evidence of high-valent oxoiron species involved in enzymatic activity was reported in the early 1980s for the haem peroxidases.[2,3] Now, after nearly 40 years of intense research in this field, crystal structures of the active sites of various haem-enzymes have been reported, including peroxidases, oxygenases and catalases such as horseradish peroxidase, cytochrome P450 (P450) and catalase.[4] In all cases, the detected high-valent iron-oxo active intermediate consists of an iron center in a ferryl state coordinated to an oxo ligand, and coupled to a cationic radical. Depending on the enzyme, the cationic radical is located in the porphyrin ring or in the amino acid residue near the haem ring.[4] The iron(IV) center in these systems is in an intermediate S = 1 state and it is either ferromagnetically or antiferromagnetically coupled to the radical, resulting in overall S = 3/2 or S = 1/2 states, respectively.[1] A relevant example of a haem-containing oxoiron intermediate is Compound-I of P450 (Cpd-I), a ferryl-porphyrin cation radical, shown in Figure 2.1 a.

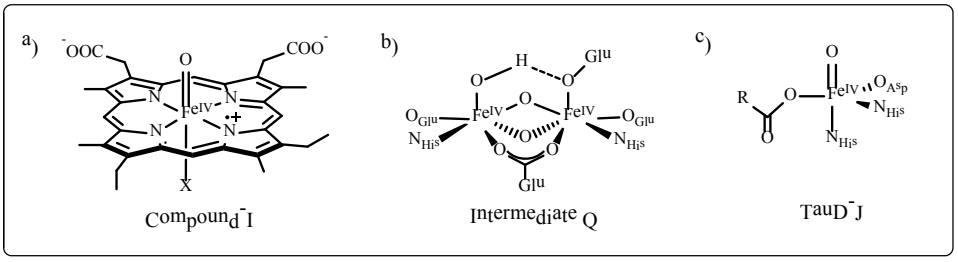

Figure 2.1: High-valent oxoiron intermediates of iron-containing enzymes: a) Compound-I intermediate of iron-containing haem enzymes, like cytochrome P450, catalase or peroxidase, X can be a cysteine, tyrosine or histidine residue; b) intermediate-Q of soluble methane monooxygenase; c) Intermediate-J of Taurine dioxygenase (TauD-J).

In non-haem iron oxygenases, on the other hand, two different types of high-valent iron-oxo active sites have been identified, depending on the nuclearity of the active site. Active dinuclear

iron centers can be found in the enzymes methane and toluene mono-oxygenases, fatty acid desaturases and the ribonucleotide-reductase. The intermediate-Q shown in Figure 2.1 b is associated with the soluble methane monooxygenase (MMO). The active site of this enzyme contains a diiron center coordinated by two histidines and four carboxylates and the intermediate-Q is postulated to involve a Fe_2^{IV}-$(\mu\text{-}O)_2$ diamond core.[5]

A third type of high-valent oxoiron active species has been detected for non-haem mononuclear sites. Despite the size and mechanistic diversity of the family of enzymes that utilize mononuclear non-haem iron centers, most of them present a common structural arrangement in which the iron center is coordinated by two histidines and a carboxylate group, forming the characteristic 2-His/1-Carboxylate facial triad, which occupies a face of the octahedron. The active species for this family of enzymes contains a high-valent iron-oxo core coordinated by the facial triad and a fifth ligand. The nature of the fifth ligand depends on the enzyme. For the Taurine dioxygenase (TauD)[6], the fifth ligand in the intermediate-J (TauD-J, Figure 2.1 c) is a succinate resulting from the decarboxylation of the co-substrate α-ketoglutarate.[7,8] In all the non-haem enzymes studied so far, the iron(IV) center has been found to be in the high-spin S = 2 state. It has been suggested that this is due to the weak ligand field exerted by the combination of histidine and carboxylate ligands present at the non-haem active sites.[1,9]

Given the extended natural occurrence of the high-valent iron-oxo units and their participation as active species in a number of valuable chemical transformations, vast attempts have been made to model these crucial intermediates in the last few decades. The first fully characterized high-valent iron-oxo complex was reported in 1981 by Groves and coworkers.[10] They were able to obtain the oxoiron(IV) porphyrin cation radical $[(TMP^{\bullet+})Fe^{IV}(O)(CH_3OH)]^+$ via the oxidation of $[(TMP)Fe^{III}(Cl)]$ (TMP = meso-tetramesityl porphinate anion), with meta-choroperbenzoic acid at −78 °C. Characterized by UV-vis absorption spectroscopy (UV-vis), electron paramagnetic resonance (EPR), Möβbauer, resonance Raman (rRaman) and extended X-ray absorption fine structure (EXAFS), the iron center of the active species was found to be in a S = 1 configuration and was active in olefin epoxidation and alkane hydroxylation reactions. After this report, a great number of oxoiron(IV) porphyrin radicals have been synthesized, spectroscopically characterized and exhaustively researched in a variety of oxidation reactions.[11]

Despite the initial success in stabilizing the iron-oxo complexes with porphyrinic ligands, it was not until 2000 that the first characterized non-haem oxoiron(IV) was reported by Wieghardt and coworkers.[12] It has been suggested that the reason for this 20-year delay was the difficulty in

characterizing non-haem iron-oxo species by routine spectroscopy techniques given the lack of suitable spectroscopic signatures for the presence of an iron-oxo unit.[9,13] However, a great breakthrough in the area came in 2003 when the groups led by Que Jr. and Nam came together and reported the first crystal structure of an oxoiron(IV) complex formed from the reaction of the complex $[(TMC)Fe^{II}(OTf)_2]$ (**TMC** = 1,4,8,11-tetramethyl-1,4,8,11-tetraazacyclotetradecane) and iodozobenzene (PhIO) at −40 °C to yield the intermediate $[(TMC)Fe^{IV}(O)(MeCN)]^{2+}$ (**Fe-TMC**) (Figure 2.2).[14]

The pale green **Fe-TMC** intermediate was characterized by a number of techniques, including UV-vis, EPR, Möβbauer, rRaman and electrospray ionization mass spectrometry (ESI-MS); the Fe(IV) center was determined to be in an intermediate S = 1 spin state. This species was found to be capable of transfering oxygen atoms to substrates such as PPh_3. However it proved to be inert towards the oxidation of C−H bonds.

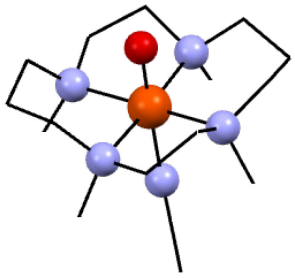

Figure 2.2: Molecular structure of the complex **Fe-TMC** previously reported in [14]. The hydrogen atoms and the counter anions have been omitted for clarity. Color code: C-black, N-blue, O-red, Fe-orange.

After the report of the **Fe-TMC** complex, the research in this field gained strength and in the past 13 years numerous mononuclear non-haem oxoiron complexes have been synthesized and characterized.[1,9,13,15–26] The ligands employed for the stabilization of such species have ranged from macrocyclic to tripodal ligands and from tetradentate to pentadentate ones, but in all cases mainly nitrogen donors have been used. The majority of the synthesized Fe(IV)-oxo cores have S = 1 ground state, in contrast to the S = 2 state of the enzymatic intermediates. Recent synthetic efforts have however also led to the characterization of five different S = 2 oxoiron(IV) complexes.[26]

The quintet oxoiron(IV) species (S = 2) have been proposed by density functional theory (DFT) calculations to be much more reactive towards C−H bond activation than their triplet (S = 1) counterparts,[1,27,28] which would explain nature's preference for iron-based enzymes that employ high-spin cores to perform the catalytic C−H bond activation reactions. The proposed mechanism for the activation of C−H bonds by oxoiron(IV) species involves two steps (Scheme 2.1).[26] In the

first step, the hydrogen atom transfer (HAT) takes place from the substrate C−H bond to the oxoiron complex, affording an alkyl radical and an [Fe^{III}(OH)] species. In the second step, an oxygen rebound (OR)[29–32] typically occurs, leading to the generation of an Fe(II) species and the oxidized substrate. The higher reactivity of the S = 2 oxoiron(IV) species compared to the S = 1 cores has been rationalized by the action of two factors both affecting the HAT step of the mechanism; the first of them relates to the way the substrate approaches the oxoiron center in each case and the second one regards the exchange interactions.

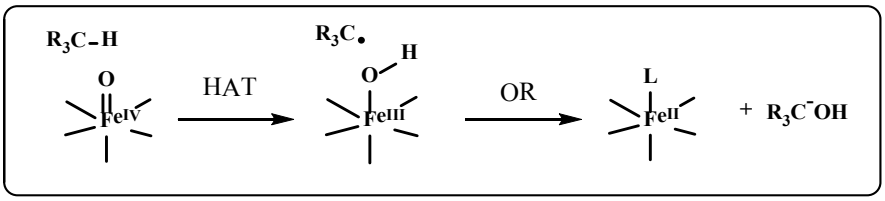

Scheme 2.1: Proposed mechanism of C−H bond activation performed by oxoiron(IV) complexes. The first step proposed is a hydrogen atom transfer (HAT), followed by an oxygen rebound (OR) step.

The orbital splitting, derived from considerations of simple ligand field theory, for an iron(IV)-oxo species in a fourfold symmetry is shown in Figure 2.3.[33] The energetic order of the *d* orbitals is a consequence of the tetragonal compression due to the strong M=O bond. The orbitals d_{z^2} and $d_{x^2-y^2}$ form strong antibonding combinations with the σ orbitals of the ligand, whereas the d_{xz} and d_{yz} orbitals form strong π* antibonding combinations with the p_x and p_y orbitals of the oxo ligand. Since the HAT reaction is an electrophilic attack by the Fe=O core, the frontier molecular orbitals (FMOs) of the oxoiron(IV) need to be low-energy, unoccupied orbitals that are highly localized and able to achieve a good overlap with the substrate FMOs.[34] The key FMOs likely to be involved in the HAT step have been determined, by experimental and theoretical methods,[34–36] to be the singly-occupied π* $d_{xz/yz}$ and the unoccupied σ* d_{z^2}.

The transfer of a hydrogen atom from the substrate to the oxoiron species would be accompanied by the introduction of one electron to either one of these FMOs. If a π-attack takes place both in the S = 1 and S = 2 cases (Figure 2.3 a and b), the insertion of the electron into the π* $d_{xz/yz}$ orbitals implies that the substrate must approach in a side-on manner to achieve maximum overlapping of the orbitals; this approach would result in a high steric interaction between the substrate and the ligand of the oxoiron complex, thereby raising the reaction energy barrier. An additional pathway, a σ attack (Figure 2.3 c), is available only for the S = 2 complexes (the triplet σ-path has been determined to be too high in energy).[37] In this pathway, the insertion of one

electron into the σ* orbital d_{z^2} involves a linear transition state where the steric interactions between the oxoiron core and the substrate are limited, thus reducing the reaction barrier.[16,21,33]

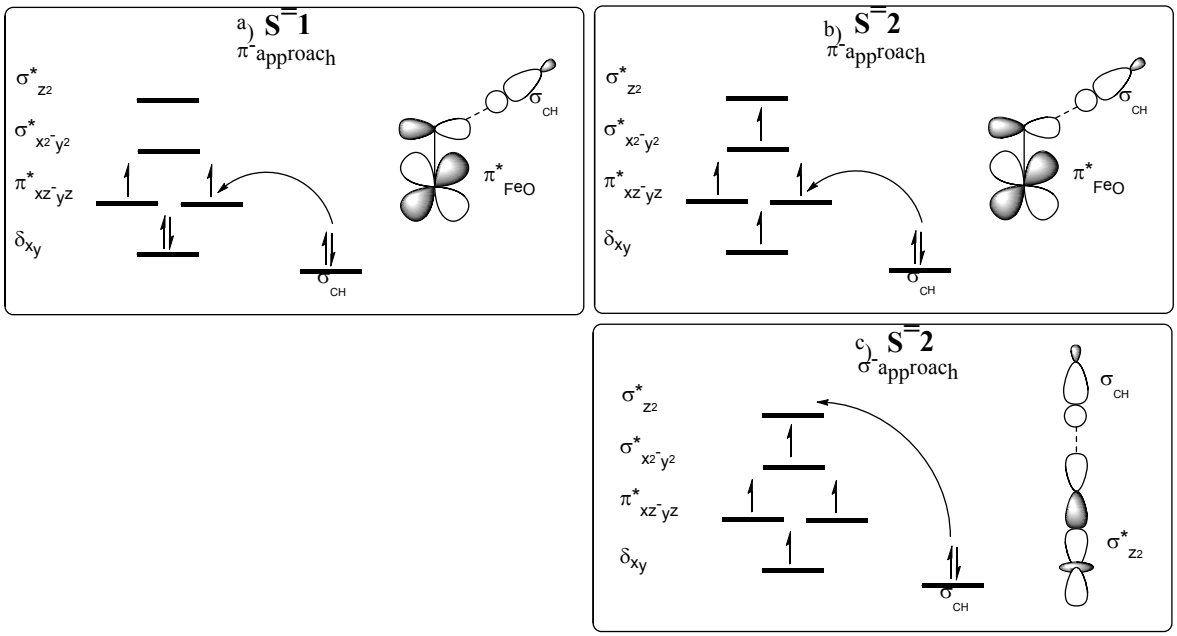

Figure 2.3: Comparison of the FMOs involved in the single electron transfer HAT process carried out by oxoiron(IV) complexes with fourfold symmetry on the S = 1 and S = 2 surfaces. Reproduced from [33].

The exchange interactions, on the other hand, measure the decrease in electron-electron repulsion between the spin-identical electrons as a result of their mutual avoidance.[33] The exchange-enhanced reactivity predicts that the pathway where the number of spin-identical electrons in the metal increases will be favored by exchange stabilization, since the number of exchange interactions will increase. This effect is maximized in an S = 2 oxoiron(IV) core in which the initial number of spin-identical electrons is four (Figure 2.3). The addition of one more electron stabilizes the system with four new exchange interactions, which is the maximum exchange stabilization.[33] In the case of an intermediate-spin S = 1 oxoiron(IV) core, the opposite occurs, since the addition of one electron to a singly-occupied π* orbital reduces the number of exchange interactions. Thus, due to the exchange interactions, the quintet barrier is lower than the triplet one (Figure 2.4).[16,33]

The reactivity of the oxoiron(IV) compounds has been shown to be affected not only by the nature of the ground spin state of the iron in the complex but also by the accessibility of the excited state. The higher reactivity of the S = 2 state was employed by Shaik and coworkers to explain the

reactivity patterns observed for S = 1 oxoiron(IV) compounds through the introduction of the two-state reactivity model (TSR).[38,39] This model postulates that the net activation barrier for the C−H bond cleavage performed by an S = 1 oxoiron compound is a weighted blend of the barrier of the reaction on the ground triplet surface and that on the excited quintet surface. Since the transition state on the quintet surface lies lower in energy than the transition state on the triplet surface, a decrease in the gap between the triplet and quintet states in a compound (ΔE_{TQ}) results in an increase in the accessibility of the quintet state and thus a decrease the activation barrier for the C−H bond activation. This phenomenon is represented in Figure 2.4 and has proven to be fundamental in understanding the reactivity of S = 1 oxoiron(IV) complexes.

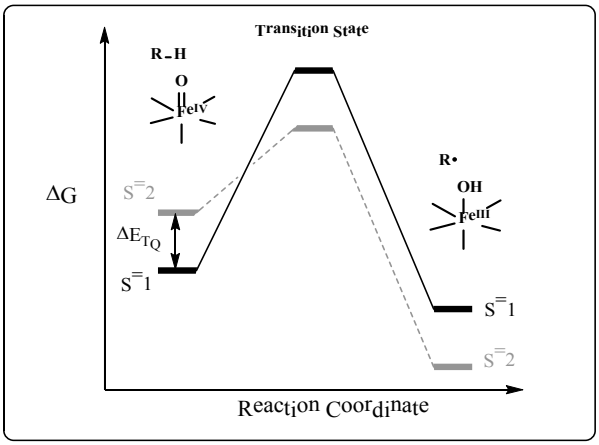

Figure 2.4: Representation of the TSR during the hydrogen atom abstraction reactions of an oxoiron(IV) compound in a tetragonal geometry. ΔE_{TQ} is the energy gap between the triplet and quintet states. Figure reproduced from reference [26].

To date, the two most reactive mononuclear non-haem oxoiron(IV) models synthesized and completely characterized are the $[(Me_3NTB)Fe^{IV}(O)(MeCN)]^{2+}$ (Me_3NTB = tris((*N*-methyl-benzimidazol-2-yl)methyl)amine)) complex reported by Latour, Shaik, Nam and coworkers,[22] and the $[(TQA)Fe^{IV}(O)(MeCN)]^{2+}$ (TQA = tris(2-quinolyl-methyl)amine)) compound reported by Bominaar, Münk, Que Jr. et al;[24] both are presented in Figure 2.5. The first one, obtained from the reaction of $[(Me_3NTB)Fe^{II}(MeCN)](OTf)_2$ with *m*-chlorperbenzoic acid in acetonitrile at −40 °C, possesses an intermediate-spin (S = 1) triplet ground state but a highly accessible S = 2 high-spin state, resulting in extremely low activation barriers and high reactivity. In contrast, the recently reported $[(TQA)Fe^{IV}(O)(MeCN)]^{2+}$ complex, obtained from the reaction of $[(TQA)Fe^{II}(OTf)_2]$ with soluble iodosobenzene (sPhIO) in MeCN at −40 °C was found to have a high-spin (S = 2) quintet ground state and reactivity rates comparable to those of the natural intermediate TauD-J.

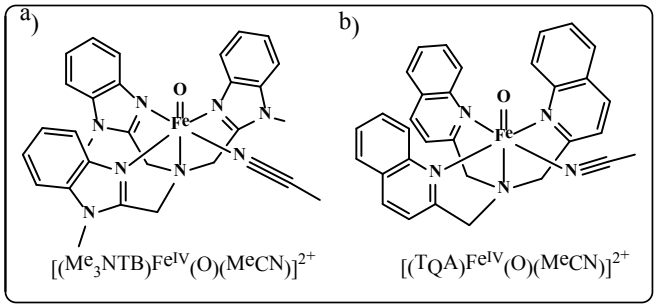

Figure 2.5: Structures of the complexes a) $[(Me_3NTB)Fe^{IV}(O)(MeCN)]^{2+}$[22] and b) $[(TQA)Fe^{IV}(O)(MeCN)]^{2+}$.[24]

The trapping of the highly reactive $[(TQA)Fe^{IV}(O)(MeCN)]^{2+}$ complex was achieved by the use of a tripodal ligand with weaker-field donors such as quinolines;[40] this approach condenses the two different strategies that have been employed to stabilize species with high-spin configurations and, desirably, higher reactivities. The first strategy refers to the enforcement of a trigonal-bipyramidal geometry on the Fe(IV) center of the intermediate by using bulky tripodal ligands. This technique has been employed for the generation of high-spin oxoiron(IV) complexes such as $[(TMG_3tren)Fe^{IV}(O)]^{2+}$[41] and $[H_3buea)Fe^{IV}(O)]^{-}$;[42] however, the reactivities of these compounds were shown to be rather sluggish due to the steric constraints of the ligands. The second strategy employed is the generation of weaker ligand field environments than those provided by the typical tertiary amine/*N*-heterocyclic combinations. This strategy was shown to be effective for Bakac and coworkers, who were able to detect the formation of a highly reactive S = 2 $[Fe^{IV}(O)(H_2O)_5]^{2+}$ species in an acidic (pH = 1) aqueous solution treated with O_3; however, it proved challenging to provide a detailed characterization of this compound due to its short lifetime.[43]

The use of oxygen donors instead of nitrogen ones to constrain the iron center in a weaker ligand field environment, and thus generate highly reactive species capable of oxidizing substrates with strong C−H bonds, has also proven successful in the work by Long and coworkers.[44] The metal-organic framework $Fe_2(dobdc)$, ($(dobdc)^{4-}$ = 2,5-dioxido-1,4-benzene-dicarboxylate) was shown to activate the C−H bonds of ethane and convert it to ethanol using nitrous oxide as the oxidant. The active species was proposed on the basis of DFT calculations to be a high-spin S = 2 oxoiron(IV) core, where the oxoiron(IV) centers are sterically accessible and site-isolated, as well as entrenched in a weak ligand field environment; however, such an intermediate has not been isolated.

Despite the success of using ligands with oxygen donors to achieve weaker ligand field environments around iron centers and thus obtain more reactive high spin oxoiron(IV) complexes,

as proved by Long[44] and Bakac[43], no study has been carried out that systematically shows the effect of replacing nitrogen donors with oxygen ones in a given ligand. Such a study could improve our understanding of the factors that control both the electronic structure as well as the reactivity patterns in non-haem oxoiron(IV) complexes, and thus help us to generate more reactive compounds and eventually design better catalysts to perform synthetic C−H bond oxidations.

In this chapter, we present a first step towards a systematic study of the effect that the replacement of nitrogen donors with oxygen ones in a given ligand has on the generation, electronic structure and reactivity of the related oxoiron(IV) compounds. The **TMC** ligand, used to obtain the first crystal structure of a mononuclear non-haem oxoiron(IV) complex (**Fe-TMC**), was taken as a point of reference and the analogous ligand **TMCO** (4,8,12-trimethyl-1-oxa-4,8,12-triazacyclotetradecane), containing one oxygen donor and three nitrogen ones, was produced. The iron complex [(TMCO)Fe^{II}(MeCN)(OTf)](OTf) (**Fe-1**) was synthesized and a new oxoiron(IV) complex, [(TMCO)Fe^{IV}(O)(MeCN)]$^{2+}$ (**Fe-2**), was generated from the reaction of **Fe-1** with sPhIO at −90 °C in CH_2Cl_2. This new complex was further characterized and tested; the results obtained are described and discussed below.

2.2. Results and discussion

2.2.1 Synthesis of the TMCO ligand

Since they were first synthesized in 1961,[45] macrocyclic polyamines, such as the 12-membered ring Cyclen (1,4,7,10-tetraazacyclododecane), also called [12]aneN_4, and its derivatives[46], have received a lot of attention, particularly after it was discovered that they were able to chelate a wide variety of metal cations and generate stable complexes.[47] Research into this family of macrocyclic polyamines and their applications has extended to various fields. In medicinal chemistry, some derivatives are employed as magnetic resonance imaging (MRI) and positron emission tomography (PET) contrasting agents as well as deoxyribonucleic acid (DNA) cleavage agents.[48,49] In the field of bioinorganic chemistry, which is of greater interest for this study, they have been utilized as versatile ligands for the biomimetic chemistry of dioxygen activation by metal complexes.[50] The most studied ligand in this large family of macrocycles is the **TMC** or Me_4[14]aneN_4, which is a 14 membered ring with four methylated amines in positions 1,5, 8 and 12 of the cycle, as shown in Figure 2.6.

The oxaaza counterparts of these tetraaza macrocycles, where one or more of the nitrogen donors are replaced by oxygen atoms, have received less attention but, nonetheless, some

interesting ligands have been synthesized and their metal complexation examined.[51] Studies of protonation and complexation with some selected metal cations were performed by the group led by Fráusto da Silva, with 12-, 13- and 14-membered oxatriaza[51,52] and dioxadiaza macrocycles.[53] More recently an oxatriaza cycle has been employed for generating Cu(II) and Zn(II) complexes with DNA and ribonucleic acid (RNA) cleavage properties.[49,54]

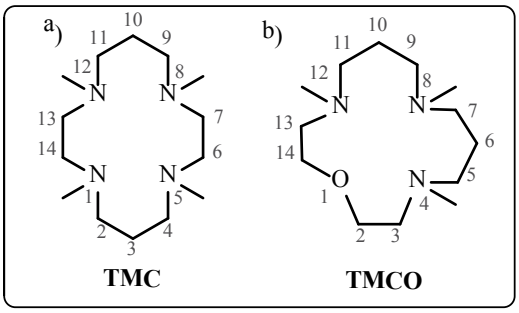

Figure 2.6: Structure of the ligands **TMC** (Me_4[14]aneN_4) and **TMCO** (Me_3[14]aneN_3O).

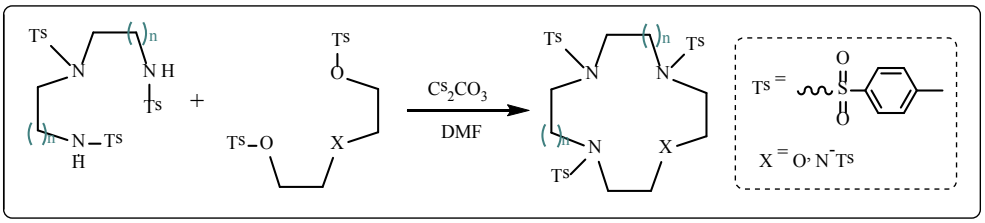

Scheme 2.2: General 3+1 synthetic route for the generation of tetraaza and oxatriaza macrocycles, first reported by Richman and Atkins.[46] The Cs_2CO_3 is not present in all the reported synthetic procedures and the temperature conditions may vary, "n" is typically 1 or 2.

The cyclization step generally followed for obtaining this vast family of macrocycles is the 3+1 cyclization,[48] first reported by Richmand and Atkins for tetraaza macrocycles[46] and depicted in Scheme 2.2. Using this methodology, it is not possible to obtain, as a single product, an oxatriaza macrocycle structurally equivalent to the **TMC** ligand; however, an analogous 14-membered ring with an oxygen donor in position 1 of the cycle and nitrogen donors in positions 4, 8 and 12 (Figure 2.6) can be synthesized. This compound has been reported before and employed as the ligand most closely related to the **TMC** ligand.[51] Its name has been typically referred to as Me_3[14]aneN_3O; in this nomenclature, the size of the macrocycle is stated in brackets and the nature of the donor atoms is stated at the end of the formula. This naming is useful for comparing a vast amount of such macrocycles, but for clarity, in this study the name **TMCO** will be employed for this compound to enable a direct comparison with the **TMC** ligand.

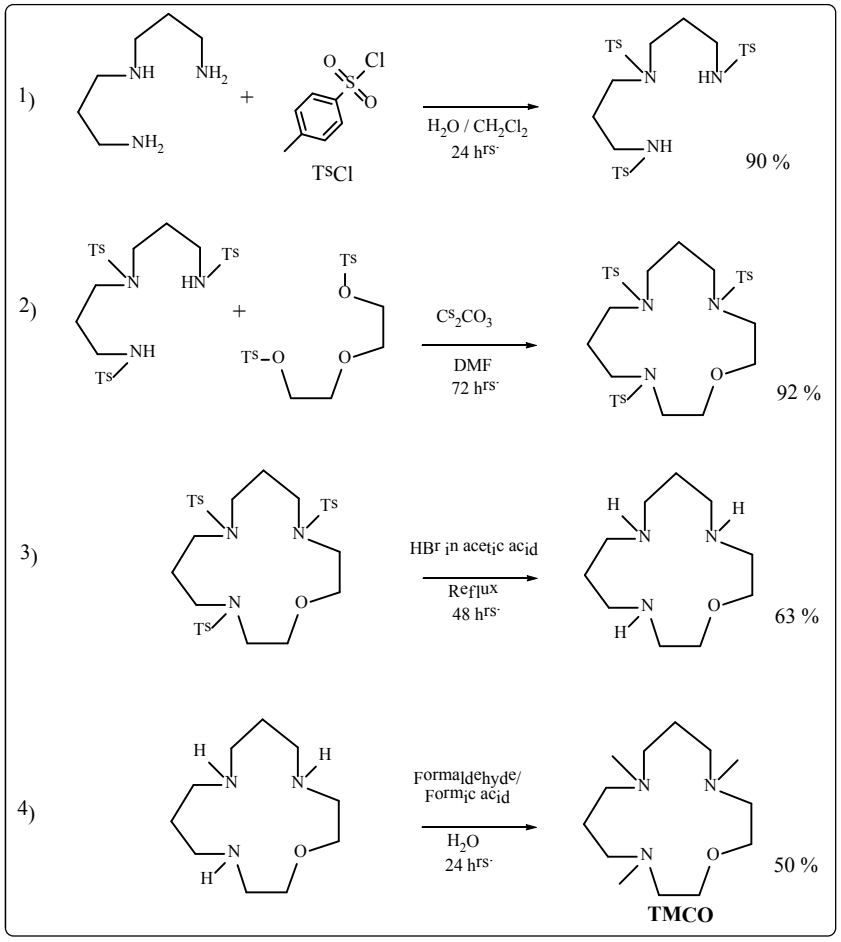

Scheme 2.3: Four-stepped synthesis of the **TMCO** ligand.

The full synthesis of the ligand **TMCO** was performed *via* the four steps shown in Scheme 2.3, with small modifications from previous reports.[51,55,56] Firstly, the 3,3'-diaminodipropyl-amine was tritosylated by using tosyl-chloride. This was a facile synthesis with a good yield of 90% of the tri-tosylated product and could be performed on a gram scale. The second step was the 3+1 macrocyclization of the protected polyamine with diethyleneglycol-di(*p*-toluenesulfonate) in the presence of Cs_2CO_3. In this reaction, the cesium carbonate acts as a base to generate the dianion of the sulfonamide-protected polyamine that would further couple with the ditosylate; in this step, the sulfonamides act as protecting groups but also provide a Thorpe-Ingold-type effect on the transition state that favors intramolecular cyclization instead of intermolecular oligomerization.[57] Despite the fact that this step requires long reaction times, the obtained yields were good. The third step consisted of the deprotection of the polyazamacrocycle using a hydrobromic acid / acetic acid mixture to obtain [14]aneN_3O in modest yields. Finally, in the last step, the methylation of the macrocycle yielded the ligand **TMCO** in the form of a yellow oil, again in only modest yields. The

formation of the ligand **TMCO** and its purity were corroborated with proton magnetic nuclear resonance (^{1}H-NMR) and ESI-MS measurements.

2.2.2 Synthesis and characterization of Fe-1

The complex [(TMCO)Fe^{II}(MeCN)(OTf)](OTf) (**Fe-1**) was synthesized by reacting equimolar amounts of [Fe^{II}(OTf)$_2$(MeCN)$_2$] and the previously synthesized **TMCO** ligand in MeCN for 72 hours under inert conditions (Scheme 2.4). After treatment of the acetonitrile solution with diethyl ether (Et_2O), the complex was obtained in the form of colorless crystals and was characterized by ESI-MS, EPR, Möβbauer, X-ray absorption (XAS) and X-ray crystallography.

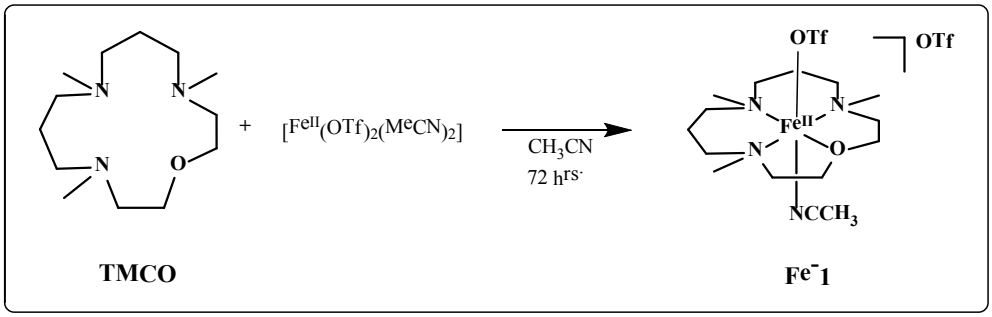

Scheme 2.4: Synthesis of the complex **Fe-1**.

The ESI-MS spectrum of **Fe-1** is shown in Figure 2.7 a; it exhibits one prominent peak at *m/z* 448.121 and a smaller one at *m/z* 334.140 whose mass and isotope distribution corresponds to [(TMCO)Fe^{II}(OTf)]$^+$ (calculated *m/z* = 448.118) and [(TMCO)Fe^{II}(Cl)]$^+$ (calculated *m/z* = 334.139). The X-band EPR spectrum of **Fe-1** shows no signals, which is consistent with **Fe-1** being an integer spin ferrous system. The spin state of the complex in solid state was determined using zero-field Möβbauer spectroscopy. The 12 K spectrum, presented in Figure 2.7 b, shows one doublet with an isomer shift (δ') of 1.1705 ± 0.002 mm/s and quadrupole splitting (ΔE_Q) of 3.3147 ± 0.003 mm/s; such a high positive isomer shift demonstrates the nature of **Fe-1** as a high-spin Fe(II) center.[58] This assignment was further confirmed by low-temperature ^{1}H-NMR studies (Figure 2.9 c), where the distribution of the signals in the range of 500 to −100 ppm corroborates the presence of a paramagnetic Fe(II) center in **Fe-1**.

Single crystals of **Fe-1** suitable for crystallographic analysis were obtained by the diffusion of diethyl ether into a concentrated acetonitrile solution of **Fe-1**. The asymmetric unit cell of **Fe-1** contains two compositionally identical units that exhibit some slight differences; a representation of one of the two independent [(TMCO)Fe(MeCN)(OTf)]$^+$ cations is shown in Figure 2.8 with selected bond distances and angles. The crystal structure shows a hexa-coordinated ferrous center

with the four donor atoms of the **TMCO** ligand in the equatorial positions and one acetonitrile and one triflate ion acting as axial ligands. The acetonitrile molecule is oriented *syn* relative to the methyl groups of the macrocycle. The coordination geometry around the iron is best described as a distorted octahedral.

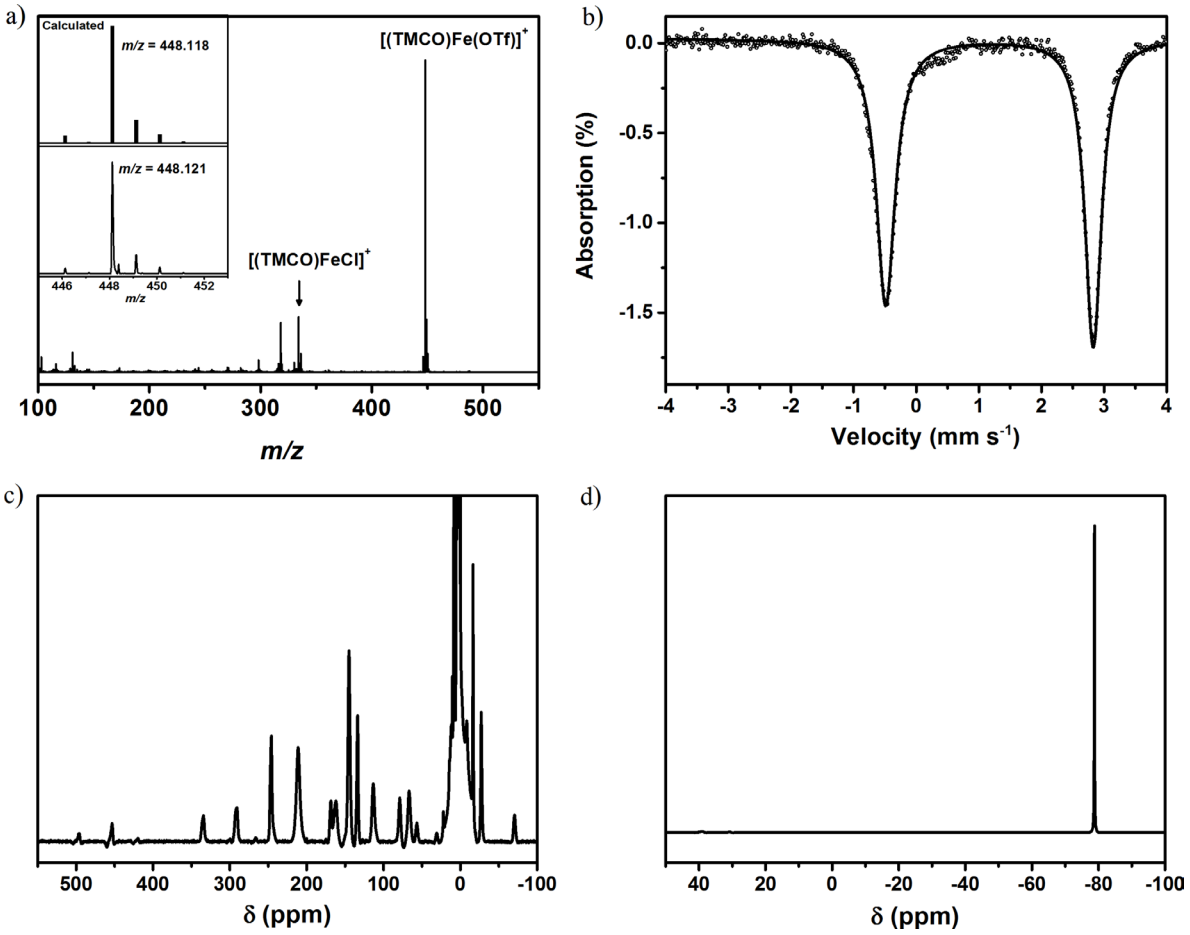

Figure 2.7: a) ESI-MS spectrum of **Fe-1** recorded in MeCN; inset: experimental and calculated isotopic distribution for the main peak; b) Möβbauer spectrum of the solid **Fe-1** recorded at 12K; black points: experimental results, black line: simulation; c) ^{1}H-NMR and d) ^{19}F-NMR of **Fe-2** in d_3-dichloromethane obtained at low temperature.

Notably, the reported Fe(II) complexes with the **TMC** ligand are penta-coordinated, and bear an anionic/neutral ligand in the axial position, oriented *syn* relative to the methyl groups;[59–62] in **Fe-1** this position is occupied by an acetonitrile molecule while the triflate occupies the sixth coordination position that remains empty for the Fe(II)-**TMC** derivatives. The only reported structure where an oxygen donor from the counterion-triflate points towards the Fe(II) center through the vacant axial position is [(TMC)Fe(SC_6H_4-*p*-OMe)](OTf);[59] however, the Fe-O distance

in this case is 4.097 Å, much larger than the 2.237 Å found for **Fe-1**. The hexa-coordinated nature of the iron center in **Fe-1,** in contrast to the penta-coordinated nature of **Fe-TMC,** is consistent with the higher electron donation of the **TMC** ligand in relation to **TMCO**. Despite the structural differences, for all the Fe(II)-**TMC** complexes, as well as for **Fe-1,** the iron center has been found to be in a high-spin configuration.[59,63]

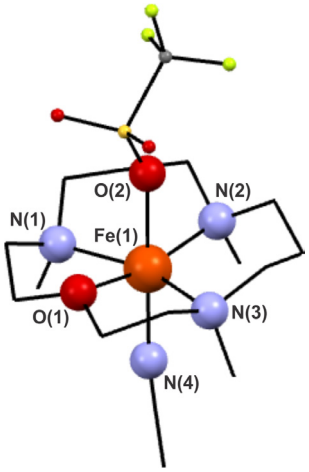

Figure 2.8: Molecular structure of **Fe-1** determined by X-ray crystallography. The hydrogen atoms and the triflate counterion have been omitted for clarity. Color code: C-black, N-blue, O-red, S-yellow, F-green, Fe-orange. Selected distances: Fe(1)-O(1) 2.085(2) Å; Fe(1)-N(1) 2.178(2) Å; Fe(1)-N(2) 2.107(2) Å; Fe(1)-N(3) 2.192(2) Å; Fe(1)-N(4) 2.130(2) Å; Fe(1)-O(2) 2.237(2) Å. Selected angles: O(1)-Fe(1)-N(2) 165.03(9)°, O(1)-Fe(1)-N(4) 96.98(9)°; N(2)-Fe(1)-N(4) 97.99(10)°; O(1)-Fe(1)-N(1) 78.63(9)°; N(2)-Fe(1)-N(1) 101.23(10)°; N(4)-Fe(1)-N(1) 89.59(9)°; O(1)-Fe(1)-N(3) 78.82(9)°; N(2)-Fe(1)-N(3) 101.71(10)°; N(4)-Fe(1)-N(3) 88.73(9)°; N(1)-Fe(1)-N(3) 157.01(9)°; O(1)-Fe(1)-O(2) 82.33(8)°; N(2)-Fe(1)-O(2) 82.71(8)°; N(4)-Fe(1)-O(2) 178.65(9)°; N(1)-Fe(1)-O(2) 91.40(8)°; N(3)-Fe(1)-O(2) 90.01(8)°.

^{19}F-NMR studies showed that the presence of the triflate in the sixth coordination position around the Fe(II) center observed in the solid state is not retained in solution. This is evident from the single NMR peak at −79 ppm (Figure 2.7 d), a position typically associated with uncoordinated triflates in paramagnetic Fe(II) compounds.[64–67]

2.2.3 Generation and characterization of Fe-2

The reaction between a colorless solution of **Fe-1** with 1.5 equivalents of sPhIO in anhydrous dichloromethane at −90 °C led to the immediate formation of the pale green intermediate **Fe-2** (Scheme 2.5) that proved to be stable at −90 °C for more than 2 hours; at −50 °C **Fe-2** was found to be metastable with a half-life of 90 minutes. **Fe-2** presented an absorption spectrum typical of oxoiron(IV) complexes (Figure 2.9), with a near-UV shoulder at ca. 390 nm

(ε_{max} > 3000 $M^{-1}cm^{-1}$) and two bands of low intensity at 585 nm (ε_{max} = 200 $M^{-1}cm^{-1}$) and 848 nm (ε_{max} = 150 $M^{-1}cm^{-1}$).

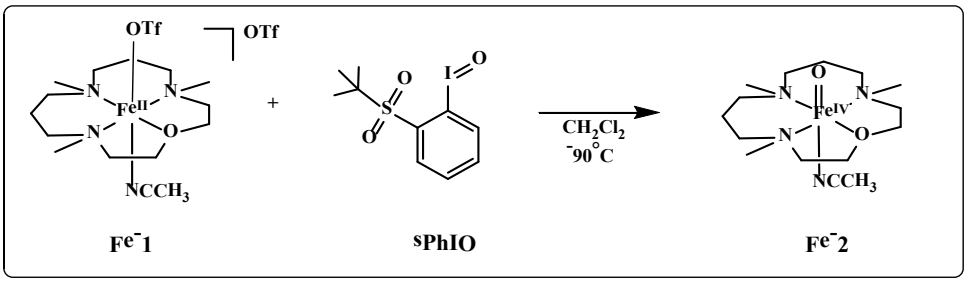

Scheme 2.5: Generation of the intermediate **Fe-2**.

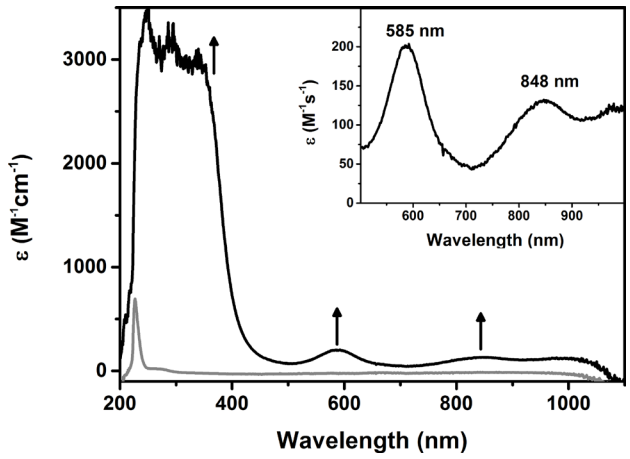

Figure 2.9: Absorption spectra of **Fe-1** (gray line) and **Fe-2** (black line) in anhydrous CH_2Cl_2 at −90°C.

Oxoiron(IV) compounds have been reported to exhibit pale green or yellowish green color[9,14,22,25] derived from near-infrared bands known to be arising from *d-d* ligand-field transitions of the Fe(IV)=O center;[20] the assignment from the origin of this band has been carefully made by magnetic circular dichroism (MCD) measurements on the **Fe-TMC** complex.[68] Furthermore, the more intense near-UV feature observed in many oxoiron(IV) complexes has been assigned to be a O^{2-} to Fe(IV) charge transfer (CT) in nature.[61] By making an analogy between these previous studies and the absorption spectrum of **Fe-2**, it was possible to assign the nature of the strong shoulder band at 390 nm to an O^{2-} to Fe(IV) CT and the two low-intensity bands at 585 and 848 nm to *d-d* transitions.

Electrospray ionization mass spectrometry (ESI-MS) analysis of **Fe-2** supported the formulation of the new intermediate as $[(TMCO)Fe^{IV}(O)]^{2+}$ (Figure 2.10). One of the dominant features in the spectra in the positive ion detection mode appeared at *m/z* = 464.1; a value that

corresponds to the $[(TMCO)Fe^{IV}(O)(OTf)]^+$ cation. However, the isotope distribution pattern suggests the presence of $[(TMCO)Fe^{III}(OH)(OTf)]^+$ (*m/z* = 465.1), probably due to the instability of **Fe-2** under the conditions of the ESI-MS experiment. Upon generation of **Fe-2** with $sPhI^{18}O$, a shift by two units in the ESI-MS *m/z* = 464.1 peak was observed, indicating that **Fe-2** contains an iron-oxo group.

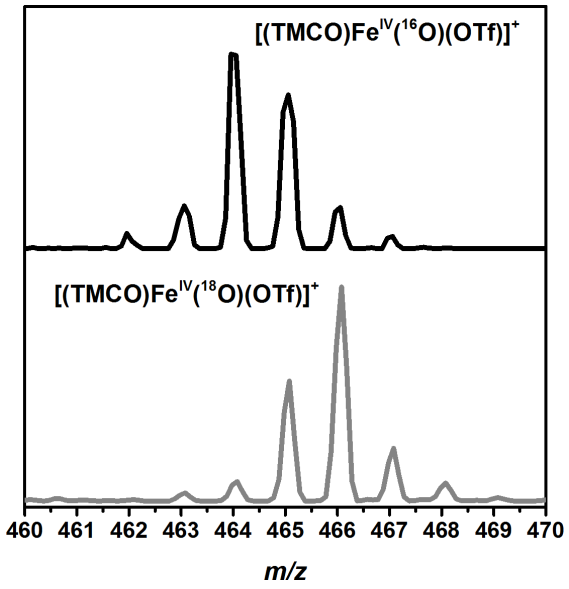

Figure 2.10: ESI-MS of **Fe-2,** generated using $sPhI^{16}O$ (black line) and $sPhI^{18}O$ (gray line), where the isotopic shift of the main peak, which relates to the oxoiron(IV) species, can be observed.

The X-Band EPR spectrum of **Fe-2** in a frozen solution of CH_2Cl_2 was also obtained. **Fe-2** proved to be EPR-silent, as observed for other non-haem iron complexes given the integer spin state of Fe(IV) with a d^4 electronic configuration.[9,17] The sample, however, contained around 15% of an Fe(III) species, probably in the form of $[(TMCO)Fe^{III}(OH)]^{2+}$, which could also be observed in the mass spectra and could have been generated due to the partial decay of **Fe-2**.

Further characterization of oxoiron(IV) compounds typically includes rRaman.[15,20] For this experiment, a laser with a wavelength close to the CT band is employed to generate the excitation. Attempts to obtain a rRaman spectra of **Fe-2** were not successful despite the use of different lasers and different experimental setups, probably due to the sensitivity of the complex towards the laser radiation. Hence, no vibrational characterization of **Fe-2** could be achieved.

To further confirm the assignment of **Fe-2** as a high-valent oxoiron(IV) compound and to evaluate its electronic ground state, Möβbauer spectroscopy was employed. The intermediate **Fe-2** can be generated easily in dichloromethane (CH_2Cl_2); however, CH_2Cl_2 is not an adequate solvent

for Möβbauer measurements since it is virtually opaque to Möβbauer radiation due to the non-resonant mass absorption effect of the atoms with larger atomic numbers, such as Cl and S.[69] Several attempts were made to generate **Fe-2** in different solvents, such as acetonitrile, tetrahydrofuran (THF), 2-methyl THF, propionitrile and acetone. However, none allowed the stabilization of **Fe-2**. Most of the reported oxoiron(IV) complexes can be generated in acetonitrile (MeCN),[20] but **Fe-2** is not stable at temperatures higher than −50 °C. It is therefore reasonable that MeCN (freezing point = -45 °C) would not be able to stabilize it. Propionitrile (EtCN), on the other hand, is similar to MeCN and has a lower freezing point (−93 °C) but was also unable to stabilize **Fe-2**. The reason for this was thought to be the strong coordination of the solvent to **Fe-1** prior to the addition of sPhIO, which would prevent the reaction between them. In order to overcome this obstacle, a highly concentrated solution of **Fe-2** was generated in CH_2Cl_2 at −90 °C and was further diluted with EtCN at the same temperature to achieve a solution with only 12% CH_2Cl_2. In this way, the coordination of the solvent was prevented and the intermediate **Fe-2** could be generated, while avoiding the large excess amount of Cl in the sample.

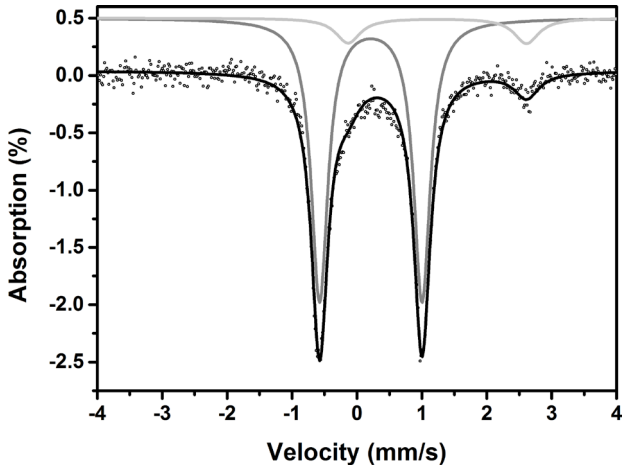

Figure 2.11: Möβbauer spectra of a 3 mM solution of ^{57}Fe-enriched **Fe-2** in propionitrile with 12% CH_2Cl_2 recorded at 13 K in the absence of an external magnetic field. Black dots: experimental points; light gray line: absorption due to the unreacted starting **Fe-1**; dark gray line: absorption due to **Fe-2**; black line: total fitting of the experimental spectra.

Figure 2.11 shows the Möβbauer spectrum of a 3 mM frozen solution of the ^{57}Fe-enriched **Fe-2** in propionitrile with 12% dichloromethane. The spectrum was recorded at 13 K with a zero applied magnetic field. It exhibits a dominant quadrupole doublet with an isomer shift δ = 0.213 mm/s and a quadrupole splitting ΔE_Q = 1.578 mm/s. Additionally, a smaller signal can be discerned, representing a minor contribution of a high-spin ferrous species, with parameters

corresponding to those of **Fe-1**. The obtained isomer shift of the major species is in the range of other non-haem oxoiron(IV) complexes,[9,24] although higher than that observed for **Fe-TMC**[14] (Table 2.1). However, the zero-field Möβbauer parameters are not sufficient to establish the spin state of the iron center. Therefore, Möβbauer measurements with the application of external magnetic fields are needed. Upon the application of large magnetic fields, the quadrupole doublet splits due to magnetic hyperfine interactions between the *d* electrons and the ^{57}Fe nucleus. The analysis of the resulting spectra allows for a distinction between an intermediate (S = 1) and a high spin (S = 2) iron(IV) center.

Magnetic Möβbauer data for the same **Fe-2** sample were collected over the temperature range from 4.2 to 50 K in a perpendicular applied field of 5.0 T (Figure 2.12). A spin-Hamiltonian simulation of the data could be achieved only under the assumption that the spin state of **Fe-2** is S = 1. An excellent fit to the data was obtained using the parameters presented in Table 2.1, where D and E are the axial and rhombic zero field spitting (ZFS) parameters respectively, A is the magnetic hyperfine tensor and η is the asymmetry parameter of the electric field gradient. The parameters reported for **Fe-TMC**[14] are also presented in Table 2.1 for the purposes of comparison. A large positive ZFS, given by the axial ZFS parameter D > 20 cm^{-1}, has been consistently observed in S = 1 oxoiron(IV) complexes.[70,71] The ZFS originates primarily from spin-orbit coupling between the ground-state spin triplet and the first excited-state quintet, and its magnitude is inversely proportional to the triplet-quintet energy separation.[72,73] The D value obtained for **Fe-2** (D = 37) is higher than that of **Fe-TMC** (D = 28) and other S = 1 oxoiron complexes.[70] This indicates that, while **Fe-2** has a triplet ground state, the quintet excited state lies closer to the triplet state in this complex than in **Fe-TMC**.

Table 2.1: Spin-Hamiltonian parameters of the Fe(IV) center in **Fe-2** and for the reported **Fe-TMC**.[14]

	S	D (cm^{-1})	E/D	g_x g_y g_z	$A/g_{N\beta N}$ (T)	δ (mm s^{-1})	ΔE_Q (mm s^{-1})	η
Fe-TMC[14]	1	28	0	2.3, 2.3, 2.3	-25, -20, -5	0.17	1.24	0.5
Fe-2	1	37.09	0.02	2.0, 2.0, 2.0	-28,-24.5,-0.9	0.2	1.6	0

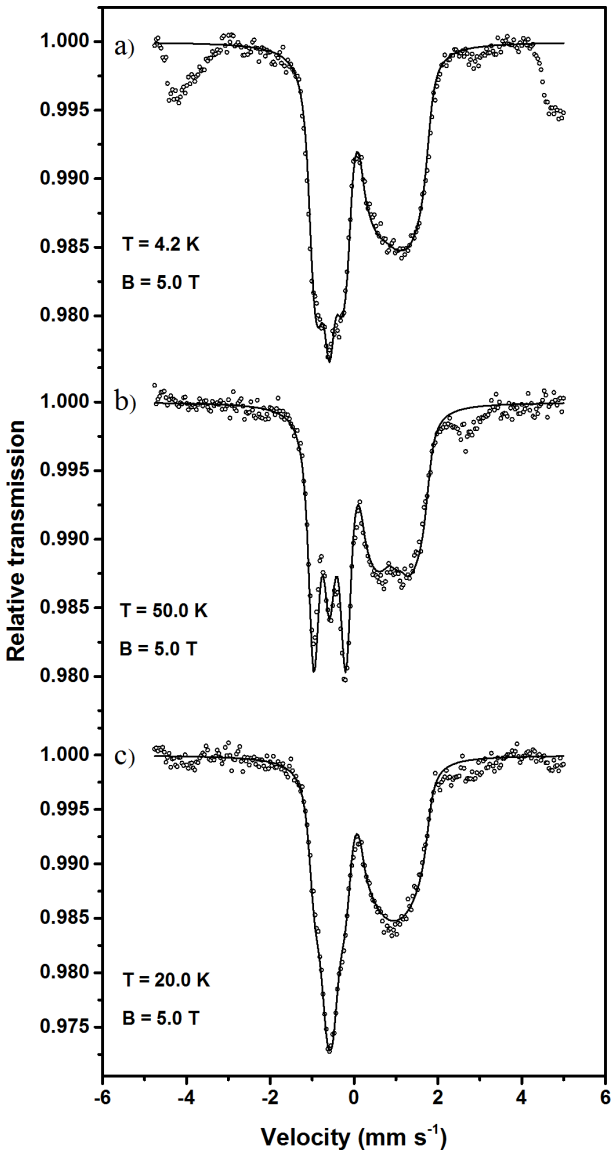

Figure 2.12: Möβbauer spectra of a solution of **Fe-2** in propionitrile with 12% CH_2Cl_2 (dots) measured at a) 4.2 K, b) 50.0 K and c) 20.0 K in a magnetic field of 5.0 T applied perpendicular to the γ-rays. Spin-Hamiltonian fitting obtained for a S = 1 configuration of the Fe(IV) species is shown as a black solid line and the parameters used are given in Table 2.1.

X-ray absorption spectroscopy (XAS) confirmed the formulation of **Fe-2** as an oxoiron(IV) complex. The normalized Fe *K*-edge spectra of **Fe-2** and **Fe-1** are shown in Figure 2.13. The spectrum of **Fe-2** shows a single intense pre-edge feature at 7113.8 eV with an edge at 7124.3 eV. Compared to **Fe-1**, the edge of **Fe-2** is shifted to higher energy, which is indicative of an increase in the Z* of the iron center, a change that is consistent with the Möβbauer assignment of an Fe(IV) oxidation state.[23,74,75] Additionally, **Fe-2** shows an intense 1*s*→3*d* pre-edge transition with an area

of 43 units. The area value observed here is comparable to those reported for other oxoiron(IV) complexes[23,74–76], albeit slightly larger (the pre-edge area of **Fe-TMC** is 30 units).[76] The occurrence of an intense 1*s*→3*d* pre-edge transition indicates significant mixing of the 3*d* and 4*p* orbitals. It has been suggested that this is caused by strong Fe=O π bonding that leads to the large deviation of centrosymmetry of the iron ligand field.[75] As the metal environment deviates from centrosymmetry, the pre-edge transition becomes more intense. The large value obtained for **Fe-2** might indicate that this complex contains a more distorted metal site[23], probably due to the presence of an oxygen donor together with 3 or 4 nitrogen donors in the first coordination sphere, in contrast to **Fe-TMC**, which only has nitrogen donors.

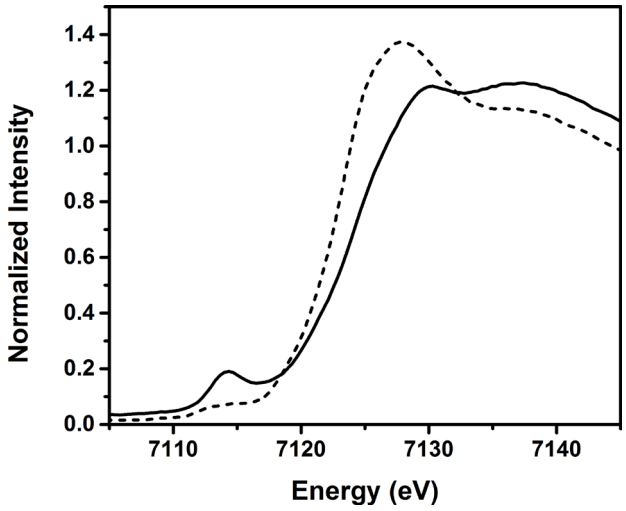

Figure 2.13: a) Normalized Fe *K*-edge X-ray absorption spectra of **Fe-1**in dichloromethane (black dashed line) and **Fe-2** 4.4 mM in propionitrile/dichloromethane 11% (black solid line).

In the absence of a crystal structure of **Fe-2**, the extended X-ray absorption fine-structure (EXAFS) analysis was employed to determine the absorber-scatterer bond lengths and the number of scatterers in the complex. The Fourier transform (FT) of the Fe *K*-edge EXAFS data for **Fe-2** is shown in Figure 2.14. It exhibits a single prominent feature in the region of 1.5-1.6 Å and a peak of lower intensity in the region of 2.0-2.4 Å. A simple simulation of the first coordination sphere of the iron center required two shells (Table 2.2). The principal shell, at 2.10 Å, consists of 4 or 5 N/O scatters, ascribed to the donor nitrogen and oxygen atoms of the polydentate ligand. The other shell, at 1.65 Å, consists of a single O/N atom and is assigned to the terminal Fe=O group.[75] The distance of 1.65 Å found for the oxo-ligand in **Fe-2** is in excellent agreement with the Fe-O distance found in the crystallographically characterized **Fe-TMC** (1.646 Å)[14] and with the Fe-O distance determined by EXAFS for other oxoiron(IV) complexes.[23,74–76] The short Fe-O distance found for

oxoiron(IV) complexes supports the description of the Fe=O bond as a highly covalent interaction between the oxo ligand and the $3d_{z^2}$, $3d_{xz}$ and $3d_{yz}$ orbitals of the iron center.[68,75]

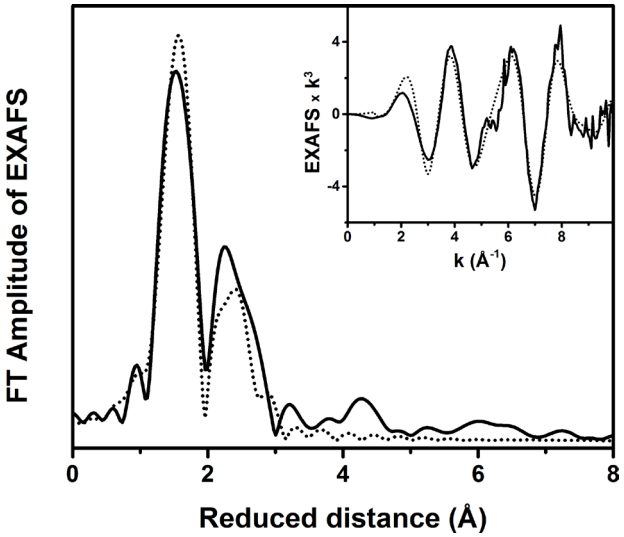

Figure 2.14: Fourier-transformed (FT) Fe *K*-edge EXAFS spectra of **Fe-2** (experimental data: solid line, simulation: dotted line). The inset shows the corresponding EXAFS data in wave-vector scale before the Fourier transformation.

Table 2.2: Results of Fe *K*-edge EXAFS simulations (fit) for **Fe-2**[a]. The best fits are presented in bold.

	Fe-O/N			Fe-N/O			Fe···C					
fit	**N**	**R**	**σ^2**	**n**	**R**	**σ^2**	**N**	**R**	**σ^2**	**ΔE_0**	**χ^2**	**R**
1	3	2.08	3.7							0.96	142.3	0.160
2	4	2.08	5.7							0.24	107.5	0.121
3	5	2.08	7.5							-0.48	101.2	0.114
4	6	2.08	9.2							-1.14	112.9	0.127
5	**4**	**2.11**	**6.9**	**1**	**1.64**	**6.7**				**5.93**	**86.5**	**0.034**
6	**5**	**2.11**	**8.9**	**1**	**1.65**	**6.9**				**4.53**	**53.3**	**0.021**
7	5	2.11	8.4	1	1.65	6.8				4.79	88.4	0.176
8	5	2.10	8.8	1	1.64	6.6	4	2.99	5.2	4.11	56.2	0.081

[a] Fitting range was k = 1.5-11.25 Å^{-1} (resolution = 0.16 Å) with back transform ranges of 1-2 Å for fits 1-6 and 1-3 Å for fits 7-8. r is in units of Å; σ^2 is in units of 10^{-3} Å; ΔE_0 is in units of eV; R represents the fractional misfit of the data, while χ^2 is the χ^2 fitting metric normalized by the number of independent data points in a given fit.

2.2.4 Oxidative reactivity of Fe-2

The oxidative reactivity of **Fe-2** was researched in hydrogen atom abstraction (HAA) reactions with a series of substrates with bond dissociation energies (BDEs) ranging from 78 to 99.3 kcal mol^{-1},[77] namely 9,10-dihydroanthracene (DHA), ethylbenzene, toluene and cyclohexane, whose structures are presented in Figure 2.15.

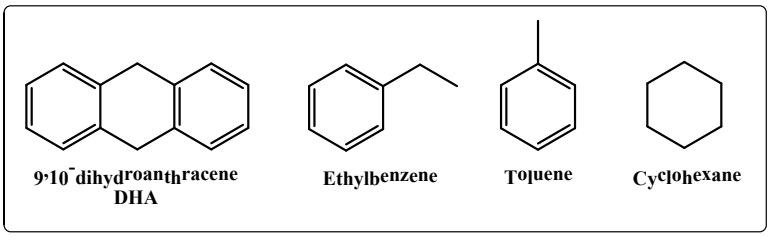

Figure 2.15: Structures of the substrates employed to test the oxidative reactivity of **Fe-2** in hydrogen atom abstraction reactions.

For every test reaction, a solution of **Fe-2** was generated *in situ* in dichloromethane at −90 °C from the addition of 1.5 equivalents of sPhIO to a 1 mM solution of **Fe-1**. The temperature of the intermediate was then warmed up to −60 °C or −50 °C (Table 2.2) and, to this solution, the substrate was added in a large excess (≥ 20 equivalents relative to the oxoiron compound) in order to ensure pseudo-first-order conditions. The decay of the intermediate upon addition of the substrate was monitored by UV-vis spectroscopy (Figure 2.16 a). The absorbance of the bands at 585 nm and 848 nm decreased with time, while the shoulder at 390 nm showed only minor changes. Given its higher absorption coefficient, the band at 585 nm was chosen to monitor the reactivity of **Fe-2**. The decay of this band was followed over time and fitted to a first-order process (Figure 2.16 b) from which k_{obs} was determined.

The described procedure was repeated using different amounts of substrate each time. The series of k_{obs} thus obtained increased linearly with the amount of added substrate (Figure 2.17), and the slope of the linear fit of the substrate concentration vs. k_{obs} is the second-order rate constant (k_2) of the reaction. As can be seen in Figure 2.17, this plot does not cross the "y" axis at the origin but has a positive intercept due to the self-decay of the species **Fe-2** at this temperature. The process for obtaining k_2 is exemplified in Figures 2.16 and 2.17 for the reaction of **Fe-2** 1 mM with cyclohexane in CH_2Cl_2 at −50 °C.

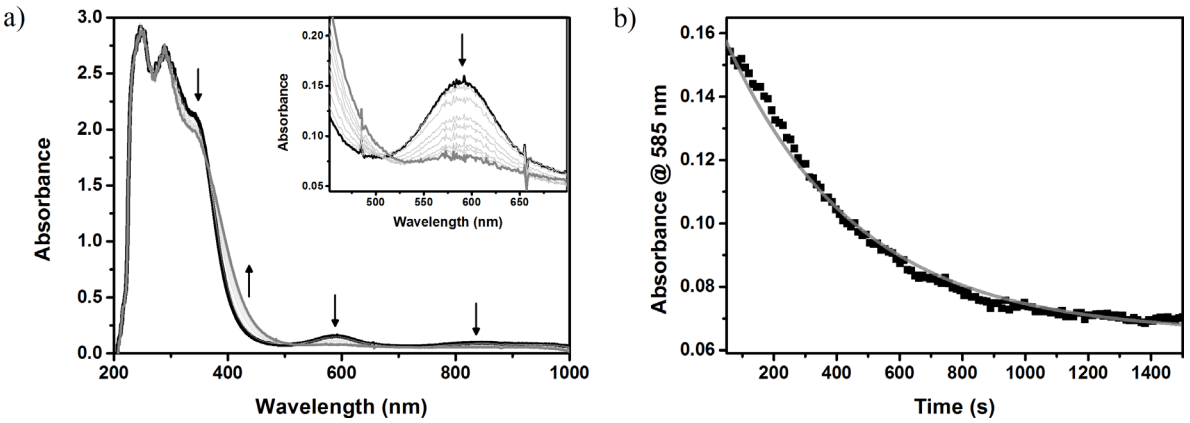

Figure 2.16: a) Decay of **Fe-2**, generated *in situ* from the reaction of **Fe-1** 1 mM with 1.5 equivalents of sPhIO at −90 °C in dichloromethane, after addition of 93 equivalents of cyclohexane in dichloromethane at −50 °C. Inset: decrease in the absorption band at 585 nm, employed for the determination of k_{obs}. b) Decay of the band at 585 nm (black dots) and fitting to a first-order decay (gray solid line) of the reaction of **Fe-2** with 93 equivalents of cyclohexane in dichloromethane at −50 °C.

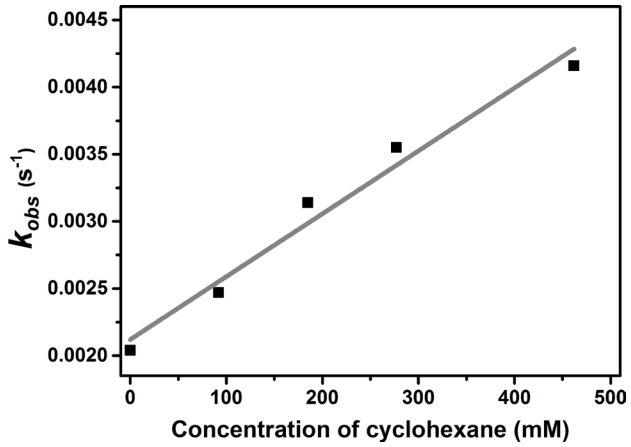

Figure 2.17: Linear dependence of k_{obs} on the concentration of the substrate for the reaction of **Fe-2** with cyclohexane at −50 °C in CH_2Cl_2.

The obtained k_2 values for the HAA reactions of **Fe-2** with the tested substrates are presented in Table 2.3. The reaction of **Fe-2** with DHA, the substrate with the weakest bond dissociation energy (BDE) among all those tested, was too fast to be monitored with our setup even at −90 °C. After the addition of DHA to a solution of **Fe-2**, the bands at 585 nm and 848 nm immediately decayed and anthracene was formed. For substrates with stronger BDEs, on the other hand, temperatures higher than −90 °C were necessary to observe the activation of the substrates and the concomitant decay of **Fe-2**; while **Fe-2** was found to be capable of oxidizing toluene and ethylbenzene at −60 °C, it required a higher temperature, namely −50 °C, to oxidize cyclohexane.

The analysis of the reaction mixture with gas chromatography (GC) after the oxidation of cyclohexane with **Fe-2** showed the formation of both cyclohexanol and cyclohexanone in a ca. 1:1 ratio.

Table 2.3: Second-order rate constants (k_2) determined in HAA reactions performed by **Fe-2** with different substrates. The temperature employed in each case is stated in brackets.

Substrate	Number of equivalent H	BDE[77] kcal mol^{-1}	k_2 L mol^{-1} s^{-1}	k_2' L mol^{-1} s^{-1}
DHA	4	77	Too fast (−90 °C)	
Ethylbenzene	2	87	5.0x10^{-2} (−60 °C)	2.5x10^{-2} (−60 °C)
Toluene	3	90	3.3x10^{-3} (−60 °C)	1.1x10^{-3} (−60 °C)
Cyclohexane	12	99.3	4.7x10^{-3} (−50 °C)	3.9x10^{-4} (−50 °C)

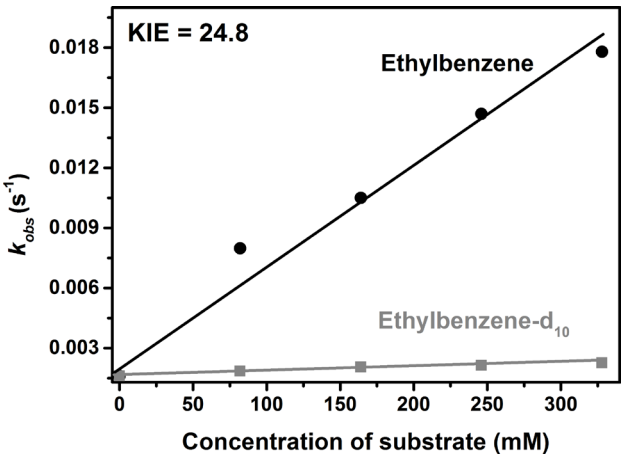

Figure 2.18: Plot of the pseudo-first-order rate constants, k_{obs} (s^{-1}), against substrate concentrations to determine the second-order rate constant (k_2) and the kinetic isotope effect (KIE) for the reaction of **Fe-2** with ethylbenzene (black circles: experimental points, black solid line: linear fitting) and deuterated ethylbenzene-d_{10} (gray squares: experimental points, gray solid line: linear fitting) in dichloromethane at −60 °C.

The obtained k_2 values were adjusted according to the reaction stoichiometry, based on the number of target C−H bonds of each substrate, to yield k_2' (Table 2.3). The k_2' values correlated well with the BDEs of the substrates since the second-order rate constant decreased as the C−H BDE of the substrate increased, a trend that had been previously observed for the oxidation of hydrocarbons with other oxoiron(IV) systems.[22,24,25,78] In addition, a deuterium kinetic isotope effect (KIE = k_H/k_D) of 24.8 was determined for the reaction of **Fe-2** with ethylbenzene and its

deuterated counterpart, ethylbenzene-d_{10} (Figure 2.18). A KIE of 16 was reported for the reaction of **Fe-TMC** with xanthene, and a KIE of 10 for its reaction with DHA, both in MeCN at 25°C.[78] The obtained KIE of **Fe-2** is therefore higher than that of **Fe-TMC,** but both exceed the semi-classical limit (KIE ≤ 7.0). This suggests hydrogen tunneling effects in the H-atom abstraction by **Fe-2**, as has been proposed for other oxoiron intermediates of non-haem enzymes and models.[22,24,25,78,79] Based on the correlation obtained between k_2' and the BDEs of substrates and the large KIE value, it can be inferred that the C−H bond cleavage of the hydrocarbons is the rate-determining step in the H-atom abstraction reactions performed by **Fe-2**.[26]

The reactivity of **Fe-2** was also investigated in oxygen atom transfer reactions (OAT), using triphenylphosphine and thioanisole as substrates. In the same way as for the HAA reactions, the intermediate **Fe-2** was formed *in situ* in dichloromethane at −90 °C and an excess of the substrate was added, this time also at −90 °C. The UV-vis spectrum of **Fe-2** was monitored over time upon addition of the substrate (Figure 2.19). A different behavior from that of HAA reactions (Figure 2.16 a) was observed in the spectral decay of **Fe-2** in OAT reactions; in both cases, the bands at 585 nm and 848 nm decayed completely, but for OAT the band at 390 nm also decayed. The distinct spectral changes observed in HAA *vs.* OAT reactions might be an indication of the difference in the final iron species generated in each case.

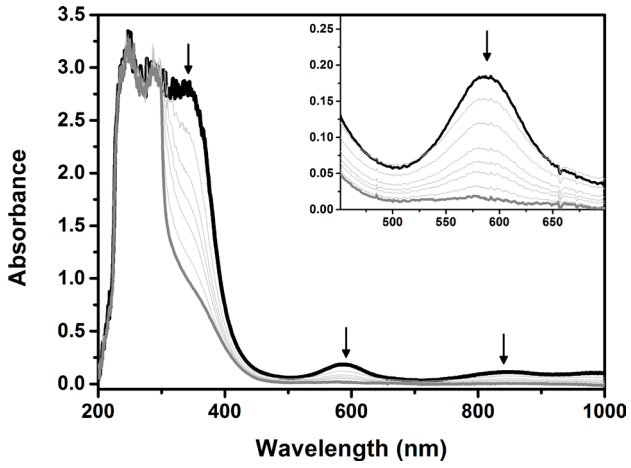

Figure 2.19: Decay of **Fe-2**, generated *in situ* from the reaction of **Fe-1** 1 mM with 1.5 equivalents of sPhIO at −90°C in dichloromethane, after the addition of 11 equivalents of thioanisole in dichloromethane at −90 °C. Inset: decrease in the absorption band at 585 nm, employed for the determination of k_{obs}.

As for the HAA reactions, the decay of the band at 585 nm was followed and fitted to a pseudo-first-order decay (Figure 2.20 a) to obtain k_{obs}. This was repeated using different substrate concentrations. A plot of k_{obs} *vs.* substrate concentrations resulted in a straight line, whose slope

represented the k_2 value (Figure 2.20 b). **Fe-2** was capable of performing OAT reactions even at −90 °C, in contrast to most of the HAT transformations, which required higher temperatures. Given that **Fe-2** is stable at −90 °C, the plot of k_{obs} vs. substrate concentration intercepts the origin unlike those obtained for HAA reactions. The k_2 values obtained for the oxygen atom transfer reactions performed by **Fe-2** at −90 °C in dichloromethane are presented in Table 2.4. The reaction with triphenylphosphine was too fast to be followed with our methodology and instrumentation; however the analysis of the reaction mixture showed the formation of triphenylphosphine oxide.

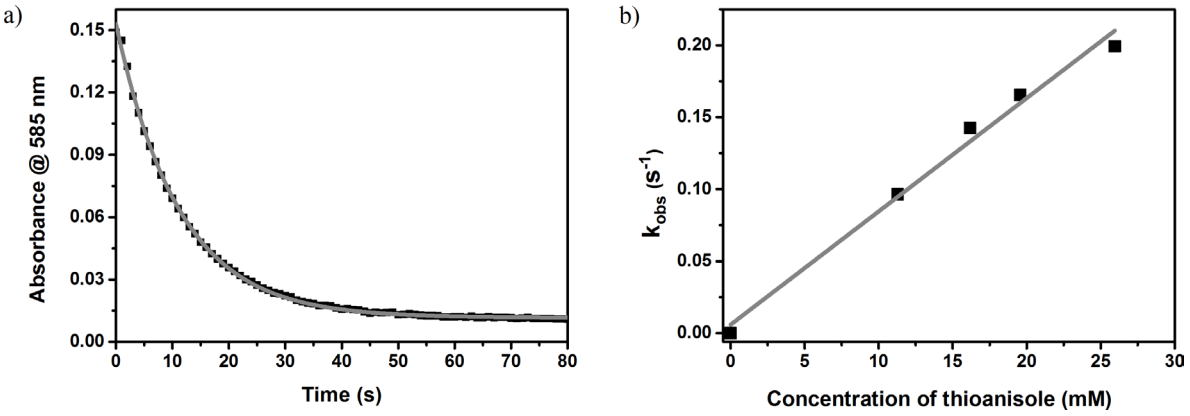

Figure 2.20: a) Decay of the band at 585 nm (black dots) and fitting to a first-order decay (gray solid line) for the reaction of **Fe-2** with thioanisole in dichloromethane at −90 °C. b) Linear dependence of k_{obs} on the concentration of the substrate for the reaction of **Fe-2** with thioanisole at −90 °C in CH_2Cl_2.

Table 2.4: Second-order rate constants (k_2) determined in OAT reactions performed by **Fe-2** with different substrates in dichloromethane at −90 °C.

Substrate	k_2 L mol^{-1} s^{-1}
PPh_3	Too fast
Thioanisole	7.87

It is interesting to compare the reactivity of **Fe-2** with that of other oxoiron(IV) models in order to evaluate the effectiveness of our ligand design and the effect of the change of the coordination sphere around the iron center: from only nitrogen donors to the inclusion of one oxygen donor in **Fe-2**. For comparison, the most active oxoiron(IV) models were chosen, as well as other oxoiron(IV) complexes capable of oxidizing cyclohexane and the model complex taken as a

reference for this study: the intermediate **Fe-TMC**. The structures of the chosen active oxoiron(IV) models are presented in Figure 2.21.

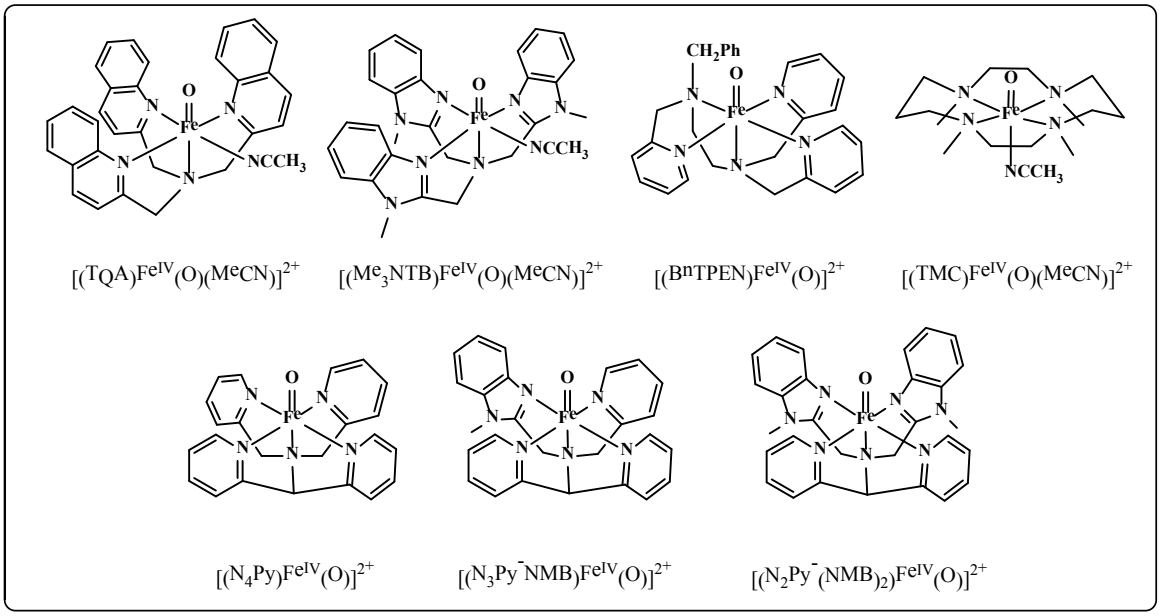

Figure 2.21: Structures of other relevant oxoiron(IV) models.

Table 2.5: Second-order rate constants (k_2) reported for the oxygen atom transfer and the hydrogen atom abstraction reactions with the substrates thioanisole and cyclohexane, respectively, performed by different oxoiron(IV) species.

Complex	Fe^{IV} spin state	k_2 thioanisole L mol^{-1} s^{-1}	k_2 cyclohexane L mol^{-1} s^{-1}	Reference
$[(TQA)Fe^{IV}(O)(MeCN)]^{2+}$	2	Not reported	$3.7x10^{-1}$ (−40 °C)	[24]
$[(Me_3NTB)Fe^{IV}(O)(MeCN)]^{2+}$	1 (2 accessible)	$2.1x10^{4}$ (−40 °C)	$2.5x10^{-1}$ (−40 °C)	[22]
Fe-2	1 (2 accessible)	7.87 (−90 °C)	$4.7x10^{-3}$ (−50 °C)	
$[(N_2Py\text{-}(NMB)_2)Fe^{IV}(O)]^{2+}$	1	$3.1x10^{-1}$ (−30 °C)	$2.9x10^{-3}$ (25 °C)	[21]
$[N_3Py\text{-}(NMB))Fe^{IV}(O)]^{2+}$	1	$3.3x10^{-2}$ (−30 °C)	$3.0x10^{-4}$ (25 °C)	[21]
$[(BnTPEN)Fe^{IV}(O)]^{2+}$	1	$1.4x10^{-2}$ (−40 °C)	$3.9x10^{-4}$ (25 °C)	[22,25]
$[(N_4Py)Fe^{IV}(O)]^{2+}$	1	$2.4x10^{-4}$ (−40 °C)	$5.5x10^{-5}$ (25 °C)	[22,25]
Fe-TMC	1	$1.3x10^{-3}$ (−40 °C)	0	[14,17]

The complexes $[(TQA)Fe^{IV}(O)(MeCN)]^{2+}$[24] and $[Me_3NTB)Fe^{IV}(O)(MeCN)]^{2+}$[22] were presented in the introduction of this Chapter, and are the most reactive oxoiron(IV) models synthesized so far. The compounds $[(N_4Py)Fe^{IV}(O)]^{2+}$,[25] $[(BnTPEN)Fe^{IV}(O)]^{2+}$,[25] $[(N_3Py\text{-}(NMB))Fe^{IV}(O)]^{2+}$,[21] and $[(N_2Py\text{-}(NMB)_2)Fe^{IV}(O)]^{2+}$,[21] on the other hand, are related complexes for which oxidation of cyclohexane has been observed and reported (N_4Py = *N*,*N*-bis(2-pyridylmethyl)-*N*-bis(2-pyridyl)methylamine; BnTPEN = *N*-benzyl-*N*,*N*',*N*'-tris(2-pyridylmethyl)-ethylenediamine; N_3Py-(NMB) = *N*-(1-methyl-2-benzimidazolyl)-methyl-*N*-(2-pyridyl)-methyl-*N*-(bis-2-pyridylmethyl)amin; $N_2Py\text{-}(NMB)_2$ = *N*-bis(1-methyl-2-benzimidazolyl)methyl-*N*-(bis-2-pyridylmethyl)-amine). Finally, **Fe-TMC**[14] is the oxoiron(IV) complex typically used for comparisons since it was the first fully characterized compound. The reaction rates k_2 reported for these complexes as well as those obtained for **Fe-2** in the oxidation reactions of thioanisole (OAT) and cyclohexane (HAA) are presented in Table 2.5.

The complex **Fe-2** was found to be more reactive than the parent compound **Fe-TMC**. While **2-Fe** could activate cyclohexane even at −50 °C, **Fe-TMC** was incapable of activating a substrate with such a high BDE. The large ZFS, in comparison with **Fe-TMC,** determined with magnetic Möβbauer spectroscopy for **Fe-2,** might reasonably explain the higher activity of this complex. While in **Fe-2** the triplet-quintet gap is lower, the more reactive S = 2 is more accessible and therefore its reactivity increases. On the contrary, for the complex **Fe-TMC** the quintet state is less accessible (lower value of D) and it exhibits poorer reactivity.

An interesting analysis in this regard can be made from the k_2 values obtained for the different species listed in Table 2.5. It is known that the nature of the equatorial ligands has an effect on the reactivity of the oxoiron(IV) complexes. Strong equatorial donation causes a destabilization of the $d_{x^2-y^2}$ orbital, which results in a higher energy gap between the triplet and quintet states (ΔE_{TQ}), lower accessibility of the S = 2 state and a lower HAA reactivity.[16] This effect can be appreciated when comparing the reactivity trend of the related complexes: $[(N_4Py)Fe^{IV}(O)]^{2+} < [(N_3Py\text{-}(NMB))Fe^{IV}(O)]^{2+} < [(N_2Py\text{-}(NMB)_2)Fe^{IV}(O)]^{2+}$. For every complex in the series, an equatorial pyridine ligand has been replaced with an *N*-methylbenzymidazol ligand that enforces a steric demand in the equatorial plane and affects its equatorial donation ability. A similar trend could be occurring between **Fe-TMC** and **Fe-2**, where one nitrogen donor is being substituted by a more electronegative oxygen donor. This new donor could be diminishing the equatorial donation on **Fe-2** and thus increasing its reactivity.

The complex **Fe-2**, however, was not as reactive as the two most efficient oxoiron(IV) oxidants reported so far. Complex $[(Me_3NTB)Fe^{IV}(O)(MeCN)]^{2+}$[22] exhibits the highest oxidation rate for cyclohexane and thioanisole for any S = 1 oxoiron(IV) complex to date. It has been suggested that its high reactivity is derived from a highly reactive S = 2 state in close proximity to the S = 1 ground state. Complex $[(TQA)Fe^{IV}(O)(MeCN)]^{2+}$,[24] on the other hand, has an S = 2 ground state and its reactivity proceeds on a single surface. While **Fe-2** is the third most reactive complex reported so far, its reactivity is still far from that of these two highly reactive complexes. The replacement of one nitrogen donor for an oxygen one, however, seems to be an effective strategy for achieving more reactive oxoiron(IV) complexes, as evidenced by the comparison of **Fe-2** with **Fe-TMC**.

In order to explain the difference in reactivity between **Fe-2** and **Fe-TMC**, distinct factors can be proposed that might enhance the reactivity of **Fe-2** in contrast to that of **Fe-TMC**. The first factor to be considered is the difference in the electronic spin state in which the reaction might proceed for each complex. The experimental evidence proves that both **Fe-TMC** and **Fe-2** have an intermediate spin S = 1 ground state. However, the unusually large zero-field splitting found for **Fe-2** shows that the intermediate- and high-spin configurations in this complex are much closer in energy than those in **Fe-TMC**. These findings were corroborated by DFT studies. It was found that while for **Fe-TMC** the energy difference between the S = 1 ground state and the S = 2 excited state is 5-6 kcal mol^{-1}, this difference is only 1-2 kcal mol^{-1} for **Fe-2** (at OLYP/TDZP or B3LYP/TDZP for both). The lower ΔE_{TQ} gap in **Fe-2** therefore increases the accessibility of the quintet state in this complex and can make **Fe-2** more reactive.

To get insights into the effect of the spin state in **Fe-2** and **Fe-TMC**, the mechanism of the oxidation of cyclohexane by both complexes was researched in detail with DFT calculations. The reaction energy surfaces and the stationary points were optimized with OLYP/TDZP (see Chapter 6 for details). The optimized geometries of the reactant (R) high-valent oxoiron(IV) complexes are shown in Figure 2.22, while Figure 2.23 shows the energy profiles found for the reaction performed by **Fe-2** and **Fe-TMC** on S = 1 and S = 2 surfaces. The reaction mechanism for the hydroxylation of cyclohexane was found to involve two steps, as expected: first a hydrogen atom transfer (HAT) from the cyclohexane to the iron-oxo, followed by a rebound (OR) step to form the cyclohexanol product (P).

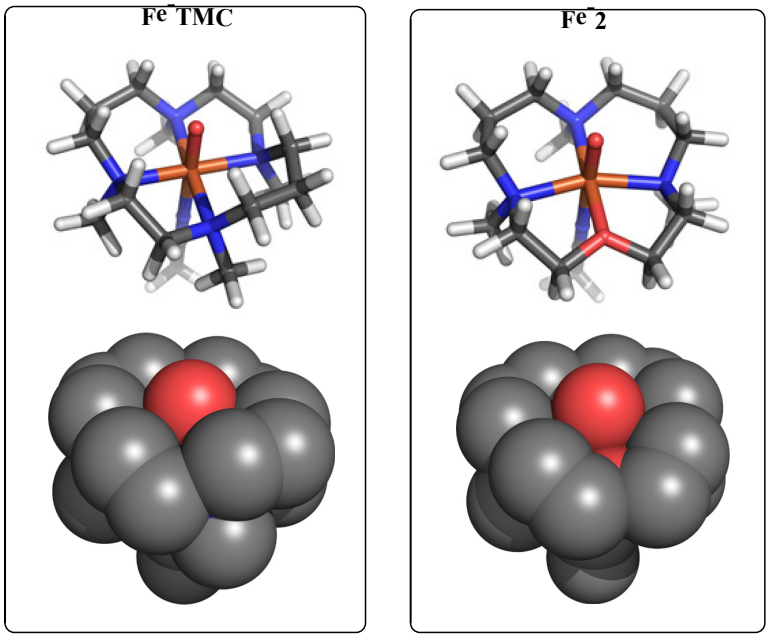

Figure 2.22: Optimized geometries of **Fe-TMC** and **Fe-2**; bottom: space-filling models where the hydrogen atoms have been omitted for clarity. Color code: C-gray, N-blue, Fe-orange, O-red, H-white.

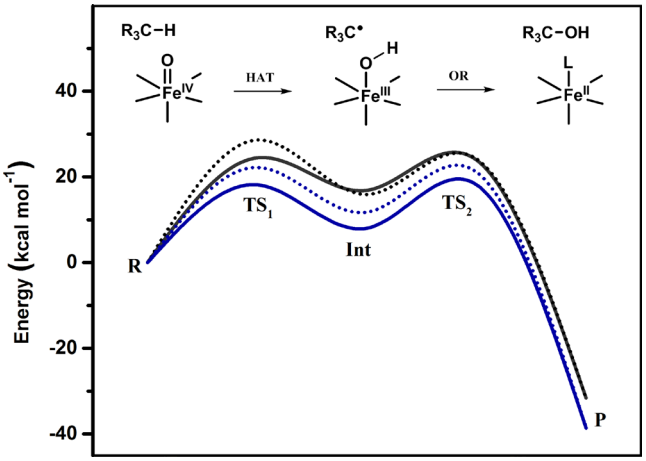

Figure 2.23: Energy profiles for the oxidation of cyclohexane with **Fe-TMC** (S = 1, dotted black line; S = 2 solid black line) and **Fe-2** (S = 1, dotted blue line; S = 2 solid blue line).

In keeping with previous studies on oxoiron(IV) systems,[1,27,28] the lowest energy pathway, for both **Fe-2** and **Fe-TMC**, was found to be that of the quintet (S = 2) state. However, regardless of the spin state, the energy barriers of the oxidation of cyclohexane were found to be significantly lower for **Fe-2** than for **Fe-TMC**. Since the energy barriers of **Fe-2** are lower than those of **Fe-TMC** regardless of the spin surface in which they proceed, the spin effect alone cannot account for the higher reactivity of **Fe-2** with regard to **Fe-TMC**.

Another factor that might have an effect on the enhanced reactivity of **Fe-2** is a steric one. The space-filling models of both compounds, obtained from their geometry optimization, are presented in Figure 2.22. While in the **Fe-TMC** complex the oxo group is hidden by the backbone of the ligand, in the **Fe-2** complex the oxo group is more exposed through the site occupied by the coordinated oxygen, leaving it more accessible to further approach by the substrate and thus increasing its reactivity. A related effect would be the possibility that the oxygen donor from the **TMCO** ligand comes out in solution, thus leaving space for the substrate to approach the oxoiron(IV) center and increasing the reactivity of **Fe-2** with regard to that of **Fe-TMC**, that has no such possibility.

However appealing it is to ascribe the observed increase in reactivity of **Fe-2** *vs* **Fe-TMC** to the exchange of one nitrogen donor for an oxygen one, such an assumption might not be entirely correct. Not only does the nature of the donor atoms vary between **Fe-2** and **Fe-TMC**, but the backbone of the ligand is also different (Figure 2.6). In order to properly analyze the effect of exchanging a nitrogen donor for an oxygen one in an otherwise identical ligand, a new ligand with the same backbone structure as **TMCO** but with four nitrogen donors, namely **TMCN** (Figure 2.24), was synthesized and its iron(II) and oxoiron(IV) complexes were studied.

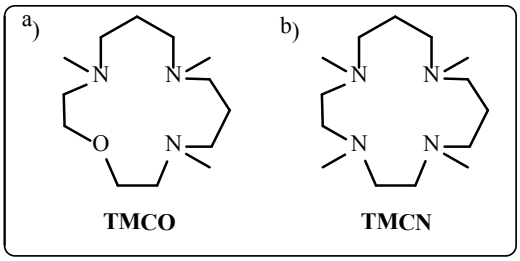

Figure 2.24: Structure of the ligands **TMCO** and **TMCN**.

2.2.5 Comparison with the TMCN system

The ligand **TMCN** was synthesized using a strategy analogous to that employed for the **TMCO** ligand (Scheme 2.3) but in the second step, *N,O,O'*-Tritosyldiethanolamine was employed instead of diethyleneglycol-di(*p*-toluensulfonate). From the reaction between **TMCN** and $[Fe^{II}(OTf)_2(MeCN)_2]$, the complex $[(TMCN)Fe^{II}]^{2+}$ (**Fe-3**) was generated (Scheme 2.6 a) and, in turn, it was set to react with the oxidant sPhIO in acetonitrile at −40 °C (Scheme 2.6 b). The formation of a transient intermediate **Fe-4** could be observed, whose very fast decay prevented its isolation at −40 °C. Unfortunately, **Fe-4** was also too unstable to be isolated in other solvents at temperatures ranging from −40 to −100 °C.

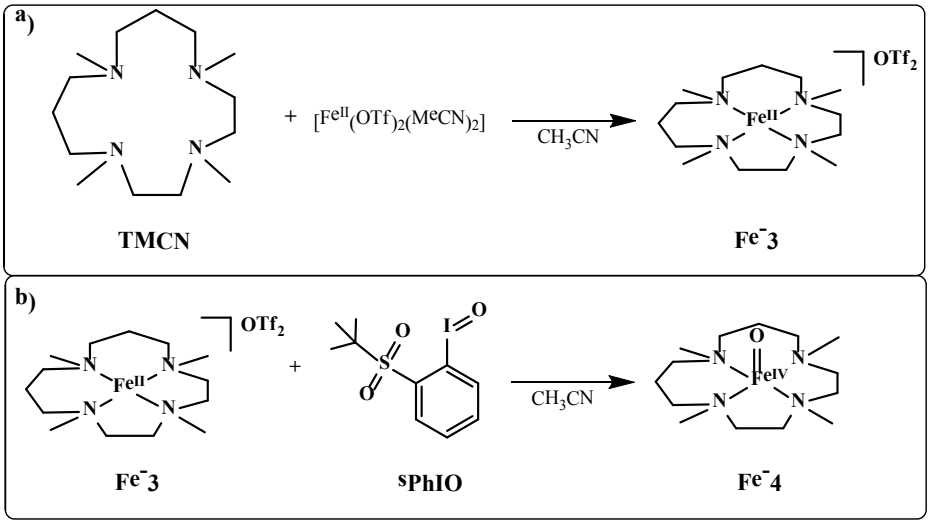

Scheme 2.6: a) Synthesis of the complex **Fe-3** and b) generation of the intermediate **Fe-4**

Since the complexes **Fe-2**, **Fe-TMC** and the related oxoiron(IV) species[61,78] can be generated and stabilized with relative ease at low temperatures, the transient nature of **Fe-4** was surprising. Such behavior might be due to an alternative decay pathway of **Fe-4** that is not accessible in **Fe-TMC** and **Fe-2,** or the result of an asymmetry within the complex. DFT calculations provided an insight into the unstable nature of **Fe-4**.

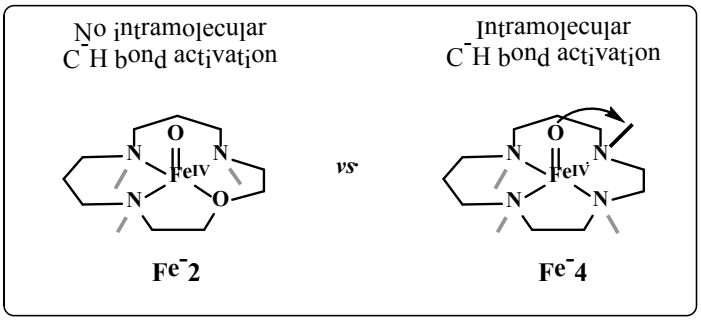

Figure 2.25: Spatial arrangement of the N-methyl groups in **Fe-2** and **Fe-4** and illustration of possible intramolecular C−H bond activation.

According to DFT calculations, the most stable conformation found for complex **Fe-2** has all the three *N*-methyl groups oriented in the same direction with respect to the FeN_3O plane and pointing away from the oxo group (*anti*, Figure 2.25), as observed in the **Fe-TMC** crystal structure.[14] In contrast, for the complex **Fe-4** the most stable conformation has one of the four methyl groups facing towards the oxo ligand (*syn*, Figure 2.25). This flip of the *N*-methyl group favors the intramolecular C−H bond activation of the methyl group of the ligand, making the complex **Fe-4** decay rapidly in solution even at low temperatures. In fact, the reaction barrier for the

auto-oxidation of the *syn*-complex was found to be 13-14 kcal mol^{-1} lower than the oxidation barrier for the reaction of this complex with cyclohexane, which explains the instability of **Fe-4**.

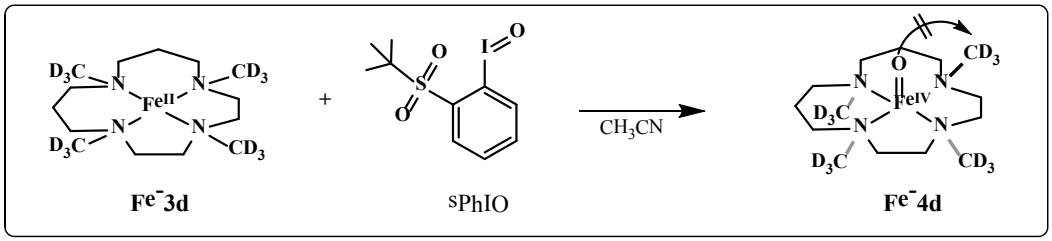

Scheme 2.7: Generation of **Fe-4d** from the reaction of **Fe-3d** with sPhIO in MeCN at 10 °C.

In order to access the oxoiron(IV) complex of this system, the ligand **TMCN-d** with deuterated *N*-methyl groups was synthesized. Since the oxoiron(IV) compounds show large deuterium kinetic isotope effects, the introduction of deuterium on the methyl groups was expected to slow down the intramolecular C−H bond activation in **Fe-4**. The **TMCN-d** ligand was synthesized following the same procedure used for the synthesis of **TMCN** but the deuterated forms of formaldehyde and formic acid were used in the last step. The **TMCN-d** ligand was set to react with $[Fe^{II}(OTf)_2(MeCN)_2]$ to generate the complex **Fe-3d**, which , in turn, was set to react with sPhIO in MeCN at 10 °C (Scheme 2.7). This time the formation of **Fe-4d** could be detected and followed by UV-vis spectroscopy (Figure 2.26). **Fe-4d** showed a characteristic UV-vis band at 820 nm (ε_{max} = 125 M^{-1} cm^{-1}) and a big shoulder rising at around 400 nm.

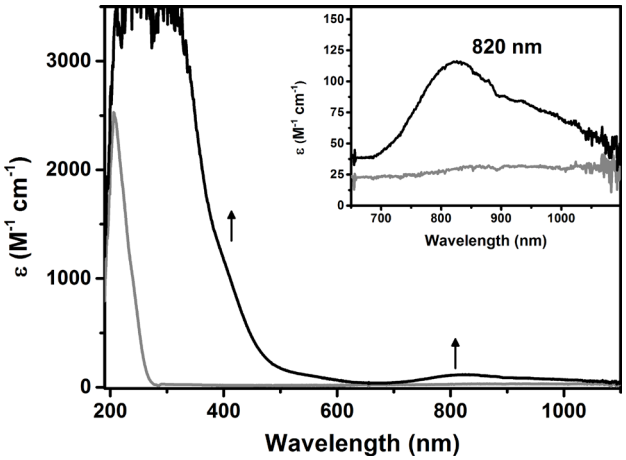

Figure 2.26: Absorption spectra of **Fe-3d** (gray line) and the intermediate **Fe-4d** (black line) in anhydrous MeCN at 10°C.

The ligand **TMCO-d** with deuterated *N*-methyl groups was also synthesized (using the same synthetic modification as for **TMCN-d**), as well as the corresponding Fe(II) complex **Fe-1d**. The oxoiron(IV) compound **Fe-2d** was generated in the reaction of **Fe-1d** with sPhIO in dichloromethane at −90 °C. Low-temperature ^{2}H-NMR studies of **Fe-4d** and **Fe-2d** were performed to further corroborate the spatial position of the methyl groups in the complexes.

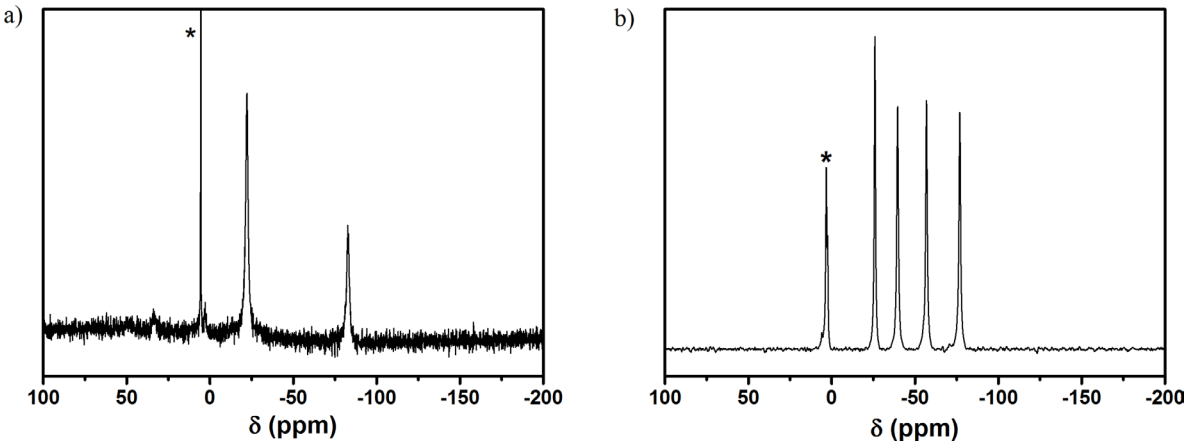

Figure 2.27: Low-temperature ^{2}H-NMR of a) **Fe-2d** in CH_2Cl_2 and b) **Fe-4d** in MeCN. The signal of the residual solvent is marked with a star.

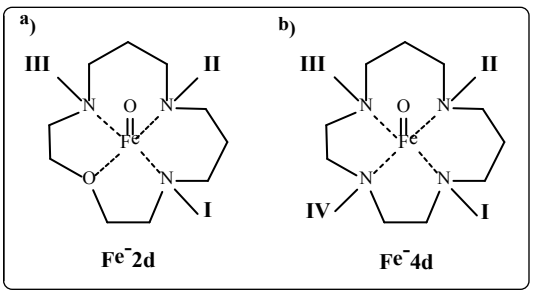

Figure 2.28: Structure of a) **Fe-2d** and b) **Fe-4d** with numbers assigned to their deuterated methyl groups. The deuterium atoms in the methyl groups have been omitted for clarity.

The ^{2}H-NMR spectra of **Fe-2d** (Figure 2.27 a) showed a set of two signals in a 2:1 ratio that indicate that the ligand is effectively symmetrical and there are two equivalent methyl groups (methyl groups I and III in Figure 2.28 a) and one non-equivalent one (methyl group II in Figure 2.28 a). The ^{2}H-NMR spectra of **Fe-4d** (Figure 2.27 b), on the other hand, showed four different signals, indicating the presence of four distinct methyl groups. If all the methyl groups in **Fe-4d** were facing the same direction in the FeN_4 plane, two of them would be equivalent (methyl groups I and III in Figure 2.28 b) and the spectra would show a set of only three signals with integration

ratios 2:1:1. The fact that the two otherwise equivalent *N*-methyl groups appear at different chemical shifts indicated that their chemical environments are different and provided evidence for the flip of one of these *N*-methyl groups above the plane, towards the oxo ligand (*syn*).

The oxidation reactivity of **Fe-4d** was tested in HAA and OAT reactions with the substrates cyclohexane and thioanisole in acetonitrile at −40 °C. The k_2 values obtained are presented in Table 2.6. The complex **Fe-4d** was not capable of activating cyclohexane at −40 °C, nor substrates with lower BDEs such as toluene. However, **Fe-4d** proved to be capable of performing group transfer reactions towards thioanisole, but at a rate three orders of magnitude slower than that obtained for **Fe-2**. This was much in keeping with the reactivity trend observed for **Fe-TMC**, which was incapable of activating substrates with high BDEs but could perform OAT to substrates like PPh_3 and thioanisole. Even though the reaction rates for the oxidation of thioanisole with **Fe-TMC** and **Fe-4d** are comparable in magnitude, the rate obtained for **Fe-4d** is three times higher than that of **Fe-TMC.** This evidence shows that asymmetry does play a role in increasing the reactivity of the **TMCO** and **TMCN-d**-derived complexes with respect to the more symmetric **TMC** one. This effect must be taken into consideration when explaining the increased reactivity of **Fe-2**.

Table 2.6: Second-order rate constants (k_2) reported for the oxygen atom transfer reaction to thioanisole and for the hydrogen atom abstraction reaction from cyclohexane by **Fe-2**, **Fe-4d** and **Fe-TMC**.

Substrate	**Fe-2** k_2 (L mol^{-1} s^{-1})	**Fe-4d** k_2 (L mol^{-1} s^{-1})	**Fe-TMC** k_2 (L mol^{-1} s^{-1})
Cyclohexane	$4.7x10^{-3}$ (−50 °C)	No reaction	No reaction
Thioanisole	7.87 (−90 °C)	$4.0x10^{-3}$ (−40 °C)	$1.3x10^{-3}$ (−40 °C)

2.3 Conclusions

A new oxoiron(IV) intermediate **Fe-2** has been generated employing the ligand **TMCO**. **TMCO** is an analogous ligand to the widely studied **TMC**, but in it one of the four nitrogen donors has been exchanged for an oxygen donor and the backbone of the ligand has been slightly modified, introducing an additional asymmetry but leaving the macrocycle size unchanged. The iron(II) complex of the **TMCO** ligand (**Fe-1**) is in a high-spin configuration and has been completely characterized by various spectroscopic methods including X-ray diffraction. Its reaction with sPhIO in CH_2Cl_2 at −90 °C led to the formation of **Fe-2**. **Fe-2** has an S = 1 ground state; however, the high spin S = 2 state is easily accessible, as demonstrated by the unusually large zero-field splitting (D)

value obtained by Möβbauer spectroscopy. **Fe-2** shows high reactivity in C−H bond activation and group transfer reactions, much higher than that of **Fe-TMC**.

The factors that have been proposed to influence the increase in reactivity in **Fe-2** in contrast with **Fe-TMC** are a) the smaller ΔE_{TQ} gap that increases the accessibility of the quintet state in **Fe-2**; b) the steric factor that exposes the oxo group in **Fe-2** through the site occupied by the coordinated oxygen, leaving it more accessible for a further approach by the substrate; c) a possible de-coordination of the oxygen donor from the **TMCO** ligand in solution, which leaves space for the substrate to approach the oxoiron center; and d) a minor role of the asymmetry of **Fe-2** in comparison with **Fe-TMC**, which has been evidenced by the difference in reactivity between the otherwise identical **Fe-TMC** and **Fe-4d**. The results presented here prove that the exchange of one nitrogen donor for an oxygen one does have an important impact on the reactivity of oxoiron(IV) complexes, making them more reactive.

2.4 References

[1] J. Hohenberger, K. Ray, K. Meyer, *Nat. Commun.* **2012**, *3*, 720-733.

[2] J. E. Penner-Hshn, T. J. McMurry, M. Renner, L. Latos-Grazynsky, K. S. Eble, I. M. Davis, A. L. Balch, J. T. Groves, J. H. Dawson, K. O. Hodgson, *J. Biol.* **1983**, *258*, 12761–12765.

[3] G. I. Berglund, G. H. Carlsson, A. T. Smith, H. Szöke, A. Henriksen, J. Hajdu, *Nature* **2002**, *417*, 463–468.

[4] H. P. Hersleth, U. Ryde, P. Rydberg, C. H. Görbitz, K. K. Andersson, *J. Inorg. Biochem.* **2006**, *100*, 460–476.

[5] M. Merkx, D. A. Kopp, M. H. Sazinsky, J. L. Blazyk, J. Müller, S. J. Lippard, *Angew. Chem. Int. Ed.* **2001**, *40*, 2782–2807.

[6] J. C. Price, E. W. Barr, L. M. Hoffart, C. Krebs, J. M. Bollinger, *Biochemistry* **2005**, *44*, 8138–47.

[7] C. Krebs, D. G. Fujimori, C. T. Walsh, J. M. Bollinger, *Acc. Chem. Res.* **2007**, *40*, 484–492.

[8] M. Costas, M. P. Mehn, M. P. Jensen, L. Que Jr., *Chem. Rev.* **2004**, *104*, 939–986.

[9] L. Que Jr., *Acc. Chem. Res.* **2007**, *40*, 493–500.

[10] J. T. Groves, R. C. Haushalter, M. Nakamura, T. E. Nemo, B. J. Evans, *J. Am. Chem. Soc.* **1981**, *103*, 2884–2886.

[11] H. Fujii, *Coord. Chem. Rev.* **2002**, *226*, 51–60.

[12] C. A. Grapperhaus, B. Mienert, E. Bill, T. Weyhermüller, K. Wieghardt, *Inorg. Chem.* **2000**, *39*, 5306–5317.

[13] W. Nam, *Acc. Chem. Res.* **2007**, *40*, 522–531.

[14] J.-U. Rohde, J.-H. In, M. H. Lim, W. W. Brennessel, M. R. Bukowski, A. Stubna, E. Münck, W. Nam, L. Que Jr., *Science* **2003**, *299*, 1037–9.

[15] S. P. de Visser, J. U. Rohde, Y. M. Lee, J. Cho, W. Nam, *Coord. Chem. Rev.* **2013**, *257*, 381–393.

[16] X. Engelmann, I. Monte-Pérez, K. Ray, *Angew. Chem. Int. Ed.* **2016**, *55*, 7632–7649.

[17] S. Hong, H. So, H. Yoon, K. B. Cho, Y. M. Lee, S. Fukuzumi, W. Nam, *Dalt. Trans.* **2013**, *42*, 7842–7845.

[18] A. R. McDonald, L. Que Jr., *Coord. Chem. Rev.* **2013**, *257*, 414–428.

[19] K. Ray, F. Felix, B. Wang, W. Nam, *J. Am. Chem. Soc.* **2014**, *136*, 13942–13958.

[20] D. Wang, K. Ray, M. J. Collins, E. R. Farquhar, J. R. Frisch, L. Gomez, T. A. Jackson, M. Kerscher, A. Waleska, P. Comba, M. Comba, L. Que Jr., *Chem. Sci.* **2013**, *4*, 282–291.

[21] M. Mitra, H. Nimir, S. Demeshko, S. S. Bhat, S. O. Malinkin, M. Haukka, J. Lloret-Fillol, G. C. Lisensky, F. Meyer, A. A. Shteinman, W. R. Browne, D. A. Hrovat, M. G. Richmond, M. Costas, E. Nordlander, *Inorg. Chem.* **2015**, *54*, 7152–7164.

[22] M. S. Seo, N. H. Kim, K.-B. Cho, J. E. So, S. K. Park, M. Clémancey, R. Garcia-Serres, J.-M. Latour, S. Shaik, W. Nam, *Chem. Sci.* **2011**, *2*, 1039–1045.

[23] S. A. Wilson, J. Chen, S. Hong, Y. Lee, R. García-Serres, T. Nomura, T. Ogura, B. Hedman, K. O. Hodgson, W. Nam, E. I, Solomon, *J. Am. Chem. Soc.* **2012**, *134*, 11791.

[24] A. N. Biswas, M. Puri, K. K. Meier, W. N. Oloo, G. T. Rohde, E. L. Bominaar, E. Münck, L. Que Jr., *J. Am. Chem. Soc.* **2015**, *137*, 2428–2431.

[25] J. Kaizer, E. J. Klinker, N. Y. Oh, J. Rohde, W. J. Song, A. Stubna, J. Kim, E. Münck, W. Nam, L. Que Jr., *J. Am Chem. Soc.* **2004**, *126*, 472–473.

[26] S. T. Kleespies, W. N. Oloo, A. Mukherjee, L. Que Jr., *Inorg. Chem.* **2015**, *54*, 5053–5064.

[27] S. Shaik, H. Hirao, D. Kumar, *Acc. Chem. Res.* **2007**, *40*, 532–542.

[28] K.-B. Cho, S. Shaik, W. Nam, *Chem. Commun.* **2010**, *46*, 4511-4513.

[29] J. T. Groves, G. A. McClusky, *J. Am. Chem. Soc.* **1976**, *98*, 859–861.

[30] F. Ogliaro, N. Harris, S. Cohen, M. Filatov, S. P. de Visser, S. Shaik, *J. Am. Chem. Soc.* **2000**, *122*, 8977–8989.

[31] S. Shaik, S. Cohen, S. P. de Visser, P. K. Sharma, D. Kumar, S. Kozuch, F. Ogliaro, D. Danovich, *Eur. J. Inorg. Chem.* **2004**, 207–226.

[32] J. T. Groves, *J. Chem. Educ.* **1985**, *62*, 928–931.

[33] S. Shaik, H. Chen, D. Janardanan, *Nat. Chem.* **2011**, *3*, 19–27.

[34] A. Decker, J. U. Rohde, E. J. Klinker, S. D. Wong, L. Que Jr., E. I. Solomon, *J. Am. Chem.*

Soc. **2007**, *129*, 15983–15996.

[35] A. Decker, M. S. Chow, J. N. Kemsley, N. Lehnert, E. I. Solomon, *J. Am. Chem. Soc.* **2006**, 4719–4733.

[36] M. L. Neidig, A. Decker, O. W. Choroba, F. Huang, M. Kavana, G. R. Moran, J. B. Spencer, E. I. Solomon, *Proc. Natl. Acad. Sci.* **2006**, *103*, 12966–12973.

[37] C. Geng, S. Ye, F. Neese, *Angew. Chem. Int. Ed.* **2010**, *49*, 5717–5720.

[38] H. Hirao, D. Kumar, L. Que Jr., S. Shaik, *J. Am. Chem. Soc.* **2006**, *128*, 8590–8606.

[39] H. Hirao, L. Que Jr., W. Nam, S. Shaik, *Chem. Eur. J.* **2008**, *14*, 1740–1756.

[40] T. K. Paine, M. Costas, J. Kaizer, L. Que Jr., *J. Biol. Inorg. Chem.* **2006**, *11*, 272–276.

[41] J. England, M. Martinho, E. R. Farquhar, J. R. Frisch, E. L. Bominaar, E. Münck, L. Que Jr., *Angew. Chem. Int. Ed.* **2009**, *48*, 3622–3626.

[42] D. C. Lacy, R. Gupta, K. L. Stone, J. Greaves, J. W. Ziller, M. P. Hendrich, A. S. Borovik, *J. Am. Chem. Soc.* **2010**, *132*, 12188–12190.

[43] O. Pestovsky, S. Stoian, E. L. Bominaar, X. Shan, E. M??nck, L. Que Jr., A. Bakac, *Angew. Chem. Int. Ed.* **2005**, *44*, 6871–6874.

[44] D. J. Xiao, E. D. Bloch, J. a Mason, W. L. Queen, M. R. Hudson, N. Planas, J. Borycz, A. L. Dzubak, P. Verma, K. Lee, F. Bonino, V. Crocella, J. Yano, S. Bordiga, D. G. Truhlar, L. Gagliardi, C. M. Brown, J. R. Long, *Nat. Chem.* **2014**, *6*, 590–595.

[45] H. Stetter, K.-H. Mayer, *Chem. Ber.* **1961**, *94*, 1410–1416.

[46] J. E. Richman, T. J. Atkins, *J. Am. Chem. Soc.* **1974**, *96*, 2268–2270.

[47] D. K. Cabbiness, D. W. Margerum, *J. Am. Chem. Soc.* **1969**, *91*, 6540–6541.

[48] M. Suchý, R. H. E. Hudson, *European J. Org. Chem.* **2008**, 4847–4865.

[49] J. Hormann, C. Perera, N. Deibel, D. Lentz, B. Sarkar, N. Kulak, *Dalt. Trans.* **2013**, *42*, 4357–4360.

[50] J. Cho, R. Sarangi, W. Nam, *Acc. Chem. Res.* **2012**, *45*, 1321–1330.

[51] M. T. S. Amorim, S. Chaves, R. Delgado, J. J. R. Fraústo da Silva, *J. Chem. Soc. Dalt. Trans.* **1991**, *938*, 3065–3072.

[52] V. Felix, R. Delgado, M. T. S. Amorim, S. Chaves, A. M. Galvao, M. T. Duarte, M. A. A. F. de C. T. Carrondo, I. Moura, J. J. R. Frausto da Silva, *J. Chem. Soc. Dalt. Trans.* **1994**, 3099–3106.

[53] M. T. S. Amorim, J. R. Ascenso, R. Delgado, J. R. Frausto da Silva, *J. Chem. Soc. Dalt. Trans.* **1990**, *41*, 3449–3455.

[54] C. S. Rossiter, R. A. Mathews, I. M. A. del Mundo, J. R. Morrow, *J. Inorg. Biochem.* **2009**, *103*, 64–71.

[55] T. W. Bell, H. J. Choi, W. Harte, M. G. B. Drew, *J. Am. Chem. Soc.* **2003**, *125*, 12196–12210.

[56] C. S. Rossiter, R. A. Mathews, J. R. Morrow, *Inorg. Chem.* **2005**, *44*, 9397–9404.

[57] J. M. Wilson, F. Giordani, L. J. Farrugia, M. P. Barrett, D. J. Robins, A. Sutherland, *Org. Biomol. Chem.* **2007**, *5*, 3651.

[58] M. Swart, M. Costas, Eds., *Spin States in Biochemistry and Inorganic Chemistry*, Wiley, Singapore, **2016**.

[59] A. T. Fiedler, H. L. Halfen, J. A. Halfen, T. C. Brunold, *J. Am. Chem. Soc.* **2005**, *127*, 1675–1689.

[60] A. R. Mcdonald, M. R. Bukowski, E. R. Farquhar, T. A. Jackson, K. D. Koehntop, M. S. Seo, R. F. De Hont, A. Stubna, J. A. Halfen, E. Münck, W. Nam, L. Que Jr., *J. Am. Chem. Soc.* **2010**, *132*, 17118–17129.

[61] C. V. Sastri, M. J. Park, T. Ohta, T. A. Jackson, A. Stubna, M. S. Seo, J. Lee, J. Kim, T. Kitagawa, E. Münck, L. Que Jr., W. Nam, *J. Am. Chem. Soc.* **2005**, *127*, 12494–12495.

[62] J. Prakash, G. T. Rohde, K. K. Meier, E. Münck, L. Que Jr., *Inorg. Chem.* **2015**, *54*, 11055−11057.

[63] K. D. Hodges, R. G. Wollmann, E. K. Barefield, D. N. Hendrickson, *Inorg. Chem.* **1977**, *16*, 2746–2751.

[64] H. Börzel, P. Comba, K. S. Hagen, Y. D. Lampeka, A. Lienke, G. Linti, M. Merz, H. Pritzkow, L. V. Tsymbal, *Inorganica Chim. Acta* **2002**, *337*, 407–419.

[65] D. W. Blakesley, S. C. Payne, K. S. Hagen, *Inorg. Chem.* **2000**, *39*, 1979–1989.

[66] G. J. P. Britovsek, J. England, A. J. P. White, *Inorg. Chem.* **2005**, *44*, 8125–8134.

[67] G. J. P. Britovsek, J. England, A. J. P. White, *Dalt. Trans.* **2006**, 1399–1408.

[68] A. Decker, J. Rohde, L. Que Jr., E. I. Solomon, *J. Am. Chem. Soc.* **2004**, *126*, 5378–5379.

[69] P. Gütlich, E. Bill, A. X. Trautwein, *Möβbauer Spectroscopy and Transition Metal Chemistry: Fundamentals and Applications*, Springer Science & Business Media, **2010**.

[70] T. A. Jackson, J. Rohde, M. S. Seo, C. V Sastri, R. Dehont, *J. Am. Chem. Soc.* **2008**, *130*, 12394–12407.

[71] M. P. Jensen, M. Costas, R. Y. N. Ho, J. Kaizer, A. Mairata I Payeras, E. Munck, L. Que Jr., Jr., J.-U. Rhode, A. Stubna, *J. Am. Chem. Soc.* **2005**, *127*, 10512–10522.

[72] J. C. Schöneboom, F. Neese, W. Thiel, *J. Am. Chem. Soc.* **2005**, *127*, 5840–5853.

[73] J. Krzystek, J. England, K. Ray, A. Ozarowski, D. Smirnov, L. Que Jr., J. Telser, *Inorg. Chem.* **2008**, *47*, 3483–3485.

[74] J. U. Rohde, a Stubna, E. L. Bominaar, E. Münck, W. Nam, L. Que Jr, *Inorg. Chem.* **2006**, *45*, 6435–6445.

[75] J. U. Rohde, S. Torelli, X. Shan, M. H. Lim, E. J. Klinker, J. Kaizer, K. Chen, W. Nam, L. Que Jr, *J. Am. Chem. Soc.* **2004**, *126*, 16750–16761.

[76] M. H. Lim, J.-U. Rohde, A. Stubna, M. R. Bukowski, M. Costas, R. Y. N. Ho, E. Munck, W. Nam, L. Que Jr., *Proc. Natl. Acad. Sci.* **2003**, *100*, 3665–3670.

[77] Y.-R. Luo, *Comprehensive Handbook of Chemical Bond Energies*, CRC Press, Boca Raton, Florida, **2007**.

[78] C. V Sastri, J. Lee, K. Oh, Y. J. Lee, T. A. Jackson, K. Ray, H. Hirao, W. Shin, J. A. Halfen, J. Kim, L. Que Jr., S. Shaik, W. Nam, *Proc. Natl. Acad. Sci.* **2007**, *104*, 19181–19186.

[79] A. Kohen, J. P. Klinman, *Chem. Biol.* **1999**, *6*, R191–R198.

Chapter 3:

Reactivity Studies of a Hexanuclear Cobalt Complex Supported on a Stannoxane Core

Compounds discussed in Chapter 3

Ligand
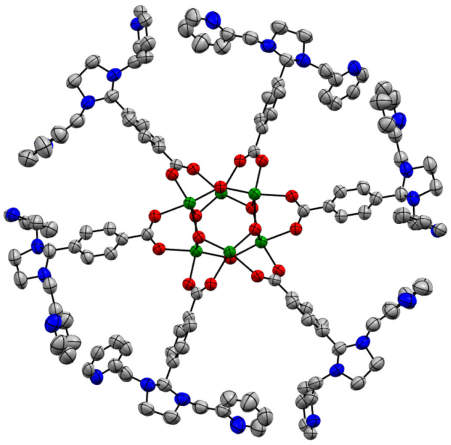
L_6
Complex
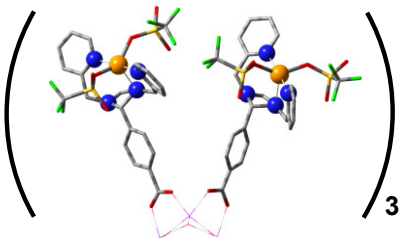
Attached to the S_6O_6 core
Co-L_6
Intermediate
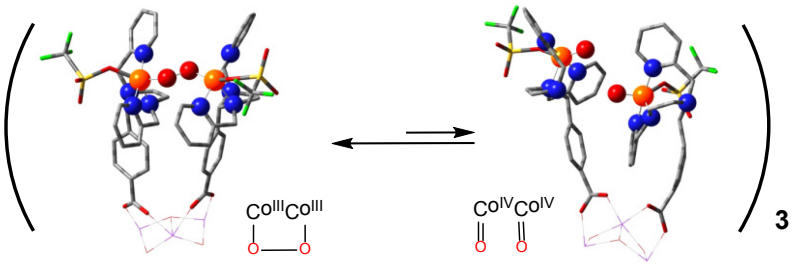
Proposed equilibrium between a bridging μ-peroxo-dicobalt(III) and oxocobalt(IV) units
Co-1

Color code: N-blue, O-red, Sn-green, C-gray, S-yellow, F-light green, Fe-orange. Hydrogen atoms have been ommited for clarity.

3.1. Introduction

Small molecules such as O_2, N_2, N_2O and CH_4 are ubiquitous, inexpensive and thermodynamically stable compounds that can be employed as reagents for the production of value-added chemicals and/or as efficient energy sources; in order to do so, however, the large kinetic barriers to their activation need to be overcome.[1] Metals provide reaction pathways with low activation barriers to activate and further modulate the reactivity of such molecules, and are widely employed in biological systems as catalysts for several important transformations.[2]

Multinuclear transition metal sites are commonly chosen by enzymes in nature to perform vital small molecule activations. Relevant examples of these kinds of enzymes include the nitrogenase that catalyzes the reduction of nitrogen to ammonia using an iron-molybdenum cofactor (Figure 3.1 a),[3] the nitrous oxide reductase that catalyzes the reduction of nitrous oxide to nitrogen in a tetranuclear Cu_z center (Figure 3.1 b),[4] and the nickel-iron and iron-iron hydrogenases that catalyze the reversible oxidation of molecular hydrogen in bimetallic centers (Figure 3.1 c).[5,6]

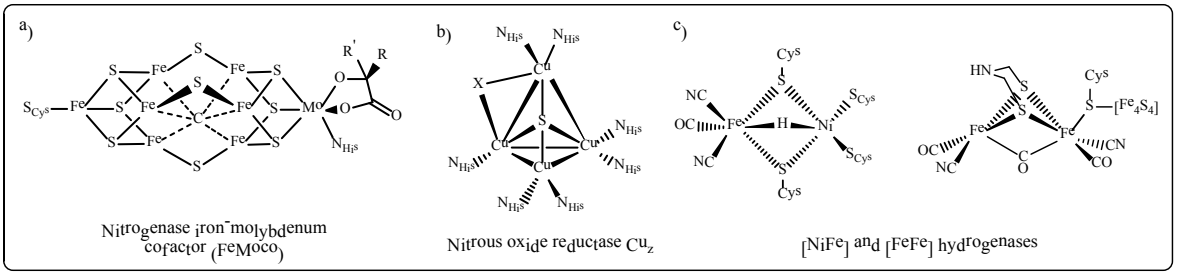

Figure 3.1: Structures of the multinuclear transition metal active sites of: nitrogenase (a) and nitrous oxide reductase (b), and binuclear active sites of nickel-iron and iron-iron hydrogenases (c).

Of particular importance are the enzymes that perform the O−O bond formation and cleavage steps during the oxygen reduction and water oxidation reactions. These processes are directly implicated in aerobic respiration and the photosynthesis, respectively, and are also promising reactions for the development of efficient fuel cells capable of converting chemical energy into electrical energy, producing only water as a byproduct.[7-9]

The water oxidation process occurs in the thylakoid membrane of plants, algae and cyanobacteria, in the protein complex called photosystem II (PSII), which is part of the photosynthetic chain. The O−O bond formation is catalyzed by a protein-bound oxygen-evolving complex (OEC) that consists of a Mn_4Ca cluster, in which the metal ions are coordinated by several μ-oxo bridges and water molecules (Figure 3.2 a).[10,11] The four-electron reduction of oxygen to

water, on the other hand, is performed by different known enzymes. Two groups of enzymes are especially important for oxygen reduction: multicopper oxidases such as laccase, which uses a tri-nuclear copper cluster as the active site (Figure 3.2 b),[12] and the cytochrome *c* oxidases, which utilize a bimetallic heterodinuclear iron-copper site (Figure 3.2 c) to perform this reaction at the end of the respiratory chain. [13,14]

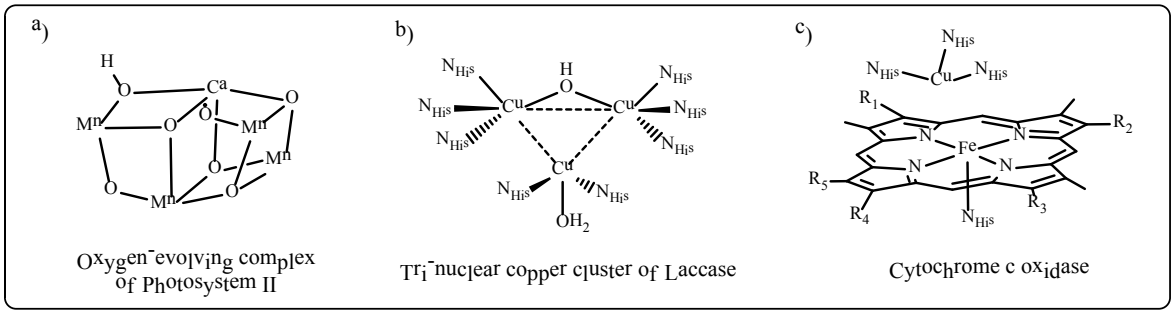

Figure 3.2: Structures of the multinuclear transition metal active sites of enzymes involved in O−O bond formation and O_2 reduction processes: a) the oxygen-evolving complex of photosystem II, b) the tri-nuclear copper cluster of laccase and c) the cytochrome c oxidase.

In order to get a better understanding of the effects of metal nuclearity in the activation of small molecules, great efforts have been made to generate multinuclear transition metal compounds in which the synergism between the multiple metal centers can be studied.[15-17] Simultaneously, much attention has been given to the incorporation of transition metals to dendrimer structures due to their potential applications in various fields[18,19] and the fact that they provide an organization frame for the metals to work together.[20,21] The convergence of these two views results in the interest in generating dendrimer-like structures capable of coordinating metals in such a way that they can work synergistically in the activation of small molecules.

The synthetic difficulties related to the generation of such multinuclear ligands have restricted research in this field; however, the organostannoxane approach has proven to be a simple and efficient methodology to generate dendrimer-like multinuclear ligands with multiple binding sites for transition metals. This methodology was first reported by Chandrasekhar and coworkers in 2005, when they used it to generate a hexanuclear Cu-porphyrin complex supported in a stannoxane Sn_6O_6 core, capable of cleaving the supercoiled DNA structure, thanks to the cooperativity between the metal centers.[21]

Following the same approach, in 2012 Kundu et al. reported the synthesis and characterization of a hexanuclear non-heme iron complex **Fe-L$_6$** supported in a stannoxane core.[22]

The hexanucleating ligand **L_6**, characterized by X-Ray, ^{119}Sn-NMR and IR, showed a drum-like stannoxane central core supporting a wheel arrangement of the six non-heme ligands with two pyridine and two amine donor sites per ligand fraction (Scheme 3.1). The hexanuclear iron complex **Fe-L_6**, obtained from the reaction of **L_6** with 6 equivalents of $Fe(OTf)_2$, was characterized by inductively coupled plasma mass spectroscopy (ICP-MS), elemental analysis, ^{119}Sn-NMR, ^{19}F NMR and Möβbauer spectroscopy together with DFT calculations and was shown to contain six high-spin Fe(II) centers supported in the intact tin core with two triflate ions per metallic ion (Scheme 3.1).

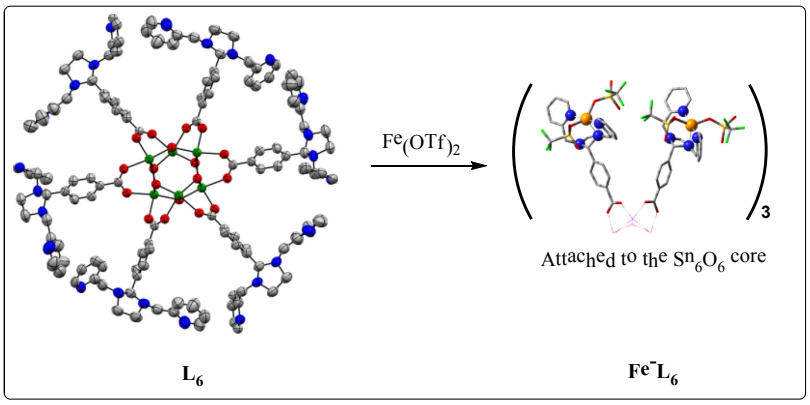

Scheme 3.1: Structures of the hexanuclear ligand **L_6** and the complex **Fe-L_6** as reported by Kundu et al.[22] Color code: N-blue, O-red, Sn-green, C-gray, S-yellow, F-light green, Fe-orange. Hydrogen atoms have been ommited for clarity.

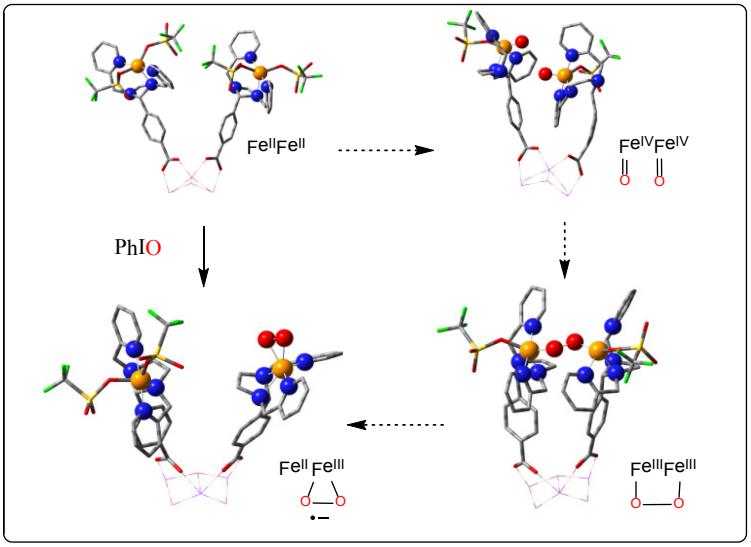

Scheme 3.2: Proposed mechanism for the O–O bond formation reaction mediated by **Fe-L_6** as reported by Kundu et al.[22] Color code: N-blue, O-red, Sn-green, C-gray, S-yellow, F-light green, Fe-orange. Hydrogen atoms have been ommited for clarity.

Kundu and coworkers showed that **Fe-L_6** performed an intramolecular O−O bond formation reaction when it was set to react with 2-(*tert*-butylsulfonyl)-iodosylbenzene (sPhIO) in CH_2Cl_2 at 25 °C. It was proposed that this reaction would proceed through the mechanism shown in Scheme 3.2. The iron centers in **Fe-L_6** initially formed transient oxoiron(IV) intermediates. The coupling of two neighboring oxoiron units generated a peroxo-bridged diiron(III) complex. Finally, this species underwent a rearrangement to generate the detected superoxo Fe^{III}-($O_2^{\bullet-}$) Fe^{II} units. These findings supported the previous reports of iron complexes as suitable catalysts for water oxidation in homogeneous conditions[23,24] and showed that the dendrimer-like ligand structure facilitates the synergistic work between the metal centers for this crucial O−O bond formation reaction.

Furthermore, Kundu also reported the synthesis of a hexanuclear cobalt(II) complex **Co-L_6** supported by the same hexanuclear ligand **L_6** and characterized it through elemental analysis, inductively coupled plasma mass spectroscopy (ICP-MS), ^{119}Sn-NMR and infrared spectroscopy (IR).[25] This characterization, which was consistent with the preliminary density functional theory (DFT) calculations, suggested that the structure of the hexanuclear cobalt complex was similar to that of the hexanuclear iron complex **Fe-L_6** (Scheme 3.1) where each cobalt is coordinated by three nitrogen donors from the ligand **L_6**, together with two triflate ligands. However, the possible interaction between the cobalt centers of the complex was not explored and more robust theoretical and experimental studies were lacking to properly determine the coordination around the cobalt centers.

In contrast to the **Fe-L_6** complex, **Co-L_6** barely reacted with sPhIO but rapidly reacted with O_2 in CH_2Cl_2 or acetone at 25 °C to yield an orange species **Co-1** with a maximum absorbance band λ_{max} (ε_{max}, M^{-1} cm^{-1}) centered at 470 nm (11600) and a half-life of 3600 s (Figure 3.3). Complex **Co-1** was further characterized by rRaman, XAS and DFT calculations. The rRaman of **Co-1** (Figure 3.4 a), measured using a 458 nm laser excitation in resonance with the 470 nm transition, showed three $^{16}O/^{18}O$ isotopically sensitive vibrational bands at 868, 825 and 611 cm^{-1} with observed isotopic downshifts of 49, 27 and 34 cm^{-1} respectively. The bands at 868 and 611 cm^{-1} were assigned to the O−O stretching vibration of a peroxo ligand and to a Co−O stretching vibration. The rR band at 825 cm^{-1}, on the other hand, was assigned to a simple Co−O harmonic oscillator; it has been proposed that this higher-energy Co−O vibrational band is an indicator of the presence of Co^{IV}=O units in solution. The band observed in the UV-vis at 470 nm was thus assigned to be predominantly a peroxo-to-cobalt charge transfer band. As for the peroxo ligand coordination mode, it was assigned to a bridging μ-peroxo-dicobalt(III) complex, given the resemblance of its spectral features with those of previously reported bridging peroxo complexes[26-28] and given that

the alternative side-on Co(III) peroxo complexes would be expected to display absorption features with much lower extinction coefficients ($\varepsilon < 1000\ M^{-1}s^{-1}$).[29–31]

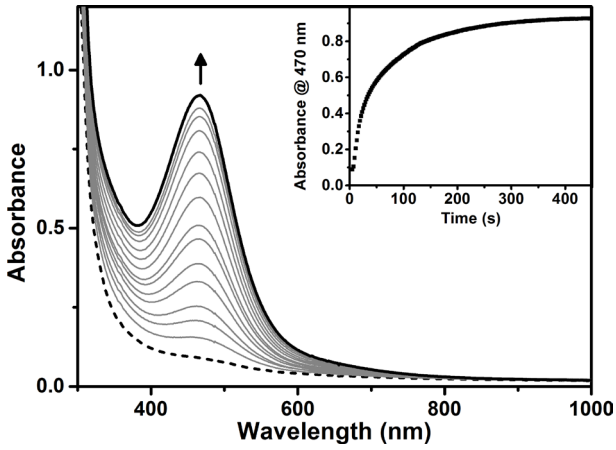

Figure 3.3: Absorption spectra showing the formation of **Co-1** (straight line) from the reaction of **Co-L$_6$** 0.75 mM (dotted line) with O_2 in CH_2Cl_2 at 25 °C. Inset: Absorbance change at 470 nm against time due to the formation of **Co-1**.

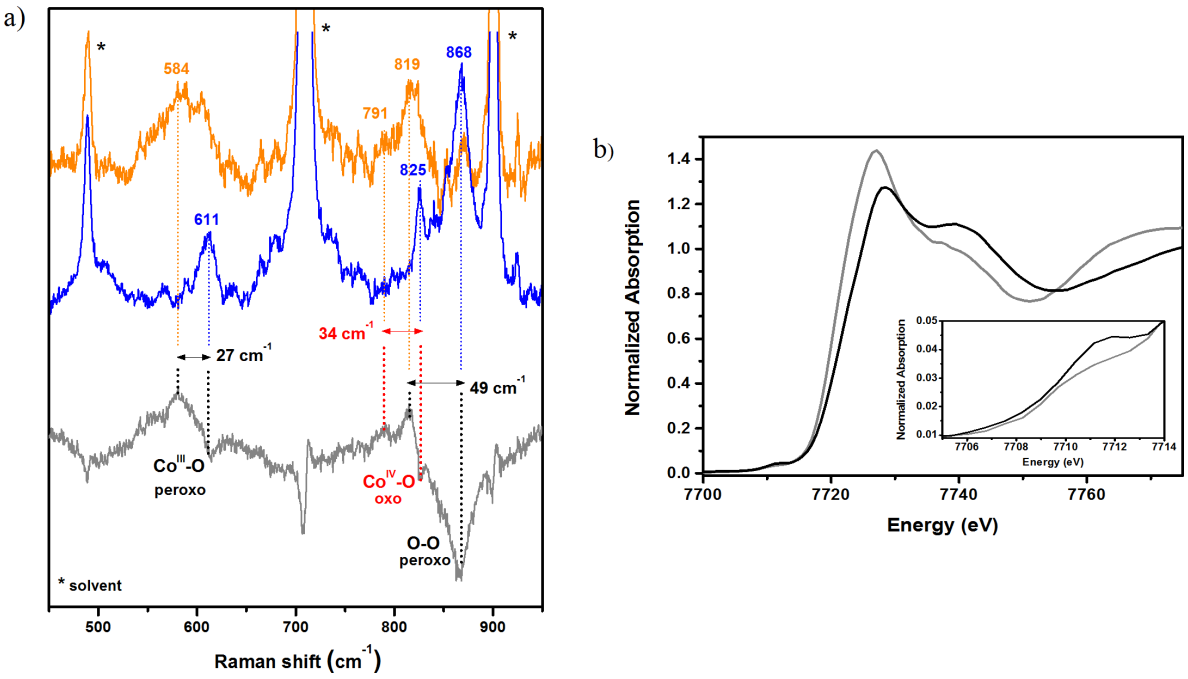

Figure 3.4: a) rRaman spectra with 458 nm laser excitation in d_6-acetone at −80 °C of **Co-1-^{18}O** (orange solid line), **Co-1-^{16}O** (blue solid line) and the difference [**Co-1-^{18}O**]-[**Co-1-^{16}O**] (gray solid line). b) normalized Co *K*-edge near edge X-ray absorption spectrum of **Co-L$_6$** (gray solid line) and **Co-1** (black solid line); the inset shows the expansion of the pre-edge. Reported by Kundu.[25]

The normalized Co *K*-edge XAS spectra of **Co-L$_6$** and **Co-1** (Figure 3.4 b) were also studied to get an indication of the oxidation state of the cobalt in the complex **Co-1**. Kundu found a 1.6 eV blue shift of the edge energy between **Co-L$_6$** and **Co-1** together with a 1.4 eV blue shift of the pre-edge feature. This indicated a higher oxidation state of the cobalt in **Co-1** in comparison with the starting compound; the magnitude of the shifts suggested a contribution of both the Co(III) and Co(IV) forms in the spectrum. DFT calculations were also performed by Kundu and coworkers to rationalize the structure of the cobalt centers in **Co-L$_6$**, as well as the viability of the identified components of **Co-1**, namely the bridging peroxo-dicobalt(III) and the terminal cobalt(IV)-oxo.

A mechanism for O_2 activation mediated by **Co-1** was proposed based on the spectroscopic results and DFT calculations. The proposed mechanism is shown in Scheme 3.3. The starting **Co-L$_6$** activates dioxygen and generates a bridging μ-peroxo-dicobalt(III) species. This species further undergoes homolytic O−O cleavage to generate the cobalt(IV)-oxo units. The spectroscopic evidence pointed towards the generation of these two intermediates; however, the reactivity of **Co-1** remained to be fully tested.

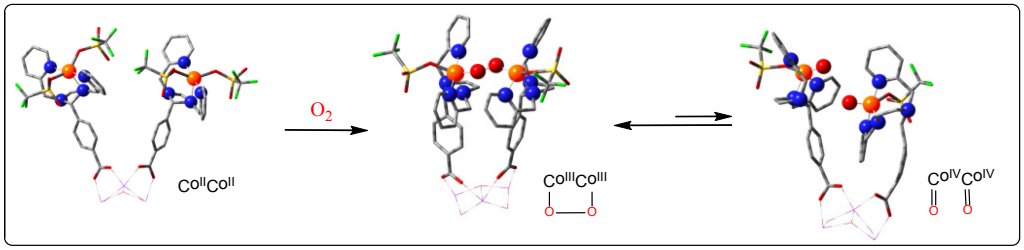

Scheme 3.3: Proposed mechanism for dioxygen activation by **Co-L$_6$** as reported by Kundu.[25] Color code: N-blue, O-red, Sn-green, C-gray, S-yellow, F-light green, Fe-orange. Hydrogen atoms have been ommited for clarity.

This Chapter will present a magnetic characterization of the **Co-L$_6$** complex with the aim of elucidating whether or not the cobalt centers in the hexanuclear complex present some form of interaction between each other and unequivocally assigning the geometry around the metal centers. Furthermore, the reactivity of the compounds **Co-1** and **Co-L$_6$** will be amply discussed; specifically, this Chapter will describe the nucleophilic and electrophilic reactivity of **Co-1** and the ability of **Co-L$_6$** to catalytically reduce oxygen.

3.2. Results and discussion

3.2.1 Characterization of Co-L_6

The complex **Co-L_6** has been characterized before with a variety of techniques, as reported by Kundu.[25] The elemental analysis confirmed the purity of the hexanuclear cobalt compound, while ICP-MS revealed the presence of six cobalt atoms per hexameric ligand **L_6**. The infra-red spectrum of **Co-L_6**, on the other hand, supported the presence of the drum core in the structure of the complex. However, the techniques employed do not provide information on any possible interaction between the cobalt centers within the molecule or in neighboring molecules.

Magnetic measurements of **Co-L_6** were performed in order to evaluate whether or not the metallic centers are interacting with each other within the hexanuclear complex. The magnetization data $M_{mol}/Ng\beta$ versus $\beta H/kT$ of **Co-L_6** was recorded in a SQUID (Superconducting Quantum Interference Device) magnetometer at fields ranging from 1 to 7 Tesla (Figure 3.5), where M_{mol} represents molecular magnetization, N is Avogadro's number, β is the Bohr magneton, H is the magnetic field, k is the Boltzmann constant and T is the absolute temperature. The collected data was properly modeled by zero-field splitting (ZFS), using the spin Hamiltonian:

$$\hat{H} = g\mu_B \boldsymbol{H} S + D[S_z^2 - S(S+1)/3] + E[S_x^2 - S_y^2]$$

where $\boldsymbol{H}$ is the applied magnetic field, g is the g-tensor, S is the electronic spin, and D and E are parameters that describe the effects of axial and rhombic ligand fields, respectively. The following magnetic parameters gave the best fits for the magnetization curves obtained: $E = 0.05$, $D = 3.5$ cm^{-1} and $g = 2.23$ for a cobalt(II) S = 3/2 complex. Small amounts of diamagnetic impurity (5%) were also taken into consideration to better fit the magnetization intensity of the raw data. The fits and the parameters thus obtained confirmed that the cobalt centers in **Co-L_6** are in an S = 3/2 ground state[32] and suggested that there is no interaction between the metallic centers in the molecule.

Further studies employing electron paramagnetic resonance (EPR) spectroscopy were performed. The X-band EPR spectrum of **Co-L_6** (10 mM in CH_2Cl_2) obtained at 8 K is presented in Figure 3.6 (solid black line). It exhibits a slightly rhombic signal with g values $g^{\perp} = 4.2$ and $g^{\parallel} \approx 2.1$, which are characteristic of a high-spin cobalt(II) center.[33,34] The spectra obtained thus support the assignation of the cobalt centers in **Co-L_6** as S = 3/2 as determined by fitting the magnetization curves. Further on, in order to evaluate the possibility of the cobalt centers interacting with each other, EPR studies varying the concentration of the hexanuclear complex **Co-L_6** in CH_2Cl_2 were carried out and are also shown in Figure 3.6. It turned out that the EPR

spectra did not depend on the concentration of the complex employed, thus proving the absence of any interaction between the metallic centers.

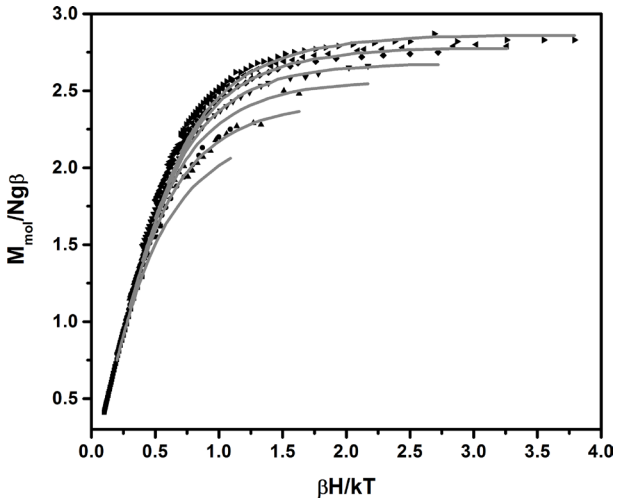

Figure 3.5: Magnetization data $M_{mol}/Ng\beta$ vs $\beta H/kT$ for **Co-L$_6$** in applied fields ranging from 1 to 7 Tesla. Raw experimental data is presented as black figures and the scaled best fits as solid gray lines (with the parameters discussed in the text).

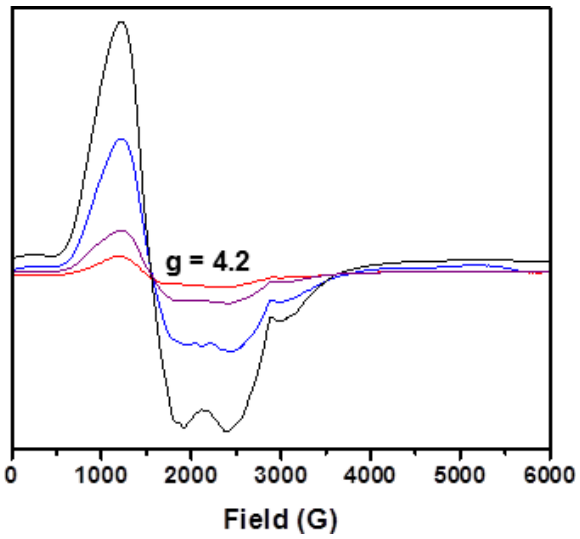

Figure 3.6: EPR spectra of **Co-L$_6$** in CH_2Cl_2 at 8 K in increasing concentrations (red: 1 Mm, purple: 3 mM, blue: 6mM and black: 10 mM).

As **Co-L$_6$** lacks a determined crystal structure, computational studies were performed to establish the geometry of the complex. An annotated model of **Co-L$_6$** was utilized for the computational study through abbreviation to a single arm extending from the stannoxane core; this model can correctly represent each of the six cobalt centers since the magnetic studies confirmed

that there is no interaction between them. As triflate was the sole counter-anion utilized during the synthesis, it was sensible to determine whether the triflates were bound to the complex, and if so, how many. Model complexes **A**, **B** and **C** were generated, in which zero, one and two triflates are bound to the cobalt(II) center, respectively. The optimized molecular structures of **A**, **B** and **C** are shown in Figure 3.7 (the computational details are described in Chapter 6).

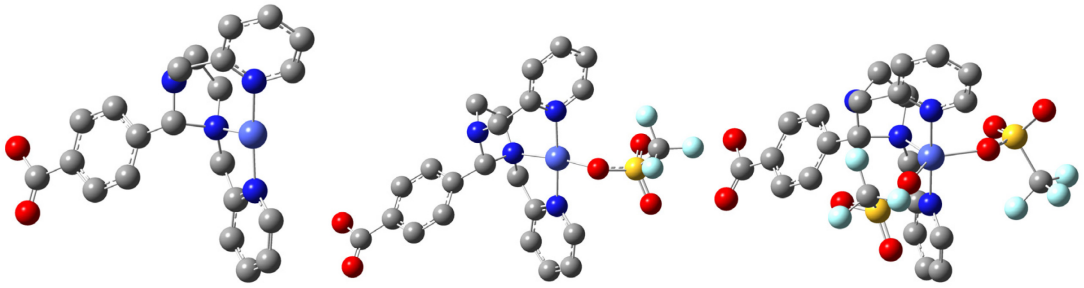

Model complex **A** Model complex **B** Model complex **C**

Figure 3.7: Optimized molecular structures of the model complexes **A**, **B** and **C** for the single-arm cobalt(II) fraction of **Co-L$_6$**. Color code: C-dark gray, N-blue, O-red, S-yellow, F-light blue, Co-bluish-gray; the hydrogen atoms are omitted for clarity.

Table 3.1: Relative energies of the model complexes **A**, **B** and **C** for comparing the relative favorability of the triflate binding in the single-arm cobalt(II) fraction of **Co-L$_6$**.

Model complex	Short formulation (L = single-arm fraction)	ΔE (kcal mol^{-1})
A	$[L\text{-}Co^{II}]^{2+} + (OTf)_2^{2-}$	135.5
B	$[L\text{-}Co^{II}(OTf)]^{+} + (OTf)^{-}$	42.9
C	$[L\text{-}Co^{II}(OTf)_2]$	0

In model complex **A**, the unsubstituted Co(II) single-arm compound, the metal coordination appears t-shaped, with approximate C_{2v} symmetry in the first coordination sphere (Figure 3.7 a). In model complex **B**, the one-triflate Co(II) single-arm compound, the metal coordination appears square planar, with approximate D_{4h} symmetry in the first coordination sphere (Figure 3.7 b). Finally, in model complex **C**, the two-triflate Co(II) single-arm compound, the metal coordination appears trigonal bipyramidal, with approximate D_{3h} symmetry in the first coordination sphere.

The relative energies of the calculated Co(II) single-arm complexes **A**, **B** and **C** are presented in Table 3.1. From the energy values calculated, it is clear that the binding of two triflates

to the cobalt(II) center provides the most favorable structure. Model complex **C**, with a trigonal bipyramidal geometry around the cobalt center, was hence predicted by this computational study to be the most energetically stable complex of the single-arm cobalt(II) fraction of **Co-L$_6$**.

The composition of the frontier orbitals (alpha and beta) of the three model complexes **A**, **B** and **C** were also determined. For compound **A**, the α-LUMO and β-LUMO, LUMO+1 orbitals were found to be composed predominantly of the cobalt(II) d_{z^2} and $d_{x^2-y^2}$ orbitals, with a_1 symmetry For compound **B**, on the other hand, the α-LUMO and β-LUMO, LUMO+1 orbitals are composed predominantly of the a_{1g} and b_{1g} symmetric d_{z^2} and $d_{x^2-y^2}$ orbitals from the cobalt(II) center. Finally, for compound **C**, the α-LUMO and β-LUMO, LUMO+1 orbitals are predominantly made up of the a_1' and e' symmetric d_{z^2} and $d_{x^2-y^2,xy}$ Co(II) orbitals with a reasonable degree of mixing (Figure 3.8).

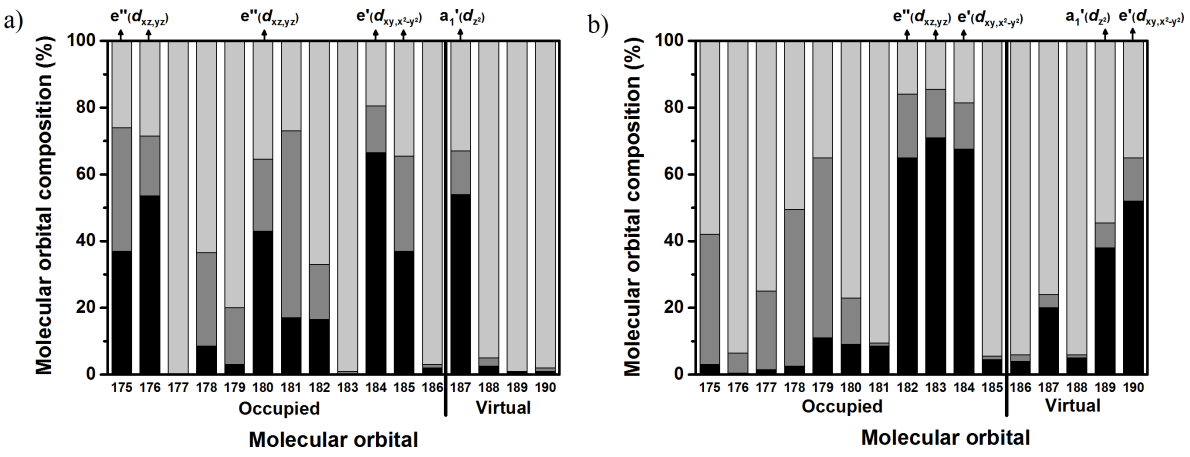

Figure 3.8: Molecular orbital composition of the a) α- and b) β-.frontier orbitals of **C**. Color code: black-contribution of the cobalt center, grey-contribution of the triflates and light gray-contribution of the ligand.

To further corroborate the formulation of each single-arm in **Co-L$_6$** with the geometry of **C**, Magnetic circular dichroism (MCD) studies were performed. The experimental room temperature absorption spectrum and the 4 K, 7 T MCD spectra of **Co-L$_6$** are shown in Figure 3.9. The broad, sloping range from 14300 to 28000 cm^{-1} in the absorption spectrum is resolved into several features in the MCD spectrum.

Time-dependent DFT (TDDFT) calculations were made to simulate and deconvolute the electronic and MCD spectra of **Co-L$_6$**. Based on TDDFT, the electronic spectrum of **A** (Figure 3.10 b) appears unable to model the intensity of the primary absorption band, which appears to begin rising at around 29000 cm^{-1} in the electronic spectra of **Co-L$_6$**. Complex **C**, on the other hand,

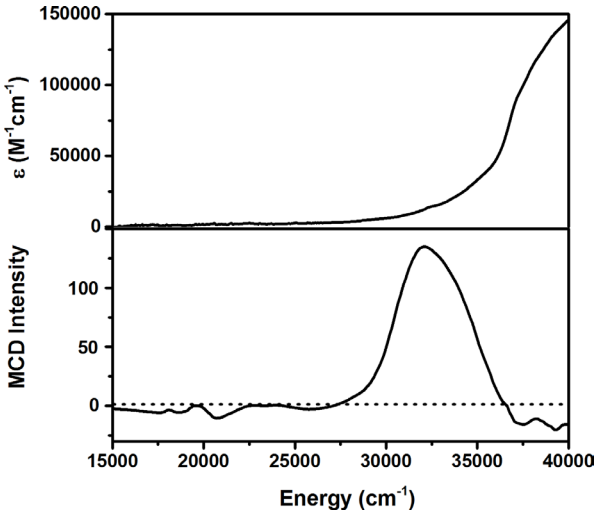

Figure 3.9: Experimental UV-vis absorption (top) and MCD spectrum (bottom). The UV-vis was recorded at room temperature. The MCD spectrum was acquired at 4 K, 7 T, and the intensity normalized to 4 K, 1 T.

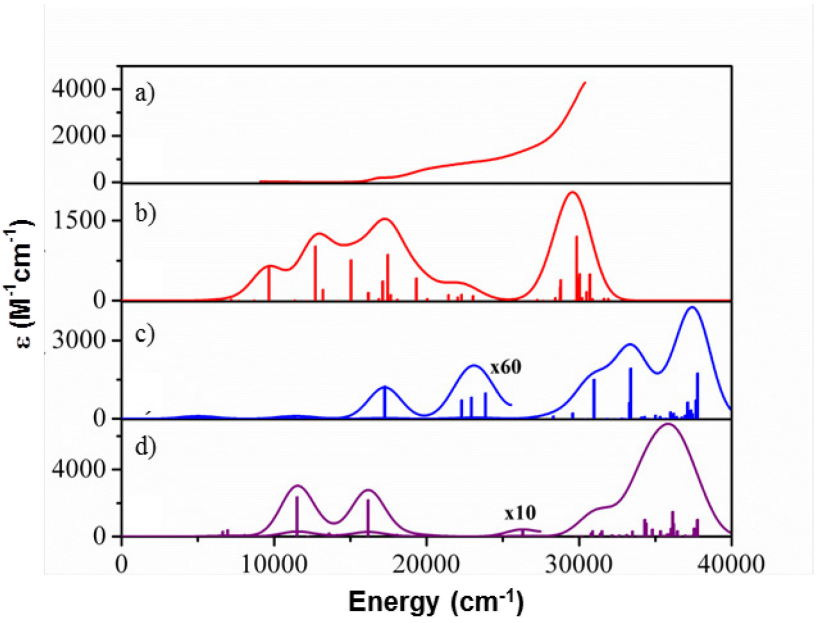

Figure 3.10: Comparison of the experimental UV-vis spectra of **Co-L$_6$** with the TDDFT-calculated spectra of **A**, **B** and **C** model complexes, as calculated by ORCA 3.0.2.

appears able to model the experimental electronic spectrum (Figure 3.10 d). The low-energy MCD spectrum, in the region of 15000 to 22000 cm^{-1}, was also deconvoluted based on TDDFT results for **C** (Figure 3.11). The first observable transition of the MCD spectrum arises from several *d*-centered e'',e'→e',a$_1$' transitions, while slightly higher energy features are due to several LMCT (ligand to metal charge transfer)-type excitations. The predominant peak of the spectrum, centered at around

32000 cm^{-1} (Figure 3.9 b) may be ascribed to several pyridine-centered π to π* transitions. Table 3.2 presents the energies, oscillator values and band assignments for the low-energy transitions for model complex **C**, which best fits the experimental results.

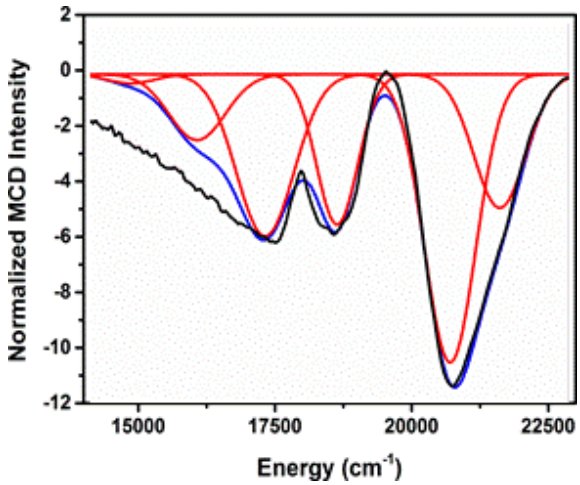

Figure 3.11: Band deconvolution analysis of the low-energy MCD region (4 K, 7 T) based on TDDFT results for **C** calculated by ORCA. Black line- experimental spectrum, red- Gaussian deconvolution bands, blue-sum of Gaussian deconvolution bands.

Table 3.2: First fifteen electronic transitions of **C** calculated via TDDFT as implemented in ORCA 3.0.2.

	TDDFT-calculated Electronic Excitations		
	Energy (cm^{-1})	f osc.	Transition type
1	7,231	0.00003	e' → e'
2	8,348	0.00003	e" → a_1'
3	9,384	0.00005	Pyr. π + e" → a_1'
4	9,633	0.00001	e' → a_1'
5	11,963	0.00008	e"→ e'
6	13,484	0.00115	Pyr. π + e" → a_1'
7	14,009	0.00361	e" → a_1'
8	16,475	0.00245	e' → a_1'
9	18,111	0.00010	e" → a_1' + π*
10	19,187	0.00006	e"→ e'
11	22,999	0.00035	LMCT (to a_1')
12	28,134	0.00024	LMCT
13	28,334	0.01091	LMCT
14	29,337	0.00008	LMCT
15	29,422	0.00001	LMCT

The results obtained so far indicate that the cobalt centers in **Co-L$_6$** are in a high spin S=3/2 configuration and no interaction exists between them, so they can be treated independently to study the geometry of the cobalt centers within the hexanuclear complex. The single-arm model complex **C**, with two triflates coordinated to the cobalt(II) and a bipyramidal geometry around the metallic center, was found to be the lowest in energy, in comparison with the **A** and **B** structures (with zero or one triflate in the cobalt coordination sphere respectively). **C** was also found to best fit the electronic and MCD experimental spectra. It was found that the main peak in the spectra could be ascribed to several pyridine-centered π to π^* transitions, while those at lower energies were *d*-centered and LMCT in nature.

3.2.2 Nucleophilic oxidative reactivity of Co-1

As described before, the reaction of the hexanuclear complex **Co-L$_6$** with oxygen at 25 °C was proposed to result in the formation of bridging μ-peroxo-dicobalt(III) units that further partially convert to cobalt(IV)-oxo units. The presence of both species was detected in the rRaman spectrum obtained via excitation of the oxidized species with a 458 nm laser in resonance with the UV-vis band at 470 nm, which indicates that **Co-1** comprises both species in solution. In order to complete the characterization of **Co-1**, reactivity studies were performed to test the reactivity-character of the intermediates detected.

Metal-peroxo species are believed to play key roles in the oxidative transformations of organic molecules by metalloenzymes.[35,36] In biomimetic studies, a number of metal-peroxo model complexes have been characterized and their reactivities have been intensely researched.[35] Late transition metal-peroxo species,[37] including cobalt-peroxo complexes,[31,38] have been found able to perform nucleophilic oxidations, such as the deformilation of aldehydes, but not electrophilic oxidations such as C−H bond activation reactions or the oxygen transfer to triphenylphosphine. In an effort to elucidate the chemical behavior of the intermediate **Co-1**, its reactivity in nucleophilic reactions was tested.

Co-1 was generated in situ by bubbling O_2 in a 0.15 mM dichloromethane solution of **Co-L$_6$**; its formation was monitored by following the rise in the 470 nm band in the UV-vis spectra. An excess of more than 20 equivalents of benzoyl chloride were then added to the reaction mixture. The decay of the band at 470 nm (Figure 3.12) was monitored and fitted to a pseudo-first-order rate (Figure 3.12, inset) from which k_{obs} was determined. An analysis of the reaction mixture with GC-MS showed the formation of benzoic acid as the product of the reaction.

The described procedure was repeated using different amounts of benzoyl chloride each time. The series of k_{obs} thus obtained increased linearly with the amount of added substrate (Figure 3.13), and the slope of the linear fit of the substrate concentration vs. k_{obs} represents the second-order rate constant (k_2) of the reaction (Table 3.3). As can be seen in Figure 3.13 this plot does not cross the axis at (x,y = 0,0) but has a positive intercept due to the self-decay of the species **Co-1** under these conditions.

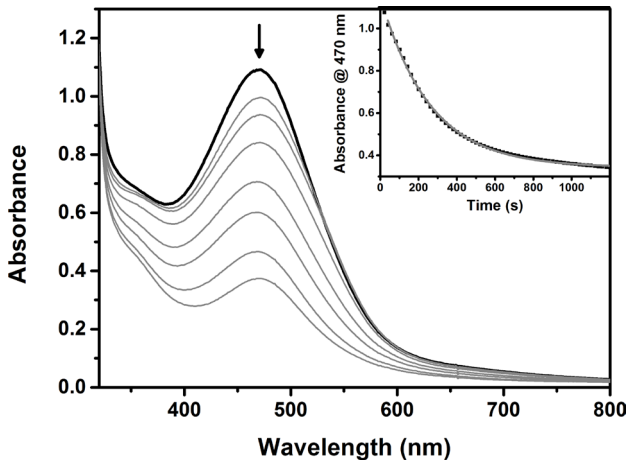

Figure 3.12: Absorption spectra showing the decay of **Co-1**, formed in situ from the reaction of a dichloromethane solution of **Co-L$_6$** (0.15 mM) with O_2, after addition of 125 equivalents of benzoyl chloride in CH_2Cl_2 at 25 °C. Inset: time trace of the decay of **Co-1** monitored at 470 nm and the pseudo-first-order fitting (gray line).

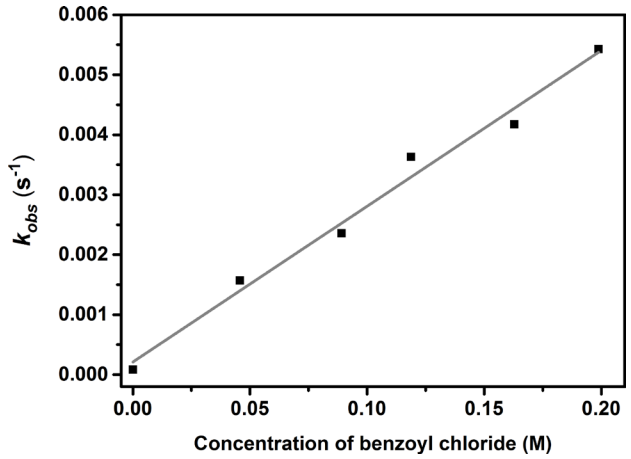

Figure 3.13: Linear dependence of k_{obs} on the concentration of benzoyl chloride as determined for the reaction of **Co-1** with the substrate in CH_2Cl_2 at 25 °C.

To get further insights into the nucleophilic character of **Co-1,** different benzoyl chlorides with a series of electron-donating and –withdrawing substituents at the *para*-position of the phenyl

group were employed as substrates, namely *para*-X-Ph-COCl where X= OMe, Me, H, Cl and CN. The second-order rate constants obtained are presented in Table 3.3.

Table 3.3: Second-order rate constants (k_2) for the nucleophilic oxidative reactions of **Co-1** with *para*-substituted benzoyl chlorides (*p*-X-Ph-COCl; X= OMe, Me, H, Cl and CN) determined in CH_2Cl_2 at 25 °C.

X	**OMe**	**Me**	**H**	**Cl**	**CN**
k_2 ($L\ mol^{-1}\ s^{-1}$)	0.0158	0.0199	0.0260	0.0393	0.2132

As expected for a nucleophilic mechanism, the rate constant increases as the electron withdrawing capability of the *para*-substituents of the benzoyl chloride is increased. However, when the log k_2 vs. the *para*-substituent constants (σ_p^+) are plotted, a notable anomaly in the trend can be observed (Figure 3.14); while the first four points reveal a good linear correlation, the last point, corresponding to the reactivity of **Co-1** with *para*-CN-Ph-COCl, is located outside of the trend (Figure 3.14). This can indicate a change in the reaction mechanism of **Co-1** with the CN-substituted benzoyl chloride; we attribute this sudden change to the possibility that the CN- group may be coordinated to the metallic complex, thus substantially increasing the rate of the reaction.

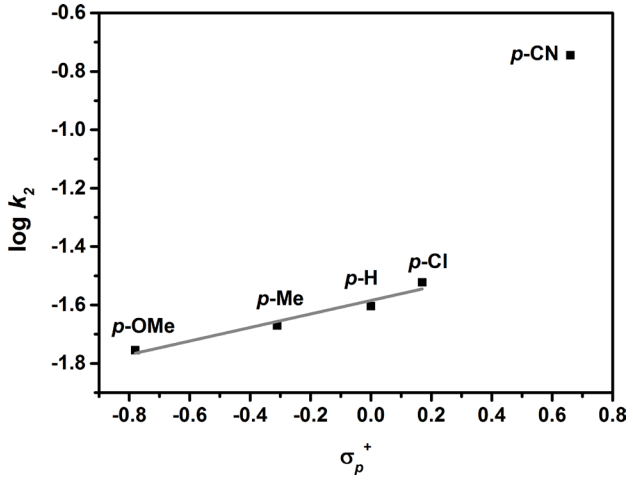

Figure 3.14: Hammett plot of log k_2 against σ_p^+ for the reaction of **Co-1** with *para*-substituted benzoyl chlorides (*para*-X-Ph-COCl; X= OMe, Me, H, Cl and CN) in CH_2Cl_2 at 25 °C.

By taking only the initial four points of the plot, a Hammett reaction constant (ρ) value of +2.0 was obtained for the reaction of **Co-1** with benzoyl chlorides. The positive value of ρ corroborates the nucleophilic character of **Co-1**, which can be ascribed to the bridging μ-peroxo-

dicobalt(III) units detected spectrophotometrically, since metal-peroxos are known to have a nucleophilic character.[35,38]

3.2.3 Electrophilic oxidative reactivity of Co-1

In order to complete the characterization of **Co-1,** the electrophilic reactivity, typically detected in metal-oxo complexes, was also tested in three kinds of reactions: C−H bond activation, group transfer and O−H bond activation reactions. For the activation of C−H bonds, five substrates were employed, namely 1-benzyl-1,4-dihydronicotinamide (BNAH), xanthene, dihydroanthracene (DHA), 1,4-cyclohexadiene (CHD) and fluorene, whose structures are shown in Figure 3.15. The oxo-group transfer reactivity, on the other hand, was tested using triphenylphosphine (PPh_3) as a substrate.

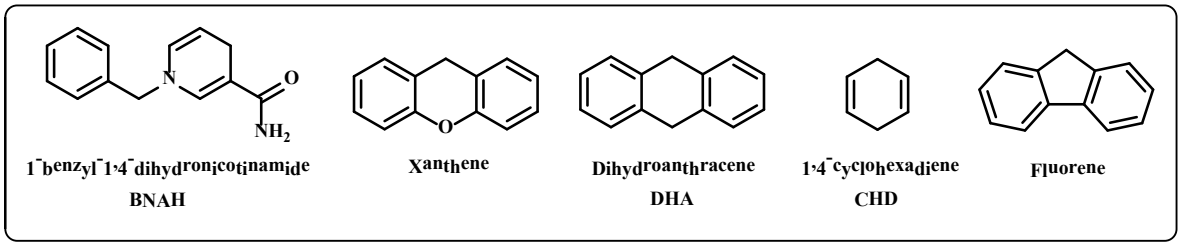

Figure 3.15: Structures of the substrates used to test the C−H bond activation capacity of **Co-1**.

The procedure followed for the evaluation of the reactivity of **Co-1** against these substrates was similar to that previously described; **Co-1** was formed *in situ* from the reaction of **Co-L$_6$** with O_2 in CH_2Cl_2 at 25 °C and then an excess of the substrate was added. The decay of the band at 470 nm was then recorded and fitted to a pseudo-first-order decay to obtain k_{obs}, which was plotted against the substrate concentration to obtain k_2. Figure 3.16 illustrates this process by taking the reaction of **Co-1** with xanthene.

Co-1 was capable of oxidizing all the substrates described above. An analysis of the reaction mixture for the DHA and CHD reactions showed the formation of anthracene and benzene as products, respectively. **Co-1** also reacted with PPh_3 to generate triphenylphosphine oxide. The obtained second-order rate constants, corrected, when applicable, with the number of equivalent target hydrogen atoms in each substrate (k_2'), are listed in Table 3.4, together with the bond dissociation energy (BDE)[39] of each substrate.

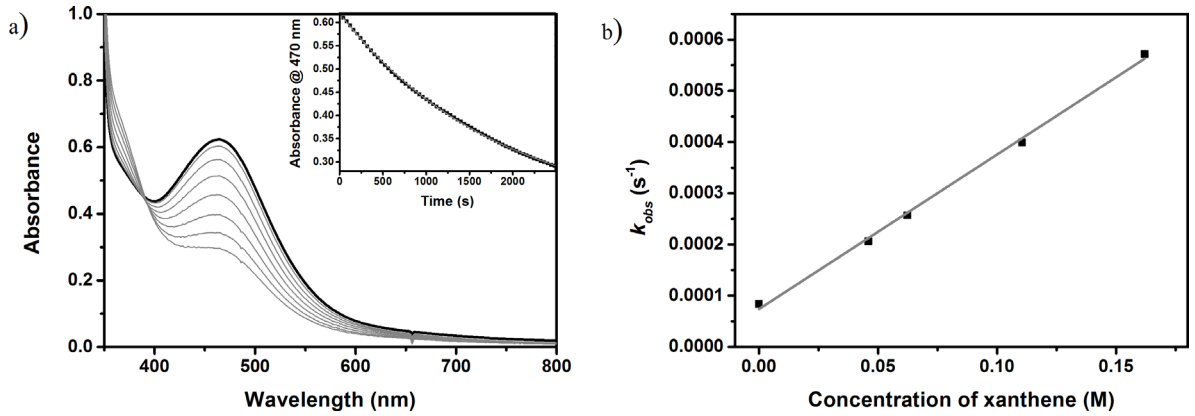

Figure 3.16: a) Absorption spectra showing the decay of **Co-1**, formed in situ from the reaction of a dichloromethane solution of **Co-L$_6$** (0.15 mM) with O_2, after addition of 200 equivalents of xanthene in CH_2Cl_2 at 25 °C. Inset: time trace of the decay of **Co-1** monitored at 470 nm and pseudo-first-order fitting (gray line). b) Linear dependence of k_{obs} on the concentration of xanthene determined in CH_2Cl_2 at 25 °C.

Table 3.4: Second-order rate constants (k_2') determined for the C−H bond activation and group transfer reactions of **Co-1** with different substrates in CH_2Cl_2 at 25 °C and C−H bond dissociation energy (BDE) of each substrate.

Substrate	**BNAH**	**Xanthene**	**DHA**	**CHD**	**Fluorene**	**PPh_3**
k_2' ($L\ mol^{-1}\ s^{-1}$)	0.1831	0.0035	0.0034	0.0025	0.0016	0.0039
BDE[39] (kcal/mol)	67.9	74	76.3	76.9	81.2	-

A trend can be observed in which the reaction rate decreases as the BDE of the substrate increases. However, when plotting the log k_2' vs. BDE of the substrates (Figure 3.17), a divergence in this trend can again be observed; this time the rate of the reaction of **Co-1** with BNAH was much faster than expected from the trend of the other four substrates. Once more, this may be a result of the coordination of the substrate to **Co-1** through the amide group, which is not possible for the rest of the substrates (Figure 3.15).

Despite the irregularity found for BNAH, the observed trend of a decrease in the reaction rate for the substrates with the strongest C−H bonds suggests that the C−H bond activation performed by **Co-1** proceeds through a rate-determining hydrogen atom abstraction step. A similar trend was found by Kundu for **Co-1** in the activation of O−H bonds,[25] which also supports this

finding. In the absence of any previous reports of Co-peroxo-mediated intermolecular C−H and O−H bond activation reactions, this behavior was initially assigned to the presence of the cobalt(IV)-oxo species (detected spectrophotometrically) which exists in equilibrium with the Co-peroxo species in solution. This assignment was supported by the ability of **Co-1** to perform group transfer reactions, a typical electrophilic behavior usually associated with metal-oxo systems.

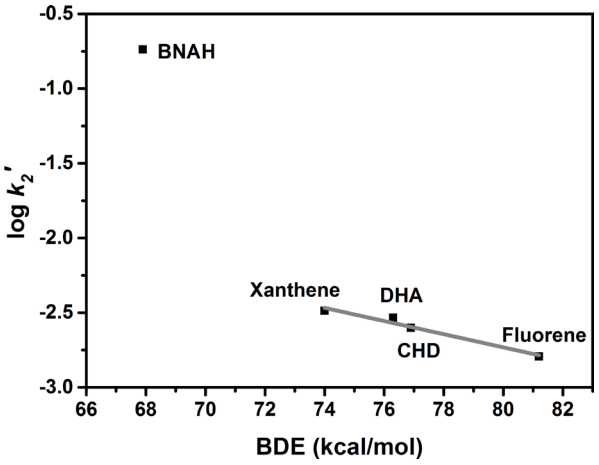

Figure 3.17 Plot of the log k'_2 vs BDE for the reactions of **Co-1** with different substrates in CH_2Cl_2 at 25 °C.

To further corroborate that the C−H/O−H bond activation reactions proceeded via a rate-determining hydrogen atom abstraction step mediated by the cobalt-oxo formed in solution, the kinetic isotope effect (KIE) was determined for the reaction of **Co-1** with DHA and d_4-DHA, and with 2,6-di-*tert*-butyl-4-methoxyphenol and its deuterated version (Figure 3.18). The KIE values (k_H/k_D) found for the C−H and O−H bond activation reactions mediated by **Co-1** were determined to be 2.57 and 2.85, respectively. These values are rather small in comparison with the KIE value of 11 given for the recently reported [(TAML)Co^{IV}(O)(Sc)][40] complex and values reported for other metal-oxo complexes.[41,42] The interpretation of such a small KIE value in the reactions catalyzed by **Co-1** is not straightforward, it might indicate that it is not the oxocobalt species that is responsible for the electrophilic behavior, but rather the bridging μ-peroxo-dicobalt species; electrophilic behavior has not typically been observed in biomimetic metal-peroxo complexes but side-on-bridged dicopper(II)-peroxo units are known to initiate electrophilic oxidation reactions.[43] It might also indicate that the mechanism by which the oxocobalt intermediate performs the C−H bond activation is different.

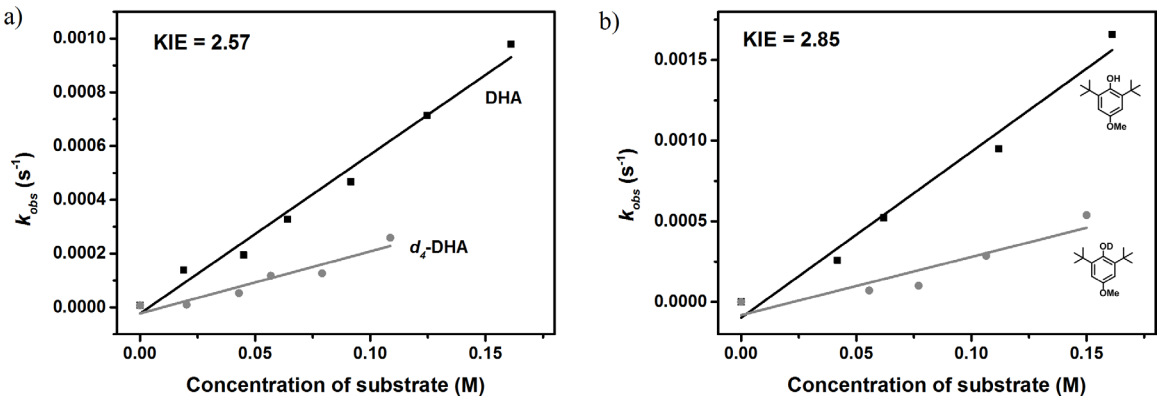

Figure 3.18: Linear dependence of k_{obs} with the concentration of substrate for the reaction of **Co-1** with a) DHA and d_4-DHA and b) 2,6-di-*tert*-butyl-4-methoxyphenol and 2,6-di-*tert*-butyl-4-methoxy-*d*-phenol in CH_2Cl_2 at 25 °C.

One indirect method frequently used to prove the presence of a metal-oxo complex in solution is to carry out the catalytic oxidation reactions in the presence of ^{18}O-labled water ($H_2{}^{18}O$), since metal-oxo complexes can exchange their O-atom with ^{18}O-labled water prior to the O-atom transfer to organic substrates.[44-46] In order to determine whether or not an oxocobalt(IV) species was forming in solution and was responsible for the electrophilic reactivity in this system, **Co-1** was set to react with PPh_3 in acetone in the presence of 0.01 mL of $H_2{}^{18}O$. The analysis of the reaction mixture after the reaction was completed showed no presence of ^{18}O incorporated in the triphenylphosphine oxide. This indicates that there is probably no oxocobalt(IV) in solution, but rather the bridging μ-peroxo-dicobalt species is responsible for both the nucleophilic and the electrophilic reactivity of **Co-1**. This is an exciting finding since bridging peroxos are not typically reported to perform electrophilic oxidations.

3.2.4 Dioxygen reduction catalyzed by Co-L_6

The catalytic four-electron reduction of oxygen to water, as mentioned at the beginning of this chapter, has attracted much interest due to its vital role in respiration as well as its technological relevance in fuel cells.[7-9,47] In nature, this process is carried out by an iron-haem/copper heterodinuclear center in cytochrome *c* oxidases[13,14] (Figure 3.2 c). By contrast, in fuel cells the same reaction is catalyzed at a cathode by platinum impregnated in carbon.[48] The high loads of Pt required for achieving adequate activity in fuel cells has prompted the development of new catalysts based on metals that are more earth-abundant and cheaper, such as Co, Fe or Cu.[26,49-57]

Until recently, electrocatalytic reduction of oxygen was the only technique available for probing the catalytic activity of synthetic catalysts in the oxygen reduction reaction. However, this

procedure prevented the detection of the active intermediates and limited the mechanistic studies of the employed homogeneous catalysts.[53,56] To overcome this limitation, in 2004 Fukuzumi, Guiliard and coworkers reported an innovative way of testing the homogeneous catalytic reduction of O_2 by using one-electron reductants such as ferrocene derivatives in the presence of an acid.[53] This technique has provided mechanistic insights into the reaction of oxygen reduction by metal complexes. In several studies, dinuclear metal-peroxos have been detected as key intermediates for this transformation. [52-57]

Given the evidence, from both spectroscopic and reactivity studies, of the occurrence of cobalt-peroxo units in the reaction of **Co-L$_6$** with O_2, and the possibility that they may perform O−O bond cleavage to generate Co(IV)-oxo units, the reactivity of **Co-L$_6$** in the oxygen reduction reaction was tested. The evaluation of the catalytic activity of **Co-L$_6$** towards oxygen reduction was carried out using Fukuzumi and Guilard's method; ferrocene derivatives were employed as one-electron donors, trifluoroacetic acid (TFA) or perchloric acid ($HClO_4$) were used as proton sources, and, in their presence, O_2 was set to react with a catalytic amount of **Co-L$_6$** in acetone. The occurrence of the oxygen reduction reaction was proved by the formation of ferrocenium ions with characteristic absorption bands (ferrocenium λ_{max}= 620 nm, ε_{620nm}= 430 $M^{-1}cm^{-1}$; dimethylferrocenium λ_{max}= 650 nm, ε_{650nm}= 360 M^{-1} cm^{-1}; decamethylferrocenium λ_{max}= 780 nm, ε_{780nm}= 520 $M^{-1}cm^{-1}$ in acetone).[54,58]

When employing Ferrocene (Fc) as a reductant (1.5 mM) in the presence of TFA (10 mM) and **Co-L$_6$** as a catalyst (0.02 mM) in an acetone solution saturated with O_2 (11 mM) at 25 °C, no oxygen reduction took place, as evidenced by the absence of ferrocenium ions in solution. Table 3.5 lists the oxidation potentials for some ferrocene derivatives. It may be noted that ferrocene is not the best reductant in the family, and therefore, better reductants such as dimethylferrocene (Me_2Fc) and decamethylferrocene ($Me_{10}Fc$) were also tested under similar conditions. When Me_2Fc was employed, no oxygen reduction took place either; however, when $Me_{10}Fc$, the strongest reductant listed, was used, the formation of decamethylferrocenium ions ($Me_{10}Fc^+$) could be detected and monitored by a rise in absorbance at 780 nm (Figure 3.19), which indicated that the oxidation of $Me_{10}Fc$ took place with the concomitant O_2 reduction in the presence of **Co-L$_6$** as a catalyst. Since $Me_{10}Fc$ is a good electron donor and is easily oxidized in the presence of acid, this reaction also occurs in the absence of **Co-L$_6$** but at a slower rate (*vide infra*); however, the non-catalytic oxidation was always taken into consideration in determining the catalytic capacity of the system.

Table 3.5: Oxidation potentials of different ferrocene derivatives referred against the saturated calomel electrode (SCE).[59]

Ferrocene derivative	**Fc**	**Me_2Fc**	**$Me_{10}Fc$**
E_{ox} vs SCE (V)	0.37	0.26	-0.08

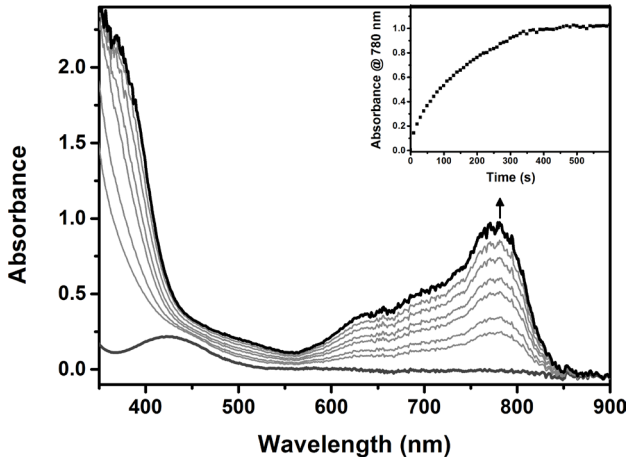

Figure 3.19: Spectral changes of the absorption during the reduction of oxygen by $Me_{10}Fc$ (1.5 mM) catalyzed by **Co-L_6** (0.02 mM) in the presence of TFA (10 mM) in O_2-saturated acetone at 25 °C. Inset: time trace of absorption at 780 nm due to the formation of $Me_{10}Fc^+$.

The dioxygen reduction reaction can occur as a two-electron reduction process, in which case H_2O_2 is liberated (Equation 1), or as a four-electron reduction process, in which the O−O bond is broken and H_2O is liberated (Equation 2); examples exist of catalysts that can selectively perform the two-electron[56,58,60,61] or the four-electron reduction.[52-55,57,62]

$$O_2 + 2\ Me_{10}Fc + 2\ H^+ \rightarrow 2\ Me_{10}Fc^+ + H_2O_2 \qquad (1)$$

$$O_2 + 4\ Me_{10}Fc + 4\ H^+ \rightarrow 4\ Me_{10}Fc^+ + 2\ H_2O \qquad (2)$$

In order to get an idea of the process occurring when **Co-L_6** is employed as a catalyst at 25 °C, O_2 was used as the limiting reagent. To 3 mL of a dry and oxygen-free acetone solution containing $Me_{10}Fc$ (3 mM), TFA (10 mM) and **Co-L_6** (0.02 mM), 0.05 mL of an oxygen saturated acetone solution were added (11 mM; final concentration 0.18 mM). The formation of $Me_{10}Fc^+$ ions was monitored (Figure 3.20, gray circles) until complete conversion of O_2 was achieved and the increase in the 780 nm band was no longer observed. The concentration of $Me_{10}Fc^+$ formed (0.34 mM), calculated with the reported value of $\varepsilon_{780nm} = 520\ M^{-1}cm^{-1}$ in acetone,[54] was found to be

around twice that of the O_2 concentration (0.18 mM) in the **Co-L$_6$** catalyzed reaction of O_2 at 25 °C; this indicated that in these conditions only two-electron oxygen reduction occurred (Equation 1).

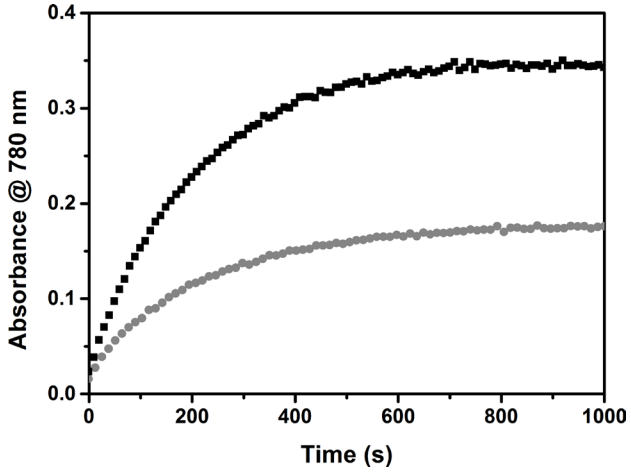

Figure 3.20: Time profiles of the formation of $Me_{10}Fc^+$ monitored at 780 nm during the electron-transfer oxidation reaction of $Me_{10}Fc$ (3 mM) with O_2 (0.18 mM) catalyzed by **Co-L$_6$** (0.04 mM) in the presence of TFA (10 mM) in acetone at 25 °C (gray circles) as well as at −50 °C (black squares).

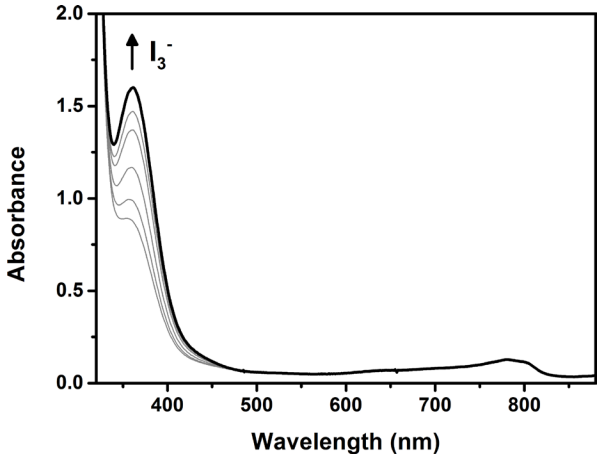

Figure 3.21: Spectral changes in the reaction of NaI (30 mM) and the 1:2 diluted reaction mixture of **Co-L$_6$** (0.04 mM), $Me_{10}Fc$ (3 mM), TFA (10 mM) and O_2 (0.18 mM) in acetone at 25 °C.

The formation of H_2O_2 from the two-electron reduction of oxygen was further corroborated by iodometric titrations. NaI reacts in the presence of H_2O_2 in acidic media to form the anion I_3^- (Equation 3).

$$3\ I^- + H_2O_2 + 2\ H^+ \rightarrow I_3^- + 2\ H_2O \qquad (3)$$

I_3^- displays strong absorbance at λ_{max}= 360 nm (ε_{360nm} = 28000 $M^{-1}cm^{-1}$)[61] and can be easily detected. A 1:2 dilution of the solution with the reduced product of the O_2 (0.18 mM) reduction catalyzed by **Co-L$_6$** was treated with sodium iodide (NaI). After a few seconds the band at 360 nm reached its maximum (Figure 3.21), indicating the presence of H_2O_2 in the reaction mixture. A 64 % yield of H_2O_2 (0.057 mM) was determined relative to the concentration of H_2O_2 (0.09 mM) expected if all the O_2 had been transformed to H_2O_2 in a two-electron process. The yield obtained is not quantitative, but lower yields have been observed before when iodometric titration is performed at 25 °C due to competition with the direct reduction of H_2O_2 with $Me_{10}Fc$ at this temperature.[56] However, these results do confirm that the process catalyzed by **Co-L$_6$** at 25 °C is the two-electron reduction of dioxygen to hydrogen peroxide.

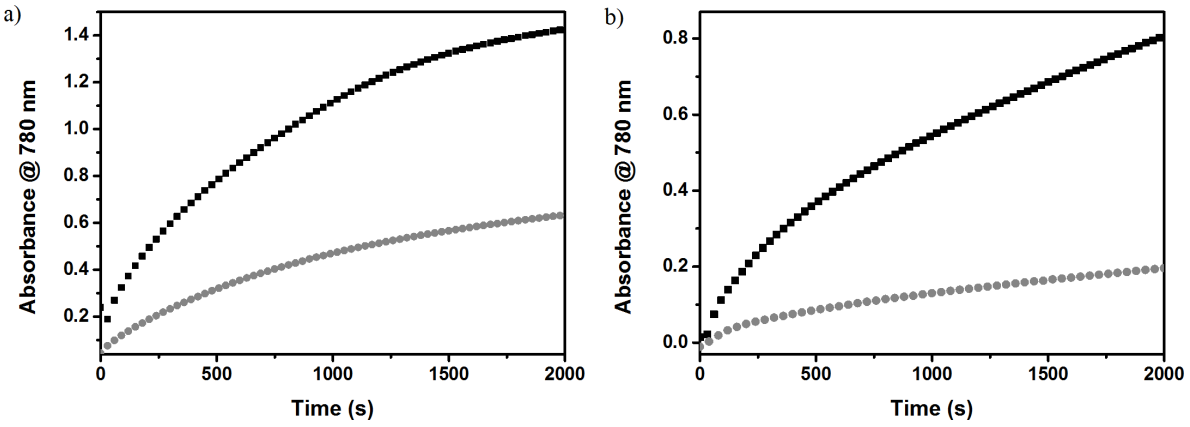

Figure 3.22: Time profiles of the formation of $Me_{10}Fc^+$ monitored at 780 nm during the oxidation reaction of a) $Me_{10}Fc$ (3 mM) with O_2 (saturated acetone solution, 11 mM) in the presence of TFA (10 mM) in acetone at 25 °C catalyzed by **Co-L$_6$** (0.05 mM) (black squares) and without a catalyst (gray circles). b) $Me_{10}Fc$ (3.75 mM) with O_2 (saturated acetone solution, 11 mM) in the presence of TFA (40 mM) in acetone at −50 °C catalyzed by **Co-L$_6$** (0.01 mM) (black squares) and without a catalyst (gray circles).

A turnover number (TON) of 16 during a lapse of 2000 seconds was determined for the catalyst **Co-L$_6$** in the reduction of O_2 to H_2O_2 in acetone at 25 °C. The TON was calculated from the moles of H_2O_2 that were the product of O_2 reduction (calculated from the moles of $Me_{10}Fc^+$ formed) divided by the initial moles of the catalyst **Co-L$_6$** from a reaction mixture containing **Co-L$_6$**, $Me_{10}Fc$ and TFA with concentrations of 0.05 mM, 3 mM and 10 mM respectively in 3 mL of O_2-saturated acetone (Figure 3.22 a, black squares). The control reaction performed in the absence of **Co-L$_6$** was also monitored (Figure 3.22 a, gray circles) and the amount of $Me_{10}Fc^+$ formed in this process was subtracted from that obtained in the catalytic reaction. Since the TONs are not frequently reported for related systems, making an assessment of the efficiency of the catalyst based on the obtained

number is not straightforward; for the two-electron reduction of O_2 to H_2O_2, the TONs of two different systems have been reported: TON = 7 for a mononuclear copper catalyst with $Me_{10}Fc$ as a reductant[55] and TON = 83,000 for cobalt chlorin derivatives as catalysts using Me_2Fc as a reductant.[61] With regard to these systems, it can only be stated that **Co-L$_6$** is a fair O_2-reduction catalyst at 25 °C.

Kinetic studies were performed in order to obtain more information about the mechanism by which **Co-L$_6$** reduces O_2 to H_2O_2 in acetone at 25 °C. The spectral changes observed at 25 °C due to the formation of $Me_{10}Fc^+$ during the course of the O_2 reduction reaction are shown in Figure 3.23 a; the initial rate of formation of $Me_{10}Fc^+$ obeys pseudo-first-order kinetics when [**Co-L$_6$**] << [$Me_{10}Fc$] < [TFA] (Figure 3.23 a). The pseudo-first-order rate constant (k_{obs}) increased linearly with an increasing concentration of **Co-L$_6$** (Figure 3.23 c). As previously discussed, it should be noted that under the experimental conditions employed, the oxidation of $Me_{10}Fc$ takes place in the presence of TFA even in the absence of a catalyst; hence, the linear plot of k_{obs} vs [**Co-L$_6$**] does not cross the "y" axis at 0 but the intercept has a positive value. The k_{obs} values were also found to be proportional to the concentration of $Me_{10}Fc$ (Figure 3.23 b and d), TFA (Figure 3.23 f) and O_2 (Figure 3.23 e).

The observed dependency of the reaction rate on the concentration of **Co-L$_6$**, $Me_{10}Fc$, O_2 and TFA is quite unique. Typically, Co and Cu catalysts for O_2 reduction show a rate that is independent of O_2 or H^+.[52,56,58] The rate's dependency on the four species has only been observed before for a dinuclear copper catalyst that performs the four-electron O_2 reduction reaction to H_2O.[62] Such dependency reveals that the rate-determining step in the catalytic cycle should involve the reactions of **Co-L$_6$** with $Me_{10}Fc$, O_2 and TFA. This indicates that the **Co-L$_6$**-catalyzed two-electron reduction to H_2O_2 at 25 °C proceeds in a rather complicated fashion and more detailed mechanistic studies are necessary. Unfortunately, since **Co-1** absorbs at the same wavelength as $Me_{10}Fc$, UV-vis mechanistic studies in this system proved unsuccessful.

It is known that factors such as temperature and acid source can alter the O_2 reaction pathways and mechanisms, so different conditions were tested for the catalytic reaction of **Co-L$_6$** with O_2.When 3 mL of a dry, oxygen-free acetone solution of $Me_{10}Fc$ (3 mM), TFA (10 mM) and **Co-L$_6$** as a catalyst (0.04 mM) were cooled down to −50 °C, and 0.05 mL of oxygen-saturated acetone (11 mM) were added (O_2 final concentration 0.18 mM), a different behavior was observed (Figure 3.20, black squares). This time, the amount of $Me_{10}Fc^+$ generated during the O_2 catalytic reduction was 0.67 mM, which represents 3.74 equivalents relative to the initial concentration of O_2 (0.18 mM). This clearly indicated that at −50 °C a four-electron reduction took place (Equation 2)

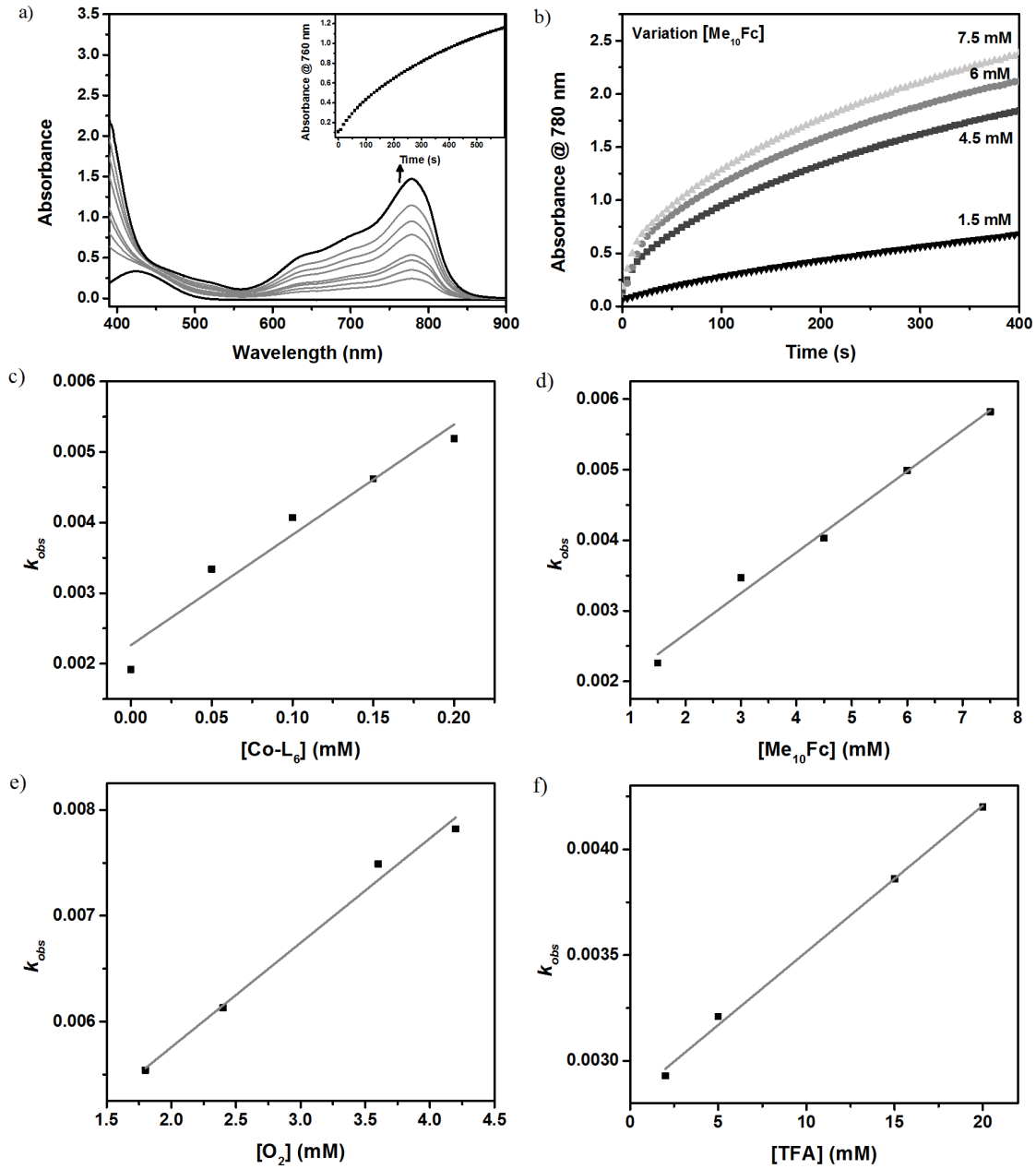

Figure 3.24: Studies on the two electron reduction of O_2 in acetone at 25 °C catalyzed by **Co-L$_6$**. a) Spectral changes due to the reduction of O_2 (11 mM) by $Me_{10}Fc$ (3 mM) catalyzed by **Co-L$_6$** (0.1 mM) in the presence of TFA (10 mM) Inset: absorption at 780 nm due to the formation of $Me_{10}Fc^+$. b) Time profiles of the absorbance at 780 nm for different initial concentrations of $Me_{10}Fc$. c) k_{obs} vs **Co-L$_6$** concentration for the reduction of O_2 (11 mM) with $Me_{10}Fc$ (3 mM) catalyzed by **Co-L$_6$** (0.05-0.2 mM) with TFA (10 mM). d) k_{obs} vs $Me_{10}Fc$ concentration for the reduction of O_2 (11 mM) with $Me_{10}Fc$ (1.5-7.5 mM) catalyzed by **Co-L$_6$** (0.1 mM) with TFA (10 mM). e) Plot of k_{obs} vs O_2 concentration for the reduction of O_2 (1.8-4.2 mM) with $Me_{10}Fc$ (3 mM) catalyzed by **Co-L$_6$** (0.1 mM) with TFA (10 mM). f) Plot of k_{obs} vs TFA concentration for the reduction of O_2 (11 mM) with $Me_{10}Fc$ (3 mM) catalyzed by **Co-L$_6$** (0.1 mM) with TFA (2-20 mM).

instead of the two-electron reduction that was observed at a higher temperature (Equation 1). The absence of H_2O_2 in solution was further corroborated with iodometric titrations.

Even though the two-electron reduction of O_2 to H_2O_2 has been targeted as a possible efficient process for obtaining hydrogen peroxide[58,61] and utilizing it as a sustainable and clean energy carrier[63–65] and an environmentally benign oxidant,[66,67] the possibility that **Co-L$_6$** may perform full O−O bond cleavage in contrast to **Fe-L$_6$**, which performs the opposite process, O−O bond formation, led us to further investigate the four-electron process of O_2 reduction catalyzed by **Co-L$_6$** at −50 °C to get a better understanding of the factors that control this process.

A turnover number (TON) of 65 during a lapse of 2000 seconds was determined for the catalyst **Co-L$_6$** in the reduction of O_2 to H_2O in acetone at −50 °C. The TON was calculated from the moles of H_2O that were the product of the O_2 reduction (calculated from the moles of $Me_{10}Fc^+$ formed) divided by the initial moles of the catalyst **Co-L$_6$** from a reaction mixture containing **Co-L$_6$**, $Me_{10}Fc$ and TFA with concentrations of 0.01 mM, 3.75 mM and 40 mM respectively, in 3 mL of O_2-saturated acetone (Figure 3.22 black squares). The control reaction performed in the absence of **Co-L$_6$** was also monitored (Figure 3.22 gray circles) and the amount of $Me_{10}Fc^+$ formed in this process was subtracted from that obtained in the catalyzed reaction. The TON (65) obtained for **Co-L$_6$** for the four-electron O_2 reduction reaction is at least 4 times higher than the TON (16) obtained for the two-electron reduction of O_2 catalyzed by **Co-L$_6$** at 25 °C in otherwise similar conditions. This indicated that **Co-L$_6$** is a much better catalyst for the four-electron reduction of O_2 to H_2O than it is for the two-electron process.

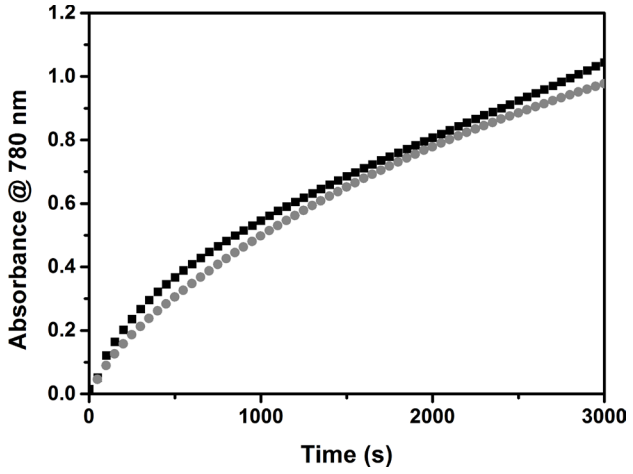

Figure 3.24: Time profile of the formation of $Me_{10}Fc^+$ monitored at 780 nm during the oxidation reaction of $Me_{10}Fc$ (3.75 mM) with O_2 (saturated acetone solution, 11 mM) catalyzed by **Co-L$_6$** (0.01 mM) in acetone at −50 °C in the presence of TFA (40 mM) (black squares) or $HClO_4$ (40 mM) (gray circles).

Besides the observed temperature effect, another factor that has been reported to affect the reduction of dioxygen is the acid employed as the proton source. In some studies it has been shown that a change in the acidity of the proton source employed, or in the nature of the acid, modulates the catalysis mechanism, even changing the process from a two-electron reduction to a four-electron one.[60,62] Other studies have found that the coordination capability of the acid counter-ion affects the rate of the oxygen reduction reaction.[68] For the reaction catalyzed by **Co-L$_6$** at −50 °C the acid employed was found to be unimportant; when using $HClO_4$ instead of TFA, the O_2 conversion rate after 3000 seconds remained unchanged (Figure 3.24).

Kinetic studies were also performed to obtain information about the mechanism by which **Co-L$_6$** reduces O_2 to H_2O in acetone at −50 °C. The spectral changes observed at −50 °C due to the formation of $Me_{10}Fc^+$ during the course of the O_2 reduction reaction are shown in Figure 3.25 a; the initial rate of formation of $Me_{10}Fc^+$ obeys pseudo-first-order kinetics when [**Co-L$_6$**] << [$Me_{10}Fc$] < [TFA] (Figure 3.25 a). The pseudo-first-order rate constant (k_{obs}) increased linearly with an increasing concentration of **Co-L$_6$** (Figure 3.25 c). Again, it should be noted that under the experimental conditions employed, the oxidation of $Me_{10}Fc$ takes place in the presence of TFA even in the absence of a catalyst; hence, the linear plot of k_{obs} vs [**Co-L$_6$**] does not cross the "y" axis at (x,y = 0,0) but the intercept has a positive value. The k_{obs} values were also found to be proportional to the concentration of $Me_{10}Fc$ (Figure 3.25 b and d) and TFA (Figure 3.25 f); however, they were not affected by the concentration of O_2 (Figure 3.25 e). The reaction rate's dependency on the concentration of **Co-L$_6$**, $Me_{10}Fc$ and TFA indicates that the rate determining step on the catalytic cycle should involve a reaction with the three of them participating.

It is likely that the catalytic cycle of the four-electron O_2 reduction by **Co-L$_6$** will start with the reaction of O_2 with the cobalt centers and the formation of the bridging-μ-peroxo-dicobalt(III) intermediate. This step should be a fast one since O_2 is not involved in the rate-determining step of the cycle. Unfortunately, since $Me_{10}Fc$ and **Co-1** absorb at very close wavelengths, it was not possible to monitor the formation of the intermediate in the reaction mixture during the course of the reaction. To investigate what occurs with **Co-1** in the next step of the cycle, its reactivity was tested towards TFA and $Me_{10}Fc$.

Co-1 was generated *in situ* in acetone at −50 °C and, after removal of the excess of O_2, one equivalent of $Me_{10}Fc$ per di-cobalt center was added to the reaction mixture. No reduction occurred as the band at 470 nm due to **Co-1** did not decrease**,** nor did the band at 780 nm rise due to $Me_{10}Fc^+$ formation. Similarly, upon addition of one equivalent of TFA per di-cobalt center to **Co-1** in the

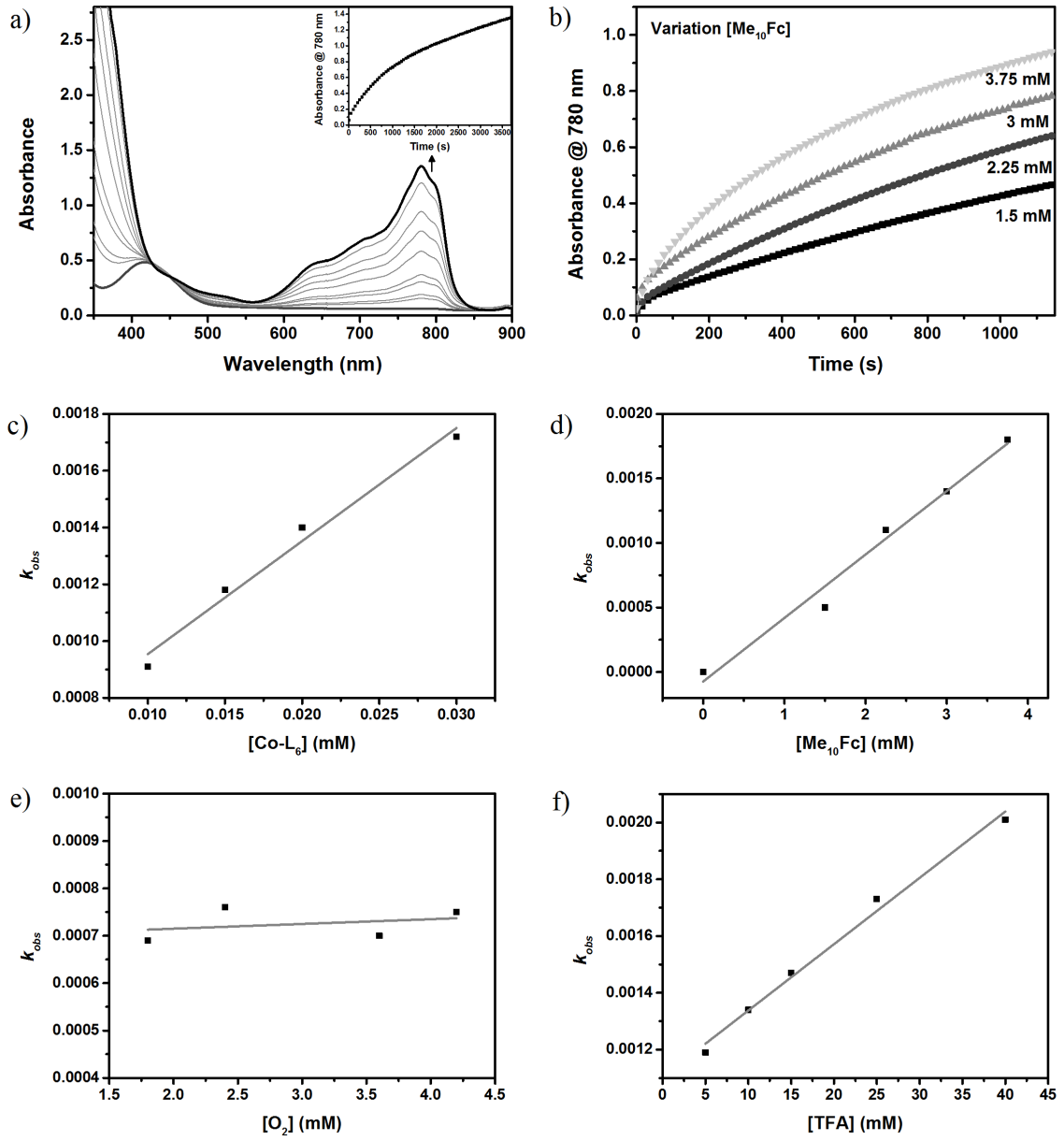

Figure 3.25: Studies on the four electron reduction of O_2 in acetone at −50 °C catalyzed by **Co-L$_6$**. a) Spectral changes due to the reduction of O_2 (11 mM) by $Me_{10}Fc$ (3 mM) catalyzed by **Co-L$_6$** (0.02 mM) in the presence of TFA (10 mM) Inset: absorption at 780 nm due to the formation of $Me_{10}Fc^+$. b) Time profiles of the absorbance at 780 nm for different initial concentrations of $Me_{10}Fc$. c) k_{obs} vs **Co-L$_6$** concentration for the reduction of O_2 (11 mM) with $Me_{10}Fc$ (3 mM) catalyzed by **Co-L$_6$** (0.01-0.03 mM) with TFA (10 mM). d) k_{obs} vs $Me_{10}Fc$ concentration for the reduction of O_2 (11 mM) with $Me_{10}Fc$ (1.5-4 mM) catalyzed by **Co-L$_6$** (0.02 mM) with TFA (10 mM). e) Plot of k_{obs} vs O_2 concentration for the reduction of O_2 (1.75-4.25 mM) with $Me_{10}Fc$ (3 mM) catalyzed by **Co-L$_6$** (0.02 mM) with TFA (10 mM). f) Plot of k_{obs} vs TFA concentration for the reduction of O_2 (11 mM) with $Me_{10}Fc$ (3 mM) catalyzed by **Co-L$_6$** (0.02 mM) with TFA (5-40 mM).

absence of O_2, the band at 470 nm did not decrease in intensity. However, when both $Me_{10}Fc$ and TFA (1 equivalent each per di-cobalt center) were added to the degassed acetone solution of **Co-1**, the band at 470 nm deceased with an increase in the band at 780 nm due to the formation of $Me_{10}Fc^+$. This proves that both species, the electron source and the proton source, are necessary in this step of the reaction and therefore a proton-coupled electron transfer (PCET) is likely.

Unfortunately, no further intermediates could be detected during the catalytic O_2 reduction, which makes the assignment of a mechanism difficult. However, with the information obtained, we can propose that the O_2-reduction catalytic cycle starts when oxygen binds to **Co-L$_6$** and the bridging-μ-peroxo-dicobalt(III) is formed. Subsequently, a proton-coupled electron transfer takes place, in what is probably the rate-determining step of the cycle. By making an analogy with the mechanism proposed for a similar system[52] this PCET should be followed by a subsequent one to generate the Co(III)-aqua complexes that are further reduced to cobalt(II) and liberate the H_2O molecules upon coordination of a new molecule of O_2 (Scheme 3.4). However, the precise assignation of a catalytic cycle is not possible with the information obtained from this system.

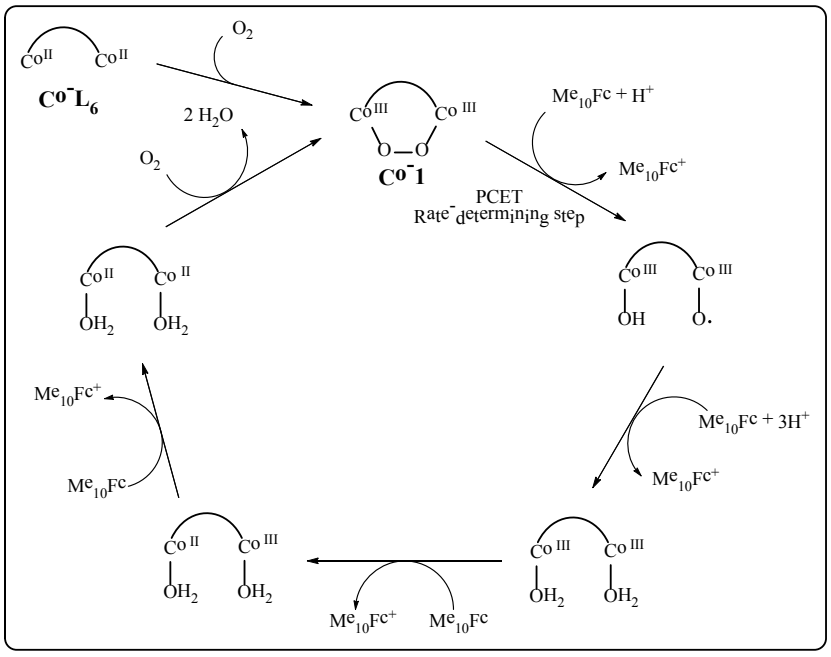

Scheme 3.4 Proposed catalytic cycle for the four-electron reduction of O_2 to H_2O by **Co-L$_6$** in dichloromethane at −50 °C by analogy with a previously reported mechanism.[52]

3.3 Conclusions

The reactivity of the hexanuclear cobalt complex **Co-L$_6$** and that of the bridging-μ-peroxo-dicobalt(III) intermediate in **Co-1** were tested. The bridging-μ-peroxo-dicobalt(III) species showed a typical nucleophilic character; however, it also proved to be capable of initiating electrophilic transformations. The electrophilic character of **Co-1** had previously been assigned to a potential oxocobalt(IV) complex; however, due to the small KIE values and the lack of ^{18}O-incoroporation to the oxidized products in the presence of $H_2{}^{18}O$ found in this work the electrophilic nature of **Co-1** could finally be assigned to the bridging-μ-peroxo-dicobalt(III) species.

Co-L$_6$ was found to be capable of catalytically reducing O_2 to H_2O_2 at 25 °C with a TON of 16 after 2000 s. Interestingly, at −50 °C, **Co-L$_6$** proved to be capable of catalyzing the four-electron reduction of O_2 to H_2O with a larger TON of 65 (also after 2000 s). The four-electron reduction of dioxygen to water proved to proceed through a rate-determining PCET step, but the complete mechanism could not be clarified. The reactivity of **Co-L$_6$** researched here is in sharp contrast with that observed for the analogous complex **Fe-L$_6$**, which proved to be capable of performing the opposite reaction, O−O bond formation, thus showing that changes in the metal centers in the same ligand structures can lead to reversed reactivity behaviors.

3.4 References

[1] F. Meyer, W. B. Tolman, *Inorg. Chem.* **2015**, *54*, 5039–5039.

[2] W. B. Tolman, Ed. , *Activation of Small Molecules*, Wiley-VCH Verlag GmbH & Co. KGaA, Weinheim, Germany, **2006**.

[3] K. M. Lancaster, M. Roemelt, P. Ettenhuber, Y. Hu, M. W. Ribbe, F. Neese, U. Bergmann, S. DeBeer, *Science,* **2011**, *334*, 974–977.

[4] A. Pomowski, W. G. Zumft, P. M. H. Kroneck, O. Einsle, *Nature* **2011**, *477*, 234–237.

[5] J. C. Fontecilla-Camps, A. Volbeda, C. Cavazza, Y. Nicolet, *Chem. Rev.* **2007**, *107*, 4273–4303.

[6] D. Schilter, J. M. Camara, M. T. Huynh, S. Hammes-Schiffer, T. B. Rauchfuss, *Chem. Rev.* **2016**, DOI: acs.chemrev.6b00180.

[7] L. Carrette, A. Friedrich, U. Stimming, *Fuel Cells* **2001**, *1*, 5–39.

[8] A. Boudghene Stambouli, E. Traversa, *Renew. Sustain. Energy Rev.* **2002**, *6*, 297–306.

[9] N. S. Lewis, D. G. Nocera, *Proc. Natl. Acad. Sci.* **2007**, *104*, 15729–15735.

[10] Y. Umena, K. Kawakami, J.-R. Shen, N. Kamiya, *Nature* **2011**, *473*, 55–60.

[11] N. Cox, M. Retegan, F. Neese, D. a. Pantazis, A. Boussac, W. Lubitz, *Science,* **2014**, *345*, 804–808.

[12] E. I. Solomon, P. Chen, M. Metz, S.-K. Lee, A. E. Palmer, *Angew. Chem. Int. Ed.* **2001**, *40*, 4570–4590.

[13] T. Tsukihara, H. Aoyama, E. Yamashita, T. Tomizaki, H. Yamaguchi, K. Shinzawa-Itoh, R. Nakashima, R. Yaono, S. Yoshikawa, *Science* **1995**, *269*, 1069–1074.

[14] C. F. Blanford, R. S. Heath, F. a Armstrong, *Chem. Commun.*. **2007**, 1710–1712.

[15] J. Klingele, S. Dechert, F. Meyer, *Coord. Chem. Rev.* **2009**, *253*, 2698–2741.

[16] A. L. Gavrilova, B. Bosnich, *Chem. Rev.* **2004**, *104*, 349–383.

[17] A. McAuley, S. Subramanian, *Coord. Chem. Rev.* **2000**, *200–202*, 75–103.

[18] V. Balzani, A. Juris, M. Venturi, S. Campagna, S. Serroni, *Chem. Rev.* **1996**, *96*, 759–834.

[19] J. W. J. Knapen, A. W. van der Made, J. C. de Wilde, A. W. van Leeuwen, P. Wijkens, D. M. Grove, G. van Koten, *Nature* **1994**, *372*, 659–663.

[20] H. P. Dijkstra, P. Steenwinkel, D. M. Grove, M. Lutz, A. L. Spek, G. Van Koten, *Angew. Chem. Int. Ed.* **1999**, *38*, 2185–2188.

[21] V. Chandrasekhar, S. Nagendran, R. Azhakar, M. R. Kumar, A. Srinivasan, K. Ray, T. K. Chandrashekar, C. Madhavaiah, S. Verma, U. D. Priyakumar, G. N. Sastri, *J. Am. Chem. Soc.* **2005**, *127*, 2410–2411.

[22] S. Kundu, E. Matito, S. Walleck, F. F. Pfaff, F. Heims, B. Rábay, J. M. Luis, A. Company, B. Braun, T. Glaser, K. Ray., *Chem.- Eur. J.* **2012**, *18*, 2787–91.

[23] W. C. Ellis, N. D. McDaniel, S. Bernhard, T. J. Collins, *J. Am. Chem. Soc.* **2010**, *132*, 10990–10991.

[24] J. L. Fillol, Z. Codolà, I. Garcia-Bosch, L. Gómez, J. J. Pla, M. Costas, *Nat. Chem.* **2011**, *3*, 807–13.

[25] S. Kundu, *PhD Thesis: Synthesis, Spectroscopic Characterization and Reactivity of the High-Valent Metal-Oxo/Imido Cores of the Late Transition Metals*, Humboldt-Universität Zu Berlin, Berlin, **2013**.

[26] E. Askarizadeh, S. B. Yaghoob, D. M. Boghaei, A. M. Z. Slawin, J. B. Love, *Chem. Commun.* **2010**, *46*, 710–712.

[27] G. Givaja, M. Volpe, M. A. Edwards, A. J. Blake, C. Wilson, M. Schröder, J. B. Love, *Angew. Chem. Int. Ed.* **2007**, *46*, 584–586.

[28] T. Tanase, T. Onaka, M. Nakagoshi, I. Kinoshita, K. Shibata, M. Doe, J. Fujii, S. Yano, *Chem. Commun.* **1997**, 2115–2116.

[29] J. Cho, R. Sarangi, H. Y. Kang, J. Y. Lee, M. Kubo, T. Ogura, E. I. Solomon, W. Nam, *J. Am. Chem. Soc.* **2010**, *132*, 16977–16986.

[30] J. Cho, R. Sarangi, W. Nam, *Acc. Chem. Res.* **2012**, *45*, 1321–1330.

[31] X. Hu, I. Castro-Rodriguez, K. Meyer, *J. Am. Chem. Soc.* **2004**, *126*, 13464–13473.

[32] R. Boča, *Coord. Chem. Rev.* **2004**, *248*, 757–815.

[33] C. Benelli, D. Gatteschi, *Inorg. Chem.* **1982**, *21*, 1788–1790.

[34] K. Fukui, H. Ohya-Nishiguchi, N. Hirota, K. Aoyagi, H. Ogoshi, *Chem. Phys. Lett.* **1987**, *140*, 15–19.

[35] B. Meunier, Ed. , *Structure and Bonding 97: Metal-Oxo and Metal-Peroxo Species*, Springer, Berlin, Germany, **2000**.

[36] M. Costas, M. P. Mehn, M. P. Jensen, L. Que Jr., *Chem. Rev.* **2004**, *104*, 939–986.

[37] S. P. de Visser, J. U. Rohde, Y. M. Lee, J. Cho, W. Nam, *Coord. Chem. Rev.* **2013**, *257*, 381–393.

[38] Y. Jo, J. Annaraj, M. S. Seo, Y. M. Lee, S. Y. Kim, J. Cho, W. Nam, *J. Inorg. Biochem.* **2008**, *102*, 2155–2159.

[39] Y.-R. Luo, *Comprehensive Handbook of Chemical Bond Energies*, CRC Press, Boca Raton, Florida, **2007**.

[40] S. Hong, F. F. Pfaff, E. Kwon, Y. Wang, M. S. Seo, E. Bill, K. Ray, W. Nam, *Angew. Chem. Int. Ed.* **2014**, *53*, 10403–10407.

[41] K. Gunay, A.; Theopold, *Chem. Rev.* **2010**, 1060–1081.

[42] X. Engelmann, I. Monte-Pérez, K. Ray, *Angew. Chem. Int. Ed.* **2016**, *55*, 7632–7649.

[43] K. Ray, F. Felix, B. Wang, W. Nam, *J. Am. Chem. Soc.* **2014**, *136*, 13942–13958.

[44] W. Nam, Y.-M. Lee, S. Fukuzumi, *Acc. Chem. Res.* **2014**, *47*, 1146–1154.

[45] M. S. Seo, J.-H. In, S. O. Kim, N. Y. Oh, J. Hong, J. Kim, L. Que, W. Nam, *Angew. Chem. Int. Ed.* **2004**, *43*, 2417–2420.

[46] I. Prat, A. Company, V. Postils, X. Ribas, L. Que, J. M. Luis, M. Costas, *Chemistry* **2013**, 6724–6738.

[47] K. Ray, F. Heims, M. Schwalbe, W. Nam, *Curr. Opin. Chem. Biol.* **2015**, *25*, 159–171.

[48] B. C. H. Steele, A. Heinzel, *Nature* **2001**, *414*, 345–352.

[49] D. K. Dogutan, S. A. Stoian, R. McGuire, M. Schwalbe, T. S. Teets, D. G. Nocera, *J. Am. Chem. Soc.* **2011**, *133*, 131–140.

[50] J. Rosenthal, D. G. Nocera, *Acc. Chem. Res.* **2007**, *40*, 543–553.

[51] F. C. Anson, C. N. Shi, B. Steiger, *Acc. Chem. Res.* **1997**, *30*, 437–444.

[52] S. Fukuzumi, S. Mandal, K. Mase, K. Ohkubo, H. Park, J. Benet-buchholz, W. Nam, A. Llobet, *J. Am. Chem. Soc.* **2012**, *134*, 9906–9909.

[53] S. Fukuzumi, K. Okamoto, C. P. Gros, R. Guilard, *J. Am. Chem. Soc.* **2004**, *126*, 10441–10449.

[54] Z. Halime, H. Kotani, Y. Li, S. Fukuzumi, K. D. Karlin, *Proc. Natl. Acad. Sci.* **2011**, *108*, 1399–13994.

[55] S. Fukuzumi, H. Kotani, H. R. Lucas, K. Doi, T. Suenobu, R. L. Peterson, K. D. Karlin, *J. Am. Chem. Soc.* **2010**, *132*, 6874–6875.

[56] S. Fukuzumi, L. Tahsini, Y. Lee, K. Ohkubo, W. Nam, *J. Am. Chem. Soc.* **2012**, *134*, 7025–7035.

[57] L. Tahsini, H. Kotani, Y.-M. Lee, J. Cho, W. Nam, K. D. Karlin, S. Fukuzumi, *Chemistry* **2012**, *18*, 1084–93.

[58] D. Das, Y.-M. Lee, K. Ohkubo, W. Nam, K. D. Karlin, S. Fukuzumi, *J. Am. Chem. Soc.* **2013**, *135*, 2825–2834.

[59] S. Fukuzumi, H. Kotani, K. A. Prokop, D. P. Goldberg, *J. Am. Chem. Soc.* **2011**, *133*, 1859–1869.

[60] S. Kakuda, C. J. Rolle, K. Ohkubo, M. A. Siegler, K. D. Karlin, S. Fukuzumi, *J. Am. Chem. Soc.* **2015**, *137*, 3330–3337.

[61] K. Mase, K. Ohkubo, S. Fukuzumi, *Inorg. Chem.* **2015**, *54*, 1808–1815.

[62] D. Das, Y.-M. Lee, K. Ohkubo, W. Nam, K. D. Karlin, S. Fukuzumi, *J. Am. Chem. Soc.* **2013**, *135*, 4018–4026.

[63] R. S. Disselkamp, *Energy & Fuels* **2008**, *22*, 2771–2774.

[64] R. S. Disselkamp, *Int. J. Hydrogen Energy* **2010**, *35*, 1049–1053.

[65] S. Fukuzumi, Y. Yamada, K. D. Karlin, *Electrochim. Acta* **2012**, *82*, 493–511.

[66] S. Abrantes, E. Amaral, A. P. Costa, A. A. Shatalov, A. P. Duarte, *Ind. Crops Prod.* **2007**, *25*, 288–293.

[67] S. H. Zeronian, M. K. Inglesby, *Cellulose* **1995**, *2*, 265–272.

[68] S. Kakuda, R. L. Peterson, K. Ohkubo, K. D. Karlin, S. Fukuzumi, *J. Am. Chem. Soc.* **2013**, *135*, 6513–6522.

Chapter 4:

Systematic Studies involving the Trapping and Characterization of Elusive Copper-Nitrenes Using Different Nitrene-Sources and Lewis Acids

Part of this work has been published in:

I. Monte-Pérez, S. Kundu, K. Ray*, *Zeitschrift für Anorg. und Allg. Chemie* **2015**, *641*, 78–82

S.-L. Abram,‡ I. Monte-Pérez,‡ F. F. Pfaff, E. R. Farquhar, K. Ray*, *Chem. Commun.* **2014**, *50*, 9852–4

‡ Equal contribution of the two authors

Compounds discussed in Chapter 4

Nitrene Source	Copper-nitrene as Lewis-acid adduct	Copper-nitrene as free species
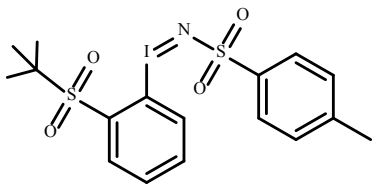	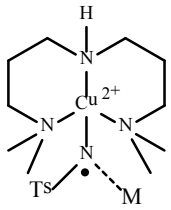	
sPhINTs	**Cu-1-M**	
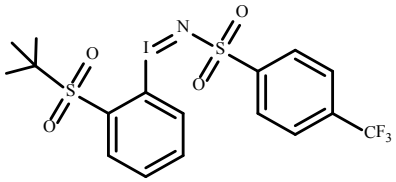	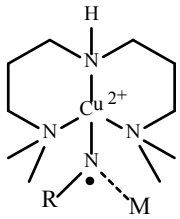 R = -SO_2-Ph^{CF3}	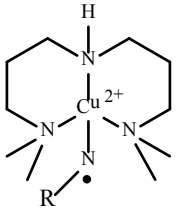 R = -SO_2-Ph^{CF3}
$sPhINAr^{CF3}$	**Cu-2-M**	**Cu-2**
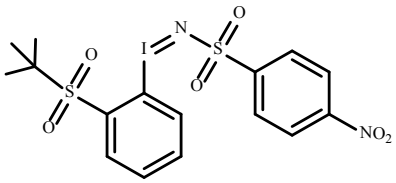	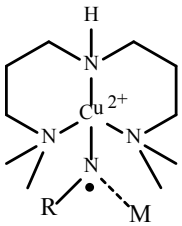 R = -SO_2-Ph^{NO2}	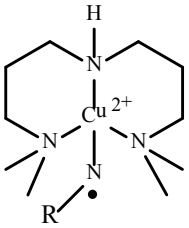 R = -SO_2-Ph^{NO2}
$sPhINAr^{NO2}$	**Cu-3-M**	**Cu-3**
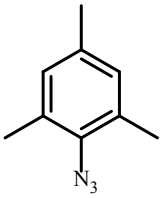	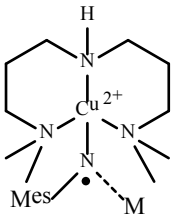	
Mes-N_3	**Cu-4-M**	

4.1. Introduction

Carbon-nitrogen bonds are ubiquitous in biologically active molecules, natural products, pharmaceuticals and agrochemicals.[1,2] Consequently, the formation of C−N bonds is a crucial chemical target and the reactions of alkane amination and aziridination are key synthetic processes. The use of transition metals has proved to be a convenient and atom-efficient way of catalyzing the activation of C−H bonds in hydrocarbons to produce the more valuable C−N bond containing analogs.[3-5] In particular, the use of catalysts based on inexpensive and biologically innocuous transition metals such as copper has experienced an explosive growth since the late 1960s, when Kwart and Khan reported the first copper-catalyzed C−H bond amination and aziridination reactions.[6,7]

A general scheme of the nitrene-based C−H bond amination and aziridination reactions catalyzed by copper is presented in Scheme 4.1; in these reactions, a nitrene source in the form of an organic azide, an iminoiodinane or chloramine-T is required and copper is employed as a catalyst in a wide variety of forms: metallic copper, simple copper salts or copper complexes,[7] the copper(I) complexes being the most effective catalysts for these processes.

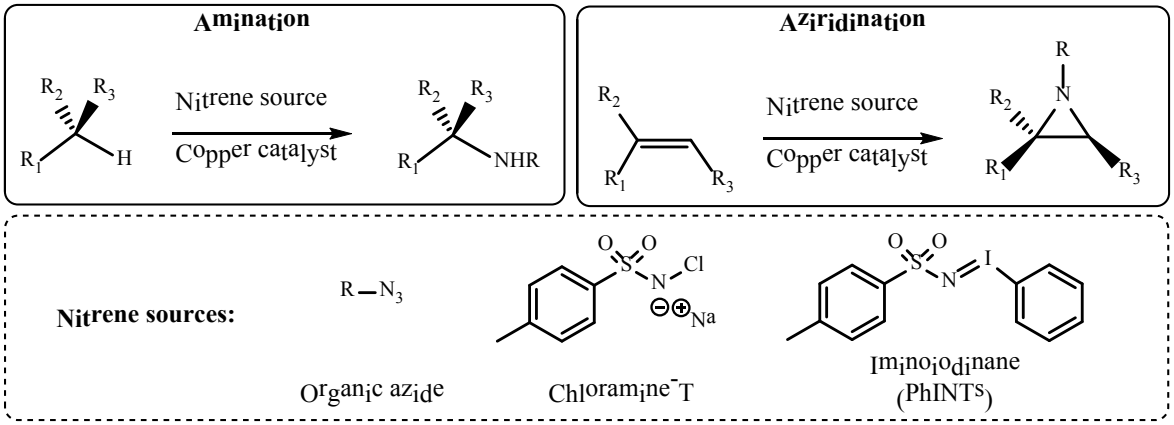

Scheme 4.1: General copper-catalyzed amination and aziridination reactions.

Since the very first report of copper-catalyzed nitrene-based C−H bond functionalization, it has been suggested that the active species in these reactions is a terminal copper-nitrene species. The first experiment performed to reveal the intermediacy of such species was done by Jacobsen et al. in 1995. They used a chiral diamine ligand (L^1) together with $CuPF_6$ and a nitrene source to aziridinate styrene and obtained an identical enantiomeric excess (ee) despite the nitrene source employed (Scheme 4.2 a), which showed the presence of an identical terminal copper-nitrene intermediate in both reactions; however, this species could not be isolated.[8] The next indirect

observation of a copper-nitrene intermediate was reported in 2004 by Vedernikov and Caulton. They were able to stabilize a purple diamagnetic species as a product of the addition of PhINTs to their copper(I) catalyst (L^2Cu^+); the ESI-MS of this species showed the presence of the ions $[(L^2Cu)\text{-}NHTs]^+$ and $[(L^2Cu)_2(NTs)]^{2+}$ (Scheme 4.2 b), the first of which they assigned to the intermediate $[(L^2Cu^{II})\text{-}N^{\bullet}Ts]^+$, which had performed a H-atom abstraction from the solvent, and the second was assigned to the trapping of the same intermediate by a second molecule of $[L^2Cu^+]$.[9]

In the search for the terminal copper-nitrene intermediate, and inspired by the successful generation of terminal cobalt-[10] and nickel-[11] nitrene complexes isolated by employing β-diketiminate ligands, Warren et al. studied the reaction of copper(I) β-diketiminate complexes $[(L^3Cu)_2(\mu\text{-}Ar)]$ with organic azides. Even though they did not manage to stabilize a terminal copper-nitrene, they crystalized the purple and green dicopper-nitrenes $[(L^3Cu)_2(\mu\text{-}N(3,5\text{-}Me_2C_6H_3))]$[12] and $[(L^3Cu)_2(\mu\text{-}N(Ad))]$[13] (Ad = adamantine) by employing 3,5-dimethylbenzeneazide and 1-adamantylazide (N_3Ad) respectively (Scheme 4.2 c). They also provided evidence of the presence of the terminal copper-nitrene species in solution by testing the exchange reactions of $[(L^3Cu)_2(\mu\text{-}N(3,5\text{-}Me_2C_6H_3))]$ with anilidoimine complexes, and obtaining a mixture of unsymmetrical binuclear species. In addition, by using a chlorinated β-diketiminate copper(I) complex as a catalyst (5 % mol) and the azide N_3Ad as a nitrene transfer agent, Warren et al. managed to perform a catalytic nitrene transfer at 110 °C to ethylbenzene and cyclohexane. However, despite all their success, no terminal copper-nitrene could be isolated.

In 2014, Bertrand, Frenking and coworkers reported the structural characterization of a copper-*bis*-nitrene complex.[14] By employing the self-designed phosphinonitrene as a nitrene source and mixing it with Cu(OTf) in the right proportions, they obtained crystals of both the bridging and the bis-nitrene copper complexes (Scheme 4.2 d). However, terminal copper nitrenes could not be isolated in these reactions either.

More recently, in 2016, Ribas, Ray, Company et al. were the first to report the synthesis and spectroscopic characterization of a terminal copper(II)–nitrene radical species that is stable at room temperature in the absence of any Lewis acid,[15] by employing azide derivatives of triazamacrocyclic ligands (Scheme 4.2 e). This species underwent nitrogen transfer reactions to organic substrates and was capable of abstracting hydrogen atoms from weak C−H bonds. This study is hailed as a landmark in the field for being the first time a terminal copper-nitrene could be stabilized, and furthermore, at room temperature.

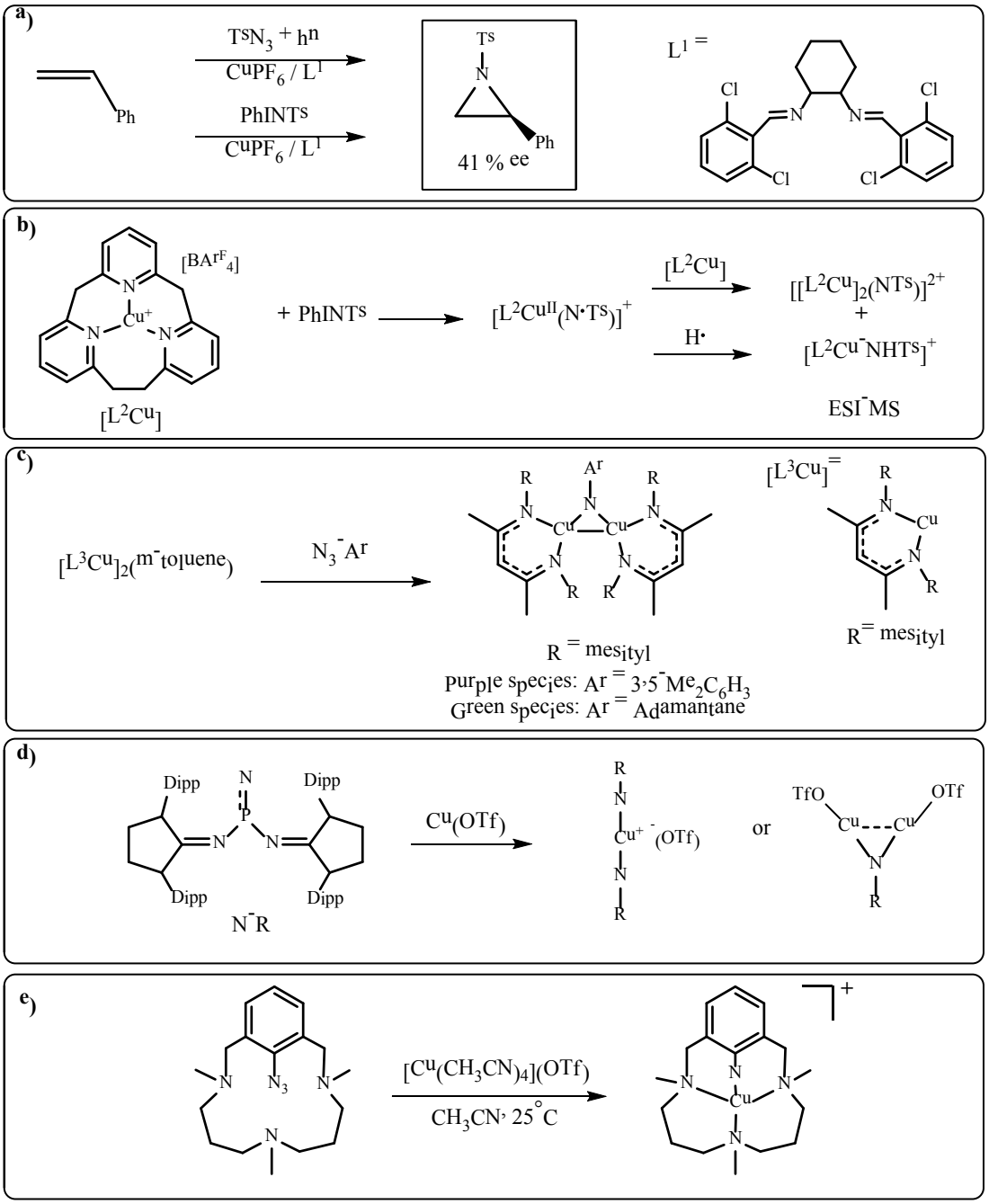

Scheme 4.2: Advances towards the comprehension of terminal copper-nitrene intermediates.

The full characterization and reactivity testing of terminal copper-nitrene species is essential for improving the design of further catalysts and processes as well as for obtaining a better understanding of the reaction mechanisms associated with the copper-catalyzed amination and aziridination reactions. Previously, in the absence of isolated examples of the proposed active species, quantum chemical calculations have been performed to elucidate the mechanisms of the copper-nitrene-mediated aziridination and amination reactions.[16–21]

Two alternative valence-bond structures for the terminal copper-nitrene have been characterized in these high-level calculations, namely a copper(III)-imido $[Cu^{III}(NR)]^+$ and a copper(II)-imidyl radical $[Cu^{II}(NR^{\bullet})]^+$, alongside their three possible spin states: closed-shell singlet $[Cu^{III}(NR)]^+$ (S = 0), open-shell singlet $[Cu^{II}(NR^{\bullet})]^+$ (S = 0) and open-shell triplet $[Cu^{II}(NR^{\bullet})]^+$ (S = 1) (Figure 4.1). Several theoretical studies on the mechanisms of aziridination and amination reactions concerning these three possible electronic states suggest that concerted aziridination reactions are favored on the closed-shell singlet surface,[16,18] while amination reactions proceed via a stepwise H-atom abstraction/radical rebound pathway, preferably on the open-shell triplet state.[20] In other studies, a mechanism involving both singlet and triplet states lying close in energy has been proposed for both amination[20] and aziridination[21] reactions. However, these theoretically predicted reactivity patterns lack the necessary experimental information such as the proper isolation and characterization of the active species, which would allow full electronic characterization and reactivity testing.

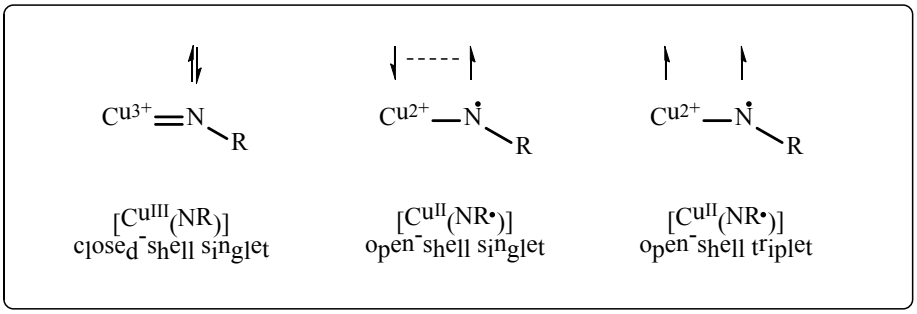

Figure 4.1: Three possible electronic configurations of copper-nitrenes.

In 2012, our group reported the trapping and characterization of the scandium adduct of a terminal copper-tosylnitrene species $[(AN)Cu^{II}(NTs^{\bullet})Sc(OTf)_3]^+$ (**Cu-1-Sc**) (Ts = tosyl) formed by the addition of the soluble substituted iminoiodinane sPhINTs (2-(tert-butylsulfonyl)(*p*-toluensulfonylimidoiodo)benzene) to the copper(I) complex $[(AN)Cu][BF_4]$ (AN = 3,3'-iminobis(*N,N*-dimethylpropylamine)) in the presence of an external Lewis acid such as $Sc(OTf)_3$ at −90 °C (Scheme 4.3).[22] This was the first time that a terminal copper-nitrene could be observed and spectroscopically characterized and its reactivity was researched in detail, albeit in the form of its scandium adduct.

The electronic structure of **Cu-1-Sc** was described as a Cu(II) core that is antiferromagnetically coupled to a nitrene radical $[Cu^{II}(NTs^{\bullet})]^+$ and its ground state was found to be an open-shell singlet. Reactivity studies were also performed and **Cu-1-Sc** was found to be capable of aminating sp^3 C−H bonds of substrates like toluene and cyclohexane by employing a hydrogen

atom transfer (HAT) mechanism, and it was also able to perform aziridination of cyclohexene and nitrene transfer to triphenylphosphine.[22]

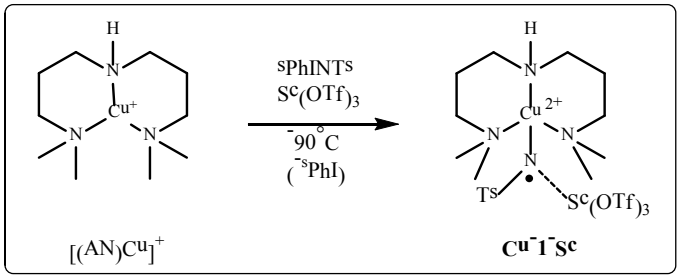

Scheme 4.3: Formation of the scandium adduct of a copper-tosylnitrene $[(AN)Cu^{II}(NTs^{\bullet})Sc(OTf)_3]^+$ (**Cu-1-Sc**) intermediate.

Despite the enormous success represented by the stabilization of **Cu-1-Sc**, some topics have yet to be researched. Firstly, the effect of the Lewis acid in the stabilized adduct has to be clarified; secondly, a variation of the nitrene in the copper-nitrene adduct is necessary to systematically show the effect of the nitrene source in the reactivity of such intermediates; and thirdly, the isolation of a terminal copper-nitrene from this family of complexes in the absence of any Lewis acid remains an important goal in fully understanding these systems. This chapter will discuss the advances in these three topics related to the chemistry of copper-nitrene.

4.2. Results and Discussion

4.2.1 Variation of the Lewis acid bound to the copper-tosylnitrene intermediate

In order to understand the effect of the Lewis acid attached to the terminal copper-tosylnitrene, the methodology of using $Sc(OTf)_3$ to trap the elusive intermediate **Cu-1-Sc** was extended to other redox-innocent metal ions (**M**). A series of $[(AN)Cu^{II}\text{-}(NTs^{\bullet})M]^{n+}$ (**Cu-1-M**) complexes were then synthesized varying the Lewis acidity of the external metal ions. The stability, spectroscopic properties and reactivity of this series of **Cu-1-M** complexes were further studied.

As reported in 2012, the complex **Cu-1-Sc** was obtained as an intense purple species from the reaction of $[(AN)Cu](BF_4)$ with the oxidant sPhINTs in the presence of $Sc(OTf)_3$ at −90 °C in dichloromethane under inert conditions (Figure 4.2 a). This species presented two intense absorption bands at λ_{max} (ε_{max}) = 530 nm (3500 L mol^{-1} cm^{-1}) and 750 nm (580 L mol^{-1} cm^{-1}) (Figure 4.2 c). Notably, in the absence of $Sc(OTf)_3$, the formal copper(III) oxidation state was not accessible and the reaction instead yielded a copper(II)-tosylamide complex (**Cu-1**) that was proposed to be the product of fast hydrogen-atom abstraction by the transient copper-nitrene intermediate

(Figure 4.2 a). The EPR spectra of species **Cu-1** and **Cu-1-Sc** were contrasting: while **Cu-1-Sc** was EPR-silent, complex **Cu-1** showed a slightly rhombic signal in X-band EPR with g-values (g_x = 2.09, g_y = 2.07 and g_z = 2.27) and hyperfine constants (A_x = 54 x 10^{-4} cm^{-1}; A_y = 15 x 10^{-4} cm^{-1}; A_z = 128 x 10^{-4} cm^{-1}) consistent with a $d_{x^2-y^2}$ ground state of the central copper(II) ions (Figure 4.2 b).[22]

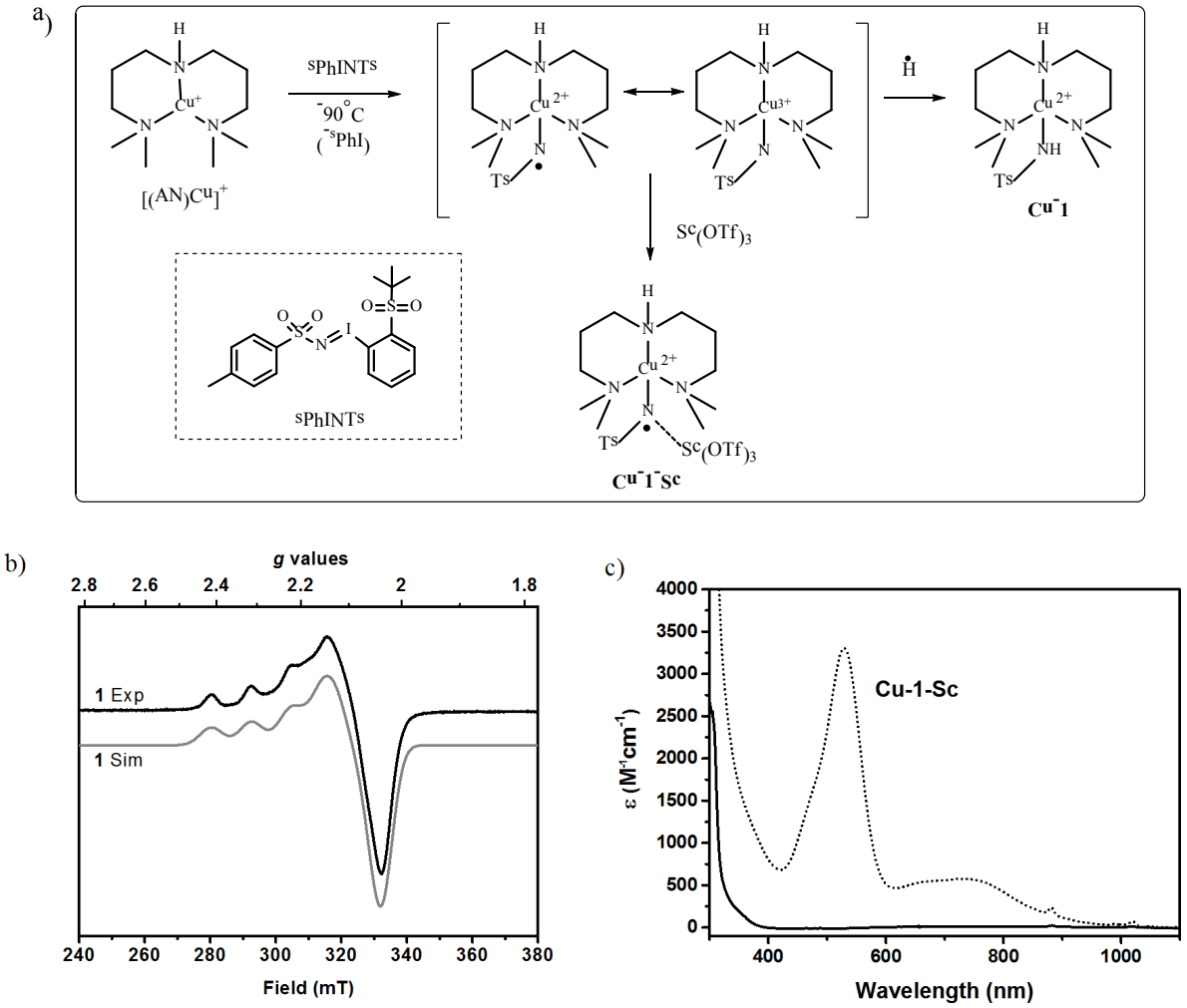

Figure 4.2: a) Scheme depicting the formation of **Cu-1** and **Cu-1-Sc**. b) Experimental (black line) and simulation (grey line) X-band EPR spectrum of **Cu-1** in CH_2Cl_2 (Temp. 10 K; Frequency 9.4347; Power 0.05 mW) c) Absorption spectra of the starting complex [(AN)Cu](BF_4) (black line) and **Cu-1-Sc** (dotted line) at −90 °C in CH_2Cl_2.

With the aim of understanding the role of the Lewis acid in the trapping of the copper-nitrene intermediate, different redox-innocent metal ions (**M**) were employed in substitution of scandium. The reactions between [(AN)Cu](BF_4) and sPhINTs at −90 °C in dry dichloromethane in the presence of the triflate salts of yttrium (Y(III)), europium (Eu(III)), cerium (Ce(III)), zinc

(Zn(II)) and calcium (Ca(II)) were then monitored. The formation of **Cu-1-M** was confirmed on the basis of the characteristic absorption features at 530 and 750 nm (Figure 4.3) and the presence of the decay product **Cu-1** was also tested by EPR spectroscopy for each solution.

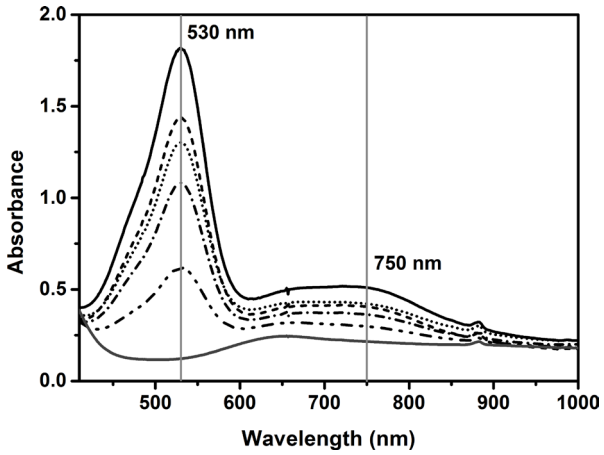

Figure 4.3: Absorption spectra of **Cu-1-M** obtained from an initial 0.5 mM [(AN)Cu](BF$_4$) solution in CH_2Cl_2 at −90 °C after addition of the **M**(OTf)$_n$ salt and sPhINTS where **M** = Sc(III) (black solid line), Y(III) (dashed line), Eu(III) (dotted line), Ce(III) (dash-dot line), Zn(II) (dash-dot-dot line), and Ca(II) (gray solid line).

It is interesting to observe that the position of the bands at 530 and 750 nm proved to be independent of the nature of the Lewis acid employed. This indicated that the redox-innocent metal ions do not affect the electronic transitions associated with the copper-nitrene unit in **Cu-1-M**. However, it is also evident that the maximum absorbance of the bands differed significantly from one **M** to another. This could have two possible explanations: it could mean that the molar extinction coefficient (ε) is different for each **Cu-1-M**, or that the yield of the formed **Cu-1-M** depends on the Lewis acid employed. In order to distinguish between these two cases, the yields of formation of **Cu-1-M** were evaluated.

The yield of **Cu-1-M** was determined from the chemical reduction of this species in the presence of a one-electron reductant like ferrocene (Fc). **Cu-1-M** performed a two-electron reduction process with Fc at −90 °C, generating a copper(I) species and two ferrocenium cations (Fc^+) with a characteristic UV-vis absorption (ε = 505 M^{-1} cm^{-1} at 620 nm in CH_2Cl_2). The reaction monitored by UV-vis showed the decay of the **Cu-1-M** species and the simultaneous formation of Fc^+ in solution, which was quantified and its yield was used to determine the amount of formal copper(III) present in solution. On the other hand, the yields of **Cu-1** were obtained by spin quantification of the copper(II) EPR signal corresponding to **Cu-1**. The obtained yields for **Cu-1-M** and **Cu-1** are presented in Table 4.1.

Table 4.1: Yields of **Cu-1-M** and **Cu-1** in the presence of different Lewis acids (1.5 equivalents) independently determined on the base of UV-vis (**Cu-1-M**) and EPR (**Cu-1**).

M	Cu-1-M yield (%)	Cu-1 yield (%)
$Sc(OTf)_3$	> 90	5
$Y(OTf)_3$	70	23
$Eu(OTf)_3$	65	33
$Ce(OTf)_3$	58	45
$Zn(OTf)_2$	28	70
$Ca(OTf)_2$	0	95

The differences in the maximum absorption observed when employing different **M**s (Figure 4.3) are clearly due to different yields of the copper-nitrene adduct **Cu-1-M** (Table 4.1). This, in turn, is inversely correlated to the yield of **Cu-1** obtained in each case. The reaction, thus, yields a mixture of the two species: the formal copper(III) purple intermediate **Cu-1-M** and the decay product copper(II)-tosylamide **Cu-1**. The proportions of each species are dependent on the **M** employed. While the $Sc(OTf)_3$ allowed an almost complete conversion to the **Cu-1-Sc** adduct, the $Ca(OTf)_2$ could not stabilize the intermediate and only led to the decay product **Cu-1**. From this analysis it is clear that, while the Lewis acidic metal ions do not alter the electronic transitions of the copper nitrene, they do play a vital role on the stability of the **Cu-1-M** adducts.

The increasing yield of the purple species **Cu-1-M** and the decreasing yield of the corresponding decay product **Cu-1** followed the order: $Sc^{3+} > Y^{3+} > Eu^{3+} > Ce^{3+} > Zn^{2+} > Ca^{2+}$, which is in agreement with the order of Lewis acidity for these cations reported by Fukuzumi et al. in 2002.[23] This means that the stronger the Lewis acidity of the cation **M**, the higher its ability to stabilize the copper-nitrene by preventing rapid decay to **Cu-1**.

To further investigate the effect of the Lewis acid on the structure of the intermediate, resonance Raman (rRaman) studies were performed on the species **Cu-1-Y** to compare it with the previously reported **Cu-1-Sc**. [24] The rRaman spectrum of **Cu-1-Y** (Figure 4.4) was obtained using 514 nm laser excitation in resonance with the 530 nm electronic transition for both **Cu-1-Y-^{14}N** and its labeled counterpart **Cu-1-Y-^{15}N**, in which the nitrene ^{14}N-nitrogen had been replaced with its isotope ^{15}N. Three bands sensitive to isotope labeling could be observed at 568, 658 and 883 cm^{-1} that shifted downfield by 2, 3 and 21 cm^{-1} respectively. It is notable that the sensitive bands

observed for **Cu-1-Y** are only slightly shifted in comparison with the corresponding bands reported previously for **Cu-1-Sc**, which appeared at 570, 660, and 887 cm^{-1}.[22] The Raman in both cases showed that the absorption band at 530 nm in **Cu-1-M** has predominantly a nitrene-to-copper charge transfer, given that it selectively enhances vibrational modes involving the copper-nitrene core.

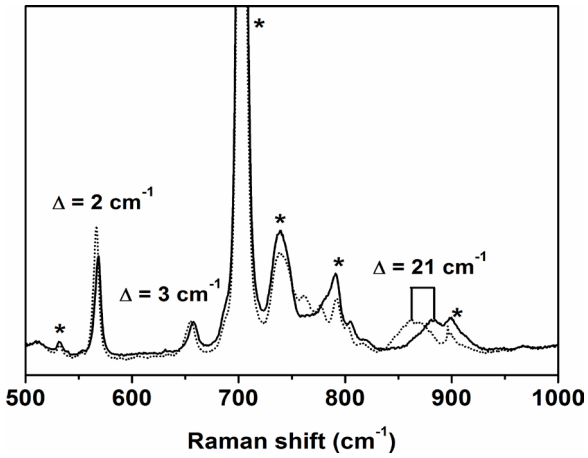

Figure 4.4: rRaman of **Cu-1-Y-^{14}N** (black solid line) and **Cu-1-Y-^{15}N** (dotted line) spectra [laser excitation: 514 nm; solvent: CH_2Cl_2/acetone (20:1); temp.: −90 °C]. Bands originating from the solvents are marked by asterisks.

X-ray absorption spectroscopy (XAS) studies were also performed, this time on the **Cu-1-Eu** species, to further compare it with the previously reported **Cu-1-Sc** complex. The normalized Cu *K*-edge spectrum of **Cu-1-Eu** is presented in Figure 4.5 a, alongside those previously reported for [(AN)Cu](BF_4) and **Cu-1-Sc**. The spectra are similar for both **Cu-1-M** complexes. The edge features of both are clearly shifted in energy relative to the Cu(I) precursor, proving that both samples are in a higher oxidation state. Both samples show a pre-edge feature at ca. 8977.5 eV, as can be determined from the analysis of the 1st derivative of the spectra (Figure 4.5 b). The position of the pre-edge band indicates that the copper center in both species is in a Cu(II) oxidation state, and therefore both are $[Cu^{II}(NR^{\bullet})]^{+}$ in nature. There is a clear difference in the pre-edge feature shape of both **Cu-1-M** species: while in the **Cu-1-Sc** the pre-edge appears broadened, in **Cu-1-Eu** the signal is sharper. The difference in the pre-edge shape is due to the beamline resolution used to measure each sample. The **Cu-1-Sc** data was measured at NSLS X3B using a Si(111) monochromator that was sagittally-focusing, while the **Cu-1-Eu** data was measured at SSRL 7-3 using a Si(220) monochromator. Si(220) has a somewhat higher resolution than Si(111) and the sagittal focusing of the X3B monochromator also degrades resolution further (see Chapter 6 for detailed descriptions of the setups). However, the areas of both signals are not

different, which proves that there is no appreciable difference in the copper-nitrene core that can be determined by X-ray absorption near-edge spectroscopy (XANES).

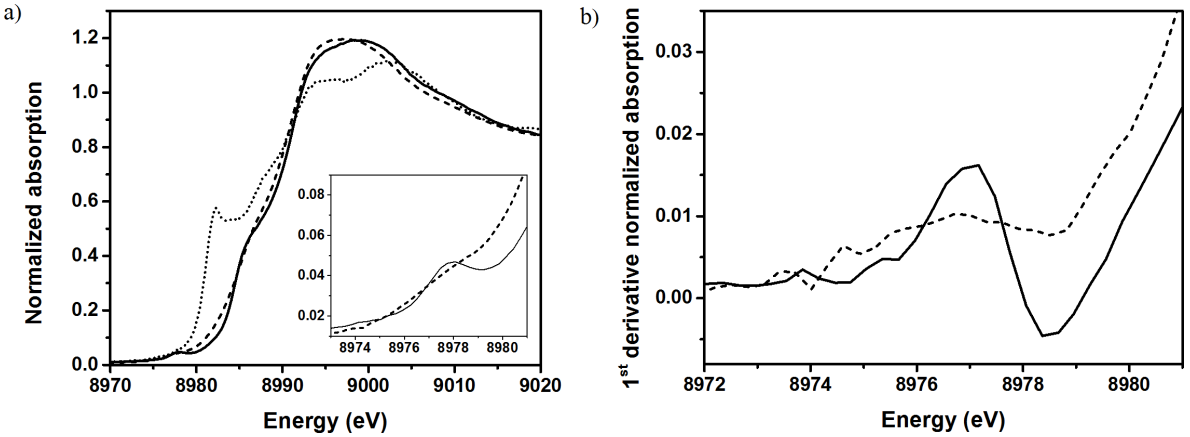

Figure 4.5: a) Normalized Cu *K*-edge X-ray absorption spectra of [(AN)Cu](BF$_4$) (dotted line), **Cu-1-Sc** (dashed line) and **Cu-1-Eu** (solid line) in acetone: dichloromethane (1:6). Inset: expansion of the pre-edge region. b) 1st derivative of the normalized absorption of the pre-edge region of **Cu-1-Sc** (dashed line) and **Cu-1-Eu** (solid line).

DFT calculations were performed with the purpose of studying the molecular structures and UV-vis spectra of the **Cu-1-M** complexes in detail. Unlike than the previous report[22] where the Sc-triflate moiety was approximated by a ScF_3 ligand, for this study the full structure of the scandium triflate moiety [Sc(OTf)$_3$] was used. A number of different conformations for both the tosyl moiety and each of the triflate groups were sampled, leading to two major conformers **A** and **B** (Figure 4.6). In conformer **A** the aromatic group of the tosyl moiety coordinates through stacking interactions with the copper-amine ligand (Fig. 4.6, left), in conformer **B**, on the other hand, the tosyl group interacts with one of the triflate anions (Fig. 4.6, right). Previous DFT calculations on **Cu-1-Sc**[22] suggested that conformer **B** was lower in energy; however, new studies suggest a clear preference for conformer **A**, which is lower in energy by ca. 14.2 kcal mol^{-1}; this energy difference was found to be unaffected by the choice of the density functional or basis employed.

Table 4.2 presents some selected coordination distances in both conformers **A** and **B** of **Cu-1-Sc**. The ligand environment around the copper center is slightly different in each conformer. While in **B** one of the tosyl group's oxygen atoms has a weak coordination towards copper (Cu-O distance of 2.41 Å), this weak coordination is absent in **A** (Cu-O distance of 3.24 Å). Moreover, the distance between the copper and the nitrogen group of the nitrene is shorter in conformer **A** than in **B** (1.89 vs 1.92 Å respectively). The ligand environment around the scandium, on the other hand, changes substantially between both conformers. In **B** the three triflate groups bind in a mono-

dentate fashion to scandium and the Sc-N(nitrene) distance is relatively short (2.06 Å). In contrast, in **A**, one of the triflate ions binds in a bidentate fashion to the scandium while the other two triflate ions bind in a monodentate fashion, and the Sc-N(nitrene) distance is greater (2.17 Å). The discussed distances indicate that in conformer **B** the nitrene and tosyl groups seem to be more strongly bound to scandium, while in conformer **A** the trend is reversed and the nitrene group seems to be more strongly coordinated to the copper center.

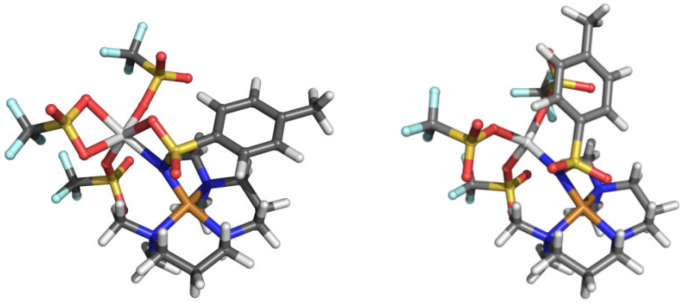

Figure 4.6: Molecular structures of the two possible conformers describing **Cu-1-Sc**: **A** (left) and **B** (right). Color code: C-dark gray, N-blue, O-red, S-yellow, F-light green, Cu-orange, Sc- light gray and H-white.

Table 4.2: Relevant coordination distances (Å) in the copper nitrenes **Cu-1-M** stabilized by different Lewis-acids (**M**) in the conformers **A** and **B**, obtained from DFT calculations.

M	$Sc(OTf)_3$ conf. **A**	$Sc(OTf)_3$ conf. **B**	$[Y(OTf)_3]$ conf. **A**	$[Y(OTf)_3]$ conf. **B**	$[Ca(OTf)_2]$ conf. **A**	$[Zn(OTf)_2]$ conf. **A**
Cu-N(tosyl)	1.888	1.924	1.893	1.917	1.882	1.897
Cu-N_1(AN)	2.048	2.061	2.041	2.064	2.041	2.065
Cu-N_2(AN)	2.035	2.014	2.040	2.014	2.045	2.011
Cu-N_3(AN)	2.056	2.071	2.042	2.060	2.041	2.063
Cu-S(tosyl)	2.844	2.691	2.835	2.681	2.798	2.730
Cu-O(tosyl)	3.236	2.409	3.185	2.428	3.096	2.610
M-N(tosyl)	2.170	2.060	2.363	2.249	2.399	1.901
M-O(tosyl)	2.202	3.777	2.385	3.905	2.389	3.094
M-$O_1(OTf_A)$	2.035	1.981	2.395	2.159	2.374	2.118
M-$O_2(OTf_A)$	-	-	2.408	-	2.420	2.188
M-$O_1(OTf_B)$	2.047	1.996	2.249	2.175	2.275	1.954
M-$O_1(OTf_C)$	2.205	1.994	2.355	2.162		

The UV-vis spectra of both conformers were calculated and are presented in Figure 4.7. Conformer **A**'s calculated spectrum shows a single band at 520 nm, while that of conformer **B** shows two bands at 860 nm and 575 nm with a shoulder at 520 nm. Experimentally, a single band is observed in the visible region around ca. 525 nm and no near-IR band is present. This corroborates the preference for conformer **A**, whose calculated spectra fits the experimental results well. Therefore, both the DFT stabilization energies and the UV-vis spectra simulation indicate that conformer **A** is the most stable for **Cu-1-Sc**.

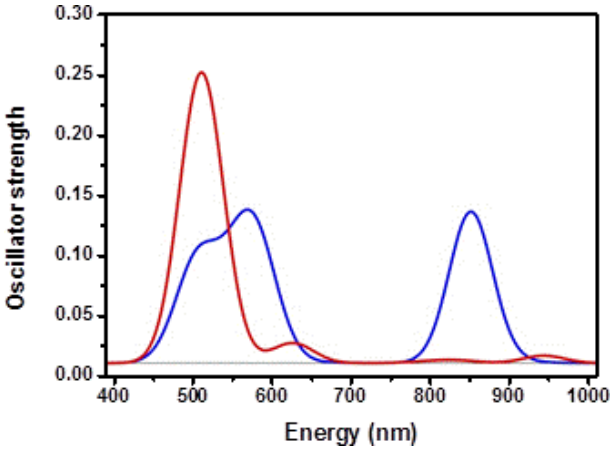

Figure 4.7: Simulated UV-vis spectra for conformers **A** (red) and **B** (blue) of **Cu-1-Sc**.

In order to study the effect that the Lewis acid **M** has on the structure of the **Cu-1-M** complexes, the DFT studies were expanded to include the copper-nitrene species with other selected Lewis acids. In a similar way to **Cu-1-Sc**, **Cu-1-Y** was found in the same two conformers **A** and **B**, but in this case conformer **A** was even more stabilized (22 kcal mol^{-1}) than conformer **B**. The same was found even for divalent **M**'s, like calcium and zinc. In conformer **A** of **Cu-1-M** (**M** = Sc(III), Y(III), Zn(II), Ca(II)), both the coordination around the copper center and the relative orientation of the tosyl group towards it were found to be hardly affected by the change of the metal **M** (Figure 4.8 and Table 4.2). These findings prove that the copper-nitrene structure is not affected by the change of **M** and could explain the fact that all the **Cu-1-M** species have the same UV-vis absorption spectra. In order to prove this, the UV-vis spectra were calculated for each **Cu-1-M** species in both conformations **A** and **B**. The spectra obtained show the same characteristics as **Cu-1-Sc**: conformer **A** has one peak at ca. 520 − 530 nm while conformer **B** presents peaks at 500 nm (with shoulder at ca. 600 nm) and around 900 nm. In all cases, therefore, only conformer **A** correctly reproduces the experimental UV-vis absorption spectra observed for the **Cu-1-M** species, which support **A** being the most stable conformer.

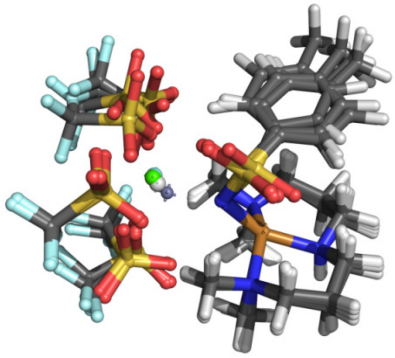

Figure 4.8: Overlay of the Lewis acid-stabilized copper nitrenes **Cu-1-M** in conformation **A**, where **M** = Sc(III), Y(III), Ca(II), Zn(II). Color code: C-dark gray, N-blue, O-red, S-yellow, F-light green, Cu-orange, **M**- green and H-white.

The molecular orbitals of **Cu-1-Sc** (conformer **A**) involved in the UV-vis absorption band at 527 nm were also computed and are presented in Figure 4.9. The band at 527 nm results from two main transitions, namely 224α → 232α (36%) and 228α → 232α (37%). As can be observed from Figure 4.9, the occupied orbitals 224α and 228α are mainly located in the nitrene-tosyl group and the copper-AN system, while the virtual 232α orbital is located mainly on the nitrene-copper-AN system. Hence, the molecular orbitals involved in the transition responsible for the 527 nm band do not contain any major contribution from the Lewis acid moiety. This may explain the lack of change in the UV-vis spectra when using different **M** ions, since the nature of **M** does not affect the main transitions responsible for the UV-vis 527 nm band.

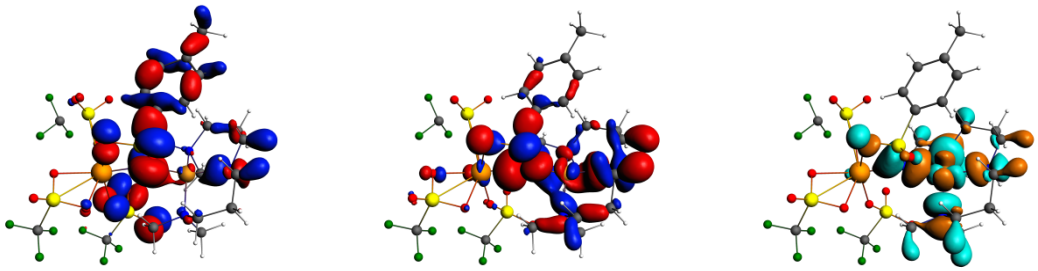

Orbital 224α Orbital 228α Orbital 232α

Figure 4.9: Main molecular orbitals involved in the UV-vis absorption band at 527 nm for **Cu-1-Sc** (conformer **A**).

The DFT calculations, together with the rRaman data and the absorption features of the **Cu-1-M** complexes, showed that the spectral features of **Cu-1-M** arise from transitions predominantly involving the copper-tosylnitrene core and are independent of the Lewis acidity of

the **M** employed for their stabilization. However, the yields and stabilities of the trapped **Cu-1-M** do depend on the Lewis acidity of the redox-innocent metal ions employed. It is therefore natural to wonder if the Lewis acidity of **M** has any effects on the reactivity of the **Cu-1-M** complexes.

The reactivity of the Lewis-acid adducts **Cu-1-M** with **M** = $Sc(OTf)_3$, $Y(OTf)_3$, $Eu(OTf)_3$ and $Ce(OTf)_3$, was therefore evaluated in the nitrene transfer reaction (NT) with PPh_3 as a substrate. Kinetic studies were performed by adding appropriate amounts of PPh_3 to 0.3 mM solutions of **Cu-1-M** in CH_2Cl_2 under completely anaerobic conditions. The decrease of the absorption band at 530 nm was monitored by UV-vis spectroscopy by recording a spectrum every 0.5 seconds. Rate constants, k_{obs}, were determined by pseudo-first-order fitting in the initial 0-150 s of the decay of this absorption band (Figure 4.10). Deviation from pseudo-first-order behavior could be observed in the latter phases of the reactions but reasonable fits were obtained for the initial phases in all cases. A product analysis of the reaction solution showed the formation of *N*-(*p*-toluenesulfonyl)iminotriphenylphosphorane (Ph_3P = NTs) as a product in each case.

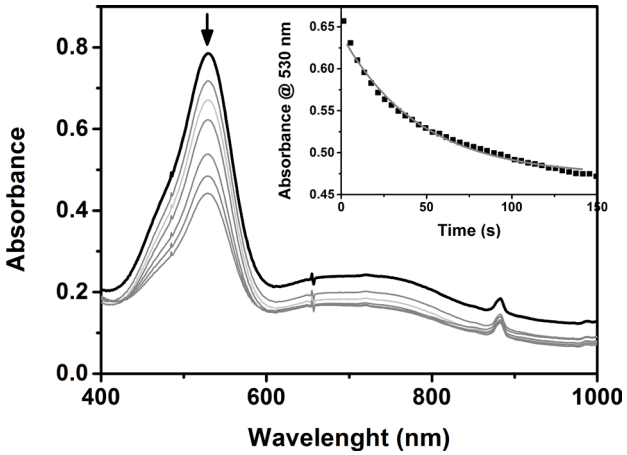

Figure 4.10: Changes in the absorption spectra of **Cu-1-Eu** associated with its reaction with 20 equivalents of PPh_3 obtained from an initial 0.5 mM solution in CH_2Cl_2 at −90 °C. Inset: Time trace of the pseudo-first-order decay of the absorption band at 530 nm in this reaction as a function of time.

Second-order rate constants (k_2) were determined from the dependence of the pseudo-first-order rate constants (k_2) on PPh_3 concentrations for each **Cu-1-M** complex (Figure 4.11). It is noteworthy that the rate constant values for the **Cu-1-M** complexes are independent of the nature of the metal ions **M** (Figure 4.9), so despite the fact that the different Lewis acids affect the yields/stability of the trapped intermediates **Cu-1-M**, they have no influence on their reactivity.

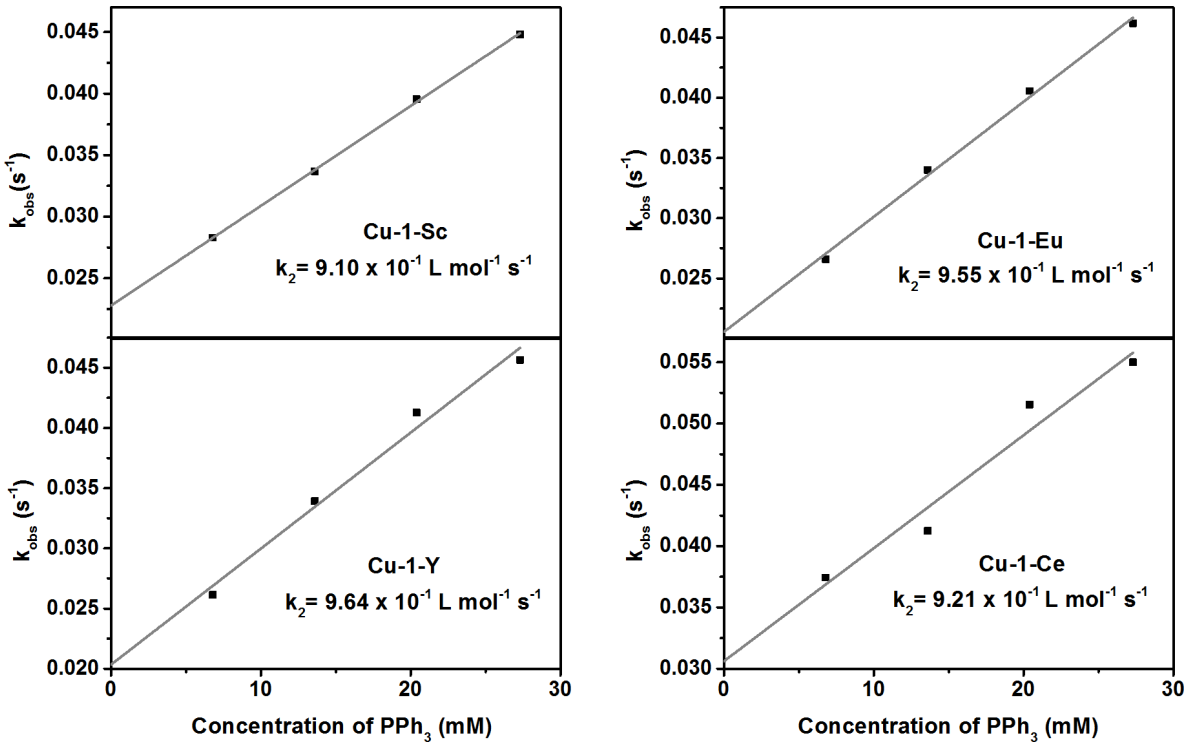

Figure 4.11: Linear dependence of k_{obs} on the concentration of PPh_3 for each **Cu-1-M** complex.

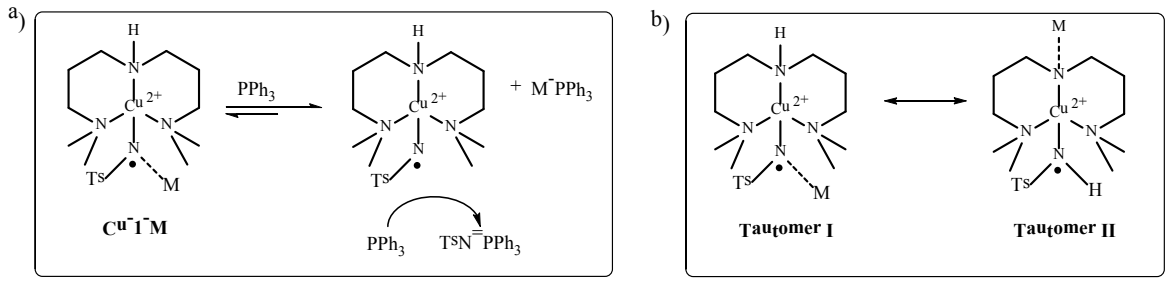

Scheme 4.4: a) Proposed generation of the metal-free copper-nitrene as the active intermediate in the reactions of **Cu-1-M** with an excess of PPh_3 b) Tautomeric forms of the **Cu-1-M** intermediates, where tautomer II could act as the active species in the reactions performed by **Cu-1-M**.

The independence of the reactivity of the **Cu-1-M** complexes on the Lewis acid **M** may indicate the presence of a common reactive intermediate in the reactions of **Cu-1-M** complexes with PPh_3. A plausible candidate for such a reactive species is the free $[(AN)Cu(NTs)]^+$ species participating in an equilibrium in solution with its corresponding Lewis acid adduct. The occurrence of such a species could be explained if the presence of an excess of PPh_3 displaces the equilibrium due to the strong binding of PPh_3 to **M** (Scheme 4.4 a). Alternatively, the metal-independent spectroscopic properties of the **Cu-1-M** complexes may point to a different binding mode for **M** than that originally proposed.[22] A tautomeric structure of **Cu-1-M** can be visualized (Scheme

4.4 b) in which **M** is bound to an amidate nitrogen of the ancillary ligand AN (tautomer II) instead of the previously proposed binding to the nitrene nitrogen (tautomer I); however, tautomer II was not found to be a likely conformer, according to the DFT calculations.

More experimental work is necessary to establish which of the aforementioned species is the active species in the **Cu-1-M** complexes. The studies on copper-nitrenes employing different nitrene sources presented below will shed light on this important question.

4.2.2 Variation of the nitrene source employed for stabilizing the copper-nitrene intermediates

4.2.2.1 The use of sPhINArCF3 and sPhINArNO2 as nitrene sources

In order to get a better understanding of the terminal copper-nitrenes, in general, and the **Cu-1-M** systems, in particular, two new nitrene sources related to sPhINTs were synthesized. The new nitrene sources, in contrast with sPhINTs, possess strong electron withdrawing groups in the para positions of the nitrene sulfonyl-phenyl ring: a nitro group in the case of $sPhINAr^{NO_2}$ (2-(*tert*-butylsulfonyl)((4-nitrophenyl)sulfonylimidoiodo)benzene) and a trifluoromethyl group in the case of $sPhINAr^{CF_3}$ (2-(*tert*-butylsulfonyl)((4-(trifluoromethyl)phenyl)sulfonylimidoiodo)benzene). With these, it was possible to stabilize new intermediates that offered new insights into the growing copper-nitrene field.

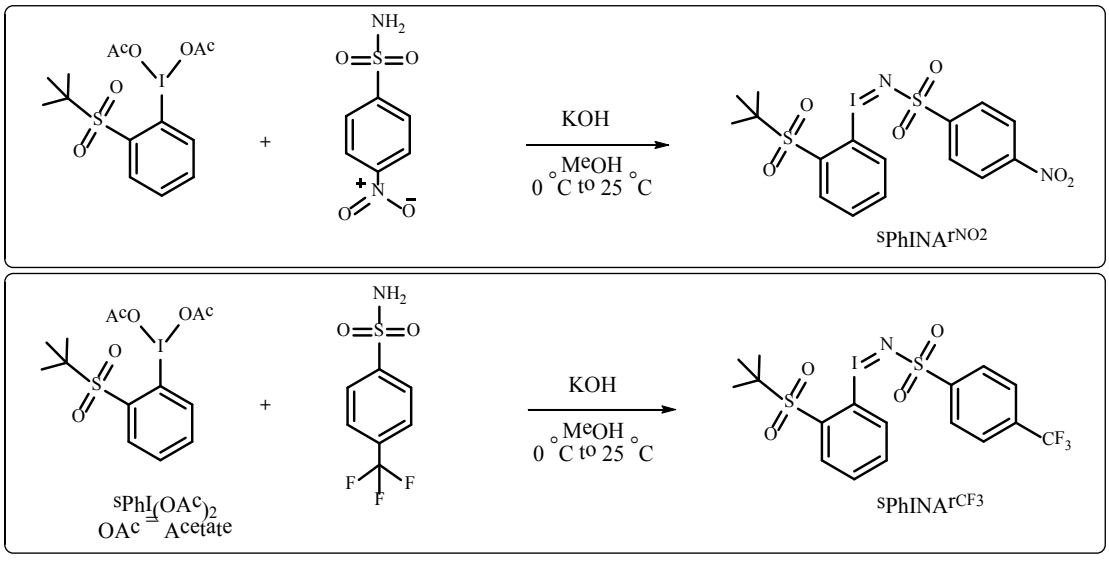

Scheme 4.5: Synthesis of the nitrene sources $sPhINAr^{CF_3}$ and $sPhINAr^{NO_2}$.

The synthesis of the oxidants sPhINR (where R = SO_2Ph^{NO2} for $sPhINAr^{NO_2}$ and R = SO_2Ph^{CF3} for $sPhINAr^{CF_3}$) was performed following the procedure reported for the synthesis of

sPhINTs with slight modifications; 4-nitrobenzenesulfonamide and 4-(trifluoromethyl)-benzene-sulfonamide were employed respectively for the reaction with $sPhI(OAc)_2$ in dry methanol to generate $sPhINAr^{NO_2}$ and $sPhINAr^{CF_3}$ (Scheme 4.5). The new nitrene sources presented the advantage of having internal electron-withdrawing groups while retaining the positive features of sPhINTs such as good solubility in dichloromethane and ease of handling and storage.

The reaction of the complex $[(AN)Cu](BF_4)$ with 1.5 equivalents of the oxidants sPhINR in the presence of 1.25 equivalents of $Sc(OTf)_3$ in dry dichloromethane at −90 °C resulted in the formation of two new purple intermediates: **Cu-2-Sc** when using $sPhINAr^{CF3}$ and **Cu-3-Sc** in the case of $^{s}PhINAr^{NO2}$ (Scheme 4.6). The absorption spectra of both intermediates (Figure 4.12) displayed an intense band at 525 nm (ε_{max} = 2150 M^{-1} cm^{-1} for **Cu-2-Sc** and ε_{max} = 2000 M^{-1} cm^{-1} for **Cu-3-Sc**) and a broad, less intense band at around 750 nm (ε_{max} = 600 M^{-1} cm^{-1} for **Cu-2-Sc** and ε_{max} = 550 M^{-1} cm^{-1} for **Cu-3-Sc**). These spectra are remarkably similar to the one obtained for **Cu-1-Sc**, which showed two bands at 530 nm (ε_{max} = 3500 M^{-1} cm^{-1}) and 750 nm (ε_{max} = 580 M^{-1} cm^{-1}). What is notably different is the observed stability for the three different adducts in dichloromethane at −90 °C; while the half-life of **Cu-1-Sc** is reported to be 1600 s,[22] the half-life measured for **Cu-2-Sc** is 2250 s, and for **Cu-3-Sc** it is 3000 s. This change in stability can be attributed to the increasing electron-withdrawing capability of the substituent group in the *p*-position of the phenyl ring in the order $–CH_3 < -CF_3 < -NO_2$.

Most notable is the effect of the electron-withdrawing groups on the stability of the free Cu-nitrene species in the absence of any externally-added Lewis acid. As discussed before, in the reaction for the complex $[(AN)Cu](BF_4)$ with the oxidant sPhINTs in the absence of an external Lewis acid, the stabilization of the formal copper(III) species was not attainable and the reaction instead yielded a copper(II)-tosylamide complex **Cu-1**. However, the complex $[(AN)Cu](BF_4)$ reacted in dry dichloromethane at −90 °C with the oxidants $sPhINAr^{CF3}$ and $sPhINAr^{NO2}$ (Scheme 4.6) to yield two new bright green intermediates: **Cu-2** and **Cu-3**, respectively, with characteristic absorption bands at 425 nm (ε_{max} = 1200 M^{-1} cm^{-1} for **Cu-2** and ε_{max} = 1300 M^{-1} cm^{-1} for **Cu-3**) and 700 nm (ε_{max} = 600 M^{-1} cm^{-1} for **Cu-2** and ε_{max} = 700 M^{-1} cm^{-1} for **Cu-3**) (Figure 4.12). Both species, **Cu-2** and **Cu-3**, decay in solution at −90 °C with half-lives of 1200 s and 1400 s respectively. Again, a trend of increasing stability could be observed when increasing the electron-withdrawing capabilities of the group in the *p*-position of the phenyl nitrene substituent; while the terminal copper nitrene with sPhINTs cannot be stabilized in the absence of a Lewis acid, under the same conditions **Cu-2** can be observed but is, in turn, shorter-lived than **Cu-3**.

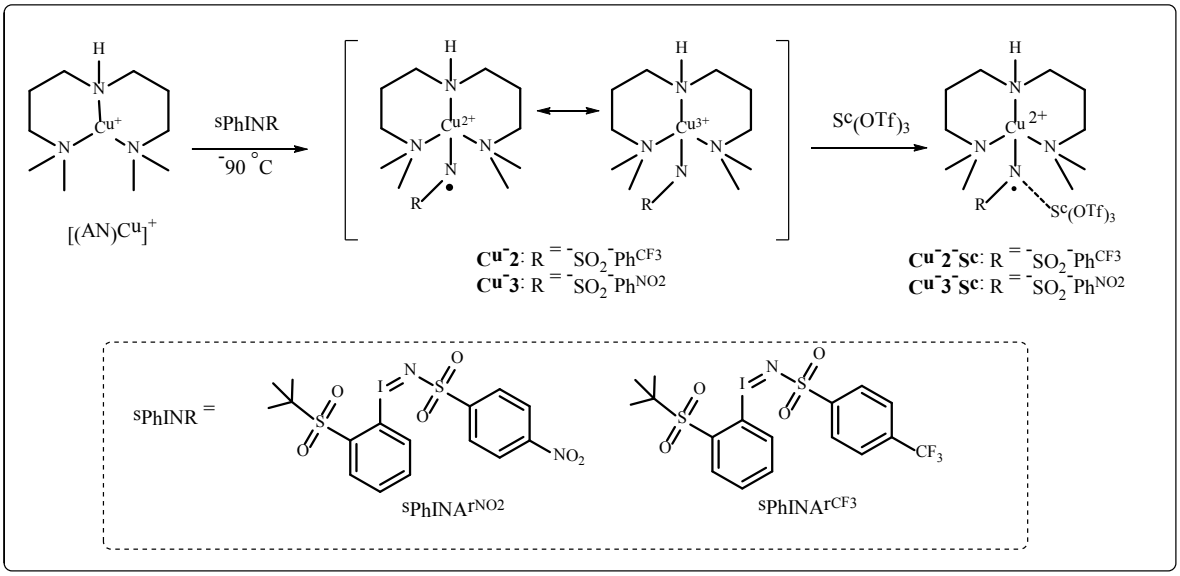

Scheme 4.6: Generation of the intermediates **Cu-2**, **Cu-3**, **Cu-2-Sc** and **Cu-3-Sc**.

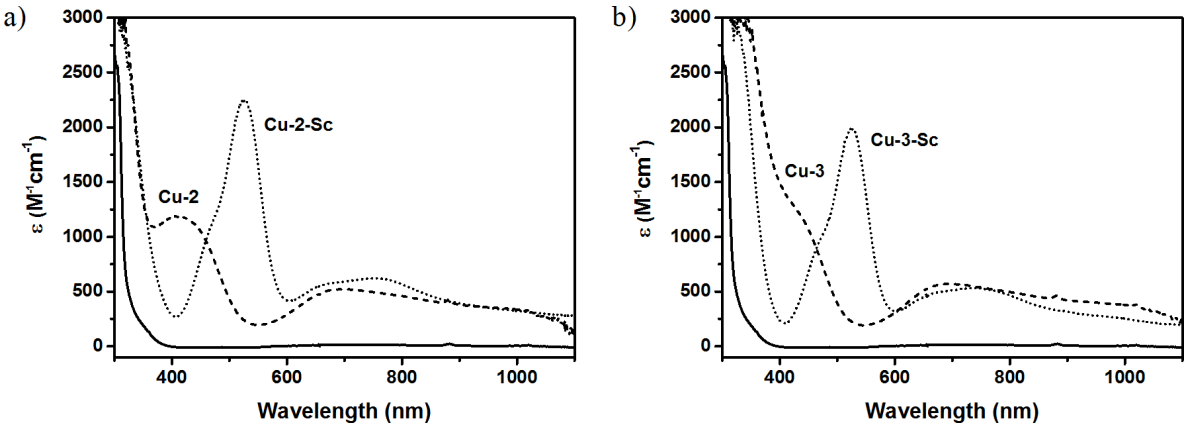

Figure 4.12: Absorption spectra of the intermediates **Cu-2** (dashed line in a)), **Cu-3** (dashed line in b)), **Cu-2-Sc** (dotted line in a)) and **Cu-3-Sc** (dotted line in b)) in CH_2Cl_2 at −90 °C. The initial [(AN)Cu](BF_4) absorption spectra is shown in black solid line.

In order to study the influence of the Lewis acid (**M**) on the formation of the new intermediates, different Lewis acids were used to generate **Cu-3-M** in the same manner as was done for **Cu-1-M**, this time employing $Sc(OTf)_3$, $Y(OTf)_3$ and $Eu(OTf)_3$ (Figure 4.13). The position of the main band at 525 nm proved to be independent of the nature of the **M** employed; however, the maximum absorbance differed significantly depending on the **M** used. As observed in the analogous **Cu-1-M** complexes, this trend is a reflection of the Lewis acidity of the metal ion **M** and is related to the decreasing yield of the Lewis-acid adduct generated in each case.

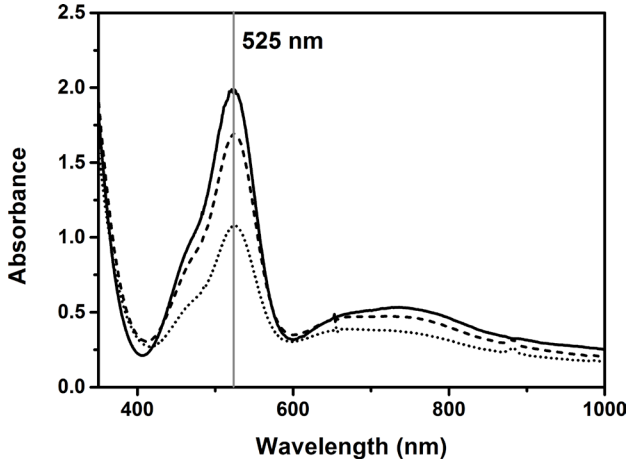

Figure 4.13: Absorption spectra of **Cu-3-M** obtained when M = Sc(III) (black solid line, Y(III) (dashed line) and Eu(III) (dotted line). All spectra were obtained from an initial 1 mM solution of [(AN)Cu](BF_4) after addition of **M**($OTf)_3$ and $sPhINAr^{NO2}$ in CH_2Cl_2 at −90 °C.

Since this is the first time that Lewis acid-free copper-nitrene intermediates have been detected from the reaction of [(AN)Cu](BF_4) with iminoiodinane derivatives, more thorough research is needed to characterize them. To find out the stoichiometry of **Cu-2** and **Cu-3**, a titration was performed in which different amounts of sPhINR were added to a 1 mM solution of [Cu(AN)](BF_4) and the maximum absorbance at 425 nm was recorded in each case. The plot of mmol of $sPhINAr^{NO2}$ added versus the maximum absorbance obtained is presented in Figure 4.14. Close after the addition of 1 equivalent of sPhINR, the maximum absorbance remained constant. This indicates that the copper and the nitrene sources react in a 1:1 stoichiometry to yield **Cu-2** and **Cu-3**, thus showing that these species are terminal copper nitrenes.

To determine the formal oxidation state of the copper in the complexes **Cu-2**, **Cu-3**, **Cu-2-Sc** and **Cu-3-Sc**, their reactivity towards one-electron reductants was tested. **Cu-2-Sc** and **Cu-3-Sc** underwent a two-electron reduction process with ferrocene (Fc; E_{ox} vs SCE = 0.37 V) at −90 °C with the corresponding formation of copper(I) and ferrocenium cations (Fc^+; 150-160%; Figure 4.15) in yields slightly lower than those reported for **Cu-1-Sc** (Fc^+; 180%). This confirmed that **Cu-2-Sc** and **Cu-3-Sc** are two oxidation levels higher [(AN)Cu](BF_4). On the other hand, it was not possible to reduce **Cu-2** and **Cu-3** using Fc. Previous studies on reactive intermediates like iron-oxos and copper-nitrenes have shown that the presence of scandium(III) is necessary for the two-electron reduction with Fc to take place.[22,25] This phenomenon has been explained by adducing that the stronger binding of the scandium(III) to the oxo- or nitrene- group facilitates the reduction of the metal to its fully reduced form.[25] In this case, **Cu-2** and **Cu-3**, having no scandium bound could

not be reduced by ferrocene; in contrast, **Cu-2-Sc** and **Cu-3-Sc** have scandium and were able to undergo the two-electron reduction.

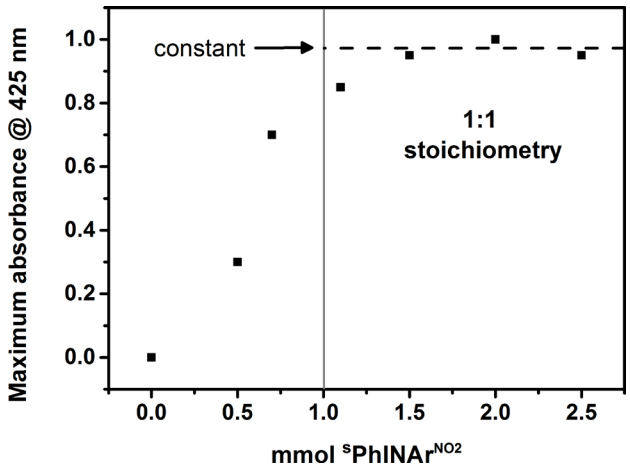

Figure 4.14: Maximum absorbance observed at 425 nm from the reaction of $[(AN)Cu](BF_4)$ with different amounts of $^{s}PhINAr^{NO2}$ in CH_2Cl_2 at −90 °C.

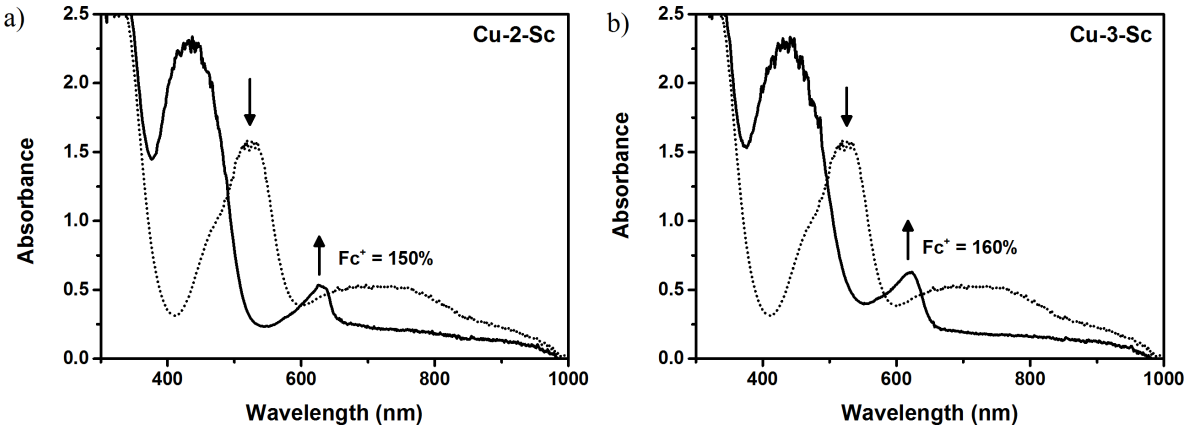

Figure 4.15: Absorption spectra of **Cu-2-Sc** and **Cu-3-Sc** (1 mM) and the product of their reaction with ferrocene (Fc) (30 equivalents) in CH_2Cl_2 at −90 °C.

The use of a stronger one-electron reductant such as decamethylferrocene ($Me_{10}Fc$) (E_{ox} vs SCE = −0.08 V) allowed complexes **Cu-2-Sc**, **Cu-3-Sc**, and also **Cu-2** and **Cu-3** to undergo a two-electron process with the corresponding formation of a copper(I) species and the decamethylferrocenium cation ($Me_{10}Fc^{+}$) with yields between 187 and 193 % (Figure 4.16). This confirmed that all the intermediates **Cu-2**, **Cu-3**, **Cu-2-Sc** and **Cu-3-Sc** are two oxidation states above copper(I), meaning that the copper in them is in a formal oxidation state of +3. It also showed that the intermediates are formed in a yield of at least 90 %.

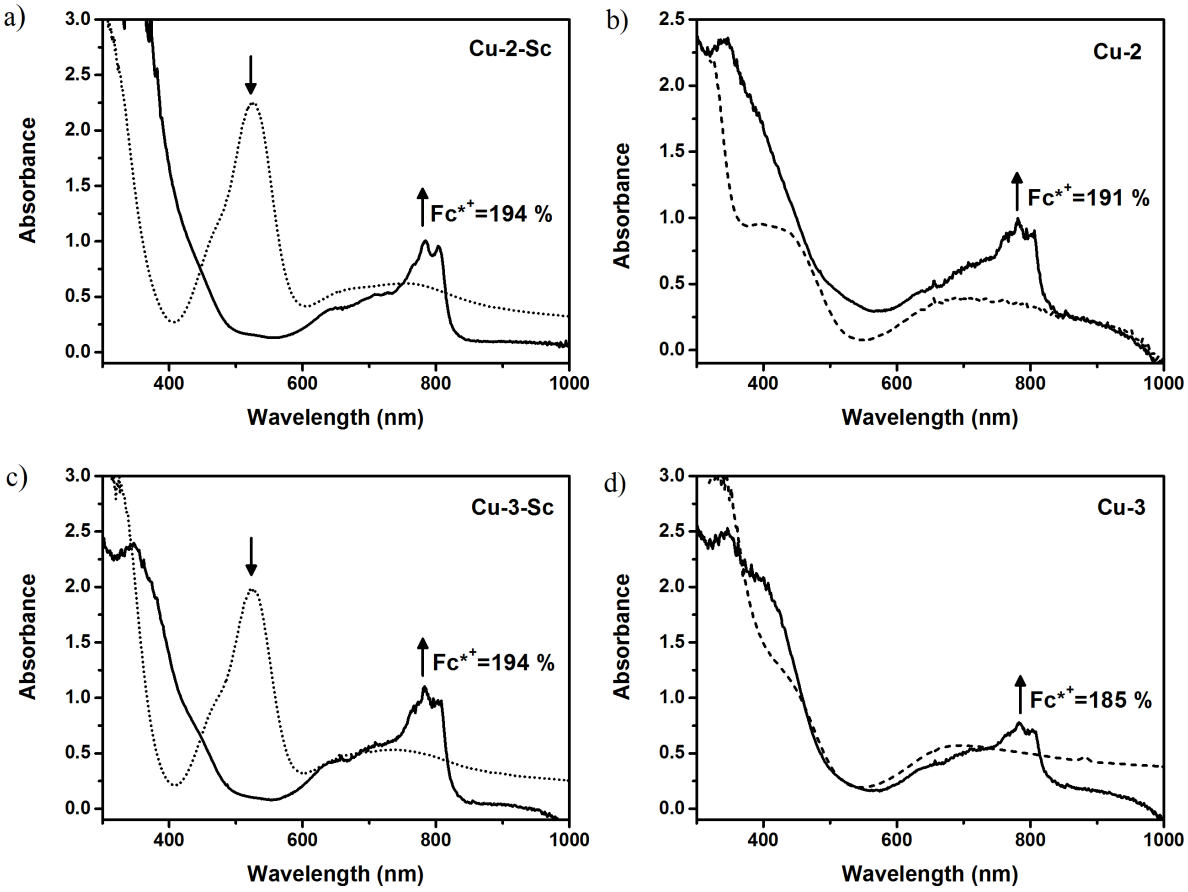

Figure 4.16: Absorption spectra of 1mM solutions of a) **Cu-2-Sc** (dotted line), b) **Cu-2** (dashed line), c) **Cu-3-Sc** (dotted line), d) **Cu-3** (dashed line) and the product of their reaction with decamethylferrocene ($Me_{10}Fc$) (30 equivalents) (black line in all) in CH_2Cl_2 at −90 °C.

This is the first time that we have access to terminal copper nitrenes both as free species, **Cu-2** and **Cu-3**, and as their scandium adducts, **Cu-2-Sc** and **Cu-3-Sc**, under the same conditions, which offers a great opportunity to perform comparative spectroscopic and reactivity studies to get a better understanding of the behavior of these important reactive intermediates.

The resonance Raman (rR) spectra of **Cu-2-Sc** and **Cu-3-Sc** were measured at 77 K using 532 nm laser excitation in resonance with the 525 nm transition of the intermediates (Figure 4.17). In both cases, three bands were observed that can be attributed to the Cu^{III}-NTs/Cu^{II}-N$^{\bullet}$Ts core on the basis of ^{15}N isotope labeling. **Cu-2-Sc** displayed a shoulder band at around 907 cm^{-1} that showed a downshift of 33 cm^{-1} when labeled, and two other bands at 609 cm^{-1} and at 557.5 cm^{-1} with lower sensitivity to labeling, which shifted by 2 and 1.5 cm^{-1} respectively. Similarly, **Cu-3-Sc** displayed a shoulder band at around 910 cm^{-1} that showed a downshift of 30 cm^{-1} when labeled, and another two bands at 609 cm^{-1} and at 562 cm^{-1} that shifted by 4 and 2 cm^{-1} respectively. The rR

spectra obtained for **Cu-2-Sc** and **Cu-3-Sc** are in close agreement with the one obtained for **Cu-1-Sc** using 514 nm laser excitation, where three isotope-sensitive bands were reported in the same regions as the ones observed here. Despite our best efforts, it was not possible to obtain the rR spectra of **Cu-2** and **Cu-3**, possibly due to decomposition or decay of the sample under the laser irradiation.

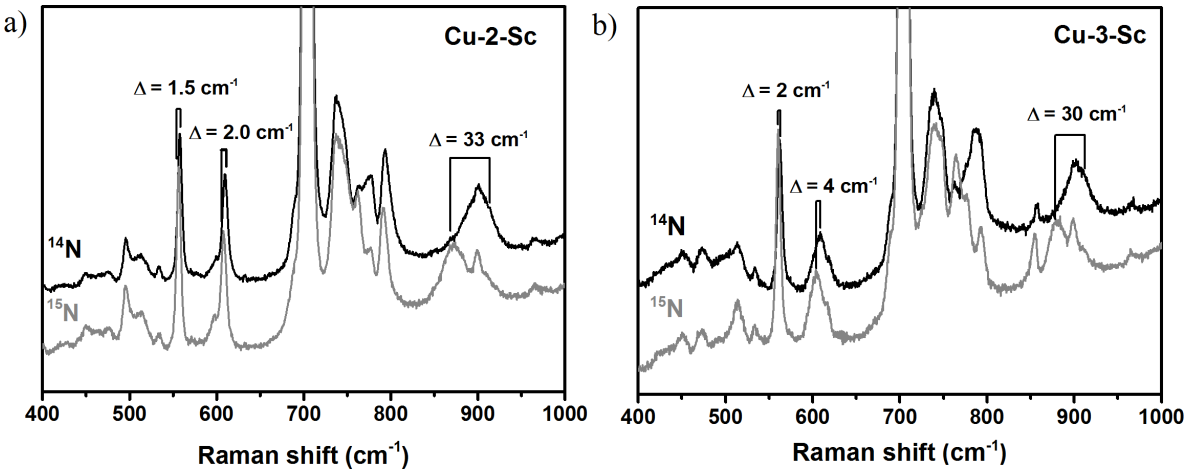

Figure 4.17: rRaman spectra of a) **Cu-2-Sc-^{14}N** (black solid line) and **Cu-2-Sc-^{15}N** (gray solid line) and b) **Cu-3-Sc-^{14}N** (black solid line) and **Cu-3-Sc-^{15}N** (gray solid line) [laser excitation: 532 nm; solvent: CH_2Cl_2/acetone (20:1); temp.: −90 °C].

The formal Cu(III) species in **Cu-2**, **Cu-3**, **Cu-2-M** and **Cu-3-M** may exist in two possible electronic structures, namely a copper(III)-imido $[Cu^{III}(NR)]^+$ and a copper(II)-imidyl radical $[Cu^{II}(NR^{\bullet})]^+$ (Figure 4.1). Shifts in the XANES features can be useful in determining the actual oxidation state of the copper center in the complexes. Figure 4.18 shows a comparison of the Cu *K*-edge XANES spectrum of $[(AN)Cu)](BF_4)$, **Cu-3** and **Cu-3-Y**. It is interesting to notice that the **Cu-3** and **Cu-3-Y** spectra are practically identical, and therefore both complexes present the same electronic structure, which is independent of the presence of an external Lewis acid **M** in their structure.

The edge features of **Cu-3** and **Cu-3-Y** are shifted to higher energy relative to the Cu(I) precursor. However, the edge energy is not a suitable indicator for distinguishing between copper(III) and copper(II) in a complex since the Cu edge includes 1*s*→4*p* transitions that are strongly influenced by geometry and the ligand environment, and therefore its features are not only functions of the oxidation state of the metal.[26] The only feature that can be used unambiguously to distinguish the copper oxidation state in the sample is the pre-edge. A pre-edge is a weak 1*s*→3*d* electric-dipole-forbidden transition ($\Delta l \neq \pm 1$) that is visible when there is 3*d*-4*p* orbital mixing

(since 1*s*→4*p* transitions are allowed). For copper(II) compounds this transition takes place at 8978.8 ± 0.4 eV, while for copper(III) it occurs at 8981 ± 0.5 eV.[26] The pre-edge energy observed for **Cu-3** and **Cu-3-Y** appears at ca. 8978 eV, this strongly suggests that both species contain a Cu(II) center bound to a nitrene radical, consistent with a $[Cu^{II}–NR•]^{+}$ formulation, as observed before for **Cu-1-M**.[22]

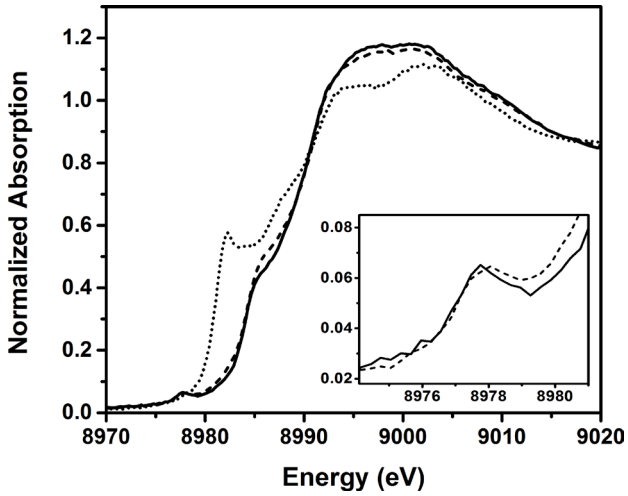

Figure 4.18: Normalized Cu *K*-edge spectra for $[(AN)Cu](BF_4)$ (dotted line), **Cu-3** (solid line) and **Cu-3-Y** (dashed line) in dichloromethane. The inset shows an expansion of the pre-edge region.

The four new intermediates were also computationally investigated using the same tools employed for the study of **Cu-1-M** species. The structure of the **Cu-2-Sc** and **Cu-3-Sc** complexes was determined to be that of conformer **A** previously described for **Cu-1-Sc**. The geometry of the Lewis acid-free complexes **Cu-2** and **Cu-3**, on the other hand, remained to be studied. A number of possible conformations could be envisioned; the three most important ones are presented in Figure 4.19 and their relevant coordination distances are presented in Table 4.3 for **Cu-3**. The simplest one is that determined for **Cu-1-Sc** (conformer **A**) after the removal of the $Sc(OTf)_3$ moiety (conformer **A'**). Another possibility is that one of the side arms of the AN ligand drifts away and the tosyl group gets protonated, instead of the middle amine group (conformer **B'**, diamine conformation). Finally, the third conformation (conformer **C'**) is found to be the lowest in energy. It is similar to the diamine conformation **B'**, but in this conformation, during the geometry optimization, the faraway amine group deprotonates the CH_2 group next to the middle amine group, thereby generating an imine in the middle and an ammonium cation on the side. Conformer **C'** is ca. 32 kcal mol^{-1} more stable than conformer **A'**.

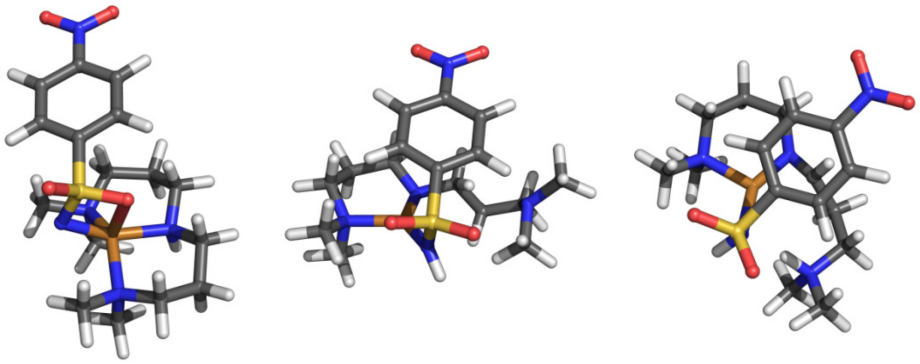

Conformer **A'** Conformer **B'** Conformer **C'**

Figure 4.19: Molecular structures of three possible conformers describing **Cu-3**: **A'**, **B'** and **C'**. Color code: C-dark gray, N-blue, O-red, S-yellow, Cu-orange and H-white.

Table 4.3: Relevant coordination distances (Å) in the possible conformers describing **Cu-3**: **A'**, **B'** and **C'**.

	A'	**B'**	**C'**
Cu-N(tosyl)	1.887	1.857	1.961
Cu-N_1(am)	2.076	4.181	3.491
Cu-N_2(am)	2.019	1.885	1.917
Cu-N_3(am)	2.053	1.999	2.023
Cu-S(tosyl)	2.649	3.036	3.140
Cu-O(tosyl)	2.538	3.695	3.762

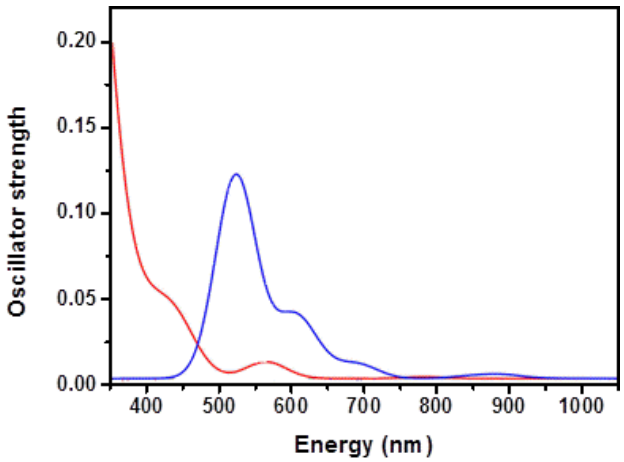

Figure 4.20: Simulated UV-vis spectra for **Cu-3-Sc** conformer **A** (blue solid line) and **Cu-3** conformer **C'** (red solid line).

The UV-vis spectra of conformer **A** for **Cu-3-Sc** and conformer **C'** for **Cu-3** were further computed. The simulated spectra are shown in Figure 4.20. Both are a perfect match with those obtained experimentally (Figure 4.12 b). The spectrum of conformer **A'** for **Cu-3** was also calculated and two broad bands at 510 and 630 nm were observed, which does not fit with the experimentally observed results. This is a further confirmation of the validity of assigning **Cu-3** and **Cu-2** to **C'**-type structural conformations.

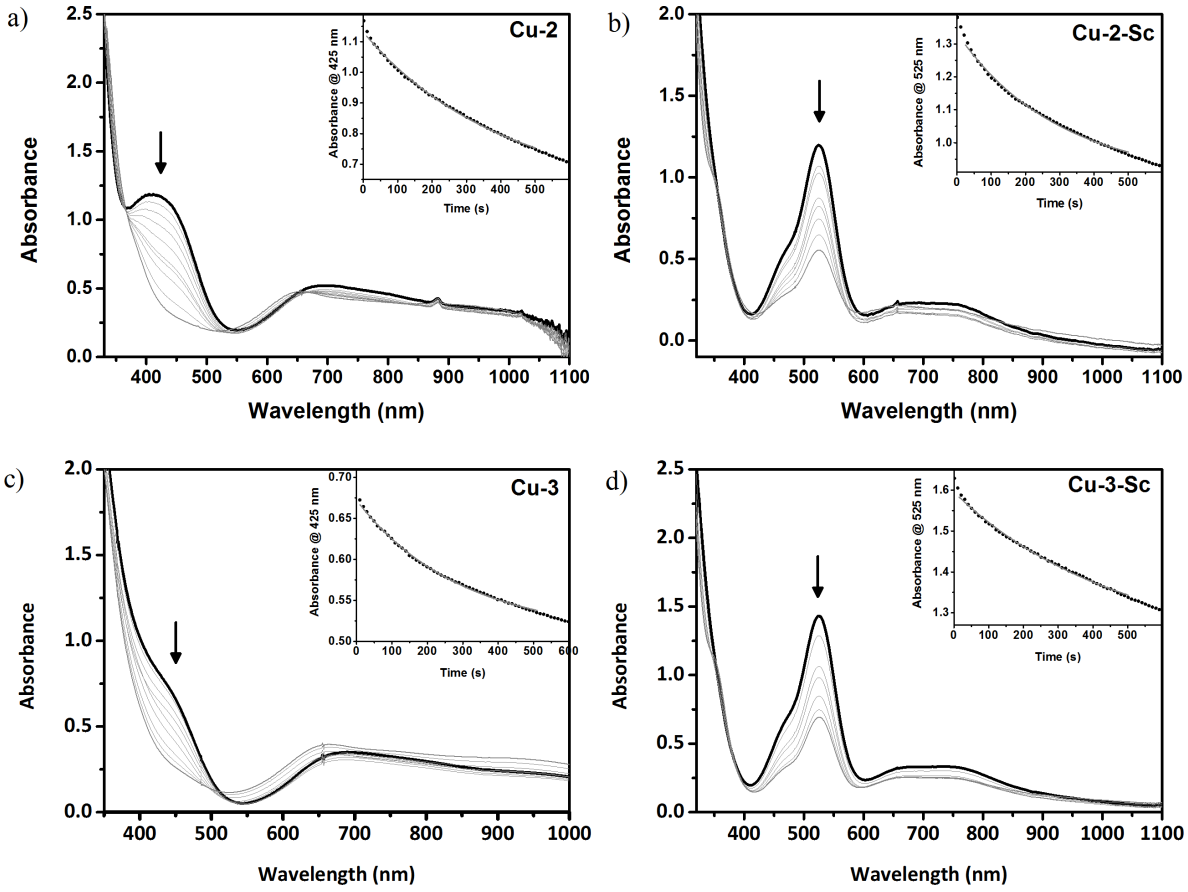

Figure 4.21: Changes in the absorption spectra associated with the reaction of a) **Cu-2**, b) **Cu-2-Sc**, c) **Cu-3** and d) **Cu-3-Sc** with toluene obtained from an initial 1 mM solution of the intermediate at −90 °C in CH_2Cl_2. Inset: Time trace of the pseudo-first-order decay of the absorption band that characterizes each intermediate, as a function of time and pseudo-first-order fitting (gray solid line).

The reactivity of the trapped intermediates **Cu-2**, **Cu-3**, **Cu-2-Sc** and **Cu-3-Sc** was examined in the oxidation of toluene, which has a C−H bond dissociation energy (BDE) of 88.6 kcal mol^{-1}.[27] The kinetics of the reactions were followed by UV-vis spectroscopy when different concentrations of toluene were added to the formed intermediates in dichloromethane at −90 °C. The decay of the characteristic absorption band was followed and fitted to pseudo-first-order decay

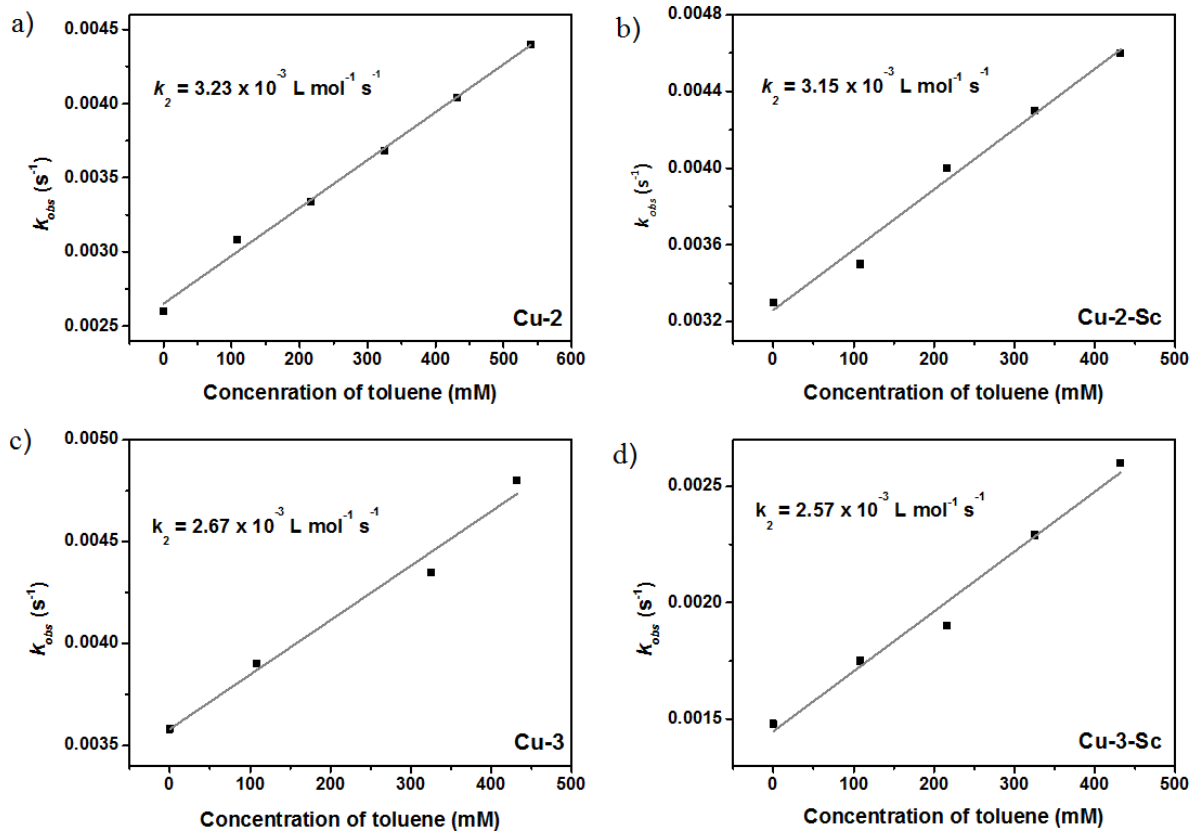

Figure 4.22: Linear dependence of k_{obs} on the concentration of the substrate for the reactions of a) **Cu-2**, b) **Cu-2-Sc**, c) **Cu-3** and d) **Cu-3-Sc** with toluene at −90 °C in CH_2Cl_2.

Table 4.4: Second-order rate constants (k_2) for **Cu-1-Sc**,[22] **Cu-2**, **Cu-2-Sc**, **Cu-3** and **Cu-3-Sc** determined for different substrates in HAA and NT reactions in dichloromethane at −90 °C.

		Cu-1-Sc	Cu-2	Cu-2-Sc	Cu-3	Cu-3-Sc
	BDE	k_2 L mol^{-1} s^{-1}	k_2 L mol^{-1} s^{-1}	k_2 L mol^{-1} s^{-1}	k_2 L mol^{-1} s^{-1}	k_2 L mol^{-1} s^{-1}
HAA						
Xanthene	74	0.311			0.106	0.104
CHD	76.9	0.155			0.061	0.060
Toluene	88.6	5.1 x 10^{-3}	3.23 x 10^{-3}	3.15 x 10^{-3}	2.67 x 10^{-3}	2.57 x 10^{-3}
NT						
Thioanisole		No reaction			0.110	0.112

(Figure 4.21). Second-order rate constants (k_2) for **Cu-2**, **Cu-3**, **Cu-2-Sc** and **Cu-3-Sc** were determined from the dependence of the pseudo-first-order rate constants on toluene concentrations (Figure 4.22, Table 4.4). As for **Cu-1-M** intermediates, only the initial 500 seconds were taken for the pseudo-first-order fitting since deviations from this behavior are observed in the latter phases of the reaction.

Different trends can be analyzed from the k_2 values obtained. First, we can compare the rate constants obtained for the oxidation of toluene with the three different scandium adducts; the observed trend for the reaction rates is the following: k_2 **Cu-1-Sc** > k_2 **Cu-2-Sc** > k_2 **Cu-3-Sc**. Notably, the reaction rate trend is opposite to that obtained for the stability of the intermediates. This is a clear display of the inverse behaviors between reactivity and stability.

Secondly, it is very interesting to compare the second-order rate constants obtained for the free species and the scandium adduct that contain the same oxidant. When comparing the reaction rates between **Cu-2** and **Cu-2-Sc** on the one hand, and **Cu-3** and **Cu-3-Sc** on the other, near-identical rate constants are found for the free- and the scandium adduct species (Table 4.4), whose differences can be located within the limits of experimental error. To provide further proof of this trend, other substrates were tested using the intermediates formed with the oxidant sPhINAr^{NO2}: **Cu-3** and **Cu-3-Sc**.

The oxidation of the substrates xanthene and 1,4-cyclohexadiene (CHD) by **Cu-3** and **Cu-3-Sc** was followed by UV-vis spectroscopy using the same methodology as before; the linear fittings of k_{obs} vs substrate concentration of xanthene are shown in Figure 4.24 and the k_2 values obtained are presented in Table 4.4. The k_2 values for these substrates' oxidation with **Cu-3** and **Cu-3-Sc** show the same conduct as was observed for toluene: the free species and the scandium adduct have the same behavior toward substrates in oxidation reactions. Additionally, **Cu-3** and **Cu-3-Sc** were also tested in nitrene transfer reaction (NT) to thioanisole at −90 °C, showing nearly identical rates consistent with the behavior observed for HAA reactions (Table 4.4).

This finding backs up the independency of the oxidation rates with the external Lewis acid employed, as observed in the **Cu-1-M** series. The near-identical reactivity of **Cu-2** compared to **Cu-2-Sc** and **Cu-3** compared to **Cu-3-Sc**, supports the hypothesis that a Lewis acid free species is responsible for the reactivity in this family of copper nitrenes. In that hypothesis the Lewis acid free species is present in solution in very low concentrations due to an equilibrium occurring between the scandium adduct of the terminal copper nitrene and its free species. In the presence of a substrate, this equilibrium is displaced as the terminal species is consumed (Scheme 4.4 a). To

further corroborate the existence of this equilibrium, experiments were performed in which a fixed amount of [(AN)Cu](BF$_4$) and the oxidant sPhINAr^{NO2} were reacted in the presence of increasing amounts of scandium and the intermediate thus formed was set to react with CHD. The trend of the reaction rates (k_2) for the oxidation reaction of CHD at −90 °C with **3-Sc** obtained with different amounts of scandium present in solution is shown in Figure 4.23 (black squares and black solid line).

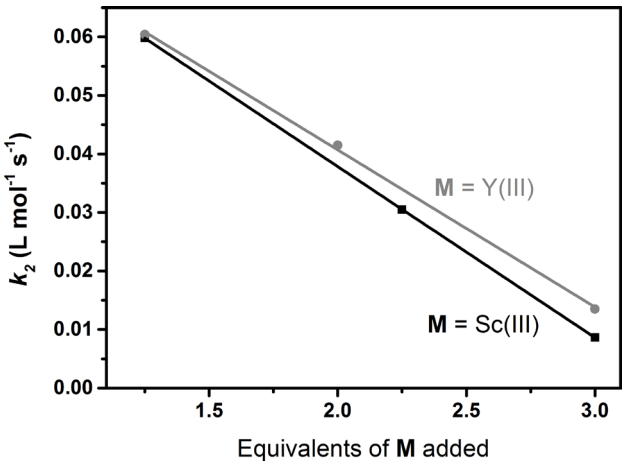

Figure 4.23: Decrease in the reaction rate (k_2) of **Cu-3-M** with CHD at −90 °C in CH_2Cl_2 in the presence of increasing equivalents of **M** present in solution when **M**=Sc(III) black squares and black solid connecting line and **M**=Y(III) gray circles and gray solid connecting line.

In Figure 4.23 it can be seen that the reaction rates unequivocally fall as the concentration of scandium increases. This corroborates the existence of an equilibrium in solution; the more scandium present, the more shifted the equilibrium is towards the scandium adduct and the less the free species is present in solution, which slows down the reaction. To further study this phenomenon, the behavior of the intermediate **Cu-3-Y**, generated with different amounts of Y(OTf)$_3$, was also tested against CHD (Figure 4.23 gray circles and gray solid line). Again, it can be seen that the k_2 values decrease as the amount of Y(III) present in solution increases, as expected in an equilibrium. It is worth noticing that the rate at which the k_2 values decrease is dependent on the **M** employed. When large equivalents of Y(OTf)$_3$ were employed, the reaction with CHD was faster than the same reaction with the same number of equivalents of Sc(OTf)$_3$. This could be a reflection of how strongly **M** is bound to the copper-nitrene core, while Sc(III) is more Lewis acidic and binds more strongly to the copper-nitrene core and the equilibrium between the scandium adduct and the free species is slower than the same equilibrium with the less strongly-bound yttrium. The differences are nonetheless quite small and only start to be evident when larger amounts of **M** are employed (more than 2 equivalents); unfortunately, given the poor solubility of

the $M(OTf)_3$ salts in the solvents at −90 °C, it is not possible to evaluate the effect of a much larger excess. However, these results do point towards the equilibrium suggested in Scheme 4.4 a.

Finally, a third analysis of the kinetic data can be made. Both **Cu-3** and **Cu-3-Sc** show an increase in the rates of the reactions, which can be correlated with a decrease in the BDEs of the substrates employed[27] (Table 4.4), reveling a rate-determining H-atom abstraction process. Furthermore, a deuterium kinetic isotope effect (KIE) of 4.24 was obtained for **Cu-3-Sc**, and 4.31 for **Cu-3**, when d_2-xanthene was used as a substrate at −90 °C (Figure 4.24). Such a KIE value corroborates the proposed hydrogen atom abstraction radical rebound (HAA/RR) mechanism and is consistent with the values obtained for other reported metal nitrenes.[7]

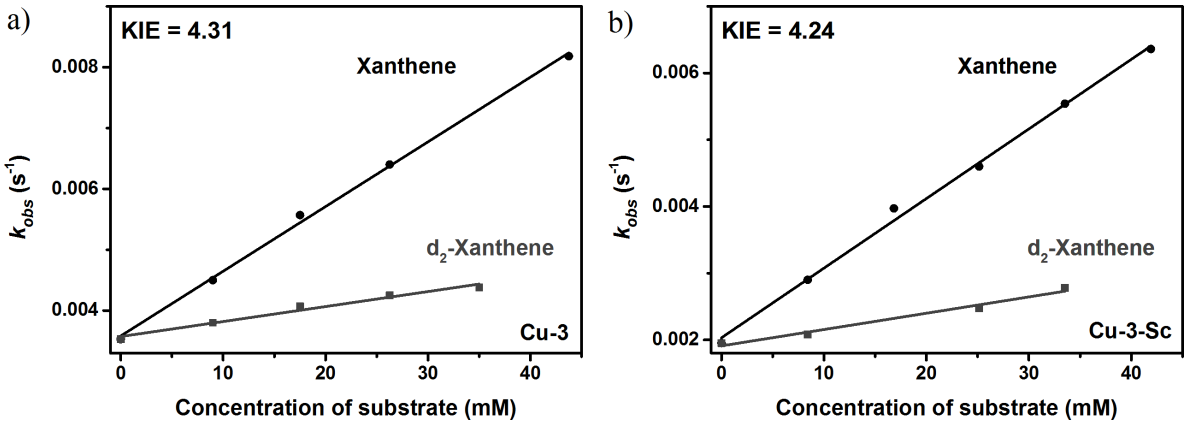

Figure 4.24: Linear dependence of k_{obs} on the concentration of the substrate for the reactions of a) **Cu-3**, b) **Cu-3-Sc**, with xanthene and d_2-xanthene at −90 °C in CH_2Cl_2.

The possibility of stabilizing the free species: **Cu-2** and **Cu-3,** as well as the scandium adducts: **Cu-2-Sc** and **Cu-3-Sc,** of terminal copper nitrenes achieved *via* nitrene source design, provided us with a unique opportunity for studying and understanding the behavior of copper nitrenes in solution. However, the studies carried out so far were performed in a family of copper-nitrenes obtained from iminoiodinane derivatives by introducing electron-withdrawing groups in the phenyl ring. To get a full image of the effect that changing the nitrene source has on the trapping of copper-nitrene intermediates and their scandium adducts, a different nitrene source, an organic azide with an electron-donating group, was employed.

4.2.2.2 The use of mesityl-azide as the nitrene source

A new scandium adduct **Cu-4-Sc** was stabilized and characterized. It was generated from the reaction of mesityl-azide with $[(AN)Cu](BF_4)$ in the presence of $Sc(OTf)_3$[28,29] and is characterized by the electron-donating mesityl (Mes) group attached to the nitrene group. The effect

of the electron-donating group was evaluated, in contrast with the electron-withdrawing groups employed before.

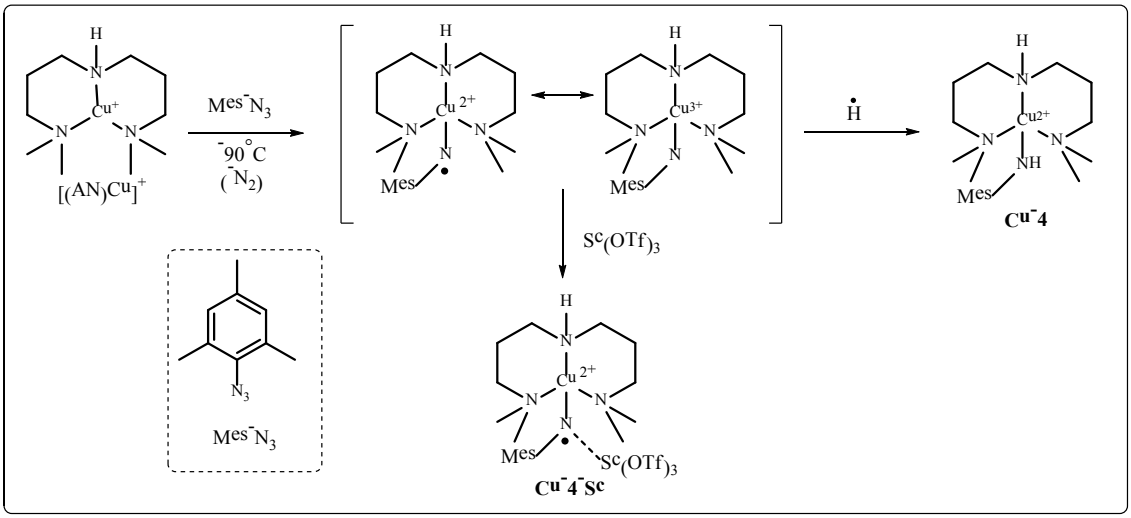

Scheme 4.7: Generation of **Cu-4** and the intermediate **Cu-4-Sc**.

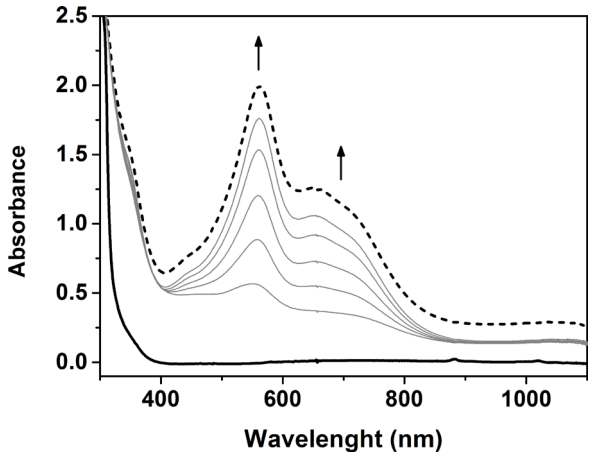

Figure 4.25: Formation of the intermediate **Cu-4-Sc** in CH_2Cl_2 at −90 °C followed by UV-vis spectroscopy. The initial [(AN)Cu](BF_4) absorption spectra is shown in a black solid line and the final **Cu-4-Sc** spectra is shown in a dashed line.

The reaction of [(AN)Cu](BF_4) in CH_2Cl_2 with one equivalent of freshly prepared mesityl-azide at −90 °C in the presence of 1.5 equivalents of $Sc(OTf)_3$ resulted in the formation of a new purple species **Cu-4-Sc** (Scheme 4.7). The formation of this species was not immediate, as occurred with **Cu-1-Sc**, **Cu-2-Sc** and **Cu-3-Sc,** but took 2 hours; the resulting species was stable at −90 °C and only showed a decay of 5% in the 2 hours after full generation. The intermediate **Cu-4-Sc** was EPR-silent and showed a characteristic UV-vis spectrum with absorption maxima centered at λ_{max}

(ε_{max}) = 560 nm (2000 L mol^{-1} cm^{-1}) and 670 nm (1227 L mol^{-1} cm^{-1}) (Figure 4.25). Interestingly, both the color and the absorption spectra are similar to those obtained for the copper-nitrene scandium adducts isolated so far in our group.

When the reaction of [(AN)Cu](BF_4) in CH_2Cl_2 with one equivalent of freshly prepared mesityl-azide at −90 °C was performed in the absence of scandium, a new copper(II) species (**Cu-4**) was formed. **Cu-4** is not a transient intermediate since it did not decay in solution. It showed a characteristic copper(II) signal in EPR. Although no further characterization of **Cu-4** was performed, based on previous studies[22] it can be assigned to the copper(II)–amidate complex [(AN)Cu^{II}(HNMes)]$^+$.

The consumption of the azide after the formation of **Cu-4-Sc** was corroborated with infrared spectroscopy (IR). Organic azides have a very specific and intense IR band due to the strong asymmetric vibration of the N≡N of the azido group, which appears in the range of 2170 to 2080 cm^{-1};[30] the mesityl-azid presented a very intense band right in the middle of this range, at 2115 cm^{-1}. In the IR spectra of the reaction mixture after the formation of **Cu-4-Sc**, this band had disappeared completely (Figure 4.26), thus confirming the full consumption of the azide in the reaction.

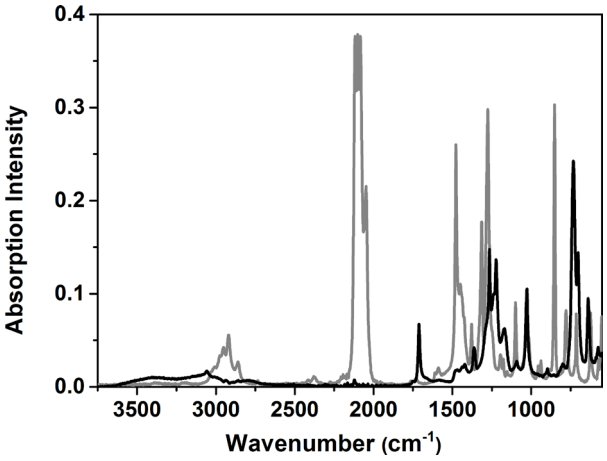

Figure 4.26: IR spectra of the mesityl-azide (gray) and of the solution after the formation of **Cu-4-Sc** (black).

To further research the nature of **Cu-4-Sc** and determine the formal oxidation state of the copper in the system, its reactivity towards one-electron reductants was tested. Unlike the copper nitrenes containing sulfonyl groups (**Cu-1-Sc**, **Cu-2-Sc** and **Cu-3-Sc**), **Cu-4-Sc** did not react with ferrocene at −90 °C. This might be a result of the electron-donating ability of the Mes group of the nitrene, which prevents the reduction from taking place. The use of a stronger reductant, namely

$Me_{10}Fc$, allowed two-electron reduction to take place in CH_2Cl_2 at −90 °C. This reaction resulted in the formation of a copper(I) species and two equivalents of the cation $Me_{10}Fc^+$ (Figure 4.27). The obtained yield of $Me_{10}Fc^+$ (183%) confirmed that **Cu-4-Sc** is two oxidation levels above [(AN)Cu](BF_4), so it is a formal copper(III), and its initial yield is above 90%.

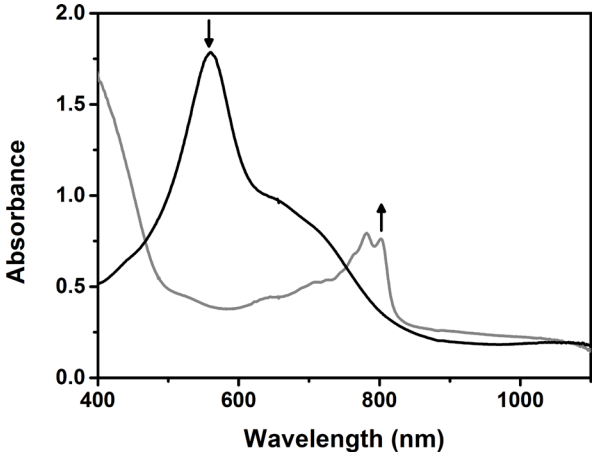

Figure 4.27: Absorption spectra of **Cu-4-Sc** (black line) (1 mM) and the product of its reaction with decamethylferrocene ($Me_{10}Fc$) (gray line) in CH_2Cl_2 at −90 °C.

To get a better picture of the geometric and electronic structure of the **Cu-4-Sc** adduct, X-ray absorption spectroscopy (XAS) was also performed. As discussed before, formal copper(III) intermediates can exist in three different electronic configurations described in Figure 4.1: a singlet copper(III)-imido $[Cu^{III}(NR)]^+$, a singlet copper(II)-radical imidyl $[Cu^{II}(NR^{\bullet})]^+$ or a triplet copper(II)-radical imidyl $[Cu^{II}(NR^{\bullet})]^+$. Cu *K*-edge XAS can provide information about the oxidation state of the copper in the sample, as well as other clues regarding the geometry around the metal center.

The Cu *K*-edge X-ray absorption spectrum obtained for **Cu-4-Sc** and those of **Cu-1-Sc** and [(AN)Cu](BF_4) are presented in Figure 4.28. When comparing the edge features of **Cu-4-Sc** with those of the precursor [Cu(AN)](BF_4), it becomes evident that there is a shift in energies similar to that observed for **Cu-1-Sc**. However, the edge energy is not a suitable indicator for distinguishing between copper(III) and copper(II) in a complex. The only feature that can be used unambiguously to distinguish the copper oxidation state in the sample is the pre-edge.[26] The pre-edge transition of **Cu-1-Sc** is visible and appears at ca. 8978 eV, thus confirming its $[Cu^{II}(NTs^{\bullet})]^+$ nature, as with **Cu-3** and **Cu-3-M**. Unfortunately, this transition is not present in the Cu *K*-edge XAS spectra of **Cu-4-Sc** (Figure 4.28 inset), which prevents the assignment of the oxidation state of the copper in this species.

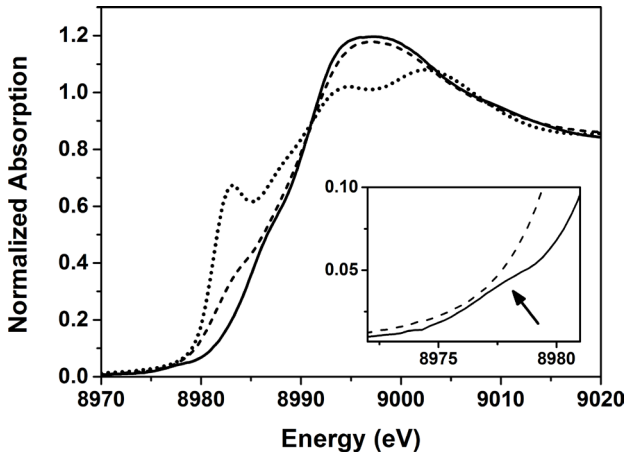

Figure 4.28: Normalized Cu *K*-edge spectra for [(AN)Cu](BF$_4$) (dotted line), **Cu-1-Sc** (solid line) and **Cu-4-Sc** (dashed line). The inset shows an expansion of the pre-edge region.

Another relevant feature that can be observed in the spectra of **Cu-4-Sc** is the shoulder along the rising edge that is absent in **Cu-1-Sc**. This shoulder appears at 8981.5 eV, an energy value that is typically associated with 1*s*→4*p* transitions.[26,31] The energy of this band might indicate that the copper is in a three-coordinate trigonal planar geometry.[31,32] This is in contrast with the geometry previously reported for copper in **Cu-1-Sc**, namely a distorted square pyramidal geometry, and it would imply that the ligand AN in **Cu-4-Sc** is acting as a bidentate ligand with one of the terminal nitrogen atoms remaining outside of the copper coordination sphere.

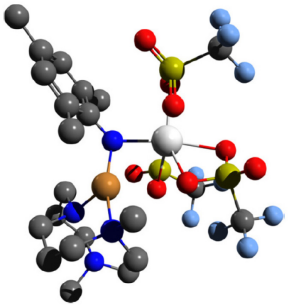

Figure 4.29: DFT energy-minimized structure for the singlet state of **Cu-4-Sc**. Gray-carbon, blue-nitrogen, red-oxygen, yellow-sulfur, orange-copper, light blue-fluorine and light gray-scandium. The hydrogen atoms are removed for clarity.

The geometry of **Cu-4-Sc** was optimized by DFT calculations. The optimized geometry is shown in Figure 4.29. In this geometry, the ligand AN is only coordinated to the copper through two of its nitrogen atom donors and the third one, one of the terminal tertiary amines, remains outside of its coordination sphere. The three-coordinate trigonal planar geometry around the copper

center is in keeping with what was observed from the shoulder on the rising edge of the Cu *K*-edge XAS of **Cu-4-Sc**. The bidentate coordination style of the ligand AN has been observed before in the hetero-bi-metallic $[Cu^{III}(\mu\text{-}O)_2Ni^{III}]^{2+}$ [33] as well as in the previously described species **Cu-2** and **Cu-3**.

To further understand the factors governing reactivity in copper-nitrene chemistry, and at the same time exploit the fact that **Cu-4-Sc** is stable at −90 °C, reactivity studies were performed. **Cu-4-Sc** was tested as an oxidant for two different kinds of reactions: hydrogen atom abstraction (HAA) and nitrene transfer (NT) reactions. As for the other complexes, the reactivity studies of **Cu-4-Sc** were performed at −90 °C under an inert atmosphere. A solution of **Cu-4-Sc** in CH_2Cl_2 was prepared in situ and a solution with a determined amount of substrate in the same solvent was injected. The decay of the 560 nm band was then monitored and fitted to a pseudo-first-order decay which yielded the rate constant (k_{obs}) for each concentration of the substrate employed (Figure 4.30). k_{obs} was found to increase linearly with the increase in the substrate concentration and the slope of this linear increase provided the second-order rate constants (k_2, Figure 4.31).

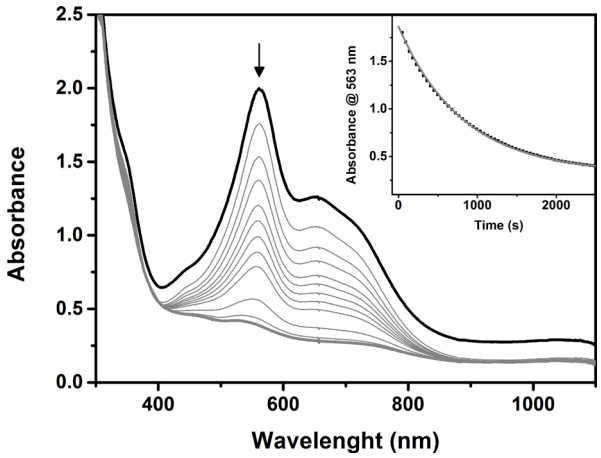

Figure 4.30: Changes in the absorption spectra of **Cu-4-Sc** associated with its reaction with 20 equivalents of CHD obtained from an initial 1 mM solution at −90 °C in CH_2Cl_2. Inset: Time trace of the pseudo-first-order decay of the absorption band at 560 nm in this reaction as a function of time and fitting to a pseudo-first-order decay (gray line).

Nitrene-transfer reactivity of **Cu-4-Sc** was tested against two substrates: triphenylphosphine and thioanisole. The plots of k_{obs} vs. substrate concentration are shown in Figure 4.31a, and the rate constants obtained are presented in Table 4.5. The products from the reaction of **Cu-4-Sc** with PPh_3 were analyzed and the formation of *N*-(mesityl)-iminotriphenyl-phosphorane was confirmed. The

resulting solution was EPR-silent, which might indicate the formation of a copper(I) species after the reaction.

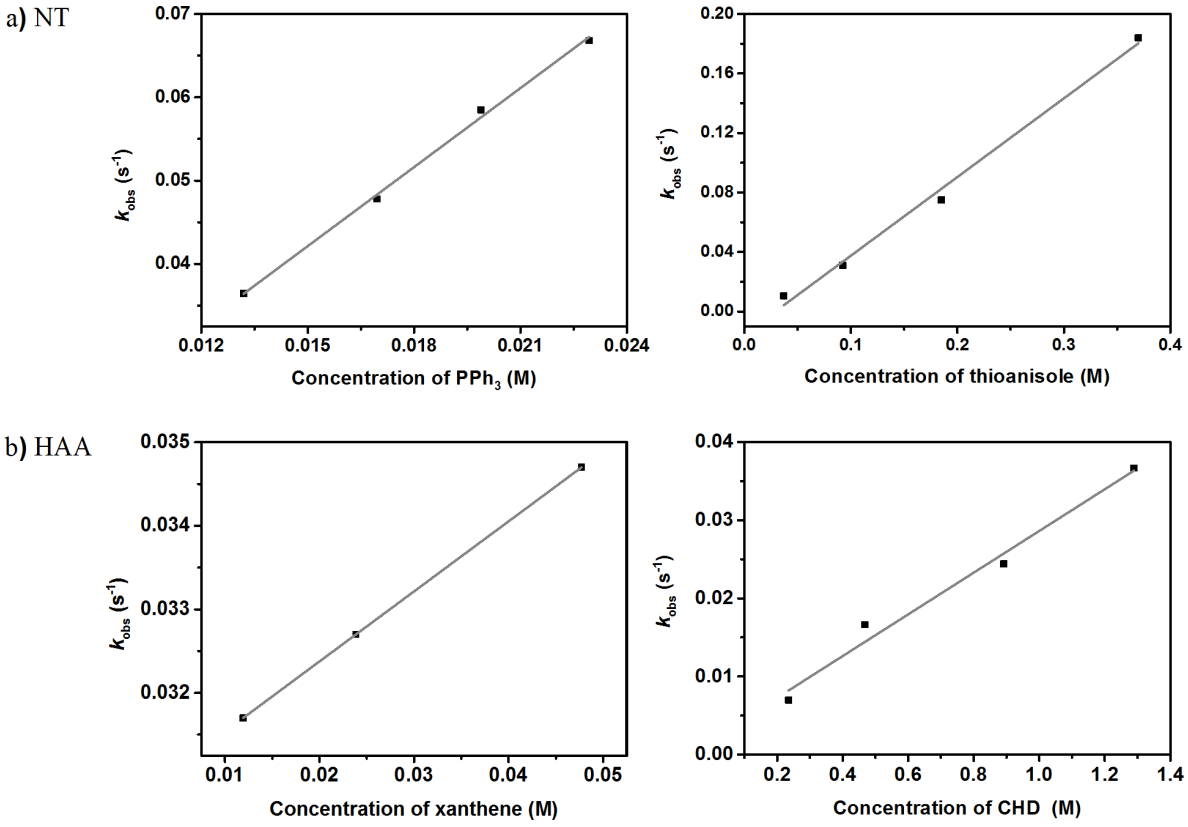

Figure 4.31: Linear dependence of k_{obs} on the concentration of the substrate for a) nitrene transfer (NT) and b) hydrogen atom abstraction (HAA) reactions with **Cu-4-Sc** at −90 °C in CH_2Cl_2.

On the other hand, the ability of **Cu-4-Sc** to perform HAA reactions was also evaluated, this time against three substrates: xanthene, 1,4-cyclohexadiene (CHD) and toluene. The plots of k_{obs} vs. substrate concentration are shown in Figure 4.31 b, and the rate constants obtained are presented in Table 4.5. **Cu-4-Sc** reacted with substrates with low bond dissociation energies (BDE)[27] such as xanthene (BDE = 74 kcal mol^{-1}) and CHD (BDE = 76.9 kcal mol^{-1}) but was not able to oxidize hydrocarbons with higher BDEs like toluene (BDE = 88.6 kcal mol^{-1}). An analysis of the reaction mixture for CHD showed the formation of benzene in near-quantitative yields.

The rate constants obtained for the scandium adducts of copper nitrenes studied so far, namely **Cu-1-Sc**, **Cu-2-Sc**, **Cu-3-Sc** and **Cu-4-Sc**, are all presented together in Table 4.5. A contrasting reactivity pattern can be appreciated, in which the complex **Cu-4-Sc** is a better oxidant in nitrene transfer reactions (with rates 4-14 times faster), while it performs worse at hydrogen atom

abstraction reactions (with rates 1.2- 5 times slower) than the sulfonated copper nitrenes (**Cu-X-Sc**, where **X=1**,**2**,**3**).

Table 4.5: Second-order rate constants (k_2) of **Cu-1-Sc**,[22] **Cu-2-Sc**, **Cu-3-Sc** and **Cu-4-Sc** determined for different substrates in HAA and NT reactions in dichloromethane at −90 °C.

	Cu-4-Sc	**Cu-1-Sc**	**Cu-2-Sc**	**Cu-3-Sc**
	k_2 (L mol^{-1} s^{-1})	k_2 (L mol^{-1} s^{-1})	k_2 (L mol^{-1} s^{-1})	k_2 (L mol^{-1} s^{-1})
HAA				
Xanthene	0.084	0.3135		0.104
CHD	0.030	0.1554		0.060
Toluene	No reaction	0.0051	0.0032	0.0026
NT				
PPh_3	2.89	0.196		
Thioanisole	0.5	No reaction		0.112

From the analysis of Table 4.5, it is clear that the introduction of an electron-donating group attached to the nitrene does has a strong effect on the reactivity of the copper-nitrene complexes. The observed reactivity trend of **Cu-4-Sc** is the inverse of that obtained for the species where the nitrene is attached to an electron-withdrawing group such as the sulfonyl group (**Cu-X-Sc**, **X=1**,**2**,**3**). The explanation for the observed reactivity patterns, however, is not straightforward. A deeper study of the electronic states and reaction mechanisms of this set of complexes is necessary to obtain a better insight into the role of copper nitrenes and their scandium adducts as reactive intermediates.

4.3 Conclusions

Terminal copper nitrenes and their Lewis acid adducts were studied using the system **Cu-1-Sc**[22] as a reference. The effects of changing the Lewis acid **M** were studied. It was found that in the stabilization of the copper-tosylnitrene intermediate via its interaction with an external redox non-innocent metal ion, the nature of **M** affected the yield of the formal Cu(III) species formed; a higher yield is obtained when a stronger Lewis acid is used. This behavior is consistent with the proposed model in which the binding of the external Lewis acids helps to reduce the hydrogen atom abstraction ability of the transient copper-nitrene intermediate, thereby preventing its spontaneous

decay to the copper(II)-amide species. Interestingly, however, the electronic structures of the **Cu-1-M** complexes were found to be independent of the nature of the Lewis-acidic metal ions. Similarly, the metal ions proved to have no influence on the reactivity of the **Cu-1-M** complexes since near-identical rates were obtained for PPh_3 when different Lewis acids were employed. This indicated the presence of a common reactive intermediate in the reactions of **Cu-1-M** complexes with PPh_3.

The use of different nitrene sources in the form of iminoiodinane-derivatives with internal electron-withdrawing groups allowed us to trap four new intermediates: **Cu-2-Sc**, **Cu-3-Sc**, **Cu-2** and **Cu-3**. For the first time, we had access to terminal copper nitrenes isolated both as free species, **Cu-2** and **Cu-3**, and as their scandium adducts, **Cu-2-Sc** and **Cu-3-Sc**, in the same conditions. The reactivity of the intermediates revealed the occurrence of an equilibrium in solution between the Lewis acid adducts and the free species, the latter being responsible for reactivity, thus proving the existence of a common reactive intermediate as proposed with the series of **Cu-1-M** complexes.

Finally, the use of mesityl azide as the nitrene source allowed the trapping and characterization of another terminal copper-nitrene scandium adduct **Cu-4-Sc**. It was observed that the introduction of an electron-withdrawing group attached to the nitrene has an effect on the reactivity of this class of complexes. A contrasting reactivity pattern was observed when comparing the reaction rates obtained for the **Cu-4-Sc** complex with those of the related **Cu-X-Sc** (**X=1**,**2**,**3**), where the former is more reactive in NT reactions while the latter are more reactive in HAA reactions. More studies are necessary to properly explain this trend.

4.4 References

[1] R. Hili, A. K. Yudin, *Nat. Chem. Biol.* **2006**, *2*, 284–287.

[2] A. Ricci, *Amino Group Chemistry: From Synthesis to the Life Sciences,* 1st Ed., Wiley-VCH Verlag GmbH & Co. KGaA, **2007**.

[3] K. Shin, H. Kim, S. Chang, *Acc. Chem. Res.* **2015**, *48*, 1040–1052.

[4] J. W. W. Chang, T. M. U. Ton, P. W. H. Chan, *Chem. Rec.* **2011**, *11*, 331–357.

[5] D. N. Zalatan, J. Du Bois, *Top. Curr. Chem.* **2010**, *292*, 347–378.

[6] H. Kwart, A. A. Kahn, *J. Am. Chem. Soc.* **1967**, *89*, 1950–1951.

[7] R. T. Gephart, T. H. Warren, *Organometallics* **2012**, *31*, 7728–7752.

[8] Z. Li, R. W. Quan, E. N. Jacobsen, *J. Am. Chem. Soc.* **1995**, *117*, 5889–5890.

[9] A. N. Vedernikov, K. G. Caulton, *Chem. Commun.* **2004**, 162–163.

[10] X. Dai, P. Kapoor, T. H. Warren, *J. Am. Chem. Soc.* **2004**, *126*, 4798–4799.

[11] E. Kogut, H. L. Wiencko, L. Zhang, D. E. Cordeau, T. H. Warren, *J. Am. Chem. Soc.* **2005**, *127*, 11248–11249.

[12] Y. M. Badiei, A. Krishnaswamy, M. M. Melzer, T. H. Warren, *J. Am. Chem. Soc.* **2006**, *128*, 15056–15057.

[13] Y. M. Badiei, A. Dinescu, X. Dai, R. M. Palomino, F. W. Heinemann, T. R. Cundari, T. H. Warren, *Angew. Chem. Int. Ed.* **2008**, *47*, 9961–9964.

[14] F. Dielmann, D. M. Andrada, G. Frenking, G. Bertrand, *J. Am. Chem. Soc.* **2014**, *136*, 3800–3802.

[15] T. Corona, L. Ribas, M. Rovira, E. R. Farquhar, X. Ribas, K. Ray, A. Company, *Angew. Chem. Int. ed.* **2016**, *128*, 14211–14214.

[16] P. Brandt, M. J. So, P. G. Andersson, P.-O. Norrby, *J. Am. Chem. Soc.* **2000**, *122*, 8013–8020.

[17] T. R. Cundari, A. Dinescu, A. B. Kazi, *Inorg. Chem.* **2008**, *47*, 10067–72.

[18] P. Comba, C. Lang, C. L. De Laorden, A. Muruganantham, G. Rajaraman, H. Wadepohl, M. Zajaczkowski, *Chem. - A Eur. J.* **2008**, *14*, 5313–5328.

[19] S. M. Tekarli, T. G. Williams, T. R. Cundari, *J. Chem. Theory Comput.* **2009**, *5*, 2959–2966.

[20] D. N. Barman, P. Liu, K. N. Houk, K. M. Nicholas, *Organometallics* **2010**, *29*, 3404–3412.

[21] L. Maestre, W. M. C. Sameera, M. M. Díaz-Requejo, F. Maseras, P. J. Pérez, *J. Am. Chem. Soc.* **2013**, *135*, 1338–1348.

[22] S. Kundu, E. Miceli, E. Farquhar, F. F. Pfaff, U. Kuhlmann, P. Hildebrandt, B. Braun, C. Greco, K. Ray, *J. Am. Chem. Soc.* **2012**, *134*, 14710–14713.

[23] S. Fukuzumi, K. Ohkubo, *J. Am. Chem. Soc.* **2002**, *124*, 10270–1.

[24] S. Kundu, *PhD Thesis: Synthesis, Spectroscopic Characterization and Reactivity of the High-Valent Metal-Oxo/Imido Cores of the Late Transition Metals*, Humboldt-Universität Zu Berlin, Berlin, **2013**.

[25] S. Fukuzumi, Y. Morimoto, H. Kotani, P. Naumov, Y.-M. Lee, W. Nam, *Nat. Chem.* **2010**, *2*, 756–759.

[26] J. L. Dubois, P. Mukherjee, T. D. P. Stack, B. Hedman, E. I. Solomon, K. O. Hodgson, S. U. V, S. Radiation, R. V August, *J. Am. Chem. Soc.* **2000**, *122*, 5775–5787.

[27] Y.-R. Luo, *Comprehensive Handbook of Chemical Bond Energies*, CRC Press, Boca Raton, Florida, **2007**.

[28] S.-L. Abram, *Diplomarbeit: Stabilizierung von Kupfer-Nitreneinheiten Zur C-H-Bindungsaktivierung*, Berlin, **2013**.

[29] S.-L. Abram, I. Monte-Pérez, F. F. Pfaff, E. R. Farquhar, K. Ray, *Chem. Commun.* **2014**, *50*, 9852–4.

[30] E. Lieber, C. N. R. Rao, T. S. Chao, C. W. W. Hoffman, *Anal. Chem.* **1957**, *29*, 916–918.

[31] L. Kau, D. J. Spira-Solomon, J. E. Penner-Hahn, K. O. Hodgson, E. I. Solomon, *J. Am. Chem. Soc.* **1987**, *109*, 6433–6442.

[32] N. P. Mankad, W. E. Antholine, R. K. Szilagyi, J. C. Peters, *J. Am. Chem. Soc.* **2009**, *131*, 3878–80.

[33] S. Kundu, F. F. Pfaff, E. Miceli, I. Zaharieva, C. Herwig, S. Yao, E. R. Farquhar, U. Kuhlmann, E. Bill, P. Hildebrandt, H. Dau, M. Driess, C. Limberg, K. Ray, *Angew. Chem. Int. Ed.* **2013**, *52,* 5622–5626.

Chapter 5:
Conclusions and outlook

High-valent metal-oxo, -peroxo and -nitrene cores of middle to late transition metals like iron, cobalt, nickel and copper have been proposed as vital intermediates in a number of fundamental biological and technologically attractive transformations like C−H bond oxidation, aziridination, epoxidation and dioxygen reduction. The isolation and characterization of these intermediates can provide a lot of information about the reaction mechanisms and is therefore helpful in designing new and improved catalysts. This Thesis has explored the chemistry of high-valent intermediates ranging from oxoiron(IV) complexes and bridging μ-peroxo dicobalt(III) systems to copper-nitrene cores. Detailed spectroscopic, theoretical and reactivity studies have been performed to reveal the correlations between the electronic structure and reactivity patterns of these highly relevant intermediates. The principal outcomes and outlook of this work are discussed below.

Chapter 2

The chemistry of a new oxoiron(IV) intermediate, **Fe-2**, was investigated with the aim of evaluating the effect of weaker ligand-field environments in oxoiron(IV) systems. **Fe-2** is supported in the **TMCO** ligand, which is analogous to the known **TMC** one, but in this ligand one of the nitrogen donors has been replaced by an oxygen one. The **TMCO** ligand was employed to generate a high-spin Fe(II) complex **Fe-1** that reacted with sPhIO at −90 °C in dichloromethane to generate **Fe-2**. The iron center in **Fe-2** is in a Fe(IV) oxidation state, as proved by Möβbauer and XAS studies, and has an S = 1 ground state, determined from magnetic Möβbauer studies.

Fe-2 proved to be highly reactive in C−H bond activation and group transfer reactions, in contrast with **Fe-TMC**, which shows poor oxidative reactivity. Four factors were detected that might account for the higher reactivity of **Fe-2** in comparison with **Fe-TMC**:

1. **Fe-2** has a smaller gap than **Fe-TMC** between the triplet and quintet electronic state, as was proved by magnetic Möβbauer studies. The quintet state is known to be the most active electronic state in oxoiron(IV) complexes.
2. **Fe-2** might have a more exposed Fe=O core through the site occupied by the oxygen donor of the ligand, which would facilitate the approach of the substrate.
3. The oxygen donor of the **TMCO** ligand in **Fe-2** might be able to de-coordinate from the iron center in solution, thus leaving more space for the substrate to approach the active center.
4. The asymmetry of the **TMCO** ligand might have a role in the increase in reactivity in **Fe-2**. This was revealed by comparing the reactivity of the **Fe-TMC** and **Fe-4d** complexes, which

have identical backbone structures but one nitrogen donor in the former has been replaced by an oxygen one in the latter.

The results obtained here prove that exchanging one nitrogen donor for an oxygen one does have an important impact on the reactivity of the oxoiron(IV) complexes, making them more reactive. This could be a starting point for further studies on oxoiron complexes with ligand systems analogous to **TMCO** but with two, three, or four oxygen donors.

Chapter 3

The previously reported hexanuclear cobalt complex **Co-L$_6$** was further studied in this Thesis with the aim of deepening our knowledge of the reactivity of multinuclear systems, and particularly, to be able to compare it with the best known **Fe-L$_6$** complex. The cobalt(II) centers in **Co-L$_6$** are in an S = 3/2 ground state with no interaction between them. Each cobalt center is in a trigonal bipyramidal geometry with two triflate ions coordinated to it.

Co-L$_6$ was found to be capable of catalytically reducing O_2. Interestingly, the mechanism of the O_2 reduction reaction catalyzed by **Co-L$_6$** is temperature-dependent. At 25 °C the two-electron reduction to H_2O_2 takes place, while at −50 °C the four-electron reduction to H_2O occurs. **Co-L$_6$** is a better catalyst for the four-electron reduction of O_2, showing a turnover number TON_{2000s} of 64, four times larger than the TON_{2000s} for the two-electron process with the same catalyst. The four-electron reduction of O_2 to H_2O proceeds through a rate-determining PCET step while the rate-determining step of the two-electron O_2 reduction involves the four reacting species. The details of the reduction mechanisms are, however, still open to discussion.

The intermediate **Co-1**, generated at 25 °C from the reaction of **Co-L$_6$** with O_2, is active both in nucleophilic as well as in electrophilic transformations. The nucleophilic and electrophilic natures of **Co-1** were originally attributed to the bridging μ-peroxo-dicobalt(III) (spectroscopically characterized) and the oxocobalt(IV) complex (suggested to be formed in solution from the O−O bond homolysis of the peroxo intermediate) respectively. However, from the obtained KIE and the results in $H_2{}^{18}O$ exchange experiments, it was determined that the electrophilic nature of **Co-1** is also attributable to the peroxo complex. This is an exciting result since peroxo-complexes active in electrophilic transformations have not typically been detected in model chemistry although they have been proposed in biological systems.

The observed reactivity of the complex **Co-L$_6$** is in sharp contrast with that reported for **Fe-L$_6$**. While **Fe-L$_6$** was capable of performing the O−O bond formation reaction, **Co-L$_6$** catalyzed

the O−O bond breaking reaction in the four-electron O_2 reduction to H_2O. This proves that varying the metal center in the same ligand structure can lead to different reactivity patterns. The results obtained here also prove that multinuclear systems have great potential as catalysts and show interesting and exceptional reactivity trends. Further studies involving other metals such as copper, in similar ligand environments, would be of great interest, since copper complexes are known to be good catalysts in the O_2 reduction reaction and have potential applications in devices such as fuel cells where the O−O bond formation and cleavage reactions are of great importance. Other types of multinuclear ligands could also lead to interesting results in catalytic transformations and their applications, particularly ligands that do not contain tin in their structures since this element complicates the characterization of the ligand, complexes and intermediates due to its large atomic weight.

Chapter 4

As a continuation of the studies on the scandium adduct of the copper(II)-tosylimidyl radical **Cu-1-Sc**, the first isolated copper-nitrene complex, we have expanded our knowledge of this family of compounds by studying the effect of the Lewis acid (**M**) and the nitrene source in the generation, structure and reactivity of terminal copper nitrenes and their Lewis acid adducts.

Three different effects were found in the stabilization of the copper-tosylnitrene intermediate *via* its interaction with external redox non-innocent metal ions (**M**):

1. The nature of **M** affects the yield of the formal Cu(III) species formed, as a higher yield is obtained when a stronger Lewis acid is used.
2. The electronic structures of the **Cu-1-M** complexes are independent of the nature of the Lewis-acidic metal ions employed. In all cases they can be described as copper(II) imidyl radicals $[Cu^{II}(NTs^{\bullet})]^{+}$.
3. The reactivity of the **Cu-1-M** complexes is unaffected by **M**.

It is proposed that the role of the external Lewis acid **M** in the stabilization of **Cu-1-M** complexes is the reduction of the strong electronic repulsion between the electron-rich nitrogen and copper atoms. In this manner, **M** reduces the hydrogen atom abstraction ability of the $[(AN)Cu^{II}(NTs^{\bullet})]^{+}$ core, preventing its spontaneous decay to the copper(II)-amide species. However, **M** has been proven to have no significant effect on the copper-nitrene $[(AN)Cu^{II}(NTs^{\bullet})]^{+}$ structure. On the other hand, the independence of the reactivity of **Cu-1-M** with the **M** employed

suggested the presence of a common reactive intermediate in the reactions of **Cu-1-M** complexes with substrates.

The effect of changing the nitrene source was also studied. Four new intermediates **Cu-2-M**, **Cu-3-M**, **Cu-2** and **Cu-3** were isolated by using different nitrene sources in the form of iminoiodinane-derivatives with internal electron-withdrawing groups. For the first time, we have access to two terminal copper-nitrenes both isolated as free species, **Cu-2** and **Cu-3**, and as their Lewis acid adducts, **Cu-2-M** and **Cu-3-M**. All the studied species both with and without **M** are two oxidation states above Cu(I) and can be described as copper(II) imidyl radicals $[Cu^{II}(NR^{\bullet})]^{+}$. The reactivity of the intermediates revealed the occurrence of an equilibrium in solution between the Lewis acid adducts and the free species, with the latter being responsible for reactivity, thus proving the existence of a common reactive intermediate as proposed with the series of **Cu-1-M** complexes.

Finally, the use of mesityl azide as the nitrene source allowed the trapping and characterization of another terminal copper-nitrene scandium adduct **Cu-4-Sc**, this time with an electron-donating group (mesityl), in contrast to the previously discussed complexes. The complex **Cu-4-Sc** is also two oxidation states above Cu(I) but its structure could not be determined by XAS. A contrasting reactivity pattern was observed when comparing the reaction rates obtained for the **Cu-4-Sc** complex with those of the related **Cu-X-Sc** (**X=1**,**2**,**3**) complexes, as the former is more reactive in NT reactions while the latter are more reactive in HAA reactions. However, more mechanistic studies are necessary to explain this interesting trend.

There is a lot yet to be explored in the field of copper nitrenes. This is a young field of research and more studies are necessary, with different nitrene sources, Lewis acids and ligand systems to generate a larger database and elucidate general trends in copper-nitrene chemistry and reactivity. Besides the interest that copper-nitrenes have *per se*, understanding the reactivity patterns of this species can also provide detailed insights into the chemical properties of the as yet non-isolated copper-oxo $[CuO]^{+}$ core, which is isoelectronic to copper nitrenes.

Chapter 6:
Equipment and experimental work

6.1 General techniques and chemicals employed

All studies and measurements were performed in the Institut für Chemie at the Humboldt Universität zu Berlin, unless otherwise stated. All the chemicals employed were purchased from the companies: SIGMA-ALDRICH, ABCR, ACROS and TCI and used without further purification unless required. Anhydrous solvents were purchased from CARL-ROTH GMBH under the tradename ROTIDRY ($\geq$ 99.5%, < 50 ppm H_2O) and degassed before use. Deuterated solvents were purchased from EURISO-TOP.

Compounds sensitive to air or water were prepared and handled under inert atmosphere using either Schleck techniques or a glovebox OMNI-LAB 2 from the company VACATMOSPHERES filled with N_2, with concentration of O_2 and moisture of less than 1 ppm. Gases (N_2 and Ar) of quality 5.0 were used for this purpose and were purchased from AIR LIQUIDE.

Before use, the glassware was set in the oven and then treated with a heat-gun under vacuum. The glassware employed was cleaned in a KOH/isopropanol bath and then treated in an HCl bath for neutralization.

6.2 Analytical techniques

Every analytical sample of air- or water-sensitive compounds was prepared in the glove box under inert atmosphere.

6.2.1. Elemental analysis

All elemental analyses were performed by the analytical service of the Institut für Chemie of the Humboldt Universität zu Berlin. The percentages of Carbon, Hydrogen, Nitrogen and Sulphur were determined using a EURO EA 3000 analyzer from the firma HEKATECH. The reported values are the result of an average of two independent measurements except for sample containing Fluorine, when only one measurement was performed.

6.2.2. Nuclear magnetic resonance spectroscopy (NMR)

The NMR measurements were performed at 27 °C using a spectrometer AV 400 or a spectrometer DPX 300 from the company BRUKER unless otherwise stated. Samples were measured in NMR tubes with 5 mm of diameter. The chemical shifts (δ) are reported in ppm relative to tetramethylsilane and the residual proton signal of the deuterated solvents was employed as an internal standard [for ^{1}H-NMR: δ (ppm): $CDCl_3$ 7.26; CD_2Cl_2 5.30; $(CD_3)_2CO$ 2.10; CD_3CN 1.94].

For low temperature measurements, a BRUKER CRYOSTAT was employed to fix the temperature. The multiplicity of the signals is indicated in the following way: s = singlet, d = doublet, t = triplet, m = multiplet.

6.2.3. Mass spectrometry

A 6210 TOF mass spectrometer form the company AGILENT was employed for recording electrospray ionization- time of flight- mass spectra (ESI-TOF-MS) of organic molecules and inorganic complexes in solution; acetonitrile was used as an eluent. For thermally unstable complexes, direct injections of the freshly thawed solution were made. The software MASSHUNTER QUALITATIVE ANALYSIS version B.02.00 from the company AGILENT was employed for the visualization and handling of the spectra. Expected mass spectra (*m/z* values and isotopic distribution patterns) were calculated with the program MOLECULAR WEIGHT CALCULATOR version 6.48.0.1 from the author MATTHEW MONROE.

6.2.4. Infrared spectroscopy (IR)

IR spectra were measured on a FTIR 8400S Fourier-transform infrared spectrometer from the company SHIMADZU in the range from 4000 to 400 cm^{-1} with a resolution of 2 cm^{-1}. For these measurements, a KBr pellet of the powder sample was prepared. Attenuated total reflectance infrared spectroscopy (ATR-IR) was also employed, using a BRUKER-ALPHA FT-IR spectrophotometer. For these measurements, the sample was placed in the ATR unit under inert atmosphere either as a solid or in a solution, in which case, the solvent was let to evaporate to measure the desired IR spectra. The intensities of the obtained vibrational bands here reported are abbreviated in the following way: s = strong, m = medium, w = weak, br = broad.

6.2.5. UV-vis absorption spectroscopy

The UV-vis absorption spectra were obtained with an AGILENT 8453 diode array spectrometer. The measurements were performed using 10 mm and 5 mm precision cuvettes from SUPRASIL® quartz. The temperature for the measurements was set with a cryostat USP-203-A from the company UNISOCU SCIENTIFIC INTSRUMENTS. The software UV-VISIBLE CHEMSTATION from the company AGILENT was employed for the recording and workup of the spectra and kinetic data.

In a typical UV-vis experiment, a stock solution with a known concentration of the complex was prepared inside the glovebox using anhydrous solvents; 2 mL of this stock solution were placed in a quartz cuvette that was later closed with a septum inside the glovebox. The cuvette was then

placed in the cryostat connected to the UV-vis spectrometer, which was set beforehand at the desired temperature. Once thermal equilibrium was achieved between the cryostat and the cuvette, the solution of the next reactant (*i.e*. oxidant/substrate) in a minimum amount of anhydrous solvent was injected into the cuvette trough the septum and the reaction was monitored following the UV-vis spectral changes.

The molar-extinction coefficient (ε_{max}) corresponding to a particular absorption maxima (λ_{max}) here reported, are the result of several individual measurements. The half-life ($t_{1/2}$) of a given species was determined form the time traces of the decay of its characteristic UV-vis band at a fixed temperature. The kinetics of the reaction of a given species with a substrate were also determined from the fitting of time traces of the decay of its characteristic band. The values thus obtained were employed for the determination of the system's rate constants.

6.2.6. Gas chromatography coupled to mass spectrometry (GC-MS)

After substrate oxidation, the reaction mixtures were analyzed in a VARIAN 3800 gas chromatograph with a flame ionization detector and a VARIAN 4000 mass detector, all from the company AGILENT. An auto-sampler VARIAN CP-8400 and an injector VARIAN 1079 were employed for the injection of the sample to the instrument. Before the analysis, the reaction mixture was passed through silica gel and eluted with ethyl acetate to remove the metal complex. The resulting ethyl-acetate solutions were then analyzed with GC-MS. The products of the reactivity studies were identified by comparing the obtained retention times with the retention times of the pure compounds.

6.2.7. X-Ray diffraction crystallography (XRD)

The crystal structure of the complex **Fe-1** was determined in collaboration with Dr. Fabian Schax. Data collection was performed at 100 K on a STOE IPDS 2T diffractometer by using Mo-K_α radiation (λ = 0.71073 Å). The radiation source was a sealed tube generator with graphite monochromator. Multi-scan (PLATON) absorption corrections were applied. The structure was solved by direct methods (SHELXS-97) and refined by full matrix least-squares procedures based on F^2 with all measured reflections (SHELXL-97). All non-hydrogen atoms were refined anisotropically. Hydrogen atoms were introduced in their idealized positions and refined as riding model.

6.2.8. Electron paramagnetic resonance spectroscopy (EPR)

For recording X-Band EPR derivative spectra, the samples were placed in quartz tubes with 3 mm internal diameter. The spectra were simulated with the program GIFT (from the author Dr. Eckhard Bill). The measurements were performed using different instruments in the following locations:

a) Max-Planck-Institut für Chemische Energiekonversion (MPI CEC)

In cooperation with Dr. Eckhard Bill, X-Band EPR derivative spectra were recorded on an ELEXSYS E500 spectrometer from the company BRUKER, equipped with the dual mode cavity (ER4116DM from BRUKER) and a Helium flow cryostat (ESR 910 from OXFORD INSTRUMENTS). Microwave frequencies were calibrated with a frequency counter (HP5352B) from HEWLETT-PACKARD, and field control was calibrated with a NMR probe (ER035M) from BRUKER.

b) Helmholtz-Zentrum Berlin für Materialien und Energie GmbH

In cooperation with Dr. Alexander Schnegg from the Institut für Silizium-Photovoltaik, X-Band EPR spectra were recorded in an ESP 300 spectrometer from the company BRUKER, equipped with a TE011 SUPER HIGH Q microwave resonator. In this set-up, the samples were cooled down to 77 K with a dewar for liquid nitrogen.

c) University of Michigan

In cooperation with Prof. Dr. Nicolai Lehnert from the University of Michigan, X-Band spectra were recorded on a BRUKER X-BAND EMX spectrometer equipped with OXFORD INSTRUMENTS liquid nitrogen and helium cryostats. EPR spectra were obtained on frozen solutions using ~20 mW microwave power and 100 kHz field modulation with the amplitude set to 1 G.

6.2.9. Resonance Raman (rR) spectroscopy

For performing rR measurements the sample was placed in NMR tubes with an internal diameter of 5 mm. rRaman spectra were obtained in cooperation with the group of Prof. Dr. Peter Hildebrandt from the Technische Universität Berlin using a LABRAM HR 800 confocal Raman spectrometer from the company HORIBA JOBIN-YVON with a detector SYMPHONY II CCD from the company HOROIBA. Kr+ or Ar + lasers INNOVA 400 from the company COHERENT in different wavelengths were employed. A cryostat R 495 from BRUKER was employed to cool down the samples.

6.2.10. Möβbauer spectroscopy

Möβbauer spectra of **Fe-1** and **Fe-2** in the absence of magnetic field were recorded on a SEECO MS6 spectrometer that comprises the following instruments: a JANIS CCS-850 cryostat, including a CTI-CRYOGENICS closed cycle 10 K refrigerator, and a CTI-CRYOGENICS 8200 helium compressor. The cold head and sample mount are equipped with calibrated DT-670-Cu-1.4L silicon diode temperature probes and heaters. Temperature is controlled by a LAKESHORE 335 temperature controller. Spectra are recorded using a LND-45431 Kr gas proportional counter with beryllium window connected to the SEECO W204 γ-ray spectrometer that includes a high voltage supply, a 10 bit and 5 μs ADC and two single channel analyzers. Motor control and recording of spectra is taken care of by the W304 resonant γ-ray spectrometer. For the reported spectra a RIVERTEC MCO7.114 source (^{57}Co in Rh matrix) with an activity of about 1 GBq was used.

The spectrum of **Fe-1** was recorded in a plastic sample holder with about 50 mg of the solid sample at 12 K and data was accumulated for about 24 hours. The spectrum of **Fe-2**, on the other hand, was recorded from a propionitrile solution with 12% dichloromethane of the ^{57}Fe enriched **^{57}Fe-2** generated *in-situ* at -90 °C (see Chapter 2). A plastic sample holder was employed and the measurement was performed at 13 K with data accumulation of about 24 hours. Mößbauer data was processed and simulated using the WMOSS4 program (www.wmoss.org). Isomeric shifts are referenced to α-iron at room temperature.

Magnetic Möβbauer spectra of **Fe-2** were recorded in collaboration with Dr. Eckhard Bill (MPI CEC) on a conventional spectrometer with alternating constant acceleration of the γ-source. The minimum experimental line width was 0.24 mm/s (full width at half-height). The sample temperature was maintained constant in an OXFORD INSTRUMENTS VARIOX or in an OXFORD INSTRUMENTS MÖβBAUER-SPECTROMAG. The latter is a split-pair super-conducting magnet system for applied fields up to 8 T where the temperature of the sample can be varied in the range 1.5 K to 250 K. The field at the sample is perpendicular to the γ -beam. The ^{57}Co/Rh source (1.8 GBq) was positioned at room temperature inside the gap of the magnet system at a zero-field position, by using a re-entrant bore. Isomer shifts are quoted relative to iron metal at 300 K. Magnetic Möβbauer spectra were simulated with the program MX (by Eckhard Bill) by diagonalization of the spin Hamiltonian for $S = 2$:

$$\hat{H} = g\beta S \cdot B + D[S_z^2 - S(S+1)/3] + E/D[S_x^2 - S_y^2]$$

where g is the average electronic g value, and D and E/D are the axial zero-field splitting and rhombicity. The hyperfine interaction for ^{57}Fe was calculated by using the usual nuclear Hamiltonian.[1]

6.2.11. X-ray absorption spectroscopy (XAS)

X-ray absorption spectroscopy was performed in collaboration with Dr. Erik R. Farquhar. The measurements were performed in the following facilities:

a) Stanford Synchrotron Radiation Lightsource

X-Ray absorption spectroscopy of **Fe-1**, **Fe-2**, **Cu-1-Eu**, **Cu-3** and **Cu-3-Y** was carried out on the Stanford Synchrotron Radiation Lightsource (SSRL, Menlo Park, California) beamline (BL) 7-3 with SPEAR3 operating at 3 GeV and 500 mA in top-off mode throughout data collection. The BL 7-3 was equipped with a Rh coated collimating mirror followed by a cryogenically cooled Si(220) double crystal monochromator. The collimating mirror angle was set to 9 and 12 keV cutoffs for Fe and Cu K-edge measurements, respectively. Consequently, the monochromator was operated in the fully tuned configuration. Samples were kept at 10-15 K using an OXFORD LHE cryostat. XAS spectra were obtained with a "28" element solid-state germanium fluorescence detector (~20 working elements). A photodiode placed before I_0 and connected to I_2 was used to obtain a metal foil reference via scattering (reference is therefore I_0/I_2); copper and iron foils were used as appropriate.

Data was generally obtained on 0.95mm x 4-6mm (vertical x horizontal) spots. Scans were monitored for evidence of photoreduction, and new spots with fresh sample were exposed as needed. A 3μ Z-1 filter and Soller slits were used to eliminate scatter, and ICR values typically ranged from 10 – 50 kcps. Data were collected with 10 eV steps before the edge (1 s integration time), 0.3 eV steps in pre-edge and edge regions (2 s integration time), and in 0.05k steps over k = 1.62 Å-1 to 14 or 15 Å-1 (integration time increased in k^2-weighted fashion from 2 to 9 sec over range of scan). Some scans were performed with XANES parameters, using a similar k-range but reducing integration times to 2-3 seconds in the EXAFS region.

b) National Synchrotron Lightsource

X-ray absorption spectroscopy of **Cu-1-Sc** and **Cu-4-Sc** was carried out on beamline X3B of the National Synchrotron Lightsource (Brookhaven National Laboratory, Upton, NY, USA). A sagitally focusing Si(111) monochromator was used for energy selection, while a cylindrically-bent

nickel-coated mirror located downstream of the monochromator provided vertical focusing and harmonic rejection. Sample temperatures were maintained at approximately 20 K using a He DISPLEX cryostat. A Cu metal foil was used for internal energy calibration, with the first inflection point of the reference foil edge set to 8979.0 eV. XAS data were collected as fluorescence spectra using a 31 element solid state germanium detector (Canberra), over an energy range of 8779 – 9540 eV. A Ni filter of 3 absorption lengths was used to reduce scatter and maintain detector linearity. Samples were monitored for photoreduction during data collection (based upon red-shifts in the absorption edge), and typically only 2 scans were collected at a given position on the sample.

Tandem Möβbauer/XAS cups with a sample window of 6 mm x 10 mm were used to provide at least 5 independent beam spots on each sample. Averaging and normalization of the XAS data was performed using Athena, a graphical implementation of the IFEFFIT[2] package. Reference spectra for individual scans were carefully aligned to ensure that the energy scale was identical for all spectra. Sets of scans at each spot were examined for photoreduction effects.

6.2.12. Magnetic Circular Dichroism (MCD)

MCD measurements on **Co-L_6** were performed in collaboration with the group of Prof. Dr. Nicolai Lehnert in the University of Michigan. The MCD setup employs an OXFORD SM4000 cryostat and a JASCO J-815 CD spectrometer. The SM4000 cryostat consists of a liquid helium-cooled superconducting magnet providing horizontal magnetic fields of 0-7 Tesla. The J-815 spectrometer uses a gaseous nitrogen-cooled xenon lamp and a detector system consisting of two interchangeable photomultiplier tubes in the UV-vis and NIR range. The samples were loaded into a 1.5-300 K variable temperature insert (VTI), which offers optical access to the sample via four optical windows made from Suprasil B quartz. Complete spectra were recorded at different temperatures (2, 5, 10, and 20 K) and magnetic fields (0-7 T).

6.2.13. Superconducting quantum interference device (SQUID) susceptibility measurements

SQUID susceptibility measurements on **Co-L_6** were performed in collaboration with the group of Prof. Dr. Nicolai Lehnert in the University of Michigan. The measurements were conducted on a QUANTUM DESIGN MPMS-XL7 equipped with an EVERCOOL Dewar. Samples were prepared as mixtures with either eicosane or silicon oil in a polycarbonate capsule. In a typical experiment, 5 mg of sample were used. Raw magnetic data were worked up using the program julX (designed by Dr. Eckhard Bill).

6.2.14. Density Functional Theory (DFT) calculations

a) DFT calculations on **Fe-2**, **Fe-TMC**, **Fe-4**, **Cu-1-M**, **Cu-3** and **Cu-3-Sc**

The DFT calculations on **Fe-2**, **Fe-TMC**, **Fe-4**, **Cu-1-M**, **Cu-3** and **Cu-3-Sc** were performed in collaboration with Prof. Dr. Marcel Swart from the Universitat de Girona. All DFT calculations were performed with the Amsterdam Density Functional (ADF) suite of program.[3,4] MOs were expanded in an uncontracted set of Slater type orbitals[5] (STOs) of triple-ζ quality containing diffuse functions and two sets of polarization functions (TZ2P), or a mixture of triple-ζ quality on the metal (TZP) and double-ζ quality (DZP) on all other atoms, in both cases with one set of polarization functions, which we dub here TDZP[5]. Core electrons (1s for 2nd period, 1s2s2p for 3rd-4th period) were not treated explicitly during the geometry optimizations (frozen core approximation), as it was shown to have a negligible effect on the obtained geometries.[6] An auxiliary set of s, p, d, f, and g STOs was used to fit the molecular density and to represent the Coulomb and exchange potentials accurately for each SCF cycle.

Geometries were optimized with the QUILD program[7] which uses superior optimization routines based on adapted delocalized coordinates[8] until the maximum gradient component was less than 10-4 a.u. This computational setup was shown to work well for transition-metal complexes.[9] The starting point for geometry optimizations were structures obtained from X-ray diffraction analysis. Energies and gradients were calculated using the BP86 functional[10,11] and the TDZP basis set with inclusion of Grimme's dispersion (D3) correction.[12] Subsequent single point calculations for obtaining spin-state splittings have been performed on all optimized geometries, with the S12g functional[13] and the all-electron electron TZ2P basis set. The UV-Vis spectra were obtained in separate single-point calculations using the SAOP[14] model potential with the all-electron TZ2P basis set.

In all cases the COSMO[15–17] dielectric continuum model has been included for implicit treatment of the environment (using dichloromethane as a solvent),[18,19] and scalar relativistic corrections have been included self-consistently by using the zeroth-order regular approximation (ZORA).[20–22]

b) DFT calculations on **Co-L$_6$**

The DFT calculations on **Co-L$_6$** were performed in collaboration with Dr. Nicolai Lehnert and Casey van Stappen from the University of Michigan. The initial geometry of the complex **Co-L$_6$** in the conformation **A** was generated using the optimized complementing Fe(II) model generated by

Kundu and co-workers,[23] which derives from an annotation of the crystallographically determined structure of the hexanuclear iron stannoxane complex utilizing the 4-(1,3-bis(pyridin-2-ylmethyl)imidazolidin-2-yl)benzoic acid ($\mathbf{L_6}$) ligand. This model involves the complexation of Co(II) with one arm of the stannoxane core. Additionally, the model complexes **B** and **C** were generated by the direct coordination of one and two molecules of triflate to the first coordination sphere of Co(II) respectively. The molecular structures of the model complexes **A**, **B**, and **C** were optimized using Becke's three-parameter hybrid exchange functional[24] with the Lee-Yang-Parr non-local correlation functional[25] (B3LYP) using an unrestricted formalism. A multi-basis set approach[26] was taken , utilizing Alrich's triple-ζ valence polarized (TZVP)[27] basis for treatment of Co, while a 6-311G(d) basis set[28] was used for all C, N, and O atoms, and H was treated with the smaller 6-31G basis[29] in both DFT and TDDFT calculations. Optimizations were performed using the Polarization Continuum Model (PCM) with toluene as solvent. Frequency calculations were performed to confirm optimized geometries. Optimization, frequency, and single point energy calculations of all complexes were carried out on the Linux version of the Gaussian09 program.[30] Additionally, single point energy and TDDFT calculations were performed using the Linux version of ORCA 3.0.2,[31] which utilizes the libint2 library for two electron integral calculations.[32] The first 50 vertical excitation energies were calculated by TDDFT for model complexes **A**, **B**, and **C**.

c) DFT calculations on **Cu-4-Sc**

The DFT calculations on **Cu-4-Sc** were performed in collaboration with Dr. Florian Pfaff using the ORCA[33] package. The structure was optimized using the BP86 exchange functional[11,10] and Default-Basis-2,3,4[34-37] increasing stepwise for the optimization process. The Default-Basis set 2 and higher include the Ahlrichs polarization functions, which were obtained from the TURBOMOLE BASIS set library under ftp.chemie.uni-karlsruhe.de/pub/basen. All calculations include the COSMO solvation model with the built-in parameters for dichloromethane and empirical dispersion correction using the Becke-Johnson damping.[12,38]

6.3. Syntheses of compounds and generation of intermediates

6.3.1. Synthesis of the ligands TMCO and TMCO-d

The **TMCO** and **TMCO-d** ligands were synthesized making small modifications on previously reported synthetic pathways.[39–41]

Synthesis of *N,N',N''*-tritosylbis(3-aminopropyl)amine

This synthesis was performed with small modifications on a previously reported procedure.[40] 3,3'-diaminodipropylamine (3.28 g, 25 mmol) and NaOH (3.6 g, 90 mmol) were dissolved in 20 mL H_2O inside a three-necked round bottom flask placed in a water bath. The reaction mixture was stirred for some minutes until the NaOH was completely dissolved. A solution of *p*-toluensulfonyl chloride (14.6 g, 76 mmol) in CH_2Cl_2 was then added dropwise with vigorous stirring over 1 hour. The resultant reaction mixture was stirred at room temperature for 2 more hours and left standing over night when two layers were formed. The CH_2Cl_2 layer was separated from the aqueous one, washed with H_2O (3 x 20 mL) and dried over $MgSO_4$. The solvent was removed and the resulting solid was dried under vacuum. *N,N',N''*-tritosylbis(3-aminopropyl)amine was collected as a colorless glassy solid. Yield: 13.12 g (22.5 mmol, 90%).

^{1}H NMR ($CDCl_3$, 400 MHz): δ [ppm] = 7.71-7.59 (m, 6H, Ar-**H**), 7.28-7.26 (m, 6H, Ar-**H**), 3.07 (t, 4H, N-C**H**$_2$), 2.92 (m, 4H, N-C**H**$_2$), 2.39 (s, 9H, C**H**$_3$), 1.68 (m, 4H, CH_2-C**H**$_2$-CH_2).

ESI-MS (+): m/z = 616.159 $[C_{27}H_{35}N_3O_6S_3+Na]^+$ (calculated= 616.160).

Synthesis of 4,8,12-Tritosyl-1-oxa-4,8,12-triazacyclotetradecane

This synthesis was performed making small modifications on a previously reported procedure.[41] In a N_2 atmosphere, *N,N',N''*-tritosylbis(3-aminopropyl)-amine (2.37 g, 4 mmol) and Cs_2CO_3 (3.26 g, 10 mmol) were mixed in 60 mL of dimethylformamide (DMF). A white suspension was formed and it was stirred for an hour. A solution of diethyleneglycol-ditosylate (1.66 g, 4 mmol) in 20 mL of DMF was then added dropwise over 5 hours. The cloudy white solution was stirred for 3 days in an inert atmosphere. After this time, the reaction mixture was opened to air, and ice (around 50 mL) was added slowly while stirring. Once the ice was almost fully melted, the reaction mixture was left in the fridge overnight. The white precipitate thus formed, was filtered and dried under vacuum. The protected macrocycle, 4,8,12-tritosyl-1-oxa-4,8,12-triazacyclotetradecane, was obtained as a white solid. Yield: 2.44 g (3.7 mmol, 92%).

^{1}H NMR ($CDCl_3$, 400 MHz): δ [ppm] = 7.65-7.63 (d, 6H, **H**-Ar), 7.29-7.27 (d, 6H, **H**-Ar), 3.61-3.58 (t, 4H, O-C**H**$_2$), 3.22 -2.89 (m, 12H, C**H**$_2$), 2.39 (s, 9H, C**H**$_3$), 2.01 (q, 4H, CH_2-C**H**$_2$-CH_2).

ESI-MS: (+): m/z = 664.220 $[C_{31}H_{41}N_3O_7S_3+H]^+$ (calculated= 664.218)

Synthesis of 1-oxa-4,8,12-triazacyclotetradecane

This synthesis was performed making small modifications on a previously reported procedure.[41] 4,8,12-tritosyl-1-oxa-4,8,12-triazacyclotetradecane (2.44 g, 3.7 mmol) and HBr 30% in acetic acid (70 mL) were refluxed under inert conditions for 48 hrs. After this time, a white precipitate was formed. It was filtered with a small pore frit, washed with cold acetone and dried under vacuum. The HBr salt of 1-oxa-4,8,12-triazacyclotetradecane was obtained as a white powder. Yield: 1.00 g (2.3 mmol, 63 %).

^{1}H NMR (D_2O, 400 MHz): δ [ppm] = 1.71 (q, 4H, CH_2-C**H**$_2$-CH_2), 2.68 (t, 8H, C**H**$_2$-CH_2-C**H**$_2$), 2.75 (t, 4H, N-C**H**$_2$-CH_2), 3.65 (t, 4H, CH_2-C**H**$_2$-O).

Synthesis of 4,8,12-trimethyl-1-oxa-4,8,12-triazacyclotetradecane (TMCO)

This synthesis was performed making small modifications on a previously reported procedure.[39] The HBr salt of 1-oxa-4,8,12-triazacyclotetradecane (0.95 g, 4.5 mmol) was refluxed with formic acid (4.8 mL), formaldehyde (4 mL) and water (0.5 mL) for 24 hrs. After this time, the clear solution was transferred to a beaker, put in an ice bath, and treated with NaOH (7.5 M) until pH > 12.0. The reaction mixture was then extracted with chloroform (5 x 10 mL). The organic phase was dried with Na_2SO_4 and the solvent was removed. The **TMCO** ligand was obtained as a yellow oil. Yield: 530 mg (2.2 mmol, 50%).

^{1}H NMR ($CDCl_3$, 400 MHz): δ [ppm] = 1.6 (q, 4H, CH_2-C**H**$_2$-CH_2), 2.18 (s, 3H, N-C**H**$_3$), 2.24 (s, 6H, N-C**H**$_3$), 2.39 (t, 4H, N-C**H**$_2$-CH_2-O), 2.53-2.59 (m, 8H, C**H**$_2$-CH_2-C**H**$_2$), 3.55 (t, 4H, O-C**H**$_2$-CH_2-N).

ESI-MS (+): m/z = 244.242 $[C_{13}H_{29}N_3O+H]^+$ (calculated= 244.239).

Synthesis of the Ligand TMCO-d

For the synthesis of the deuterated version of the ligand **TMCO**, the HBr salt of 1-oxa-4,8,12-triazacyclotetradecane (0.95 g, 4.5 mmol) was refluxed with formic acid-d_2 (4.8 mL), formaldehyde-d_2 (4 mL) and D_2O (0.5 mL) for 24 hours. After this time, the clear solution was transferred to a beaker, put in an ice bath, and treated with NaOH (7.5 M) until pH > 12.0. The reaction mixture was then extracted with chloroform (5 x 10 mL). The organic phase was dried with Na_2SO_4 and the solvent was removed. The ligand **TMCO-d** was obtained as a yellow oil. Yield: 580 mg (2.4 mmol, 55%).

ESI-MS (+): m/z = 275.279 $[C_{13}H_{20}D_9N_3O+Na]^+$ (calculated= 275.276).

6.3.2. Synthesis of the complexes Fe-1, Fe-1d and ^{57}Fe-1

Synthesis of the complex Fe-1

In an inert atmosphere, a solution of the **TMCO** ligand (100 mg, 0.4 mmol) in 2mL of dry acetonitrile (MeCN) was added to a solution of $Fe(OTf)_2(MeCN)_2$ (174 mg, 0.4 mmol) in 2 mL of dry MeCN. The resulting brown solution was left stirring in a N_2 atmosphere for 3 days. After this time, 10 mL of dry diethyl ether (Et_2O) were added and the reaction mixture was left standing at −20°C for one hour. After this time, a brown oil was formed in the bottom of the vial. The clear colorless solution was carefully decanted, placed in a larger flask and more Et_2O (50 mL) was added to it. The solution was left at -40°C and overnight crystals were formed. The complex **Fe-1** was obtained pure as colorless needle-like crystals (white when dry). Yield: 183 mg (0.29 mmol, 72%).

ESI-MS (+): m/z = 448.121 $[C_{14}H_{29}F_3FeN_3O_4S]^+ = [(TMCO)Fe(OTf)]^+$ (calculated= 448.118).

Elemental analysis: $C_{17}H_{32}N_4O_7S_2F_6Fe$ Calculated (%): C, 31.98; H, 5.05; N, 8.78. Found (%) C, 32.19; H, 5.22; N, 8.87.

EPR: silent

^{19}F-NMR (CD_2Cl_2): δ [ppm] = -79 (s).

^{1}H-NMR (CD_2Cl_2): paramagnetic; signals distributed in the range of 500 to -100 ppm.

Möβbauer (solid sample): High-spin Fe(II) center with isomer shift (δ') = 1.17 mm/s and quadrupole splitting (ΔE_Q) = 3.31 mm/s.

Fe *K*-edge XANES (CH_2Cl_2, 4 mM): pre-edge at 7112 eV, edge inflection point at 7123 eV.

Synthesis of the complex Fe-1d

The exact procedure for the synthesis of **Fe-1** was followed, this time employing the ligand **TMCO-d** instead of the ligand **TMCO**. The complex **Fe-1d** was obtained as colorless needle-like crystals (white when dry).

ESI-MS (+): m/z = 455.181 $[C_{14}H_{20}D_9F_3FeN_3O_4S]^+$ (calculated = 455.178)

Synthesis of the complex ^{57}Fe-1

A ^{57}Fe-enriched **^{57}Fe-1** complex was necessary for performing Möβbauer studies in solution. In order to synthesize **^{57}Fe-1**, the compound $^{57}Fe(OTf)_2(MeCN)_2$ was generated first. In an inert atmosphere, metallic ^{57}Fe (42 mg, 0.74 mmol) and a degassed HCl concentrated solution (4 mL) were stirred at 65°C for one night until all the iron was dissolved. The solvent was then removed with vacuum and the resultant white residue was suspended in dry MeCN (4 mL). $(CH_3)_3Si(OTf)$ (820 mg, 3.69 mmol) in dry MeCN (2 mL) was added dropwise over 2 minutes. The solution obtained was kept stirring overnight and then solvent was removed by vacuum. The remaining solid was re-dissolved in dry MeCN (minimum amount) and an excess of dry Et_2O was added. The mixture was left overnight at -20°C and white crystals were formed. The crystals were filtered, washed with dry Et_2O and dried. $^{57}Fe(OTf)_2(MeCN)_2$ was obtained as a white solid. Yield: 175mg (0.4 mmol, 55%).

This product was directly employed in the synthesis of **^{57}Fe-1** without further analysis given the high cost of the starting ^{57}Fe. The procedure described for the synthesis of **Fe-1** was followed, this time using $^{57}Fe(OTf)_2(MeCN)_2$ instead of $Fe(OTf)_2(MeCN)_2$. **^{57}Fe-1** was obtained as colorless needle-like crystals (white when dry).

6.3.3. Synthesis of the oxidants sPhIO and sPhI^{18}O

For the synthesis of this oxidant, the precursor compound 2-(tert-butylsulfonyl)-(diacetoxyiodo)benzene ($sPhI(OAc)_2$) was prepared in the group,[42] following a previously reported procedure.[43]

Synthesis of the oxidant sPhIO

The synthesis of sPhIO was performed following the previously reported procedure.[43] $sPhI(OAc)_2$ (0.9 g, 2.0 mmol) was placed in a round bottom flask with three stirring bars. Under vigorous stirring, NaOH (3 M in H_2O) was added to the solid in 0.5 mL portions until the pH of the resulting mixture was kept constant for 5 minutes. The obtained yellow solid was filtered (H_2O was used for transferring the solid to the frit funnel) and washed with H_2O and Et_2O. sPhIO was obtained as a yellow fine powder. Yield: 450 mg (1.3 mmol, 66%).

ESI-MS (+): m/z = 340.986 $[C_{10}H_{13}IO_3S+H]^+$ = $[sPhIO+H]^+$ (calculated= 340.963).

AT-IR: (solid) $\tilde{\nu}$ [cm^{-1}] = 1567 (s), 1457 (m), 1420 (m), 1277 (m), 1133 (s), 1109 (s), 1079 (s), **823** (w), 765 (s), 735 (s), **682** (s), **645** (s), 568 (s), 518 (s), 459 (s).

Synthesis of the oxidant sPhI^{18}O

For generating the ^{18}O-containing sPhI^{18}O oxidant, Na^{18}OH was prepared *in-situ* from the reaction of NaH (38 mg, 1 mmol) and $H_2{}^{18}O$ (1 g) under inert conditions. To this solution, sPhI(OAc)$_2$ (300 mg, 0.7 mmol) was added and the reaction mixture was stirred for 30 min. After this time, the reaction mixture was filtrated using specially made teflon-tube-funnels. The solid was washed with 0.5 mL $H_2{}^{18}O$ fractions until neutral pH, then it was washed two times with dry Et_2O and finally it was dried under vacuum. sPhI^{18}O was obtained as a yellow fine powder. Yield: 185 mg (0.56 mmol, 80 %).

ESI-MS (+): m/z = 342.974 $[C_{10}H_{13}IO_2{}^{18}OS+H]^+ = [sPhI^{18}O+H]^+$ (calculated= 342.963).

AT-IR: (solid) $\tilde{\nu}$ [cm^{-1}] = 1567 (s), 1457 (m), 1420 (m), 1277 (m), 1133 (s), 1109 (s), 1079 (s), **787** (w, shoulder), 765 (s), 735 (s), **654** (shoulder), **640** (s), 568 (s), 518 (s), 459 (s).

6.3.4. Generation of the intermediates Fe-2, Fe-2d, Fe-2-^{18}O and ^{57}Fe-2

Generation of Fe-2

In a typical experiment, a colorless solution of the complex **Fe-1** in dry CH_2Cl_2 (1 mM, 2 mL) was cooled down to -90°C under inert conditions. Then 1.5 equivalents of sPhIO in dry CH_2Cl_2 (0.1 mL) were added. The formation of a light green intermediate was monitored following the growth of the 585 nm band in the UV-vis spectrum.

Larger concentrations were used for preparing samples for spectroscopic techniques different than UV-vis, the characteristics of those samples are indicated in the text.

UV-vis (CH_2Cl_2, -90°C): λ_{max} (ε_{max}, M^{-1}cm^{-1}) 385 (shoulder), 585 (200), 848 (150).

EPR: silent

ESI-MS (+): m/z = 464.1 $[C_{14}H_{29}F_3FeN_3O_5S]^+$ (calculated= 464.11).

Fe *K*-edge XANES (CH_2Cl_2, 4 mM): pre-edge at 7113.8 eV, edge inflection point at 7124.3 eV.

Generation of Fe-2d

The exact procedure for the generation of **Fe-2** was followed, this time employing the complex **Fe-1d** instead of **Fe-1**. The formation of a light green intermediate was monitored following the growth of the 585 nm band in the UV-vis spectrum.

UV-vis (CH_2Cl_2, -90°C): λ_{max} (ε_{max}, $M^{-1}cm^{-1}$) 385 (shoulder), 585 (200), 848 (150).

^{2}H-NMR (CH_2Cl_2): δ [ppm] = -22 (s), -83 (s)

Generation of Fe-2-^{18}O for ESI-MS

The procedure for the generation of **Fe-2** was followed but the oxidant sPhi^{18}O was employed instead of sPhIO. The formation of a light green intermediate was monitored following the growth of the 585 nm band in the UV-vis spectrum.

UV-vis (CH_2Cl_2, -90°C): λ_{max} (ε_{max}, $M^{-1}cm^{-1}$) 385 (shoulder), 585 (200), 848 (150).

ESI-MS (+): m/z = 466.1 $[C_{14}H_{29}F_3FeN_3O_4{}^{18}OS]^+$

Generation of ^{57}Fe-2 for Möβbauer studies

A colorless solution of the complex **^{57}Fe-1** 30 mM in 0.2 mL dry CH_2Cl_2 was cooled down to −90 °C under inert conditions. Then, 1.5 equivalents of sPhIO in 0.1 mL of dry CH_2Cl_2 cooled to −90 °C were added. Finally, 2 mL of propionitrile cooled down to −90 °C were added to get a 3 mM solution of **^{57}Fe-2** in propionitrile with 12% dichloromethane.

UV-vis (CH_2Cl_2, -90°C): λ_{max} (ε_{max}, $M^{-1}cm^{-1}$) 385 (shoulder), 585 (200), 848 (150).

Möβbauer (propionitrile with 12% dichloromethane, 3 mM): main species low-spin Fe(IV) center with isomer shift (δ') = 0.213 mm/s and quadrupole splitting (ΔE_Q) = 1.578 mm/s.

6.3.5. Synthesis of the ligand TMCN and TMCN-d

The **TMCN** and **TMCN-d** ligands were synthesized making modifications on previously reported synthetic pathways.[39–41]

Synthesis of 1,4,7,11-tetratosyl-1,4,7,11-tetraazacyclotetradecane

This synthesis was performed making small modifications from a previously reported procedure.[41] In a N_2 atmosphere, *N,N',N''*-tritosylbis(3-aminopropyl)amine (2.37 g, 4 mmol) and Cs_2CO_3 (3.26 g, 10 mmol) were mixed in 60 mL dimethylformamide (DMF). A white suspension was formed and it was stirred for an hour. A solution of *N,O,O'*-tritosyldiethanolamine (2.27 g, 4 mmol) in 20 mL DMF was then added dropwise over 5 hours. The cloudy white solution was stirred for 2 days in an inert atmosphere. After this time, the reaction mixture was opened to air and ice (around 50 mL) was added slowly while stirring. When all the ice was almost melted, the

reaction mixture was left in the fridge overnight. The white precipitate thus formed, was filtered and dried under vacuum. The protected macrocycle, 1,4,7,11-tetratosyl-1,4,7,11-tetraazacyclotetradecane, was obtained as a white solid. Yield: 2.7 g (3.3 mmol, 83%).

^{1}H NMR ($CDCl_3$, 400 MHz): δ [ppm] = 7.74-7.62 (m, 8H, **H**-Ar), 7.34-7.31 (d, 8H, **H**-Ar), 3.37-2.88 (m, 16H, C**H**$_2$-CH$_2$-C**H**$_2$, N-C**H**$_2$-C**H**$_2$), 2.44 (m, 12H, C**H**$_3$), 1.91 (q, 4H, CH$_2$-C**H**$_2$-CH$_2$).

Synthesis of 1,4,7,11-tetraazacyclotetradecane

For this synthesis some modifications on a previously reported procedure were performed.[41] The protected macrocycle, 1,4,7,11-tetratosyl-1,4,7,11-tetraazacyclotetradecane (2.7 g, 3.6 mmol) and H_2SO_4 80% (20 mL) were stirred at 250 °C under inert conditions for 1 hr. After this time, the brown reaction mixture was allowed to cool down and 50 mL of a mixture MeOH:Et_2O (1:1) were added. A white precipitate was formed, filtered, washed with Et_2O and re-dissolved in a NaOH solution. The aqueous solution was extracted three times with CH_2Cl_2. The resulting organic fractions were dried under Na_2SO_4 and the solvent was removed with vacuum. The product 1,4,7,11-tetraazacyclotetradecane was obtained as a white powder in modest yields. Yield: 390 mg (1.9 mmol, 53%)

^{1}H NMR (D_2O, 400 MHz): δ [ppm] = 1.83 (q, 4H, CH$_2$-C**H**$_2$-CH$_2$), 2.75-2.82 (m, 16H, C**H**$_2$-CH$_2$-C**H**$_2$, N-C**H**$_2$-C**H**$_2$), 3.13 (m, 4H, N**H**).

Synthesis of the ligand TMCN

Small modifications on a previously reported procedure[39] were performed for this synthesis. The previously obtained 1,4,7,11-tetraazacyclotetradecane (0.39 g, 1.9 mmol) was refluxed with formic acid (4.8 mL), formaldehyde (4 mL) and water (0.5 mL) for 24 hrs. After this time, the clear solution was transferred to a beaker, put in an ice bath, and treated with NaOH (7.5 M) until pH > 12.0. The reaction mixture was then extracted with chloroform (5 x 10 mL). The organic phase was dried with Na_2SO_4 and the solvent was removed. The **TMCN** ligand was obtained as an oil. Yield: 360 mg (1.4 mmol, 74%).

^{1}H NMR ($CDCl_3$, 300 MHz): δ [ppm] = 1.67 (q, 4H, CH$_2$-C**H**$_2$-CH$_2$), 2.25 (s, 12H, C**H**$_3$), 2.49-2.62 (m, 16H, C**H**$_2$-C**H**$_2$, C**H**$_2$-CH$_2$-C**H**$_2$).

Synthesis of the Ligand TMCN-d

For the synthesis of the deuterated version of the ligand **TMCN-d**, the 1,4,7,11-tetraazacyclotetradecane (0.4 g, 2 mmol) was refluxed with formic acid-d_2 (4.8 mL), formaldehyde-d_2 (4 mL) and D_2O (0.5 mL) for 24 hours. After this time, the clear solution was transferred to a beaker, put in an ice bath, and treated with NaOH (7.5 M) until pH > 12.0. The reaction mixture was then extracted with chloroform (5 x 10 mL). The organic phase was dried with Na_2SO_4 and the solvent was removed. The **TMCN-d** ligand was obtained as an oil. Yield: 378 mg (1.4 mmol, 70%).

^{1}H NMR ($CDCl_3$, 300 MHz): δ [ppm] = 1.67 (q, 4H, CH_2-C**H**$_2$-CH_2), 2.49-2.62 (m, 16H, C**H**$_2$-C**H**$_2$, C**H**$_2$-CH_2-C**H**$_2$).

6.3.6. Synthesis of the complexes Fe-3 and Fe-3d

Synthesis of the complex Fe-3

In an inert atmosphere, a solution of the **TMCN** ligand (100 mg, 0.38 mmol) in dry MeCN (2 mL) was added to a solution of $Fe(OTf)_2(MeCN)_2$ (165 mg, 0.38 mmol) in MeCN (2 mL). The resulting brown solution was left stirring in a N_2 atmosphere for 24 hours. After this time, 10 mL of dry Et_2O were added and the reaction mixture was left standing at -20°C for one hour. A brown oil was formed in the bottom of the vial. The clear colorless solution was carefully decanted, placed in a larger flask and more Et_2O (50 mL) was added to it. The solution was left at -40°C and overnight crystals were formed. The complex **Fe-3** was obtained pure as colorless needle-like crystals (white when dry). Yield: 175 mg (0.28 mmol, 75 %).

ESI-MS (+): m/z = 461.161 $[C_{15}H_{32}F_3FeN_4O_3S]^+$ (calculated = 461.154).

^{19}F-NMR (CD_2Cl_2): δ [ppm] = -79 (s).

^{1}H-NMR (CD_2Cl_2): paramagnetic; signals distributed in the range of 500 to -100 ppm.

Synthesis of the complex Fe-3d

The exact procedure for the synthesis of **Fe-3** was followed, this time employing the ligand **TMCN-d** instead of the ligand **TMCN**. The complex **Fe-3d** was obtained as colorless needle-like crystals (white when dry).

ESI-MS (+): m/z = 473.230 $[C_{15}H_{20}D_{12}F_3FeN_4O_3S]^+$ (calculated = 473.228)

^{19}F-NMR (CD_2Cl_2): δ [ppm] = -76 (s).

6.3.7. Generation of the intermediates Fe-4 and Fe-4d

Generation of the intermediate Fe-4

A colorless solution of the complex **Fe-3** in dry MeCN (1 mM, 2 mL) was cooled down to ─40 °C under inert conditions. 1.5 equivalents of sPhIO in dry MeCN (0.1 mL) were added. The formation of the transient intermediate could be detected with UV-vis spectroscopy; however, its self-decay is too fast to stabilize such species.

UV-vis (CH_2Cl_2, -90°C): λ_{max} 400 (shoulder), 820; the ε_{max} could not be determined.

Generation of the intermediate Fe-4d

In a typical experiment, a colorless solution of the complex **Fe-3d** in dry MeCN (1 mM, 2 mL) was cooled down to 10 °C under inert conditions. Then 1.5 equivalents of sPhIO in dry MeCN were added. The formation of a light greenish-brown intermediate was monitored following the growth of the 820 nm band in the UV-vis spectrum.

UV-vis (CH_2Cl_2, -90°C): λ_{max} (ε_{max}, $M^{-1}cm^{-1}$) 400 (shoulder), 820 (125).

^{19}F-NMR (CD_2Cl_2): δ [ppm] = -77 (s).

^{2}H-NMR (CD_2Cl_2): δ [ppm] = -26 (s), -40 (s), -58 (s), -77(s).

6.3.8. Synthesis of the ligand L_6

The ligand $\mathbf{L_6}$ was synthesized following a previously reported procedure.[23] To a suspension of 4-(1,3-bis(2-pyridylmethyl)-2-imidazolidinyl)benzoic acid (1.03 g, 2.74 mmol) in anhydrous toluene (100 mL) was added n-butylstannoic acid (0.57 g, 2.74 mmol). The reaction mixture was refluxed at 120 °C for 5 hours with continuous removal of H_2O by using a dean-Stark apparatus. After this time, the reaction mixture was allowed to cool down to room temperature and then filtered. The solvent from the filtrate was removed under reduced pressure. $\mathbf{L_6}$ was obtained as a yellow solid. Yield: 1.24 g (0.36 mmol, 80%).

^{1}H NMR ($CDCl_3$, 400 MHz): δ [ppm] = 0.85 (t, 36H, C$\mathbf{H_3}$), 1.01-1.77 (m, 72H, C$\mathbf{H_2}$), 2.88-3.51 (m, 24H, C$\mathbf{H_2}$-N), 3.95 (d, 12H, C$\mathbf{H_2}$-py), 4.25 (s, 6H, C**H**), 6.90-7.09 (m, 12H, H-Ar), 7.30-7.58 (m, 48H, **H**-Ar), 7.85-8.02 (m, 12H, **H**-Ar), 8.16 (m, 12H, **H**-Ar), 8.35 (m, 12H, **H**-Ar).

^{119}Sn NMR ($CDCl_3$, 150 MHz): δ [ppm] = -482.47 (s).

IR: (KBr pellet) $\tilde{\nu}$ [cm^{-1}] = 3447 (br), 3061 (w), 2953 (m), 2927 (m), 1703 (w), 1604 (s), 1590 (s), 1561 (m), 1529 (s), 1445 (m), 1413 (s), 1292 (m), 1148 (m), 1018 (m), 865 (m), 779 (m), 751 (w), 622 (s), 507 (m).

6.3.9. Synthesis of the complex Co-L_6

Co-L_6 was synthesized following a previous report.[44] A solution of **L_6** (0.40 g, 0.12 mmol) in anhydrous dichloromethane (2mL) was added to a suspension of $Co(OTf)_2$ (0.49 g, 1.3 mmol) in anhydrous dichloromethane (2 mL). The orange-pink reaction mixture was stirred in anhydrous conditions at room temperature for 24 hours. The solution was then filtered. After the addition of 50 mL of anhydrous *n*-hexane to the filtrate, **Co-L_6** precipitated as a light-orange powder. The remaining solvent was removed by decantation and **Co-L_6** was dried in vacuum overnight.

Elemental analysis: $C_{168}H_{180}N_{24}F_{36}O_{54}S_{12}Sn_6Co_6$ Calculated (%): C, 36.42; H, 3.38; N, 6.07. Found (%): C, 35.51; H, 3.64; N, 5.52.

EPR (CH_2Cl_2, 10 K): $g^{\perp} \approx 4.2$ and $g^{\parallel} \approx 2.1$.

Further characterization of this complex is discussed in Chapter 3.

6.3.10. Generation of the intermediate Co-1

Co-1 was generated following a previous report.[44] Under inert conditions, a pale orange solution of the complex **Co-L_6** in anhydrous dichloromethane or acetone (1 mM, 2 mL) was kept at 25 °C. Anhydrous O_2 was then bubbled into the solution. The formation of a deep orange intermediate was monitored following the growth of the 470 nm band in the UV-vis spectrum.

UV-vis (CH_2Cl_2, -90°C): λ_{max} (ε_{max}, $M^{-1}cm^{-1}$) 470 nm (11600).

EPR: silent.

Further characterization of this intermediate is discussed in Chapter 3 and in previous reports.[44]

6.3.11. Synthesis of the Complex [(AN)Cu]BF_4

The complex [(AN)Cu]BF_4 was prepared following a previously reported procedure.[45] A solution of the ligand 3,3'-iminobis-*N,N*,-dimethylpropylamine (AN; 0.345 g, 1.84 mmol) in dry CH_2Cl_2 (5 mL) was added to the solid [$Cu(MeCN)_4$][BF_4] (0.579 g, 1.84 mmol). The resultant solution was stirred under inert atmosphere for 30 minutes. After this time, 25 mL of *n*-Hexane were added to the colorless, clear solution to produce a cloudy solution that was kept at -35 °C for

2 hours. After that, the solvent was decanted and the resultant white solid was dried in *vacuo* to obtain the compound in pure form. Yield: 0.509 g (1.51 mmol, 82%).

Elemental analysis: $C_{10}H_{25}N_3BCuF_4$ Calculated (%): C, 35.57; H, 7.46; N, 12.44. Found (%): C, 35.81; H, 7.53; N, 12.30.

IR: (KBr pellet) $\tilde{\nu}$ [cm^{-1}] = 3289 (s), 2924 (s), 2844 (s), 2794 (s), 1480 (s), 1466 (s), 1429 (s), 1387 (m), 1345 (m), 1324 (m), 1293 (m), 1263 (m), 1239 (m), 1203 (m), 1139 (s), 1107 (s), 1054 (s), 978 (s), 950 (m), 919 (w), 899 (m), 859 (s), 851 (s), 771 (s), 756 (w), 523 (m), 492 (w), 458 (w).

EPR: silent.

6.3.12. Synthesis of the oxidants sPhINTs and sPhI^{15}NTs

For the synthesis of these oxidants, the precursor compound sPhI(OAc)$_2$ (2-(*tert*-butylsulfonyl)(diacetoxyiodo)benzene) was prepared in the group,[42] following a previously reported procedure.[43]

Synthesis of the oxidant sPhINTs

p-Toluenesulfonamide (0.4 g, 2.3 mmol) and KOH (0.32 g, 5.6 mmol) were dissolved in 40 mL of MeOH. The resultant solution was stirred in an ice bath at 0 °C for 15 minutes. After this time, the compound sPhI(OAc)$_2$ (1.0 g, 2.3 mmol) was slowly added. The reaction mixture was kept stirring for 1 hour at 0°C and then for 2 hours at room temperature. The white suspension thus obtained, was poured to crashed ice and this mixture was filtrated before the ice was completely melted. The white residue was washed with water until neutral pH and then with Et_2O, finally, it was dried in vacuum overnight. The oxidant sPhINTs was obtained as white solid. Yield: 0.870 g, (1.75 mmol, 76%).

^{1}H NMR ($CDCl_3$, 300 MHz): δ [ppm] = 8.33 (d, 1H, **H**-Ar), 7.93-7.80 (m, 4H, **H**-Ar), 7.73-7.66 (m, 1H, **H**-Ar), 7.23 (m, 2H, **H**-Ar), 2.31 (s, 3H, C**H**$_3$), 1.37-1.35 (s, 9H, C-(C**H**$_3$)$_3$).

ESI-MS (+): m/z= 494.10 $[C_{17}H_{21}INO_4S_2]^+$ (calculated= 493.99).

AT-IR: (solid) $\tilde{\nu}$ [cm-1] = 1272 (s), 1195 (w), 1133 (s), 1105 (s), 1079 (s), 1028 (m), 849 (s), 809 (s), 793 (m), 766 (s), 735 (s), 695 (s), 667 (s), 641 (s), 615 (m), 570 (s), 555 (s), 546 (s), 516 (m), 463 (m).

Synthesis of the oxidant sPhI^{15}NTs

For the preparation of the labeled sPhI^{15}NTs the same procedure as for sPhINTs was followed but ^{15}N-*p*-toluensulfonamide was used (bought with 98+ atom % ^{15}N from ISOTECH-SIGMA ALDRICH).

ESI-MS (+): m/z= 495.10 $[C_{17}H_{21}I^{15}NO_4S_2]^+$ (calculated= 494.99).

AT-IR: (solid) $\tilde{\nu}$ [cm^{-1}] = 1272 (s), 1195 (w), 1133 (s), 1105 (s), 1079 (s), 1028 (m), **832** (s), **806** (s), 793 (m), 766 (s), 735 (s), 695 (s), **660** (s), 641 (s), **602** (m), 570 (s), 555 (s), 546 (s), 516 (m), 463 (m).

6.3.13. Generation of the intermediates Cu-1-M and Cu-1-Y-^{15}N

Generation of Cu-1-M intermediates

Cu-1-M intermediates were generated following a procedure previously reported for **Cu-1-Sc**.[45] Under inert conditions, a solution of [(AN)Cu](BF$_4$) in CH_2Cl_2 (1 mM, 2 mL) was cooled down to -90°C. 1.5 equivalents of Lewis Acid (**M**) [Sc(OTf)$_3$, Y(OTf)$_3$, Eu(OTf)$_3$, Ce(OTF)$_3$, Zn(OTf)$_2$] and 1.5 equivalents of the oxidant sPhINTs were added in that order. The formation of the purple intermediate was monitored by UV-vis spectroscopy by following the increasing absorbance at 530 nm.

Larger concentrations were used for preparing samples for spectroscopic techniques different than UV-vis, the characteristics of those samples are indicated in the text.

UV-vis (CH_2Cl_2, -90°C): λ_{max} 530, 750 (the intensity of the signal varies with the **M** employed, thus no ε_{max} is reported). For [(AN)Cu(NTs)(Sc^{3+})] λ_{max} (ε_{max}, M^{-1}cm^{-1}) 530 (2500), 750 (580).

Cu K-edge XANES (acetone with 15% dichloromethane, 8 mM): pre-edge feature at 8977.5 eV, edge inflection point at 8988 eV.

Generation of the intermediate Cu-1-Y-^{15}N for rRaman

In strict inert conditions, a colorless solution of the complex [(AN)Cu][BF$_4$] in anhydrous CH_2Cl_2 (4 mM, 2 mL) was cooled down to -90 °C. Then, 1.5 equivalents of Sc(OTf)$_3$ in anhydrous acetone (0.1 mL) and 1.5 equivalents of sPhI^{15}NTs in anhydrous CH_2Cl_2 (0.1 mL) were added, in that order, to yield a deep purple intermediate. The formation of this species was monitored following the growth of the 530 nm band in the UV-vis spectrum.

UV-vis (CH_2Cl_2, -90°C): λ_{max} (ε_{max}, $M^{-1}cm^{-1}$) 530 (2500), 750 (580).

rRaman (CH_2Cl_2, laser excitation: 514 nm): shift upon labeling ($^{14}N \rightarrow ^{15}N$) in cm^{-1} = 568→566, 658→655, 883→862.

6.3.14. Synthesis of the oxidants sPhINAr^{CF3} and sPhI^{15}NAr^{CF3}

For the synthesis of these oxidants, the precursor compound sPhI(OAc)$_2$ (2-(*tert*-butylsulfonyl)(diacetoxyiodo)benzene) was prepared in the group,[42] following a previously reported procedure.[43]

Synthesis of the oxidant sPhINAr^{CF3}

4-(trifluoromethyl)benzenesulfonamide (0.15 g, 0.68 mmol)) and KOH (0.10 g, 1.70 mmol) were dissolved in 5 mL of MeOH. The resultant solution was stirred in an ice bath at 0°C for 15 minutes. After this time, the compound sPhI(OAc)$_2$ (0.30 g, 0.68 mmol) was slowly added. The reaction mixture was kept stirring for 1 hour at 0°C and then for 2 hours at room temperature. The white suspension thus obtained, was poured to crashed ice and this mixture was filtrated before the ice was completely melted. The white residue was washed with water until neutral pH and then with Et_2O. It was finally dried in vacuum overnight. The oxidant sPhINR^{CF3} was obtained as white solid. Yield: 0.214 g, (0.39 mmol, 58%).

^{1}H NMR (CD_2Cl_2, 300 MHz): δ [ppm] = 8.11 (d, 1H, **H**-Ar), 8.01 (d, 2H, **H**-Ar), 7.92 (d, 1H, **H**-Ar), 7.81 (t, 1H, **H**-Ar), 7.73 (d, 1H, **H**-Ar), 7.68 (d, 3H, **H**-Ar), 1.42 (s, 9H, C-(C**H**$_3$)$_3$).

$^{13}C\{^1H\}$-NMR (CD_2Cl_2, 101 MHz) δ [ppm] = 149.0 (**C**-SO_2N), 137.5 (**C**H-Ar), 135.2 (**C**H-Ar), 133.4 (**C**$SO_2{}^tBu$), 132.5 (**C**H-Ar), 129.3 (**C**H-Ar), 128.5 (**C**H-Ar), 127.3 (q, J = 3.6 Hz, **C**F_3), 116.1 (**C**-I), 65.0 (**C**$(CH_3)_3$),24.5 (**C**H_3).

ESI-MS (+): m/z = 569.950 $[C_{17}H_{17}F_3INO_4S_2+Na]^+$ (calculated= 569.949).

Synthesis of the oxidant sPhI^{15}NAr^{CF3}

For the preparation of the labeled sPhI^{15}NR^{CF3} the same procedure as for sPhINR^{CF3} was performed but ^{15}N-4-(trifluoromethyl)benzenesulfonamide was used.

ESI-MS (+): m/z = 570.952 $[C_{17}H_{17}F_3I^{15}NO_4S_2+Na]^+$

6.3.15. Synthesis of the oxidants sPhINAr^{NO2} and sPhI^{15}NAr^{NO2}

For the synthesis of these oxidants, the precursor compound sPhI(OAc)$_2$ (2-(*tert*-butylsulfonyl)(diacetoxyiodo)benzene) was prepared in the group,[42] following a previously reported procedure.[43]

Synthesis of the oxidant sPhINAr^{NO2}

4-nitrobenzenesulfonamide (0.14 g, 0.68 mmol)) and KOH (0.10 g, 1.70 mmol) were dissolved in 4 mL of MeOH. The resultant solution was stirred in an ice bath at 0°C for 15 minutes. After this time, the compound sPhI(OAc)$_2$ (0.30 g, 0.68 mmol) was slowly added. The reaction mixture was kept stirring for 1 hour at 0°C and then for 2 hours at room temperature. The white suspension thus obtained, was poured to crashed ice and this mixture was filtrated before the ice was completely melted. The white residue was washed with water until neutral pH and then with Et_2O. Finally, it was dried in vacuum overnight. The oxidant sPhINR^{NO2} was obtained as white solid. Yield: 0.284 g, (0.23 mmol, 80%).

^{1}H NMR (CD_2Cl_2, 300 MHz): δ [ppm] = 8.26 (d, 1H, **H**-Ar), 8.19 (d, 1H, **H**-Ar), 8.06 (d, 1H, **H**-Ar), 7.94 (dd, 1H, **H**-Ar), 7.87 (td, 1H, **H**-Ar), 7.75 (td, 2H, **H**-Ar), 1.44 (s, 9H, C(C**H**$_3$)$_3$).

ESI-MS (+): m/z = 546.946 $[C_{16}H_{17}IN_2O_6S_2+Na]^+$ (calculated= 546.947)

AT-IR: (solid) $\tilde{\nu}$ [cm^{-1}] = 1518 (s), 1474 (m), 1443 (m), 1425 (m), 1346 (s), 1290 (s), 1263 (s), 1166 (m), 1146 (w), 1137 (w), 1124 (s), 1108 (m), 1077 (s), 1010 (m), 1001 (m), 877 (s), 851 (s), 779 (m), 733 (s), 698 (w), 687 (m), 650 (s), 569 (s), 549 (s), 516 (m), 464 (s)

Synthesis of the oxidant sPhI^{15}NAr^{NO2}

For the preparation of the labeled sPhI^{15}NR^{NO2} the same procedure as for sPhINR^{NO2} was performed but ^{15}N-4-nitrobenzenesulfonamide was used.

ESI-MS (+): m/z = 547.950 $[C_{16}H_{17}IN^{15}NO_6S_2+Na]^+$

AT-IR: (solid) $\tilde{\nu}$ [cm^{-1}] = 1518 (s), 1474 (m), 1443 (m), 1425 (m), 1346 (s), 1290 (s), 1263 (s), 1166 (m), 1146 (w), 1137 (w), 1124 (s), 1108 (m), 1077 (s), 1010 (m), 1001 (m), **865** (s), **845** (s), 779 (m), 733 (s), 698 (w), 687 (m), **642** (s), 569 (s), 549 (s), 516 (m), 464 (s)

6.3.16. Generation of the intermediate Cu-2

In strict inert conditions, a colorless solution of the complex [(AN)Cu][BF_4] in anhydrous CH_2Cl_2 (1 mM, 2 mL) was cooled down to -90 °C. Then 1.5 equivalents of $sPhINR^{CF3}$ in anhydrous CH_2Cl_2 (0.1 mL) were added with extreme precaution to avoid any oxygen or water getting in contact with the solution. The formation of a deep green intermediate was monitored following the growth of the 425 nm band in the UV-vis spectrum.

Larger concentrations were used for preparing samples for spectroscopic techniques different than UV-vis, the characteristics of those samples are indicated in the text.

UV-vis (CH_2Cl_2, -90°C): λ_{max} (ε_{max}, $M^{-1}cm^{-1}$) 425 nm (1200), 700 nm (600).

6.3.17. Generation of the intermediates Cu-2-Sc and Cu-2-Sc-^{15}N

Generation of the intermediate Cu-2-Sc

Under inert conditions, a colorless solution of the complex [(AN)Cu][BF_4] in anhydrous CH_2Cl_2 (1 mM, 2 mL) was cooled down to -90 °C. Then, 1.5 equivalents of $Sc(OTf)_3$ in anhydrous acetone (0.1 mL) and 1.5 equivalents of $sPhINR^{CF3}$ in anhydrous CH_2Cl_2 (0.1 mL) were added in that order to yield a deep purple intermediate. The formation of this species was monitored following the growth of the 525 nm band in the UV-vis spectrum.

Larger concentrations were used for preparing samples for spectroscopic techniques different than UV-vis, the characteristics of those samples are indicated in the text.

UV-vis (CH_2Cl_2, -90°C): λ_{max} (ε_{max}, $M^{-1}cm^{-1}$) 525 (2150), 750 (600).

Generation of the intermediate Cu-2-Sc-^{15}N for rRaman

Under inert conditions, a colorless solution of the complex [(AN)Cu][BF_4] in anhydrous CH_2Cl_2 (4 mM, 2 mL) was cooled down to -90 °C. Then, 1.5 equivalents of $Sc(OTf)_3$ in anhydrous acetone (0.1 mL) and 1.5 equivalents of $sPhI^{15}NR^{CF3}$ in anhydrous CH_2Cl_2 (0.1 mL) were added in that order to yield a deep purple intermediate. The formation of this species was monitored following the growth of the 525 nm band in the UV-vis spectrum.

UV-vis (CH_2Cl_2, -90°C): λ_{max} (ε_{max}, $M^{-1}cm^{-1}$) 525 (2150), 750 (600).

rRaman (CH_2Cl_2 with 5% acetone, laser excitation: 532 nm): shift upon labeling ($^{14}N \rightarrow ^{15}N$) in cm^{-1} = 907→874, 609→607, 557.5→556.

6.3.18. Generation of the intermediate Cu-3

Under strict inert conditions, a colorless solution of the complex [(AN)Cu][BF_4] in anhydrous CH_2Cl_2 (1 mM, 2 mL) was cooled down to -90 °C. Then 1.5 equivalents of $sPhINR^{NO2}$ in anhydrous CH_2Cl_2 (0.1 mL) were added with extreme precaution to avoid any oxygen or water getting in contact with the solution. The formation of a deep green intermediate was monitored following the growth of the 425 nm band in the UV-vis spectrum.

Larger concentrations were used for preparing samples for spectroscopic techniques different than UV-vis, the characteristics of those samples are indicated in the text.

UV-vis (CH_2Cl_2, -90°C): λ_{max} (ε_{max}, $M^{-1}cm^{-1}$) 425 nm (1300), 700 nm (700).

Cu K-edge XANES (dichloromethane, 3.5 mM): pre-edge feature at 8977.5 eV, edge inflection point at 8987.5 eV.

6.3.19. Generation of the intermediates Cu-3-M and Cu-3-^{15}N

Generation of the intermediate Cu-3-M

Under inert conditions, a colorless solution of the complex [(AN)Cu][BF_4] in anhydrous CH_2Cl_2 (1 mM, 2 mL) was cooled down to -90 °C. Then, 1.5 equivalents of $Sc(OTf)_3$ in anhydrous acetone (0.1 mL) and 1.5 equivalents of $sPhINR^{NO2}$ in anhydrous CH_2Cl_2 (0.1 mL) were added in that order to yield a deep purple intermediate. The formation of this species was monitored following the growth of the 525 nm band in the UV-vis spectrum.

Larger concentrations were used for preparing samples for spectroscopic techniques different than UV-vis, the characteristics of those samples are indicated in the text.

UV-vis (CH_2Cl_2, -90°C): λ_{max} (ε_{max}, $M^{-1}cm^{-1}$) 525 (2000), 750 (550).

Cu K-edge XANES (for **Cu-3-Y** in dichloromethane with 5% acetone, 3.5 mM): pre-edge feature at 8977.5 eV, edge inflection point at 8987.5 eV.

Generation of the intermediate Cu-3-Sc-^{15}N for rRaman

Under inert conditions, a colorless solution of the complex [(AN)Cu][BF_4] in anhydrous CH_2Cl_2 (4 mM, 2 mL) was cooled down to -90 °C. Then, 1.5 equivalents of Sc(OTf)$_3$ in anhydrous acetone (0.1 mL) and 1.5 equivalents of sPhI^{15}NR^{NO2} in anhydrous CH_2Cl_2 (0.1 mL) were added in that order to yield a deep purple intermediate. The formation of this species was monitored following the growth of the 525 nm band in the UV-vis spectrum.

UV-vis (CH_2Cl_2, -90°C): λ_{max} (ε_{max}, $M^{-1}cm^{-1}$) 525 (2070), 740 (470).

rRaman (CH_2Cl_2 with 5% acetone, laser excitation: 532 nm): shift upon labeling ($^{14}N \rightarrow {}^{15}N$) in cm^{-1} = 910→880, 609→605, 562→560.

6.3.20. Synthesis of the oxidant Mes-N_3

2,4,6-trimethylaniline (1,01 g, 7.5 mmol) was added to a mixture of concentrated HCl (10 mL) and H_2O (10 mL) at 0 °C. In small portions, sodium nitrite (0.62 g, 9.0 mmol) was slowly added too. The reaction mixture was stirred for 2 hours keeping the temperature constant at 0 °C. A solution of sodium acetate (12.3 g, 150 mmol) in H_2O (33 mL) was then added, followed by the addition of sodium azide (0.97 g, 15 mmol) in small portions. The reaction mixture was stirred for 30 min at room temperature, and then extracted with *n*-pentane (50 mL x 3 times). The organic phase was washed with a concentrated NaCl solution and dried with $MgSO_4$. After vacuum removal of the solvent, a red oil was obtained that was further purified with a chromatographic column using *n*-hexane as eluent to get mesityl-azide as a yellow oil. Yield: 1.00 g (6.2 mmol, 83%).

^{1}H NMR ($CDCl_3$, 400 MHz): δ [ppm] = 6.83 (s, 2H, C**H**), 2.32 (s, 6H, o-C**H**$_3$), 2.25 (s, 3H, p-C**H**$_3$).

^{13}C NMR ($CDCl_3$, 400 MHz): δ [ppm] = 135.5 (1C, p-CH_3-**C**), 134.5 (1C, **C**-N), 132.0 (2C, o-CH_3-**C**), 129.6 (2C, **C**H), 20.8 (1C, p-**C**H_3), 18.2 (2C, o-**C**H_3).

IR: (KBr pellet) $\tilde{\nu}$ [cm-1] = 2920 (vw), 2115 (vs), 2089 (m), 2058 (w), 1479 (w), 1316 (w), 1279 (m), 853 (m).

6.3.21. Generation of the intermediate Cu-4-Sc

Under inert conditions, a colorless solution of the [(AN)Cu][BF_4] complex in anhydrous CH_2Cl_2 (1 mM, 2 mL) was cooled down to -90 °C. Then, 1.5 equivalents of Sc(OTf)$_3$ in anhydrous acetone (0.1 mL) and 1.5 equivalents of Mesitylazide in anhydrous CH_2Cl_2 (0.1 mL) were added in

that order to yield a deep purple intermediate. The generation of this species was monitored following the growth of the 560 nm band in the UV-vis spectrum.

Larger concentrations were used for preparing samples for spectroscopic techniques different than UV-vis, the characteristics of those samples are indicated in the text.

UV-vis (CH_2Cl_2, -90°C): λ_{max} (ε_{max}, $M^{-1}cm^{-1}$) 560 (2000), 670 (1360).

Cu K-edge XANES (for **Cu-3-Y** in dichloromethane with 5% acetone, 3.5 mM): shoulder at edge inflection point at 8981.5 eV.

6.4. References

[1] P. Gütlich, E. Bill, A. X. Trautwein, *Möβbauer Spectroscopy and Transition Metal Chemistry*, Springer, Berlin, **2011**.

[2] B. Ravel, M. Newville, *J. Synchrotron Radiat.* **2005**, *12*, 537–541.

[3] E. J. Baerends, T. Ziegler, J. Autschbach, D. Bashford, A. Bérces, F. M. Bickelhaupt, C. Bo, P. M. Boerrigter, L. Cavallo, D. P. Chong, et al., *ADF2013*, SCM, Theoretical Chemistry, Vrije Universiteit, Amsterdam, The Netherlands, **2013**.

[4] G. te Velde, F. M. Bickelhaupt, E. J. Baerends, C. Fonseca Guerra, S. J. a. van Gisbergen, J. G. Snijders, T. Ziegler, G. T. E. Velde, C. F. Guerra, S. J. Gisbergen, *J. Comput. Chem.* **2001**, *22*, 931–967.

[5] E. van Lenthe, E. J. Baerends, A. T. Chemie, V. Universiteit, D. Boelelaan, *J. Comput. Chem.* **2003**, *24*, 1142–1156.

[6] M. Swart, J. G. Snijders, *Theor. Chem. Acc.* **2003**, *110*, 34–41.

[7] M. Swart, F. M. Bickelhaupt, *J. Comput. Chem.* **2008**, *29*, 724–734.

[8] M. Swart, F. M. Bickelhaupt, *Int. J. Quantum Chem.* **2006**, *106*, 2536–2544.

[9] M. Swart, *Chem. Commun.* **2013**, *49*, 6650–6652.

[10] J. P. Perdew, *Phys. Rev. B* **1986**, *33*, 8822–8824.

[11] A. D. Becke, *Phys. Rev. A* **1988**, *38*, 3098–3100.

[12] S. Grimme, J. Antony, S. Ehrlich, H. Krieg, S. Grimme, J. Antony, S. Ehrlich, H. Krieg, *J.*

Chem. Phys. **2010**, *132*, 154104.

[13] M. Swart, *Chem. Phys. Lett.* **2013**, *580*, 166–171.

[14] P. R. T. Schipper, O. V Gritsenko, S. J. A. van Gisbergen, E. J. Baerends, *J. Chem. Phys.* **2000**, *112*, 1344.

[15] A Klamt, G. Schuurmann, *J. Chem. Soc. Perkin Trans. 2* **1993**, 799–805.

[16] A. Klamt, *J. Phys. Chem.* **1995**, *99*, 2224–2235.

[17] A. Klamt, V. Jonas, *J. Chem. Phys.* **1996**, *105*, 9972–9981.

[18] M. Swart, E. Rösler, F. M. Bickelhaupt, *Eur. J. Inorg. Chem.* **2007**, 3646–3654.

[19] C. C. Pye, T. Ziegler, *Theor. Chem. Acc.* **1999**, *101*, 396–408.

[20] E. van Lenthe, A. Ehlers, E.-J. Baerends, *J. Chem. Phys.* **1999**, *110*, 8943.

[21] E. van Lenthe, E. J. Baerends, J. G. Snijders, *J. Chem. Phys.* **1994**, *101*, 9783.

[22] E. van Lenthe, E. J. Baerends, J. G. Snijders, *J. Chem. Phys.* **1993**, *99*, 4597.

[23] S. Kundu, E. Matito, S. Walleck, F. F. Pfaff, F. Heims, B. Rábay, J. M. Luis, A. Company, B. Braun, T. Glaser, K. Ray, *Chem. a Eur. J.* **2012**, *18*, 2787–91.

[24] A. D. Becke, *J. Chem. Phys.* **1993**, *98*, 5648–5652.

[25] C. Lee, W. Yang, R. G. Parr, *Phys. Rev. B* **1988**, *37*, 785–789.

[26] *Basis sets were obtained from Extensible Comput. Chem. Environ. Basis Set Database, Version 4/22/01, Dev. Distrib. by Mol. Sci. Comput. Facil. Environ. Mol. Sci. Lab. Pacific Northwest*

[27] A. Schaefer, C. Huber, R. Alrichs, *J. Chem. Phys.* **1994**, *100*, 5829–5835.

[28] J. P. Perdew, K. Burke, Y. Wang, *Phys. Rev. B* **1996**, *54*, 16533–16539.

[29] R. Ditchfield, W. J. Hehre, J. A. Pople, *J. Chem. Phys.* **1971**, *54*, 724.

[30] M. J. Frisch; G. W. Trucks; H. B. Schlegel; G. E. Scuseria; M. A. Robb; J. R. Cheeseman; G. Scalmani; V. Barone; B. Mennucci; G. A. Petersson; H. Nakatsuji; M. Caricato; X. Li; H. P. Hratchian; A. F. Izmaylov; J. Bloino; G. Zheng; J. L. Sonnenberg; M. Hada; M. Ehara; K.

Toyota; R. Fukuda; J. Hasegawa; M. Ishida; T. Nakajima; Y. Honda; O. Kitao; H. Nakai; T. Vreven; J. A. Montgomery; J. E. Peralta; F. Ogliaro; M. Bearpark; J. J. Heyd; E. Brothers; K. N. Kudin; V. N. Staroverov; R. Kobayashi; J. Normand; K. Raghavachari; A. Rendell; J. C. Burant; S. S. Iyengar; J. Tomasi; M. Cossi; N. Rega; J. M. Millam; M. Klene; J. E. Knox; J. B. Cross; V. Bakken; C. Adamo; J. Jaramillo; R. Gomperts; R. E. Stratmann; O. Yazyev; A. J. Austin; R. Cammi; C. Pomelli; J. W. Ochterski; R. L. Martin; K. Morokuma; V. G. Zakrzewski; G. A. Voth; P. Salvador; J. J. Dannenberg; S. Dapprich; A. D. Daniels; O. Farkas; J. B. Foresman; J. V. Ortiz; J. Cioslowski; D. J. Fox, *Gaussian 09*; Gaussian, Inc., Wallingford CT, **2009**.

[31] F. Neese, U. Becker, D. Ganyushin, A. Hansen, D. Liakos, R. Izsak, C. Kollmar, S. Kossmann, T. Petrenko, C. Reimann, R. Christoph, R. Michael; Riplinger; Cristoph; B. Sandhoefer; I. Schapiro; K. Sivalingam; B. Wezisla; F. Wennmohs, *Program Version 3.0.2; 79 ORCA*, Max Planck Institute for Bioinorganic Chemistry. Muelheim/Ruhr, Germany.

[32] E. F. Valeev, J. T. Fermann, *libint2, Copyright ©,* 1996–2012.

[33] F. Neese, *Wiley Interdiscip. Rev. Comput. Mol. Sci.* **2012**, *2*, 73–78.

[34] A. Schäfer, H. Horn, R. Ahlrichs, *J. Chem. Phys.* **1992**, *97*, 2571.

[35] F. Weigend, R. Ahlrichs, *Phys. Chem. Chem. Phys.* **2005**, *7*, 3297–305.

[36] K. Eichkorn, O. Treutler, H. Ohm, H. Marco, R. Ahlrichs, *Chem. Phys. Lett.* **1995**, *240*, 283–290.

[37] K. Eichkorn, F. Weigend, O. Treutler, R. Ahlrichs, *Theor. Chem. Acc.* **1997**, *97*, 119–124.

[38] C. Steffen, K. Thomas, U. Huniar, A. Hellweg, O. Rubner, A. Schroer, *J. Comput. Chem.* **2010**, *31*, 2967–2970.

[39] M. T. S. Amorim, S. Chaves, R. Delgado, J. J. R. Fraústo da Silva, *J. Chem. Soc. Dalt. Trans.* **1991**, *938*, 3065–3072.

[40] T. W. Bell, H. J. Choi, W. Harte, M. G. B. Drew, *J. Am. Chem. Soc.* **2003**, *125*, 12196–12210.

[41] C. S. Rossiter, R. A. Mathews, J. R. Morrow, *Inorg. Chem.* **2005**, *44*, 9397–9404.

[42] F. F. Pfaff, *PhD Thesis: Synthese, Charakterisierung und Reaktivitätsstudien zu*

Hochvalenten Metalloxidoverbindungen, Humboldt Universität Zu Berlin, Berlin, Germany, **2015**.

[43] D. Macikenas, E. Skrzypczak-jankun, J. D. Protasiewicz, *J. Am. Chem. Soc.* **1999**, *121*, 7164–7165.

[44] S. Kundu, *PhD Thesis: Synthesis, Spectroscopic Characterization and Reactivity of the High-Valent Metal-Oxo/Imido Cores of the Late Transition Metals*, Humboldt-Universität Zu Berlin, Berlin, **2013**.

[45] S. Kundu, E. Miceli, E. Farquhar, F. F. Pfaff, U. Kuhlmann, P. Hildebrandt, B. Braun, C. Greco, K. Ray, *J. Am. Chem. Soc.* **2012**, *134*, 14710–14713.

Appendices

A1	Crystallographic data
A2	Lists of abbreviations
A3	Declaration
A4	Publications and presentations

A1. Crystallographic data

	Fe-1
Empirical formula	$C_{17}H_{30}F_6FeN_4O_7S_2$
Formula mass	636.42
Crystal habit, color	Colorless needles
Crystal dim. (mm)	0.08x0.25x0.1
Space group	P21/n
a [Å]	14.691(3)
b [Å]	19.067(3)
c [Å]	18.222(4)
α [°]	90
β [°]	90.354(15)
γ [°]	90
V [$Å^3$]	5104.1(17)
Z	8
T [K]	100
D [g cm^{-1}]	1.656
F000	2624.0
μ [mm^{-1}]	0.8444
T range	0.817-0.920
Refl. Collected	14061
R_{int}	0.0527
Parameters refined	675
wR_2	0.0963

A2. Lists of abbreviations

Techniques and technical terms

Asp	Aspartic acid
ATP	Adenosine triphosphate
B	Magnetic field
BDE	Bond disociation energy
Calc.	Calculated
CT	Charge transfer
Cys	Cysteine
DFT	Density functional theory
e^-	Electron
EA	Elemental analysis
EPR	Electron paramagnetic resonance
eqv.	Equivalents
ESI	Electrospray ionization
EXAFS	Extended X-ray absorption fine structure
Exp.	Experimental
GC	Gas chromatography
Glu	Glutamic acid
HAA	Hydrogen atom abstraction
HAT	Hydrogen atom transfer
His	Histidine
k_{obs}	Pseudo-first order rate constant
k_2	Second order rate constant
KIE	Kinetic isotope effect
MS	Mass spectroscopy
m/z	Mass per charge
$[M]^+$	Molecular ion peak
NMR	Nuclear magnetic resonance
PCET	Proton coupled electron transfer
rR	Resonance Raman
S	Electron spin
SCE	Saturated Calomel Electrode

Sim.	Simulated
SQUID	Superconducting quantum interference device
Tyr	Tyrosine
UV-vis	Ultraviolet-visible
XAS	X-ray absorption spectroscopy
XANES	X-ray absorption near edge spectroscopy

Units

Å	Angstrom (10^{-10} m)
Cm	Centimeter
°C	Degree Celsius
G	Gauss
Hz	Hertz
K	Kelvin
Kcal	Kilo calories
Mg	Milligram (10^{-3} g)
Min	Minute
mL	Milliliter (10^{-3} L)
mM	Millimolar (10^{-3} M)
Mm	Millimiter (10^{-9} m)
S	Second
T	Tesla
W	Watt

Latin expressions

ca.	Around
et al.	and coworkers
in situ	In the original place
per-se	In itself, intrinsically
tert-	Tertiary
via	By means of
vs.	Versus, against

Symbols

δ	Chemical shift (ppm)
δ’	Isomer shift (mm/s)
ΔE_Q	Quadrupole splitting (mm/s)
ε	Extinction coefficient ($M^{-1}cm^{-1}$)
λ	Wavelength (nm)
ν	Wavenumber (cm^{-1})

Chemicals

AcO^-	Acetate
AN	3,3’-iminobis(*N,N*-dimethylpropylamine)
BNAH	1-benzyl-1,4-dihydronicotinamide
CHD	Cyclohexadiene
DHA	Dihydroanthracene
Fc	Ferrocene
Fc^+	Ferrocenium
$Me_{10}Fe$	Decamethylferrocene
$Me_{10}Fc^+$	Decamethylferrocenium
Mes	Mesityl
^-OTf	Triflate (trifluoromethane sulfonate)
sPhIO	2-(*tert*-butylsulfonyl)-iodosylbenzene
sPhINTs	2-(tert-butylsulfonyl)(*p*-toluensulfonylimidoiodo)benzene
$sPhINAr^{NO2}$	2-(*tert*-butylsulfonyl)((4-nitrophenyl)sulfonylimidoiodo)benzene
$sPhINAr^{CF3}$	2-(*tert*-butylsulfonyl)((4-(trifluoromethyl)phenyl)sulfonylimidoiodo)benzene
TFA	Trifluoroacetic acid
Ts	Tosyl (*p*-tolysulfonyl)

A3. Declaration

Selbstständigkeitserklärung

Hiermit versichere ich, Inés Monte Pérez, dass ich die vorliegende Arbeit selbstständig und nur unter Einsatz der angegebenen Hilfsmittel und Quellen am Institut für Chemie der Humboldt-Universität zu Berlin angefertigt habe.

Inés Monte Pérez Berlin, den

A4. Publications and presentations

Publications:

- *Evidence of two-state reactivity in alkane hydroxylation by Lewis-acid bound copper–nitrene complexes*, S.-L. Abram, **I. Monte-Pérez**, F. F. Pfaff, E. R. Farquhar, K. Ray, *Chemical Communications*, **2014**, *50*, 9852-9854.

- *An Open-Shell Spin Singlet Copper-Nitrene Intermediate Binding Redox-innocent Metal Ions: Influence of the Lewis Acidity of the Metal Ions on Spectroscopic and Reactivity Properties* **I. Monte-Pérez**, S. Kundu, K. Ray, *Z. Anorg. Allg. Chem*., **2015**, *641*, 78-82.

- *Oxidation Reactions with Bioinspired Mononuclear Non-Heme Metal-Oxo Complexes*, X. Engelmann, **I. Monte-Pérez**, K. Ray, *Angew. Chem. Int. Ed.*, **2016**, *55*, 7632-7649.

Presentations:

- 2nd FUSION conference on activation of small molecules in Cancun, Mexico, 2016
Poster presentation: "*Isolation, characterization and reactivity evaluation of a series of copper-nitrene intermediates active in C-H bond activation*"

- ICIQ – UniCat summer school in Berlin, Germany, 2015
Poster presentation: "*A new reactive iron(IV)-oxo species: importance of subtle electronic changes in the reactivity of biologically relevant intermediates*"

- COST (European cooperation in science and technology) Meeting, Belgrade, Serbia, 2015
Oral presentation: "*Study of Reactive Intermediates of Late-Transition-Metal Compounds with Oxidizing Agents in C-H Bond Activation*"

- Koordinationschemie-Treffen in Paderborn, Germany, 2015
Oral presentation: "*Study of Reactive Intermediates of Late-Transition-Metal Compounds with Oxidizing Agents in C-H Bond Activation"*

- Niedersächsisches Katalyse Symposium (NiKaS) in Göttingen, Germany 2014
Poster presentation: "*A hexanuclear cobalt complex and its reactivity"*